Coordination Chemistry Reviews 426 (2021) 213544

Contents lists available at ScienceDirect

Coordination Chemistry Reviews

journal homepage: www.elsevier.com/locate/ccr

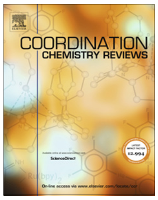

Review

Recent advances in process engineering and upcoming applications of metal–organic frameworks

UnJin Ryu [a,1], Seohyeon Jee [a,1], Purna Chandra Rao [b,1], Jeeyoung Shin [c,d], Changhyun Ko [d,e], Minyoung Yoon [b,*], Kyo Sung Park [f,*], Kyung Min Choi [a,d,*]

[a] Department of Chemical and Biological Engineering, Sookmyung Women's University, 100 Cheongpa-ro 47 gil, Yongsan-gu, Seoul 04310, Republic of Korea
[b] Department of Chemistry & Green-Nano Materials Research Center, Kyungpook National University, Daegu 41566, Republic of Korea
[c] Department of Mechanical Systems Engineering, Sookmyung Women's University, Seoul 04310, Republic of Korea
[d] Institute of Advanced Materials & Systems, Sookmyung Women's University, 100 Cheongpa-ro 47 gil, Yongsan-gu, Seoul 04310, Republic of Korea
[e] Department of Applied Physics, College of Engineering, Sookmyung Women's University, Seoul 04310, Republic of Korea
[f] Corporation R&D, Research Park, LG Chem, LG Science Park, 30, Magokjungang-10-Ro, Gangseo-Gu, Seoul, Republic of Korea

ARTICLE INFO

Article history:
Received 20 June 2020
Received in revised form 5 August 2020
Accepted 7 August 2020
Available online 18 September 2020

Keywords:
Metal–organic framework
Commercialization
Mass production
Future applications
Shaping
Dispersion

ABSTRACT

Progress in metal–organic frameworks (MOFs) has advanced from fundamental chemistry to engineering processes and applications, resulting in new industrial opportunities. The unique features of MOFs, such as their permanent porosity, high surface area, and structural flexibility, continue to draw industrial interest outside the traditional MOF field, both to solve existing challenges and to create new businesses. In this context, diverse research has been directed toward commercializing MOFs, but such studies have been performed according to a variety of individual goals. Therefore, there have been limited opportunities to share the challenges, goals, and findings with most of the MOF field. In this review, we examine the issues and demands for MOF commercialization and investigate recent advances in MOF process engineering and applications. Specifically, we discuss the criteria for MOF commercialization from the views of stability, producibility, regulations, and production cost. This review covers progress in the mass production and formation of MOFs along with future applications that are not currently well known but have high potential for new areas of MOF commercialization.

Abbreviations: MOF, metal–organic framework; ZIF, zeolitic imidazolate framework; DMF, *N,N*-Dimethyl formamide; DEF, *N,N*-Diethyl formamide; DMA, Dimethylacetamide; TEA, Triethylamine; STY, space–time yield, grams of MOF per cubic meter of reaction mixture per day of synthesis; NMP, N-methyl-2-pyrrolidone; CNG, compressed natural gas; PEI, Polyetherimide; PS, Polystyrene; PVA, Polyvinyl alcohol; MRA, mesoporous ρ-alumina; ABS, acrylonitril-butadiene-styrene; CA, Cellulose-acetate; PXRD, Powder x-ray diffraction; PVC, Polyvinylchloride; PVF, Polyvinylformal; PVB, Polyvinyl Butyral; DLS, Dynamic light scattering; BET, Brunauer–Emmett–Teller; PEG-CCM, polyethylene-glycol-modified mono-functional curcumin; MB, methylene blue; DDM, n-dodecyl β-D-maltoside; ECS, Extrusion-crushing-sieving; TIPS-HoP, Thermally induced phase separation-hot pressing; PM, Particulate matter; VOC, Volatile organic compound; CWA, Chemical warfare agent; PPC, Polypropylene/polycarbonate; PAN, Polyacrylonitrile; SEM, Scanning electron microscope; SBU, Secondary building unit; DFT, Density functional theory; SALI, Solvent assisted ligand incorporation; FT-IR, Fourier-transform infrared spectroscopy; NMR, Nuclear magnetic resonance; DRIFTS, Diffuse reflectance infrared fourier transform spectroscopy; XPS, X-ray photoelectron spectroscopy; SCXRD, Single-crystal X-ray diffraction; CWC, Chemical weapons convention; POM, Polyoxometalate; DMMP, Dimethyl methylphosphonate; GC–MS, Gas chromatography–mass spectrometry; EXAFS, Extended X-ray absorption fine structure; MMP, Methyl methylphosphonate; DIFP, Diisopropylfluorophosphate; MVTR, Moisture vapor transport rate; CEES, 2-Chloroethyl ethyl sulfide; DCP, Diethylchlorophosphonate; DFP, Diisopropyl fluorophosphate; ROS, Reactive oxygen species; *E. Coli*, Escherichia coli; MRSA, Methicillin-resistant staphylococcus aureus; MIC, Minimum inhibitory concentration; MBC, Minimum bactericidal concentration; PSM, Post-synthetic modification; CNF, Cellulose nanofiber; GRGDS, Gly-Arg-Gly-Asp-Ser; Fn, Fusobacterium nucleatum; Pg, Porphyromonas gingivalis; PEMFCs, Proton-exchange membrane fuel cells; SSEs, Solid-state electrolytes; MOGs, Metal-organic gels; LIBs, Lithium-ion batteries; SIBs, Sodium-ion batteries; hXAS, Hard X-ray absorption spectroscopy; sXAS, Soft X-ray absorption spectroscopy; EDLCs, Electrochemical double-layer capacitors; PANI, Polyaniline; ILDs, Interlayer dielectrics; ITRS, International technology roadmap for semiconductors; CVD, Chemical vapor deposition; MIM, Metal-insulator–metal; LMOF, Luminescent metal–organic framework; UPS, Ultraviolet photoelectron spectroscopy; EPA, Environmental protection agency; WHO, World health organization; LOD, Limit of detection; TNT, 2,4,6-trinitrotoluene; TNP, 2,4,6-trinitrophenol; 2,4-DNT, 2,4-dinitrotoluene; 4-NP, 4-nitrophenol; RDX, 1,3,5-trinitro-1,3,5-triazinane; LED, Light-emitting diode; WLED, White light emitting diode; CIE, Commission international ed'Eclairage.

[*] Corresponding authors at: Department of Chemistry & Green-Nano Materials Research Center, Kyungpook National University, Daegu 41566, Republic of Korea (M. Yoon); Corporation R&D, Research Park, LG Chem, LG Science Park, 30, Magokjungang-10-RoGangseo-Gu, Seoul, Republic of Korea (K.S. Park); Department of Chemical and Biological Engineering and Institute of Advanced Materials & Systems, Sookmyung Women's University, 100 Cheongpa-ro 47 gil, Yongsan-gu, Seoul 04310, Republic of Korea, Department of Chemical and Biological Engineering, Sookmyung Women's University, 100 Cheongpa-ro 47 gil, Yongsan-gu, Seoul 04310, Republic of Korea (K.M. Choi).

E-mail addresses: myyoon@knu.ac.kr (M. Yoon), kyosungp@lgchem.com (K.S. Park), kmchoi@sookmyung.ac.kr (K.M. Choi).

[1] These authors have equally contributed to the manuscript.

https://doi.org/10.1016/j.ccr.2020.213544
0010-8545/

Contents

1. Introduction

Metal–organic frameworks (MOFs) have attracted interest from various industrial and engineering fields such as petrochemicals, vehicles, gas, and even cosmetic and biomedical areas because of their high surface area, different porous environments, designable pore sizes, and synergistic effects of the metal ions and ligand functional groups [1–8]. Excellent progress has been made in MOF synthesis, structure, chemistry, properties, and applications on the fundamental level [9–13], but challenges remain both in the development of engineering processes and exploring game-changing applications on the industrial level. Recently, many research groups have focused on the development of MOF manufacturing, activation, shaping, and dispersion processes, and various startup and global companies have increased their efforts toward the development of MOFs for new business areas. However, these developments in engineering and industrial processes typically arise from studies performed according to the specific demands and goals of the individual projects. Therefore, the challenges and findings are difficult to share with researchers across various MOF-related fields.

In this review, we examine MOF issues and demands from process engineering and industrial points of view (Scheme 1). The criteria for MOF commercialization are discussed in terms of stability, producibility, regulations, and production cost. We also explore recent advances in processes for the scaled-up synthesis, product recovery, activation, drying, shaping, and dispersion of MOFs. Furthermore, we investigate possible future applications that are not currently well known but have significant potential to serve as new business areas for MOF commercialization. In this regard, we focus on purification, biological toxicant removal, antibacterial implementation, ion transport for solid-state electrolytes (SSEs), electrode materials, low-kappa dielectric materials, and sensors. We believe that this review will enhance the understanding of recent progress and future demands for MOF commercialization.

2. MOF commercialization criteria

MOFs have experienced rapid development in the last two decades, and there have been many reports on their synthesis, structure, processes, and applications. However, there are still several challenges in adapting MOFs to different industries. First, only a few MOFs maintain their properties in aqueous acidic/basic conditions [14–18]. Second, syntheses for the mass production of many MOFs have not yet been established [19–22]. Third, MOF production costs are still higher than those of competing materials (activated carbon, silica, and zeolites). In this section, we focus on criteria for MOF commercialization in terms of stability, producibility, regulations, and production costs.

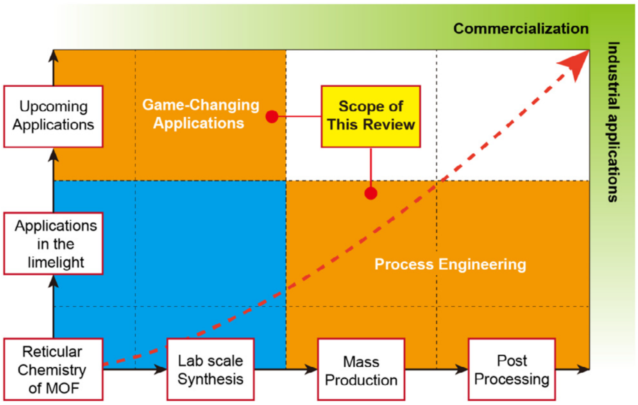

Scheme 1. Scope of this review paper: From process engineering to upcoming applications.

2.1. Stability

Since MOF-5 was first published as a model compound in 1997 [23], most related research interest has focused on increasing the surface area, which has resulted in values as high as ~7,000 $m^2 g^{-1}$ [24]. However, many MOFs, especially those based on Zn, decompose easily from humidity and chemicals. Other MOFs synthesized through hydrothermal reactions have been reported to have better stabilities but are still below the necessary specifications [25,26]. Many studies have suggested potential MOF applications in various devices and appliances. Adapting MOFs to such industrial applications places key emphasis on the lifetime of the components. The acceleration test is the standard method to judge the lifetime of a module or set and is usually performed under 85 °C/85% humidity or 120 °C steam conditions to shorten the test period. Unfortunately, most MOFs lose their properties under these conditions because of their lack of aqueous acid/base stability. There is a pioneer reference mentioning the steam stabilities of MOFs [27]. Steam stability was investigated through experimental and calculated observations on 10 types of MOF consisting of Zn, Cu, Cr and Al metal source. It demonstrates that the bonding strength of metal oxide and linker is the most important factor of steam stability. Zr/Hf/Al-based MOFs and zeolitic imidazolate frameworks (ZIFs) have been demonstrated as capable of passing the standard acceleration test, and an interesting method has also been reported for fortifying the hydrothermal stability of MOFs [15]. For example, the HKUST-1 consists of three different sized cages and these cages form a ship-in-a-bottle complex that is preventing access to reactants and improving stability.

2.2. Producibility

The second challenge in MOF commercialization is scaling up their production. Approximately 70,000 MOFs have been reported [28], but their typical synthetic schemes are designed to yield <1 g per batch to achieve high-quality crystallinity. Crystallization is highly sensitive to many factors such as reaction temperature, heating rate, ligand/metal ion concentration, the empty space of the reaction vessel, and even the roughness of the reactor surface. Therefore, the crystallization process is one of the factors hindering the producibility of MOFs. Sometimes, a synthetic scheme must be completely modified to increase the reaction volume. There are also several reaction types that are not conducive to a large-volume scale such as vapor/base diffusion, solvent layering, and solvent evaporation because of their limited reaction volumes. Thus far, solvothermal/hydrothermal/mechanochemical reactions have been regarded as appropriate for the mass production of MOFs.

Another factor in producibility is reaction temperature. The usual MOF synthesis involves heating of the reaction medium, and in many cases, the temperature must exceed the boiling points of the solvents [29–31]. Usually, water-based reactions are heated to above 100 °C and require a high-pressure reactor, called a "digestion bomb." This approach is inadequate for large-scale production because it requires costly, large-scale, pressure-proof reactors, which decreases the producibility. Room-temperature (RT) or mild heating (below the solvent boiling points) is highly recommended to enhance the producibility of manufacturing processes. Finally, the reactant concentration is also important for improving the production efficiency. Usually, the product crystallinity improves in dilute conditions, but the yield per batch reaction decreases, which could result in higher labor and facility costs. High concentrations also typically worsen the crystallinity and surface area. There are good references that considered concentration in their cost assumptions [32]. This patent from BASF SE introduced a strong base for large-scale synthesis of zinc methylimidazole (ZIF). The synthesized ZIF has a high Langmuir surface area of 2000 m^2/g while showing a high synthesis yield of 760 kg m^{-3} day^{-1}.

2.3. Regulations

Regulations are perhaps the least-considered factor but the most serious issue for commercialization. Based on previous reports, many studies used Hg, Cd, Mn, Cr, or Ni as the metal for the prepared MOFs. In the EU and many countries including the US, Japan, and Korea, these metals are highly controlled and restricted by the government because of their potential negative environmental effects and toxicity. Ligands and solvents are under the same regulations. For example, *N,N*-dimethylformamide (DMF), dimethylacetamide (DMA), and *N*-methyl-2-pyrrolidone (NMP) are highly controlled materials in the EU, where their concentrations in products must be <3000 mg kg^{-1} [33]. Furthermore, many MOFs are synthesized in amide solvents and can contain them after activation. For the performance and regulation of MOF mass product, an efficient activation process is mandatory.

Another issue is a chemical registration with the government. For example, the Korean government has enforced a chemical registration law since 2015 dictating that all chemicals and their safety information must be reported to the government if over 1000 kg $year^{-1}$ is produced and sold to customers. Since MOFs can have multiple topologies even with the same starting components, it could become mandatory to file safety information (oral/inhale/dermal toxicity data) for all the different variations.

2.4. Production cost

Production cost, another key factor in MOF commercialization, usually comprises the costs of materials, labor, and facilities. Facility costs are directly connected to the reaction conditions (pressure, concentration, yield) and procedures (number of washing and drying cycles), which have been aptly discussed in the literature [34–40]. This review focuses only on material costs in terms of yield.

There are four components in MOF syntheses: solvent(s), metal source(s), organic ligand(s), and acid/base catalyst. The material cost can be categorized into three groups based on the types of components: 1) Standard ligand and standard metal (e.g., terephthalic acid and Zn/Cu/Zr); 2) specialized ligand and standard metal (e.g., 2,5-dihydroxyterephthalic acid and Zn/Cu/Mg); and 3) standard ligand and specialized metal (e.g., terephthalic acid and Hf/Pd). The prices of the materials in the examples below were obtained from SciFinder without further inquiry.

A typical example of the first cost case is MOF-5, where the parameters and yield for synthesis were adapted from a previous paper [41]. Obtaining 1 kg of activated MOF-5 requires 81.30 L of DMF, 1.03 kg of terephthalic acid, and 3.45 kg of zinc acetate dihydrate for 63% yield; these component amounts cost 414.6, 34.0, and 78.7 USD, respectively. The total material cost for MOF-5 is 527.3 USD kg^{-1}, of which 78.6% comes from the solvent. In this case, solvent recycling, cheaper solvent, and concentrated formulas are strongly recommended to achieve competitive prices compared with other candidates (activated carbon, zeolites, silicas).

Ni-MOF-74 is an example of the second cost case, with a specialized ligand and standard metal; the synthesis parameters and yield were adapted from a previous paper [42]. Obtaining 1 kg of activated Ni-MOF-74 requires 4.75 L of water, 959.9 g of 2,5-dihydroxy-1,4-benzenedicarboxylic acid, and 941.14 g of nickel acetate, which cost 8.9, 689.6, and 188.2 USD, respectively. The total material cost of Ni-MOF-74 is 886.7 USD kg^{-1}, of which approximately 78% is for the ligand. The biggest challenge in this case is to find an adequate material supplier or alternative ligand. One example of an alternative ligand is 4,6-dihydroxy-1,3-benzenedicarboxylic acid, the MOF of which has similar properties and topology to those of MOF-74 [43]. Unlike 2,5-dihydroxy-1,4-benzenedicarboxylic acid, 4,6-dihydroxy-1,3-benzenedicarboxylic acid can be synthesized by a one-step reaction and thus costs less.

UiO-66 is an example of the third cost case, with a standard ligand and specialized metal. The parameters and yield of UiO-66 were adapted from a previous paper [44]. Obtaining 1 kg of activated UiO-66 requires 23.81 L of DMF, 924.7 g of zirconium chloride, 659.2 g of terephthalic acid, and 401.9 g of concentrated HCl; these amounts cost 121.4, 358.0, 21.8, and 2.7 USD, respectively. The total material cost of UiO-66 is 503.9 USD kg^{-1} (Fig. 1).

The material costs of MOFs are much higher than those for other adsorbents such as activated carbon, zeolites, and silica gel (40, 47.5, and 33.5 USD kg^{-1}, respectively). A target cost for MOFs of 15 USD kg^{-1} has been reported [40], toward which several approaches have been suggested. First, the solvent must be collected and reused several times. DMF is used in the synthesis of MOF-5 and UiO-66 and accounts for 78.6% and 71.7%, respectively, of the material costs. Solvent recycling is the most important factor for cost-saving with MOF synthesis. Solvent recovery systems are usually installed in petrochemical factories. Another approach is to use water as a solvent, as is the case for Ni-MOF-74, where the water solvent accounts for only 1% of the material cost. However, water-based syntheses require high-pressure reaction vessels, which are difficult to adapt to large-scale production. The third method is mechanochemical synthesis, which requires only a small amount of solvent compared with solvo/hydrothermal reactions. The mechanochemical synthesis of a MOF was first reported in 2006 [45] and has since been used to synthesis several MOFs such as COF [46–48], MOF-5 [49], ZIF-8 [50–52], MIL-53 [53], MIL-101 [54]. However, no mechanochemical syntheses for Zr-based MOFs have been established. UiO-66 MOFs with functional groups (amine, fluoride) have been reported, but pristine UiO-66 still requires a solvothermal method. The pioneer of mechanochemical synthesis is MOF Technologies [54] in Belfast, UK.

Another cost factor is the choice of an appropriate metal source. Metal sources for MOF syntheses are usually selected from nitrates, sulfates, acetates, halides, or oxides. One factor determining the metal selection is its solubility in the reaction solvent. MOF synthesis is highly similar to crystallization, and thus solubility is critical for obtaining high-quality products. Metal nitrates, acetates, and sulfonates are popular choices in many studies because they are

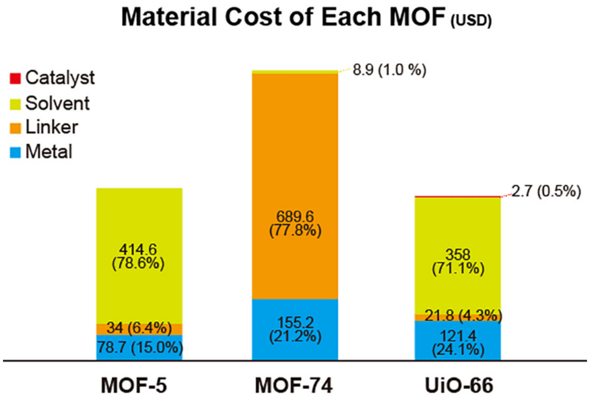

Fig. 1. Material Cost of MOF-5, Ni-MOF-74, UiO-66(USD).

highly soluble in the typical solvents employed in MOF syntheses, such as DMF, alcohol, and water. Halides are another common choice, especially for UiO MOFs, whereas oxides are perhaps the least common because of their poor solubility in many solvents. Nitrates, acetates, and sulfates remain as anions in the solution after the reaction, leading to higher costs for waste chemical deposition and limiting the recycling of used solvents. Halide metal sources have the additional disadvantage of producing HCl gas from some metal ions (for example, $ZrCl_4$) when dissolved in DMF. This necessitates an acid-resistant coating on the walls of the reactor or changing to a higher quality reactor material such as stainless steel.

Finally, the organic ligands are generally selected from polymer monomers or the intermediates of drugs or pesticides. One example is terephthalic acid, which is a monomer of polyethylene terephthalate and is thus already established for mass production. Other examples are imidazole and its derivatives. Imidazole is a component of many drugs, such as antifungal and antibacterial medicines. Since various derivatives are on the market for the drug industry, they are easy to adapt to MOF chemistry.

2.5. Road to commercialization: from hydrogen/methane storage by BASF and startups

The most established application in MOF is a gas storage of hydrogen, methane, acetylene and SF_6. The advantage of MOF is to reduce tank pressure for storage or increase the capacity in same volume. A typical example is a hydrogen storage. Since MOF-5 was firstly reported as hydrogen adsorbent in 2003 [55], series of papers have been reported for hydrogen storages [56–59]. The hydrogen storage material is the core component of fuel cell vehicle and the requirement is given by the department of energy (DOE). The DOE targets are 4.5 wt% (gravimetric working capacity) and 30 g L^{-1} (volumetric working capacity) by 2020. Some MOFs satisfy the DOE gravimetric target so far [60].

The front runner in MOFs commercialization is BASF. BASF started MOF research in 1999 and they launched the first Product in 2013 for compressed natural gas (CNG) storage in heavy duty trucks [61]. However, the CNG vehicle is not still popular yet and the commercialization is still on the way. The application in next generation vehicle is not ripen and would take more times to sell in market. Another application on market is specific gas storage. NuMat tech announced its ION-X technology in 2017 for AsH_3, PH_3, BF_3 storage with Linde (current Versum Materials). Those gases are used in semiconductor manufacturing. The company reported their materials improved the tank gas capacity and delivered to the customers [62].

Now there are some startups trying to launch MOFs in market or selling MOFs. The list is following, MOF technologies, Promethean Particles, Immaterial, Porous Liquid Technologies, Tarsis Technology (UK), NuMat technologies, Framergy, Mosaic Materials, Coordination Pharmaceuticals, Matrix Sensors, Inmondo Tech, Water Harvesting, MPower, Nanoshel, Panacenano (US), MOFapps, ProfMOF (Norway), MOFwork (Australia), ACSYNAM (Canada), NovoMOF (Switzerland), Atomis, Fuji Pigments (JP), Chemsoon(China) (Fig. 2).

3. MOF mass production processes

For more than two decades, numerous MOFs have been discovered and synthesized in academia. Their characteristics and applications have been widely studied, and now it is time to move forward with their practical mass production and application. MOF synthesis requires chemical components such as organic ligands, metal ions, solvents, and modulators, as well as thermal energy and pressure conditions. Research on the academic level has yielded diverse MOFs and synthetic techniques on the gram scale. However, the units required for commercial usage are tons and kilograms, which necessitate entirely new synthetic procedures for mass production. In this context, the areas of concern are the chemical costs, reaction vessel efficiency, reaction yields, reproducible quality, environmental regulations, and mild conditions for safety. In general and lab-scale MOF synthetic procedures, the organic ligands and metal precursors are chemically combined in organic solvents to afford powder products, which are then recovered from the reaction solution. Finally, the product is activated to afford empty pores in the resulting MOFs. This section will discuss how to produce MOFs on a large scale and what kinds of procedures have been chosen for industrial-scale production. The scaling methods are divided into static and continuous processes, and we will introduce various synthetic strategies and methods for each.

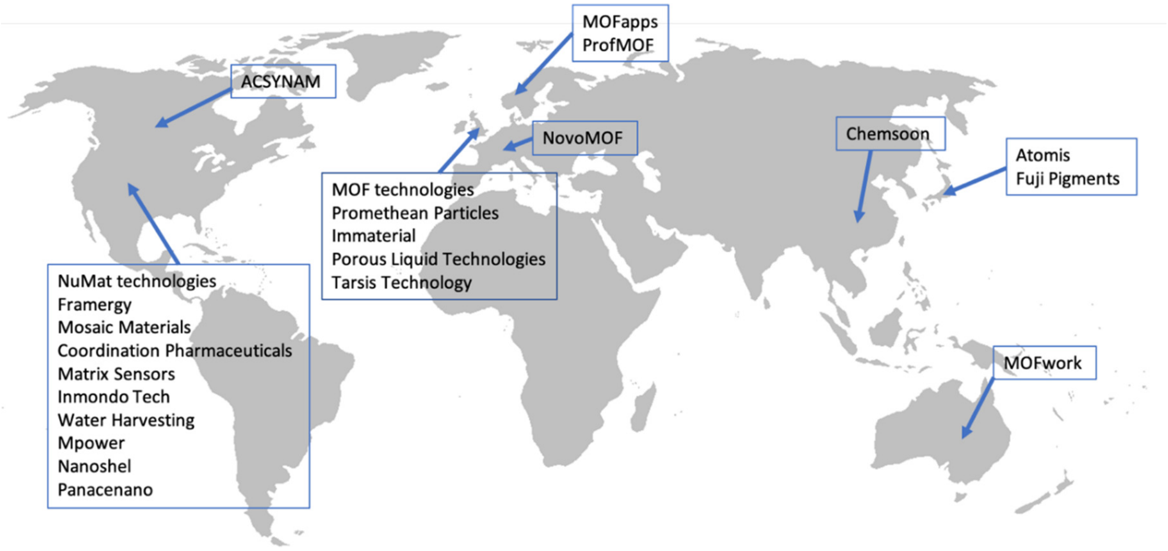

Fig. 2. Global map for MOF companies.

3.1. Synthesis scaling

3.1.1. Static processes

Static processes are based on fixed reaction vessels, and for scaling, most approaches expand the size of the container based on the lab-scale method. A majority of static processes employ solvents to mediate the reaction between the organic ligands and metal ions. Considering environmental regulations and cost concerns, it is desirable to develop more solvent-free synthetic systems, but the common synthetic procedures still rely on solvent-based systems. Depending on the equipment and energy source, solvent syntheses can be divided into ambient temperature (RT) and ambient pressure (1 atm), high-temperature (>RT) and ambient pressure (1 atm), high-temperature (>RT) and high pressure (>1 atm), microwave heating, sonochemical, and electrochemical syntheses. Solvent-free processes are mainly mechanochemical, typically via grinding or ball-milling. In the next section, these methods will be introduced and discussed in terms of their pros and cons with representative cases.

3.1.1.1. Solvent-based static processes. In solvent-based static syntheses, MOFs are synthesized by adding energy to the solvent in which the organic ligands and metal precursors are dissolved in a fixed vessel. Because solvent-based static syntheses are the most common in the traditional academic community, a database of MOF syntheses for various conditions has accumulated, allowing for easy access to scaled-up syntheses by expanding the reactor size. This type of method also facilitates diverse reaction conditions for general MOF syntheses as well as more specific conditions. However, the larger the reaction becomes, the more solvent is required. In particular, polar aprotic solvents, which are widely used in MOF synthesis due to their ability to solubilize the reactants, generally have a high boiling point and thus require a high temperature for hydrothermal synthesis. Most of these solvents are organic, such as DMF, DEF (*N,N*-diethylformamide), and DMA, which are environmentally regulated and expensive, accounting for 60% of the total MOF synthesis cost. In addition, the use of fixed vessels makes it difficult to automate static solvent syntheses into continuous processes.

- Ambient temperature (RT) and ambient pressure (1 atm) processes

The types of MOFs that can be easily synthesized at RT are primarily based on Cu and Zn, such as MOF-5 [41], HKUST-1 [41,63], and ZIF-8 [64] as well-known examples. The organic ligands and metal salts are usually pre-activated in separate solutions, ready for vigorous nucleation upon mixing (Fig. 3a). Ligands can be pre-activated ligand by either using a salt-like ligand [65] or deprotonating the ligand by adding a base [41,64,65] (Fig. 3b). This increases the solubility of the ligand in polar solvents to improve the reactivity, and the deprotonated moiety has a pre-activated form that can immediately participate in the synthesis. As examples, MIL-53(Al) and MOF-5 were synthesized at RT using a sodium carboxylate-type pre-activated ligand (sodium terephthalate) and a general carboxylic acid-type ligand (terephthalic acid) with added NaOH, respectively [65]. In addition, with other bases, MOF-5 and ZIF-8 were synthesized by inducing ligand deprotonation with trimethylamine (TEA) [41,64]. For the metal reagent, the reactivity depends on the type of counter anion in the metal salt. It is advantageous to use metal salts with acetate ($CO_2CH_3^-$) as the counter anions since they exhibit faster nucleation than nitrate (NO_3^-), sulfate (SO_4^{2-}), and chloride (Cl^-) salts [41,63,65,66]. Huo et al. synthesized HKUST-1 with $Cu(NO_3)_2$ and $Cu(CO_2CH_3)_2$ and

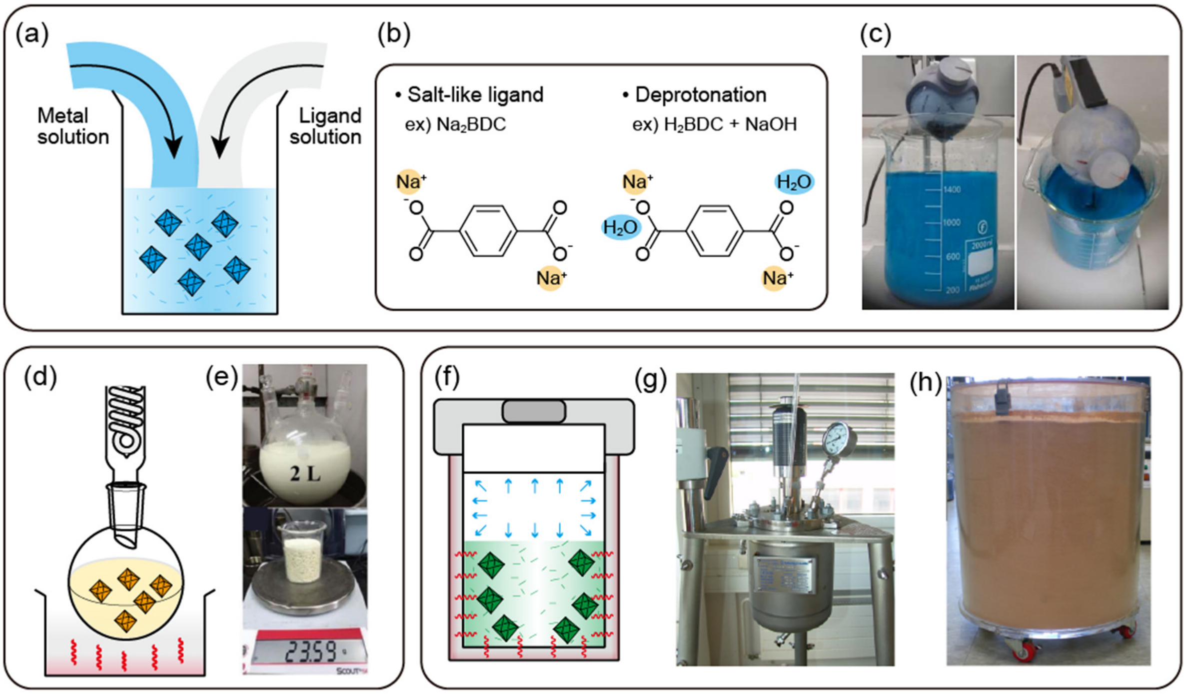

Fig. 3. Ambient temperature (RT) and ambient pressure (1 atm) process (a) Schematic illustration (b) Strategies to synthesize MOF (c) Photographs of synthesizing HKUST-1 in 1.2 L aqueous solvent. Reproduced with permission from [63]. Copyright 2013 Royal Society of Chemistry. **High-temperature (>RT) and ambient pressure (1 atm) process** (d) Schematic illustration (e) Photographs of UiO-66-NH_2 (upper) reaction equipment (lower) synthesized to 23.59 g. Adopted with permission from [69]. Copyright 2017 Royal Society of Chemistry. **High-temperature (>RT) and pressure (>1 atm) process** (f) Schematic illustration (g) Photograph of 3 L autoclave for large-scale MIL-101(Cr) production. Reproduced with permission from [75]. Copyright 2015 by Royal Society of Chemistry. (c) Digital image of 70 L box containing large-scale produced MIL-100(Fe). Reproduced with permission from [76]. Copyright 2012 Elsevier.

compared the synthetic properties. The use of the acetate yielded a higher amount of particles in a shorter time due to rapid nucleation, where the precursors achieved efficiencies of 41 and 2035 g m^{-3} d^{-1} STY (space–time yield; grams of MOF per cubic meter of reaction mixture per day of synthesis), respectively (Fig. 3c) [63].

Ambient-temperature solvent synthesis is the most facile way to produce MOF particles and can be scaled up without additional costs or energy for nucleation and growth. It is advantageous to use heat-labile ligands such as acetylenedicarboxylic acid and functionalized ligands [41,65]. In addition, ligands in the form of a salt (e.g., Na_2BDC) generate harmless salts ($NaNO_3$, NaCl) rather than corrosive acids (HNO_3, HCl) as byproducts, which is eco-friendly and safe [65], and the issue of surface area reduction due to ligand insertion into the pores during synthesis is alleviated. Nitrates have strong oxidizing properties and may explode with organic ligands, and thus other metal salts should be selected for mass production. Solvent costs and environmental issues must also be considered as the amount of solvent increases relative to the reaction capacity for mass production. In addition, there are limitations on the types of MOFs that can be synthesized at RT, and a deprotonated ligand can only be used if the ligand or metal is stable under basic conditions (Table 1).

- High-temperature (>RT) and ambient pressure (1 atm) processes

Most RT MOF syntheses studied in academic laboratories have yield limitations below the gram scale with exceptions such as HKUST-1, and thus it is a challenge to produce MOFs on an industrial scale at RT. On the other hand, in a high-temperature reaction, the injected thermal energy increases the solubility and reactivity of the precursors with the solvent and promotes nucleation, allowing for the production of MOFs with high yields in short reaction times (Fig. 3d). Additionally, high-temperature synthesis enables the production of tetravalent metal-based MOFs, which

Table 1

Summary of MOF that synthesized with ambient temperature (RT) and ambient pressure (1 atm) process.

MOF	Metal source	Ligand	Modulator	Solvent	Time	STY (kg m^{-3} day^{-1})	Yield (g)	Yield (%)	Surface area (m^2 g^{-1})	Ref
MOF-5	Zinc acetate dihydrate	Terephthalic acid	TEA	DMF	2.5 h	–	4.92	63	3909	[41]
MOF-5	Zinc acetate dihydrate	Terephthalic acid	–	DMF	45 min	–	–	–	–	[41]
MOF-74	Zinc acetate dihydrate	2,5-Dihydroxyterephthalic acid	–	DMF	18 h	–	0.27	69	1187	[41]
MOF-177	Zinc acetate dihydrate	Benzenetribenzoic acid	–	DEF	3 h	–	0.49	60	4944	[41]
HKUST-1*	Copper acetate monohydrate	1,3,5-Benzenetricarboxylic acid	TEA	DMF/EtOH/water	23 h	–	0.32	44	–	[41]
IRMOF-0	Zinc acetate dihydrate	Acetylenedicarboxylic acid	TEA	DMF	overnight	–	–	–	–	[41]
HKUST-1	Copper(II) acetate monohydrate	1,3,5-Benzenetricarboxylic acid	–	water	1 h	2035	–	84.8	1763	[63]
HKUST-1	Copper(II) nitrate hemi (pentahydrate)	1,3,5-Benzenetricarboxylic acid	–	water	1 h	41	–	34.2	1403	[63]
ZIF-8	Zinc nitrate hexahydrate	2-Methylimidazole	TEA	water	30 min	–	–	90	491.54	[64]
MIL-53(Al)	Aluminum nitrate nanohydrate	Disodium terephthalate	–	water	4 h-7d	–	–	–	1048	[65]
MIL-53(Al)	Aluminum nitrate nanohydrate	Terephthalic acid	NaOH	water	24 h	–	–	–	1072	[65]
NH_2-MIL-53(Al)	Aluminum chloride hexahydrate	2-Aminoterephthalic acid	NaOH	water	24 h	–	–	–	–	[65]
NO_2-MIL-53(Al)	Aluminum nitrate nanohydrate	2-Nitroterephthalic acid	NaOH	water	24 h	–	–	–	–	[65]
MOF-74(Zn)	Zinc acetate dihydrate	2,5-Dihydroxyterephthalic acid	NaOH	water	24 h	–	–	–	–	[65]
MOF-5	Zinc nitrate hexahydrate	Disodium terephthalate	–	DMF	24 h	–	–	–	–	[65]
MOF-74(Zn)	Zinc acetate dihydrate	2,5-Dihydroxyterephthalic acid	–	DMF	20 h	–	–	–	867	[67]
MOF-74(Ni)	Nickel acetate tetrahydrate	2,5-Dihydroxyterephthalic acid	–	DMF	20 h	–	–	–	402	[67]
MOF-74(Co)	Cobalt acetate tetrahydrate	2,5-Dihydroxyterephthalic acid	–	DMF	20 h	–	–	–	521	[67]
MOF-74(Mn)	Manganese acetate tetrahydrate	2,5-Dihydroxyterephthalic acid	–	DMF	20 h	–	–	–	491	[67]
MOF-74(Mg)	Magnesium acetate tetrahydrate	2,5-Dihydroxyterephthalic acid	–	DMF	20 h	–	–	–	1007	[67]

Table 2
Summary of MOF that synthesized with high-temperature (>RT) and ambient pressure (1 atm) process.

MOF	Metal source	Ligand	Modulator	Solvent	Time	Temperature (℃)	STY (kg m^{-3} day^{-1})	Yield (g)	Yield (%)	Surface area (m^2 g^{-1})	Ref
Al-fum*,[a]	Aluminum sulfate octadecahydrate	Fumaric acid	NaOH	water	10 min	RT	4742	26.2	76%	723	[68]
Al-fum*	Aluminum sulfate octadecahydrate	Fumaric acid	NaOH	water	10 min	60	5339	29.5	86%	1140	[68]
MOF-74(Ni)	Nickel acetate tetrahydrate	2,5-Dihydroxyterephtalic acid	–	water	1 h	160 (reflux)	680	17.9	91.60%	1233	[42]
MOF-74(Mg)	Magnesium nitrate hexahydrate	2,5-Dihydroxyterephtalic acid	–	DMF/EtOH/water	24 h	120 (reflux)	–	7.6	–	984	[73]
MOF-174(Mg)	Magnesium nitrate hexahydrate	4-(4-carboxy-3-hydroxy-phenyl)-2-hydroxy-benzoic acid	–	DMF/EtOH/water	12 h	120 (reflux)	–	3.82	–	2465	[73]
MOF-184(Mg)	Magnesium nitrate hexahydrate	4-[2-(4-carboxy-3-hydroxy-phenyl)ethynyl]-2-hydroxy-benzoic acid	–	DMF/EtOH/water	24 h	120 (reflux)	–	0.78	–	3154	[73]
MOF-74(Ni)	Zinc nitrate hexahydrate	2,5-Dihydroxyterephtalic acid	–	DMF/EtOH/water	24 h	120 (reflux)	–	46.4	–	1176	[73]
MOF-174(Ni)	Zinc nitrate hexahydrate	4-(4-carboxy-3-hydroxy-phenyl)-2-hydroxy-benzoic acid	–	DMF/EtOH/water	12 h	120 (reflux)	–	2.82	–	1444	[73]
MOF-184(Ni)	Zinc nitrate hexahydrate	4-[2-(4-carboxy-3-hydroxy-phenyl)ethynyl]-2-hydroxy-benzoic acid	–	DMF/EtOH/water	12 h	120 (reflux)	–	1.95	–	2449	[73]
UiO-66	Zirconyl chloride octahydrate	Terephthalic acid	Formic acid	DMF	2 h	140 (reflux)	–	100	–	604	[71]
MOF-801	Zirconyl chloride octahydrate	Fumaric acid	Formic acid	DMF	2 h	140 (reflux)	–	100	–	838	[71]
UiO-66-NH$_2$	Zirconium chloride	2-Aminoterephthalic acid	Acetic acid/water	DMF	15 min	120 (reflux)	–	23.59	90.70%	1075	[69]
UiO-66	Zirconium chloride	Terephthalic acid	Acetic acid/water	DMF	15 min	120 (reflux)	–	–	–	995	[69]
UiO-66-(OH)$_2$	Zirconium chloride	2,5-Dihydroxyterephtalic acid	Acetic acid/water	DMF	15 min	120 (reflux)	–	–	–	575	[69]
UiO-66–2,6-NDC	Zirconium chloride	2,6-naphthalenedicarboxylic acid	Acetic acid/water	DMF	15 min	120 (reflux)	–	–	–	781	[69]
UiO-67	Zirconium chloride	Biphenyl-4,4′-dicarboxylic acid	Acetic acid/water	DMF	15 min	120 (reflux)	–	–	–	2087	[69]
BUT-12	Zirconium chloride	H_3CTTA**	Acetic acid/water	DMF	15 min	120 (reflux)	–	–	–	1254	[69]
PCN-222-Ni	Zirconium chloride	Tetrakis(4-carboxyphenyl)porphyrin-Ni	Acetic acid/water	DMF	15 min	120 (reflux)	–	–	–	1724	[69]
PCN-222-Co	Zirconium chloride	Tetrakis(4-carboxyphenyl)porphyrin-Co	Acetic acid/water	DMF	15 min	120 (reflux)	–	–	–	–	[69]
Hf-UiO-66	Hafnium tetrachloride	Terephthalic acid	Acetic acid/water	DMF	15 min	120 (reflux)	–	–	–	–	[69]
Hf-UiO-66-NH$_2$	Hafnium tetrachloride	2-Aminoterephthalic acid	Acetic acid/water	DMF	15 min	120 (reflux)	–	–	–	–	[69]
Hf-UiO-66-(OH)$_2$	Hafnium tetrachloride	2,5-Dihydroxyterephtalic acid	Acetic acid/water	DMF	15 min	120 (reflux)	–	–	–	–	[69]
Hf-UiO-66–2,6-NDC	Hafnium tetrachloride	2,6-naphthalenedicarboxylic acid	Acetic acid/water	DMF	15 min	120 (reflux)	–	–	–	–	[69]
Hf-BUT-12	Hafnium tetrachloride	H_3CTTA	Acetic acid/water	DMF	15 min	120 (reflux)	–	–	–	–	[69]
CAU-10-H	Aluminum sulfate	Sodium isophthalate	NaOH	water	3 h	reflux	–	–	–	–	[74]
CAU-10-H	Aluminum sulfate	Sodium isophthalate	Sodium aluminate	EtOH	10 h	reflux	–	500	93%	–	[74]

*Basolite A520, **5′-(4-carboxyphenyl)-2′,4′,6′-trimethyl-[1,1′:3′,1″-terphenyl]-4,4″-dicarboxylic acid), [a] Control condition of Al-fum.

Table 3
Summary of MOF that synthesized with high-temperature (>RT) and pressure (>1 atm) process.

MOF	Metal source	Ligand	Modulator	Solvent	Reactor	Time (h)	Temperature (°C)	STY(kg m^{-3} day^{-1})	Yield (g)	Yield (%)	Surface area (m^2 g^{-1})	Ref
MIL-100(Fe)	Iron(III) nitrate nonahydrate	Trimesic acid	–	water	200L Metal alloy reactor	12	160	1700	–	–	2280	[76]
MIL-101(Cr)	Chromium(III) nitrate nonahydrate	Terephthalic acid	Nitric acid	water	3L Autoclave	15	200	–	127.1	82.3	3450	[75]
HKUST-1 (Cu-BTC)	Copper(II) nitrate hemi (pentahydrate)	Trimesic acid	–	EtOH/ water	Autoclave	18	150	–	80	–	964.5	[77]
UiO-66	Zirconium chloride	Terephthalic acid	HCl	DMF	100L Glass reactor	24	120	–	–	93	1387	[44]
MIL-101(Cr)	Chromium(III) nitrate nonahydrate	Terephthalic acid	–	water	Teflon rector	11	210	–	0.1	–	3800	[78]
MIL-100(Fe)	Iron chloride	Trimesic acid	–	water	Teflon rector	8	160	–		–	1500	[78]
UiO-67	Zirconium chloride	Biphenyl-4,4′-dicarboxylic acid	–	DMF	–	24	120	–	–	–	1800	[79]
Zr-TPDC (UiO-68)	Zirconium chloride	Terphenyl dicarboxylic acid	–	DMF	–	24	120	–	–	–	4000	[79]
NH_2-UiO-66	Zirconium chloride	2-Aminoterephthalic acid	–	DMF	–	24	120	–	–	–	–	[79]
MOF-867	Zirconium chloride	2,2′-bipyridine-5,5-dicarboxylic acid	–	DMF	–	48	100	–	–	–	–	[79]

are difficult to nucleate without added energy. Because tetravalent metal-based MOFs have a stronger M^{n+}-O interaction than di- and trivalent metals, ligand exchange for crystallization is slower.

High-temperature processes are favorable in terms of high yields and time efficiency compared with RT processes. In a previous study on Al-MOF, the synthetic conditions were kept the same, and the temperature was adjusted to RT or 60 °C (68,72). The higher reaction temperature not only increased the STY from 4742 to 5339 g m^{-3} d^{-1} but also nearly doubled the surface area from 723 to 1140 m^2 g^{-1}.

In particular, heating processes allow for the synthesis of Zr-, Hf-, and Ti-based MOFs, which are difficult to react at RT because thermal energy is needed to accelerate the binding of the metal salts and ligands for nucleation [69,70]. However, even with heating, the M^{n+}-O bond is strong, and thus ligand exchange is still slow, requiring several hours to several days. The table below summarizes the conditions under which MOFs have been synthesized in short periods. First, when $ZrOCl_2$ was used as a metal source, nucleation occurred faster than with other metal sources like $ZrCl_4$ due to the influence of the counter ions [71]. Second, to promote the nucleation of Zr-MOFs, He at al. introduced water to accelerate the hydrolysis of the metal salt and deprotonation of the ligands. Additionally, acetic acid was used as a modulator to control the reactivity because a fast reaction results in poor crystallinity of the grown MOF. Finally, 23.59 g of UiO-66-NH_2 was synthesized in a 2-L flask under reflux at 120 °C for 15 min by controlling the reaction rate (Fig. 3e) [69].

This type of high-temperature and ambient-pressure process is one of the more moderate syntheses conducted under reflux. However, it is still more reactive than ambient-temperature processes, making it advantageous for mass production. In addition, since the solubility of the precursor is increased by the high temperature, the reaction can be optimized using less solvent, and solvent loss can be reduced by recovering the evaporated solvent through a reflux system. However, most such reactions take longer than one day without adjusting the metal source or adding a modulator, and there are still many MOFs that are synthesized at reflux conditions harsher than 100 °C. In addition, it is disadvantageous in terms of cost and the environment to mass-produce MOFs using mainly organic solvents such as DMF, DEF and dimethylsulfoxide (DMSO) for their increased solubility and high-temperature heating (Table 2).

- High-temperature (>RT) and pressure (>1 atm) processes

Traditional heating synthesis, which has been studied the most, is conducted by dissolving the precursors in a solvent at a high temperature and pressure. Synthetic conditions for this traditional process have been well established for most types of MOFs, making their customization straightforward through modification of the underlying conditions.

When the reaction temperature is above the boiling point of the solvent, the autogenous pressure generated by the solvent vapor also affects the synthesis. Therefore, it is necessary to use heat- and pressure-resistant vessels. A high temperature and autogenous pressure enhance the solubility to the point where even reactants that are insoluble in a specific medium (e.g., organic ligands in water) can be used, which can expand the options for combinations of solvents and reactants. In general, Teflon-sealed glass vials can be used for low vapor pressures near the boiling point, but digestion bombs (Teflon-lined autoclave reactor, high-pressure digestion tank) are necessary for harsh conditions such as high temperatures and pressures for long-term reactions(Fig. 3f). To apply such a container to mass synthesis, a large-capacity pressure vessel can be manufactured and employed like that reported previously [75] (Fig. 3g). These traditional heating methods can be largely divided into hydrothermal and solvothermal approaches, which use water and organic solvents, respectively. Hydrothermal methods are advantageous in terms of environmental regulations and solvents when scaled to industrial production, which require a large amount of solvent due to the usage of water. While ionic precursors are highly soluble in water, typical organic ligands are poorly water soluble, and hydrogen bonding between the solvent and precursor can interfere with nucleation. Typical examples of large-scale solvothermal synthesis include MIL-100(Fe) in a 200-L reactor [76] and MIL-101(Cr) in a 3-L reactor [75]. Seo at al. synthesized MIL-100(Fe), also known as Basolite F300 (trade name of BASF SE), with 70 L of reaction solvent in a 200-L metal alloy reactor vessel (Hastalloy C-276) at 160 °C for 12 h. The amount of product was 15.6 kg per batch, and the STY of approximately 450 kg m^{-3} d^{-1} was improved to 1700 kg m^{-3} d^{-1} by controlling the synthesis time [76] (Fig. 3h). Furthermore, Zhao at al. produced MIL-101(Cr) in a 3-L autoclave at 200 °C for 15 h at a yield of 82.3% based on Cr [75].

Solvothermal synthesis mainly employs polar solvents (DMF, DEF, DMSO, alcohols, etc.) that dissolve the inorganic precursors, where the solvent selection affects the precursor reactivity and crystal growth. In this case, the temperature in the reactor is usually 100–240 °C. With a solvent that does not dissolve the ligand or metal source well, the reaction should be carried out at higher pressures and temperatures to improve the solubility. Therefore, proper solvent selection is important for large-scale syntheses. Another option for solvent selection is ionic thermal synthesis using an ionic liquid, which gives a temperature above the melting point of the salt and rarely generates pressure from the solvent or reactant.

Although these thermal syntheses are well known and widely applied, they do have limitations. Nucleation occurs on the surface of the vessel; thus, since increasing the vessel volume decreases the ratio of the vessel surface area to the solvent volume, the reaction efficiency decreases. In addition, issues can occur with uneven MOF synthesis due to non-uniform heat and pressure distributions. The reactions are also long, from several hours to several days, and require a large amount of solvent (Table 3).

- Microwave heating synthesis

Microwaves are electromagnetic radiation with wavelengths between 1 m and 1 mm. Microwave heating synthesis applies dipole rotation and ion conduction to heat the solution, unlike traditional heating systems [80]. Many molecules have a dielectric moment, which causes them to rotate and align with the alternating direction of the microwave electric field [81]. Therefore, solvents with high dipole moments are considered optimal for microwave heating synthesis. Loss of tangent (tan δ) determines the ability of a solvent to convert electromagnetic energy into heat at a certain frequency and temperature, where a higher tan δ leads to faster heating (Table 4) [82].

However, this does not mean that a solvent with a low tan δ cannot react in a microwave system if the mixed solution of MOF precursors is polar. The molecular movement of the solvent produces heat, which disperses as the molecules collide. Microwave heating synthesis is energy efficient because it only transfers energy inside the reaction solution. Conventional heating methods first heat the surface of the vessel to add heat energy, but microwave synthesis produces heat directly throughout the material (Fig. 4a). Therefore, uniform heat transfer occurs inside the vessel within a short time (a few seconds to hours), resulting in rapid nucleation and enabling the easy synthesis of small, uniformly sized MOF particles. The power level, temperature, and reaction time of the microwave irradiation can be adjusted to control the MOF size and characteristics. Although the synthesis time is short, solvent evaporation makes pressure control difficult and requires the use of a pressure vessel.

Taddei et al. optimized the large-scale synthesis of UiO-66 with a microwave system [84]. A DMF mixture of zirconium chloride, terephthalic acid, acetic acid, and water was placed in a PTFE vessel and subjected to microwave heating using a CEM MARS 5 multimode instrument in 2 stages (1st stage: 200 W for 3 min; 2nd stage: 80 W for 15 min). UiO-66 was obtained in only 18 min at a high STY of 2241 kg m^{-3} d^{-1} compared with that of conventional heating (23 kg m^{-3} d^{-1}).

On the industrial scale, it is expected that large-scale MOF synthesis using microwaves can be carried out using a SAIREM reactor (Fig. 4b) [83]. However, microwave synthesis conditions have yet to be confirmed for many MOFs, which limits suitable synthesis conditions. In addition, using different equipment from the reference method makes it difficult to reproduce the same conditions, and thus ultimately the reproducibility is limited (Table 5).

- Sonochemical synthesis

Sonochemical synthesis applies ultrasonic irradiation as energy for reactions at RT. Similar to microwave heating, sonochemical methods can afford MOF particles of a uniform size in a short time using concentrated vibrational energy. Sonochemical synthesis employs extreme transients using powerful ultrasonic waves (20 kHz–1 MHz) that create localized hotspots, which can reach temperatures above 5000 K, heating and cooling rates above 1010 K s^{-1}, and pressures above 1000 atm [80,96]. This phenomenon arises from "acoustic cavitation," which involves the formation, growth, and implosive collapse of bubbles (Fig. 4c).

Sonochemical syntheses can employ two types of equipment. The reaction vessel can be immersed in an ultrasonic bath, where energy is transferred from outside the vessel to the inside. Alternatively, as commonly used in laboratories, tips for generating ultrasound are immersed in the reaction solution to transfer energy directly. This method is 100 times more powerful than the use of an ultrasonic bath. In addition, industrial ultrasonic devices can be applied for mass production (Fig. 4d).

The sonochemical syntheses of only a few types of MOFs have been studied, including ZIF-8, HKUST-1, MOF-5, and MIL-53. Cho

Table 4
Loss tangents (tan δ) of various solvents (2.45 GHz, 20 °C). Reproduced with permission from [82].

High microwave-absorbing (tan δ > 0.5)		Medium microwave-absorbing (0.1 < tan δ < 0.5)		Low microwave-absorbing (tan δ < 0.1)	
Solvent	tan δ	Solvent	tan δ	Solvent	tan δ
Ethylene glycol	1.35	2-butanol	0.447	Chloroform	0.091
Ethanol	0.941	1,2-dichlorobenzene	0.28	Acetonitrile	0.062
Dimethyl sulfoxide	0.825	1-methyl-2-pyrrolidone	0.275	Ethyl acetate	0.059
2-propanol	0.799	**Acetic acid**	0.174	Acetone	0.054
Formic acid	0.722	**N,N'-dimethylformamide**	0.161	Tetrahydrofuran	0.047
Methanol	0.659	1,2-dichloroethane	0.127	Dichloromethane	0.042
Nitrobenzene	0.589	**Water**	0.123	Toluene	0.04
1-butanol	0.571	**Chlorobenzene**	0.101	Hexane	0.02

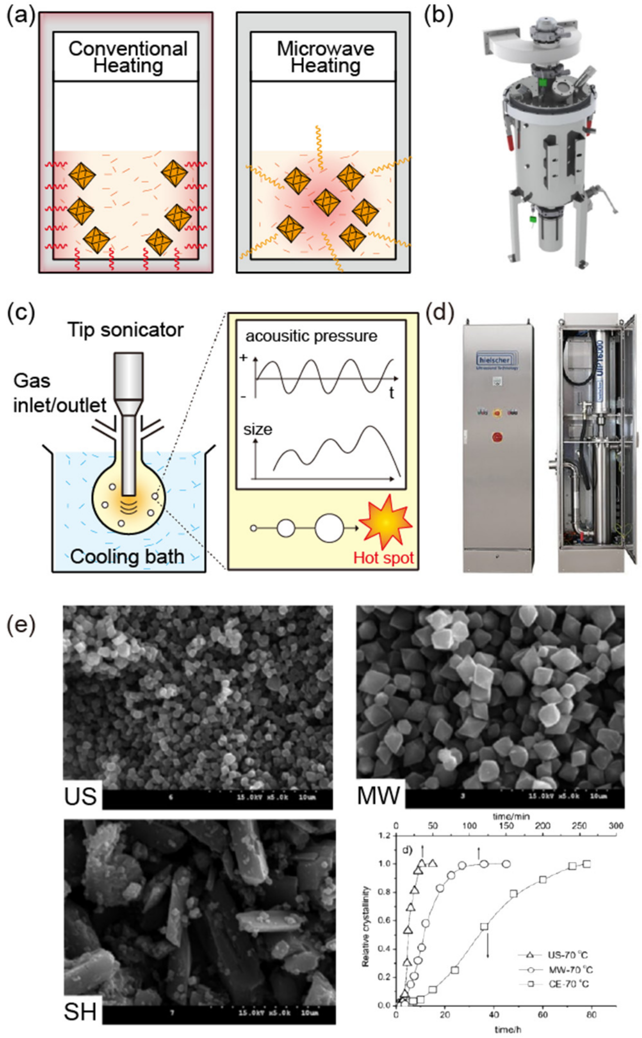

Fig. 4. Microwave heating synthesis (a) Schematic illustration for principle (b) Digital images of large-scale microwave instrument of SAIREM. Copyright SAIREM. **Sonochemical synthesis** (c) Schematic illustration for principle. (d) Digital images of large-scale sonochemical instrument of Hielscher Ultrasonics GmbH. Copyright by © Hielscher Ultrasonics GmbH. (e) SEM images and crystallization curves for the synthesis of MIL-53(Fe) by sonochemistry synthesis (US), microwave heating synthesis (MW) and heating synthesis (SH). Adopted with permission from [87]. Copyright 2010 John Wiley and Sons.

et al. synthesized ZIF-8 with TEA and NaOH as a pH modulator in as little as 1 h with a probe-type sonicator (60% power of 500 W, 20 kHz) and achieved a high synthetic yield of 85% and STY of 2140 kg m^{-3} d^{-1} [97]. The dependence of MOF characteristics on the heating method was explored by a study comparing MIL-53 (Fe) prepared by solvothermal heating (SH), microwave heating (MW), and sonochemical syntheses (US) [80,87]. The nucleation and crystal growth times decreased in the order of US > MW≫SH. The morphologies of the MOFs formed at the same temperature were compared by scanning electron microscope (SEM) imaging, which showed that MW and US syntheses produced uniformly sized MOF particles, and the particle sizes increased in the order of US < MW < SH (Fig. 4e).

MOF synthesis with ultrasound can generate uniformly nanosized MOF particles. Additionally, the intense ultrasonic waves accelerate chemical reactions such as homogeneous nucleation and crystal growth, and it is easy to combine ultrasound with additional cooling and heating systems or stirring processes. However, unlike conventional heating syntheses, it will be difficult to control the predetermined synthetic conditions from existing methods due to the lack of autogenous pressure. The sonochemical synthesis of MOFs has not yet been actively studied in the laboratory, but it is expected to be applicable to industrial production under mild conditions instead of high temperatures and pressures (Table 6).

- Electrochemical synthesis for MOF film production

Electrochemical synthesis uses electrical reactions between metal electrodes and ligand solutions. This method was first introduced by a BASF patent in 2005, which detailed the synthesis of HKUST-1 (Cu-BTC) in thin layers via Cu plate electrodes (Fig. 5c) [102]. Despite being a static synthesis, this method allows for continuous production as long as reactants are present. In addition, electrochemical syntheses have the significant advantages of mild conditions and short reaction times compared with hydrothermal synthesis. The MOF is synthesized by a reaction between the electrode and precursor, which is controlled by adjusting the current and voltage. Electrochemical syntheses can be classified into anodic dissolution and cathodic deposition, which produce a MOF film on the electrode (Fig. 5) [103]. The mechanism of anodic dissolution consists of four phases: initial nucleation, growth of islands, intergrowth, and detachment. As the metal ions are released from the electrode into the ligand solution, nucleation initiates at defects on the metal substrate. Nuclei continue to grow next to the initial nuclei, forming intergrown MOF islands. This has been confirmed not only for Cu-based HKUST-1 but also for Zn and Fe-based MOFs [103–105]. After the MOF film is formed, the metal ions dissolved from the metal substrate pass through the MOF layer to continuously synthesize the MOF at the MOF–solution interface. As a result, a void forms between the first MOF layer and the metal substrate, which separates the two. This method requires time for MOF electrodeposition, which depends on the current, and the size of the crystal depends on the reaction time and solvent. In addition, the use of metal anodes limits the MOFs that can be synthesized depending on the type of metal selected. Additionally, in terms of the reaction solvent, it should be noted that an aqueous solvent can generate hydrogen in the cathode.

The second electrochemical method is cathodic deposition, where the electrode is immersed in a mixed solution of metal ions, ligand, and probase, and the MOF is synthesized from the electrode through electrical energy. Unlike anodic dissolution, cathodic deposition does not require a metal electrode but instead uses a conductive substrate to grow the MOF film. The cathodic deposition mechanism consists of three steps: nucleation of dispersed nuclei, formation of crystal islands, and intergrowth [103,106]. The difference from the anodic method is that after the first layer, another layer forms between the electrode and MOF, and thus no MOF detachment occurs. The reaction rate can be adjusted by controlling the protonation of the ligand via the pH.

Electrochemical synthesis can produce MOFs by either anodic dissolution or cathodic deposition depending on the characteristics of the metal source and the conditions of the reaction solution. Using electrochemistry, MOFs can be synthesized continuously in a short time at RT and atmospheric pressure. In particular, anodic dissolution is advantageous in that no counter ion waste is generated from the metal precursor. Comparing metal materials in terms of cost efficiency, anodic dissolution uses a metal substrate, whereas cathodic deposition uses metal ions, making the latter reaction easier and cheaper. However, in terms of reaction solvents and electrolytic baths, the cathodic method requires expensive solvents such as DMF, and the bath has a short lifetime of several days. The anodic method, on the other hand, is more suitable for long-term and large-scale syntheses due to the inexpensive solvents like alcohol and long lifetime of the bath [103]. In electrochemical synthesis, MOFs are synthesized by coating on the elec-

Table 5
Summary of microwave heating synthesized MOF.

MOF	Metal source	Ligand	Modulator	Solvent	Instrument	Reactor	Time	Power (W)	Temperature (°C)	STY (kg m^{-3} day^{-1})	Yield (g)	Yield (%)	Surface area (m^2 g^{-1})	Ref
UiO-66	Zirconium chloride	Terephthalic acid	Acetic acid	DMF	Multi-mode microwave synthesizer	PTFE vial	18 min	100	120	2241	2.72	78	1206	[84]
Cu-BDC	Copper(II) nitrate trihydrate	Terephthalic acid	–	DMF	Domestic microwave	–	30–90 min	300/100	–	–	–	–	624	[85]
HKUST-1	Copper(II) nitrate trihydrate	Trimesic acid	–	Water/DMF/EtOH	900 W magnetron	Teflon pot	10 min	360	70	–	0.27	50	1185	[86]
MIL-53(Fe)	Iron(III) chloride hexahydrate	Terephthalic acid	–	DMF	Mars-5, CEM	–	2 h	–	60–70	–	–	–	–	[87]
MIL-101(Cr)	Chromium(III) nitrate nonahydrate	Terephthalic acid	HF	Water	Mars-5, CEM	Teflon autoclave	1–60 min	600	210	–	–	–	3891	[88]
MIL-53(Al)	Aluminum chloride hexahydrate	Terephthalic acid	–	Water	Mars-5, CEM	Teflon autoclave	5.5 h	1200	150	–	–	–	1282	[89]
MIL-53(Cr)	Chromium(III) chloride hexahydrate	Terephthalic acid	–	Water	Mars-5, CEM	Teflon autoclave	7 h	1200	175	–	–	–	1419	[89]
MIL-47(V)	Vanadium(III) chloride	Terephthalic acid	–	Water	Mars-5, CEM	Teflon autoclave	3 h	1200	135	–	–	–	1049	[89]
MIL-88A	Iron(III) chloride hexahydrate	Fumaric acid	–	Water	Mars-5, CEM	Stirring	2–10 min	600	80	–	–	–	–	[90]
MOF-5	Zinc nitrate tetrahydrate	Terephthalic acid	–	NMP	MDS-2100. CEM	Teflon autoclave	15–30 min	600	105	–	–	–	2798	[91]
MOF-5	Zinc nitrate hexahydrate	Terephthalic acid	Water	DMF	–	Teflon pot	210 s	–	80	–	0.123	47	2489	[92]
IRMOF-1	Zinc nitrate hexahydrate	Terephthalic acid	–	DEF	520A, Resonance Instrument Inc.	Pyrex vial	25 s	150	–	–	–	–	–	[93]
IRMOF-2	Zinc nitrate hexahydrate	2-Bromoterephthalic acid	–	DEF	520A, Resonance Instrument Inc.	Pyrex vial	40 s	150	–	–	–	–	–	[93]
IRMOF-3	Zinc nitrate hexahydrate	2-Aminoterephthalic acid	–	DEF/EtOH	520A, Resonance Instrument Inc.	Pyrex vial	35 s	150	–				–	[93]
MOF-74(Ni)	Nickel nitrate hydrate	2,5-dihydroxyterephthalic acid	–	DMF/EtOH/Water	Multiwave 3000/Synthos 3000, Anton Paar	Teflon autoclave	90 min	–	100	–	–	–	1252	[94]
MOF-74(Mg)	Magnesium nitrate hydrate	2,5-dihydroxyterephthalic acid	–	DMF/EtOH/Water	–	Teflon autoclave	90 min	–	125	–	–	–	1416	[94]
MIL-101(Cr)	Chromium(III) chloride hexahydrate	Terephthalic acid	NaOH	Water	MDS-2002A	Teflon autoclave	3 min	–	210	–	–	–	3208	[95]

Table 6
Summary of sonochemical synthesized MOF.

MOF	Metal source	Ligand	Modulator	Solvent	Instrument	Max power	Power	Time	Temperature (°C)	STY (kg m^{-3} day^{-1})	Yield (%)	Surface area (m^2 g^{-1})	Ref
ZIF-8	Zinc nitrate hexahydrate	2-methylimidazole	TEA, NaOH	DMF	Probe (VCX 500)	500 W, 20 kHz	60%	1 h	–	2140	85	1174	[97]
MIL-53(Fe)	Ferric chloride hexahydrate	Terephthalic acid	–	DMF	Probe (VCX 750)	–	25–40%	0.58–1.5 h	50–80	–	–	–	[87]
MIL-53(Fe)	Ferric chloride hexahydrate	Terephthalic acid	–	DMF	Probe (VCX 500)	500 W, 20 kHz	60%	15 min	–	–	30.2	–	[98]
Zn-HKUST-1	Zinc acetate dihydrate	Trimesic acid	–	DMF	–	–	305 W, 40 kHz	30 min	–	–	–	–	[99]
TMU-4	Zinc nitrate hexahydrate	4,4′-Oxybis(benzoic acid) 4-BPDB*	TEA	DMF	Bath (SONICA-2200 EP)	40 kHz	40 kHz	30–90 min	–	–	88	–	[100]
CPO-27(Zn)	Zinc nitrate hexahydrate	2,5-dihydroxyterephthalic acid	Water	DMF	Probe (VCX 500)	500 W, 20 kHz	35%		70	–	–	979	[101]
CPO-27(Co)	Cobalt nitrate hexahydrate	2,5-dihydroxyterephthalic acid	Water	DMF	Probe (VCX 500)	500 W, 20 kHz	35%		70	–	–	1083	[101]
CPO-27(Ni)	Nickel nitrate hexahydrate	2,5-dihydroxyterephthalic acid	Water	DMF	Probe (VCX 500)	500 W, 20 kHz	35%		70	–	–	1113	[101]

*1,4- bis(4-pyridyl)-2,3-diaza-1,3-butadiene.

trode, and thus it is difficult to produce uniformly sized particles since they are aggregated rather than separated. Thus far, electrochemical methods have yet to be applied to many MOFs, and most research has been aimed at MOF film coating. Electrochemical syntheses are more suitable for producing large-area MOF films (Table 7).

3.1.1.2. Solvent-free static processes (mechanochemical synthesis). Mechanochemical syntheses are well known as solvent-free (or solvent-less) methods involving grinding or milling a solid mixture of metal and organic ligands. Typically, in academic research, the reactants are ground by a mortar and pestle (Fig. 6a) or ball-milled (Fig. 6b, c). The mechanical force breaks the intramolecular bonds, and new bonds form between the metal and ligands to drive MOF formation. Since this is a quantitative reaction, the proportion of metal to ligand is an important element affecting the reaction yield and efficiency. Additionally, a catalytic amount of liquid or ionic material (salts) can be employed to accelerate the reaction, also called liquid-assisted grinding or ion-assisted grinding, respectively. The small amount of solvent increases the mobility of the reagent [112], and anionic salts induce templating effects [113].

Kimakow et al. synthesized the Cu-based MOFs HKUST-1 and MOF-14 by ball-milling with copper acetate. The surface area of HKUST-1 was low at 758 m^2 g^{-1} without activation but increased to 1713 m^2 g^{-1} after EtOH washing. This was caused by the byproduct, acetic acid, blocking the product pores [112]. Thus, a washing process is required to remove any byproducts other than water.

Mechanochemical syntheses are advantageous for their simplicity, rapidity, high yields, RT conditions, low cost, and solvent-free reactions yielding small-sized MOF products. It is also possible to use various types of metal sources, such as pure metals, metal oxides, metal hydroxides, metal carbonates, and even insoluble metals [114]. Furthermore, mechanochemical synthesis can be applied to a stoichiometric ratio of mixed distinct metal components to synthesize mixed-metal MOFs by milling [115]. However, if the byproducts also react under the employed conditions, a solvent may be necessary, as is the case for pore activation by solvent exchange. For mass production, the grinding operation is simple and cost-effective. In particular, solvent-free methods reduce the cost of solvents and environmental regulations. However, the worn metallic impurities from ball milling equipment are the main drawback of this method for certain applications [116] (Table 8).

3.1.2. Continuous processes

In Section 3.1.1, we examined static processes for industrial MOF production. Static syntheses use one large reactor, which is not suitable for mass production by repeated synthesis and recovery processes. This section introduces continuous flow systems capable of continuous synthesis, recovery, and wash steps, where the ligands and metal precursors are synthesized into MOFs as they enter the reactor. With a constant pump pressure, the reagents are continuously supplied to the reactor, and the product is sent out. Finally, flow systems can be managed with a computer program, and it is possible to maintain uniform synthesis conditions by checking and adjusting the temperature and flow rate at different points. In addition, continuous processes can result in improved MOF reproducibility because the continuous reaction maintains the same synthetic conditions. Continuous processes can be classified as solvent-based or mechanical depending on the use or lack of a solvent, respectively, as a reaction medium. We take a closer look in the following subsections.

3.1.2.1. Solvent-based continuous processes. The static heating syntheses described in Section 3.1.1 involve expanding the laboratory-scale synthetic methods to a large-scale reactor. At this

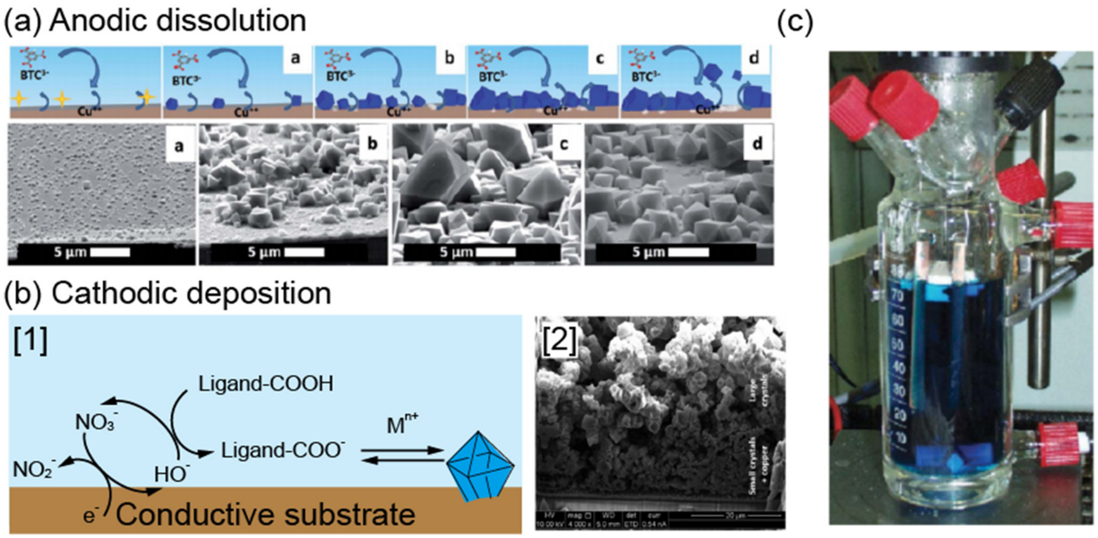

Fig. 5. (a) Schematic illustration and SEM images for synthesized HKUST-1 with anodic dissolution. (b) (left) Schematic illustration and (right) SEM images for synthesized HKUST-1 with cathodic deposition (c) Digital image of HKUST-1 synthesis cell for electrochemical preparation of MOFs with Cu-plates as electrode material. Both (a) and (b) (left) have been reprinted with permission from [103]. Copyright 2016 American Chemical Society. Part (c) has been reproduced with permission from [102]. Copyright 2006 Royal Society of Chemistry.

time, the use of a large amount of solvent causes environmental and cost problems, and larger containers have lower surface-to-volume ratios and thus poor reactivity. On the other hand, flow heating systems are optimal for industrial production with their high surface-to-volume ratios, which improve the mass and heat transfer, reaction efficiency, and reaction rate. Such flow systems are commercially available and have been studied for the synthesis of various materials, such as quantum dots, metal nanoparticles, and metal oxides [120] (Fig. 7). Therefore, flow systems are an effective approach that can be easily applied to industrial production.

As shown in Fig. 8a, in flow heating synthesis, the metal and ligand precursors are transported by a pump to be mixed in a reactor and receive energy to synthesize MOFs. Immediately afterward, the reaction is stopped by the cooling system to obtain MOFs with a uniform and controlled shape. Then, the as-synthesized MOFs are moved to a constant pressure by a back pressure regulator (BPR), which solves the tube clogging problem caused by MOF powders. This type of system is eco-friendly and cost-efficient because it expends a small amount of solvent and reuses the separated solvent through recovery. In addition, the activated final product can be manufactured by simultaneously performing the synthesis, recovery, and washing steps. The reactors can be divided into 5 types depending on their shape and the manner of mixing of the ligand and metal source (Fig. 8b): column, counter-current mixing, continuous stirred tank, tubular flow, and microfluidic reactors. Additionally, various types of energy sources can be applied to the reaction by irradiating with microwaves and ultrasound in addition to heat.

- Column reactor

In a column reactor, the reaction occurs as the reactants are mixed in a fixed column. This is the simplest reactor with no mixing device, where the reactants are instead blended by the flow rate (Fig. 9). Kim et al. obtained HKUST-1 at 2.04 g h^{-1} with a column reactor, where the size and crystal phase of the MOF were controlled by adjusting the EtOH/water ratio of the metal source and the reaction temperature (Fig. 9a) [121]. Bayliss et al. prepared a metal, ligand, and hydrothermal line to synthesize MIL-53(Al) [122], where the reagent line with an aqueous solution at RT met the hydrothermal line in a column reactor (Fig. 9b). However, since terephthalic acid (H_2BDC) as an organic ligand is not soluble in cold water, disodium terephthalate (Na_2BDC) was used instead as a soluble salt. Importantly, this study established a system capable of simultaneous synthesis and recovery, which is the goal of industrial production. After the reaction, it was possible to perform continuous recovery in the flow system by a filter replacement method through two divided filter lines. The filtered MOF product was transferred to a critical EtOH extraction reactor for pore activation, which demonstrates the possibility of extending flow heating synthesis to the washing process. This system achieved 500 g of MIL-53(Al) in 4 h with an STY of 1300 kg m^{-3} d^{-1}. The surface areas of HKUST-1 and MIL-32(Al) synthesized through this column reactor were 1673 and 1010 m^2 g^{-1}, respectively, which are higher than those of the same MOFs synthesized by static solvent methods. This illustrates that the porous properties of MOFs are properly maintained when mass-produced.

Column reactors are the simplest flow systems and are capable of connecting to a recovery system for one-step flow. However, since there is no specific mixing element, it is difficult to obtain instant and powerful mixing. Other systems are subsequently introduced to address this need (Table 9).

- Counter-current mixing reactor (CCR)

A CCR consists of a pipe-in-pipe concentric arrangement as shown in Fig. 10a, b. This reactor rapidly mixes a preheated solution down through the inner pipe with a RT solution flowing upward. The advantage of this method is that the reagents are mixed quickly and uniformly in a few seconds by the stream, resulting in a short residence time [125]. Thereafter, the reaction is terminated through rapid cooling, and a sample is collected by a BPR (Fig. 10c).

The synthesis of the MOFs, HKUST-1 and CPO-27, using a CCR was first introduced in 2012 [123]. Preheated water was used for the downward flow in the inner tube, and a mixed solution of ligand and metal (RT) was used for the upward flow. The size and surface area of the MOF were controlled by optimizing the temperature of the reactor and the concentration of the metal

Table 7
Summary of MOF with electrochemical synthesis.

a. Anodic deposition

MOF	Metal source	Ligand	Solvent	Electolyte	Voltage (V)	Current (mA)	Time (min)	Temperature (℃)	Productivity (g h^{-1})	Surface area (m^2 g^{-1})	Ref
HKUST-1	Cu plate (5 mm)	Trimesic acid	MeOH	–	19–12	1.3 A	150	–	–	1820	[102]
HKUST-1	Cu plate	Trimesic acid	EtOH/Water	MTBS*	2–30	50	–	40	0.215	1404	[107]
ZIF-8	Zinc plate	2-methylimidazole	DMF	MTBS	–	50	–	25	0.25	1656	[107]
MIL-100(Al)	Aluminium plate	Trimesic acid	EtOH/Water	–	–	–	–	60	–	969	[107]
MIL-53(Al)	Aluminium plate	Terephthalic acid	Water/DMF	KCl	–	10–100	–	90	0.775	910	[107]
NH_2-MIL-53(Al)	Aluminium plate	2-Aminoterephthalic acid	Water/DMF	KCl	–	10–100	–	20–90	–	875	[107]
$Zn_3(BTC)_2$	Zinc plate	Trimesic acid	Water	NH_4F	2	–	40 s	65	–	–	[108]
ZIF-4	Zinc foil	Imidazole	DMF/Water	MTBAMS**	2.5	–	15–60	85	–	75	[109]
ZIF-7	Zinc foil	Benzimidazole	DMF	MTBAMS	2.5	–	120	55	–	358	[109]
ZIF-8	Zinc foil	2-methylimidazole	Water	MTBAMS	2.5	–	60	55	–	1730	[109]
ZIF-14	Zinc foil	2-ethylimidazole	DMF/Water	MTBAMS	2.5	–	60	85	–	598	[109]
ZIF-67	Cobalt foil	2-methylimidazole	DMF/Water	MTBAMS	2.5	–	60–300	55–100	–	1521	[109]

*methyltributylammonium methyl sulfate, **methyltributylammonium methyl sulphate

b. Cathodic deposition

MOF	Metal source	Ligand	Solvent	Electrolyte	Substrate	Ref
MOF-5	Zinc nitrate hexahydrate	Terephthalic acid	DMF	$(NBu_4)PF_4$	FTO	[106]
MOF-5	Zinc nitrate hydrate	Terephthalic acid	DMF/water	$TBAPF_6$	FTO	[110]
MOF-5	Zinc Chloride	Terephthalic acid	DMF/water	$TBAPF_6$	FTO	[110]
MOF-5	Zinc nitrate hexahydrate	Terephthalic acid	DMF	$TBAPF_6$	FTO	[111]
IRMOF-3	Zinc nitrate hydrate	2-Aminoterephthalic acid	DMF/water	$TBAPF_6$	FTO	[111]

source. In a subsequent work, ZIF-8 was synthesized using an organic ligand and base solution as the pre-heated downward stream and metal solution (RT) as the upward stream [124]. The synthesized MOF was then transferred to a coil in a water bath by BPR, and pore activation was performed by heating and sonication to manage the surface area. This demonstrated the advantages of a continuous process with simultaneous synthesis and activation in one flow system. The system produced ZIF-8 with a high STY of 3875 kg m^{-3} d^{-1}. The surface areas of HKUST-1, CPO-27, and ZIF-8 produced by CCR were 1950, 1030, and 1800 m^2 g^{-1}, which were similar to or higher than the reference values of 1694 (Basolite C300), 1200, and 1654 m^2 g^{-1}, respectively. Additionally, HKUST-1 produced in a CCR had a 300–400 m^2 g^{-1} higher surface area than those of the MOFs prepared in the other two kinds of column reactors.

The advantage of the CCR is that it can achieve highly uniform reactant mixing in a short time, which also improves the reaction extension and transport properties. It has also been shown that the synthesis and washing steps can be performed sequentially in one flow system [124]. Although CCRs produce MOFs with a well-controlled size, surface area, and yield, the required high temperature and pressure are limiting factors for practical applications (Table 9).

- Continuous stirred tank reactor (CSTR)

In a CSTR, the ligand and metal solution flow into the reactor and mix through direct stirring to perform the reaction. Choline et al. synthesized MOF-5 using a CSTR and analyzed the product according to synthesis time to confirm that impurity-free MOF-5 could be obtained after 5 h, then adjusted the reaction time to increase the yield (Fig. 10d, e). The resulting MOF-5 had a surface area of 2302 m^2 g^{-1}, which was higher than the reference value of 2200 m^2 g^{-1} [126].

The CSTR system is a semi-flow reactor that combines batch and flow reactor features. In particular, the MOF-5 synthesis system described above can be considered as introducing flow characteristics into reflux synthesis. Therefore, the advantage is that the reaction can proceed at ambient pressure, but the reaction time is 4–5 h longer than that for other flow methods (Table 9).

- Tubular flow reactor

In a tubular flow reactor, reactants mix and flow in a post-mixing line, and the MOF is synthesized by irradiation of the line with energy. This type of reactor not only allows for control of the concentration, temperature, pressure, and reaction time but also enables optimization of the reaction rate by adjusting the residence time and reactor volume through the length and diameter of the line itself. In addition, in the previously described mixing reactors, synthesis is performed using heated reactants or heat transferred instantaneously to the reactor, whereas flow line reactors can not only heat the reaction zone but also progress the reaction by irradiation with microwave energy.

The scale, residence time, and reaction rate in tubular flow reactors have been controlled in two ways by directly adjusting the length (Fig. 11a) and inner diameter (Fig. 11b) of the tubular reactor. The first strategy was to adjust the length and volume of the entire reactor from 10 to 40 mL by connecting four 1.0-mm inside diameter (ID) perfluoroalkoxy polymer coil reactors, each with a volume of 10 mL [127]. When the reactor length was fixed, the residence time was adjusted by the flow rate of the reaction solution. When the total volume of the reactor was fixed at 20 mL, the reaction was carried out at increasing total flow rates of 2, 10, and 20 mL min^{-1} and decreasing residence times of 10, 5, and 1 min, respectively. Further, when the flow rate was fixed at 2 mL min^{-1},

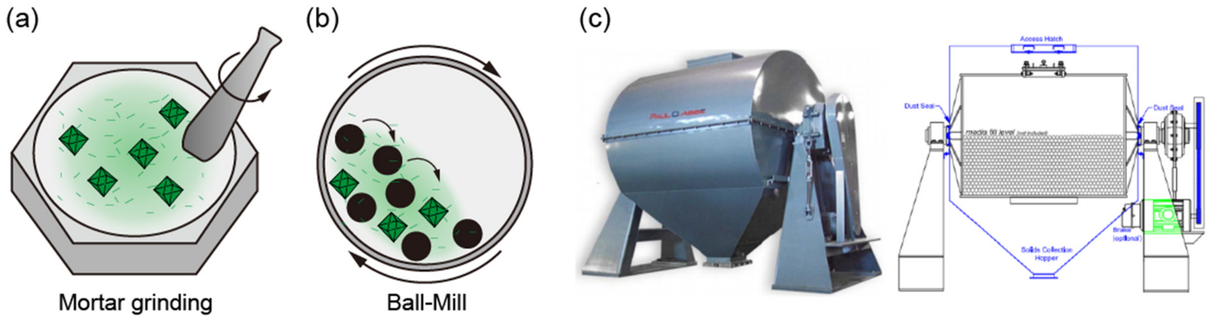

Fig. 6. (a) Schematic illustration of mortar grinding synthesis (b) Schematic illustration of ball-mill synthesis (c) Pictures of industrial ball-mill instrument of Paul O. Abbe®. Copyright by Paul O. Abbe®.

the residence time was 10 min for a total reactor volume of 20 mL, but the reaction time was adjusted to 15 min when the volume was increased to 30 mL. The total volume was increased by adjusting the length of the reactor, but because the tube diameter remained the same, the surface-to-volume ratio was not affected. After optimizing the synthetic conditions for the mesoscale reactor, 4533 kg m^{-3} d^{-1} STY of HKUST-1 was ultimately synthesized with a macroscale reactor.

The second strategy for controlling the reaction parameters is to maximize the reactor volume by adjusting the diameter of the tube within a range that does not increase the surface-to-volume ratio (Fig. 11b). The degree of reactant mixing in the reactor tube is an important factor, where more uniform mixing results in greater mass and heat transfer to the reactor wall and thus improves the yield. This degree of mixing, or homogeneity, is related to the fluid flow dynamics of the stream. The reaction surface area decreases as the tube diameter increases, but this can be attenuated by increasing the mixing degree of the solution, as turbulent flow prevails over laminar flow. One study showed that upon increasing the reactor diameter (volume) from 1 mm (10 mL) to 10.9 mm (1394 mL), the STY increased from 81,120 to 97,159 kg m^{-3} d^{-1} without any significant changes in the MOF properties (Fig. 11c) [128]. It is necessary to determine an appropriate tubular diameter to increase the reaction volume as much as possible while maintaining the yield. Finally, to expand the reaction capacity for mass synthesis, length and diameter adjustments must be performed through the simultaneous series connection of reactors.

One prominent advantage of tubular flow reactors is the ability to use not only electrical heat energy but also microwave energy (Fig. 12). Several MOFs such as UiO-66, MIL-53(Al), and HKUST-1 were synthesized by microwave tubular flow synthesis at high STY values of 7204, 3618, and 64,800 kg m^{-3} d^{-1} [129]. In addition, each MOF had a high surface area compared with that of the same MOF synthesized by a general method.

In particular, thin-diameter tubular reactors exhibit effective heat and mass transfer in a short time and easily allow for increasing the volume-to-volume ratio between the reactant and reactor, which is necessary for optimized mass synthesis systems. However, the role of the BPR in this type of reactor is key because the synthesized powder sample must pass through a small-diameter tube. To prevent clogging, a constant pressure is applied from the rear of the reactor to enable a constant reaction speed and production (Table 10).

- Microfluidic synthesis

Microfluidic flow methods control the size of the reaction space by limiting the reaction solution to a droplet. This approach involves mild reaction conditions that require thermal energy for nucleation, but pressurization is not essential. The microfluidic flow system, unlike other flow methods, requires an additional oil carrier line. The organic ligand and metal salt are dissolved in a polar solvent and injected as polar nanoliter droplets into the oil carrier line. This limited-sized droplet becomes a reaction space and flows through the reaction tube, which is immersed in a hot oil bath or oven for heating (Fig. 13).

In 2013, Faustini et al. synthesized the general MOFs HKUST-1, MOF-5, IRMOF-3, and UiO-66 by a microfluidic flow method [133]. Although the STY of HKUST-1 was only 5.8 kg m^{-3} d^{-1}, only a few minutes were required to obtain the MOF crystals, and the crystal size and surface area could be adjusted by the flow rate, reaction time, and temperature. The authors suggested microfluidic synthesis with a high pressure from a BPR (2.4 MPa) for MOFs requiring high-pressure synthetic conditions. The micro-droplets functioned as small autoclaves, in which the Ru_3BTC_2 crystals were synthesized (Fig. 13c).

Microfluidic methods are optimal for fine-tuning the MOF crystal size and various morphologies and combinations, like core–shell, metal composited [133], post-synthetic modification (PSM)-functionalized [134], and hollow MOFs [135]. The reaction occurs only in the nanoliter droplets, where the high surface-to-volume ratio enhances the heat and mass transfer and reduces the reaction time. The limited reaction space is advantageous in that it prevents agglomeration of the MOF particles, and the product does not directly contact the reactor wall, thus avoiding clogging problems. However, despite its excellent performance, the yield from microfluidic reactors is so low that it is not suitable for mass production except in special cases (Table 11).

- Overview of flow-type reactors

Flow-type reactors seem to be the most suitable for the mass production of MOFs. The MOFs can be continuously produced through an uninterrupted reactant supply, and a product with a uniform quality can be synthesized by controlling the progress via a computer system in the middle of the process. In particular, the tubular flow reactor appears to be the most influential method due to its high reaction efficiency and high STY for the representative MOFs ZIF-8 and Al-Fum of 210,000 and 97,159 kg m^{-3} d^{-1}, respectively. Since the reactants flow at a constant speed along the line, the reproducibility of the reaction is excellent, and it is easy to control the product size and surface area according to the reaction conditions. In addition, as described above, the length and diameter of the tubular reactor can be optimized to establish a suitable surface-to-volume ratio. However, since these reactors require high temperatures and high pressures, the robustness of the tubular reactor becomes more important for mass production. In addition, the possibility of the tube becoming clogged due to the

Table 8
Summary of MOF synthesized by Ball-mill (mechanochemical synthesis).

MOF	Metal source	Ligand	M:L ratio	Reactor size (mL)	Solvent	Ion	By-product	Time	Temperature (℃)	Rotational speed	Yield (g)	Yield (%)	Surface area (m^2 g^{-1})	Ref
$Cu(INA)_2$	Copper acetate monohydrate	Isonicotinic acid (INA)	1:2	20	–	–	Water, Acetic acid	10 min	–	25 Hz	–	–	–	[117]
MOF-5	Zinc acetate dihydrate	Terephthalic acid	3:1	80	–	–	–	60 min	–	1100 rpm	–	–	3465.9	[49]
HKUST-1	Copper acetate monohydrate	Trimesic acid	3:2	10	EtOH	–	Water, Acetic acid	25 min	–	25/40 Hz	–	–	1713	[112]
MOF-14	Copper acetate monohydrate	H_3BTB	3:2	10	EtOH	–	Water, Acetic acid	25 min	–	25/40 Hz	–	–	628	[112]
Ni-MOF	Nickel(II) acetate tetrahydrate	Trimesic acid	3:2	80	Water	–	–	1–180 min	–	10–50 Hz	–	79.76	10.08	[118]
UiO-66	Zirconium(IV) propoxide/ Methacrylic acid	Terephthalic acid	1:6	10	MeOH	–	–	75 min	–	30 Hz	2.85	–	1020	[119]
NH_2-UiO-66	Zirconium(IV) propoxide/ Methacrylic acid	2-aminoterephthalic acid	1:6	10	MeOH	–	–	42 min	–	30 Hz	1.34	–	945	[119]
$Zn_2(ta)_2(dabco)$	Zinc oxide	Terephthalic acid (ta) Triethylenediamine (dabco)	1:1:0.5	–	DMF	$NaNO_3$	–	60 min	20–25	30 Hz	–	–	–	[113]

mass-synthesized MOF should also be kept in mind, which may necessitate an additional device.

3.1.2.2. Solvent-free continuous processes: Extrusion synthesis (mechanochemical). The principle of extrusion is the same as that of grinding and ball-milling, which utilize mechanochemistry, but its attractive feature is that continuous synthesis is possible. Extrusion is widely used in the plastic, food, and pharmaceutical industries with two main methods, single-screw extrusion (SSE) and twin-screw extrusion (TSE) (Fig. 14). The root diameter gradually increases as the solid moving with the screw is subjected to a higher compressive force. TSE functions based on two parallel screws moving either by co-rotation or counter-rotating to induce a mechanical force by their interpenetration.

Researchers at Queen's University Belfast synthesized HKUST-1, ZIF-8, and Al-Fum using SSE and TSE (Fig. 14b, c) [139]. Although they were basically solvent-free syntheses, small amounts of industrial alcohol and NaOH were used respectively for HKUST-1 and Al-Fum. The STYs were 144,000 kg m^{-3} d^{-1} for HKUST-1, 7826 kg m^{-3} d^{-1} for ZIF-8 (SSE), 144,000 kg m^{-3} d^{-1} for ZIF-8 (TSE), and 27,000 kg m^{-3} d^{-1} for Al-Fum. Extrusion with two screws, i.e., TSE, resulted in a more rapid and efficient reaction than with SSE. These MOFs had activated surface areas of 1738, 1750, 1603.5, and 1010 m^2 g^{-1}, respectively, which are within the literature value ranges. MOF Technologies was founded by Queen's University Belfast [37] and holds patents for the extrusion syntheses of about 20 kinds of MOFs based on Zn, Co, Mg, Cu, Al, lanthanides, Fe, Li, Sc, Mg, Cr, and Ti metal sources, including HKUST-1, ZIF-8, and Al-Fum [140,141]. Compared with other synthetic methods, the STY for extrusion is very high, almost 150,000 kg m^{-3} d^{-1}, and the system can be optimized for mass production with simple operation and a continuous process. Extrusion is also cost-effective because it allows for the use of commercialized and widely used equipment, and it is a solvent-free process with low operating costs.

3.2. Product recovery

3.2.1. Vacuum filtration

- Batch vacuum systems

Vacuum filtration is a common method for separating solid–liquid mixtures. On the laboratory scale, Buchner funnels and filter paper are used to separate solid products from reaction solutions. For scaling, the simplest approach is to enlarge the laboratory scale by bulk filtering on a larger scale. This type of filter system can separate approximately 10–50 L of solution at once. Although this simple system is capable of solid–liquid separation at a low cost, continuous production is impossible because the filter must be replaced after separating a certain amount of product. Therefore, it is suitable for use in the laboratory on a small test amount before proceeding to mass synthesis. Nutsche filtration operates on the same principle as basic vacuum filtration but is suitable for industrial production as a continuous method capable of simultaneous washing, drying, and filtration (Fig. 15a). An automatic system charges and then filters the sample in the chamber. Thereafter, fresh solution is sprayed on the sample cake, and washing is performed through a re-slurry process. The wet cake is obtained again through a filter process, and then the sample is dried by vacuum or convection in the chamber. Finally, the dried product is discharged from the bottom by rotating the agitator. This approach is excellent for producing high-quality products with recovery and refinement occurring at the same time. There are various system options and capacities depending on the usage and portions, from experimental laboratory scale to industrial scale (19–15,000 L) [142].

Fig. 7. Commercially available flow chemistry systems. Reproduced with permission from [120]. Copyright 2014 John Wiley and Sons.

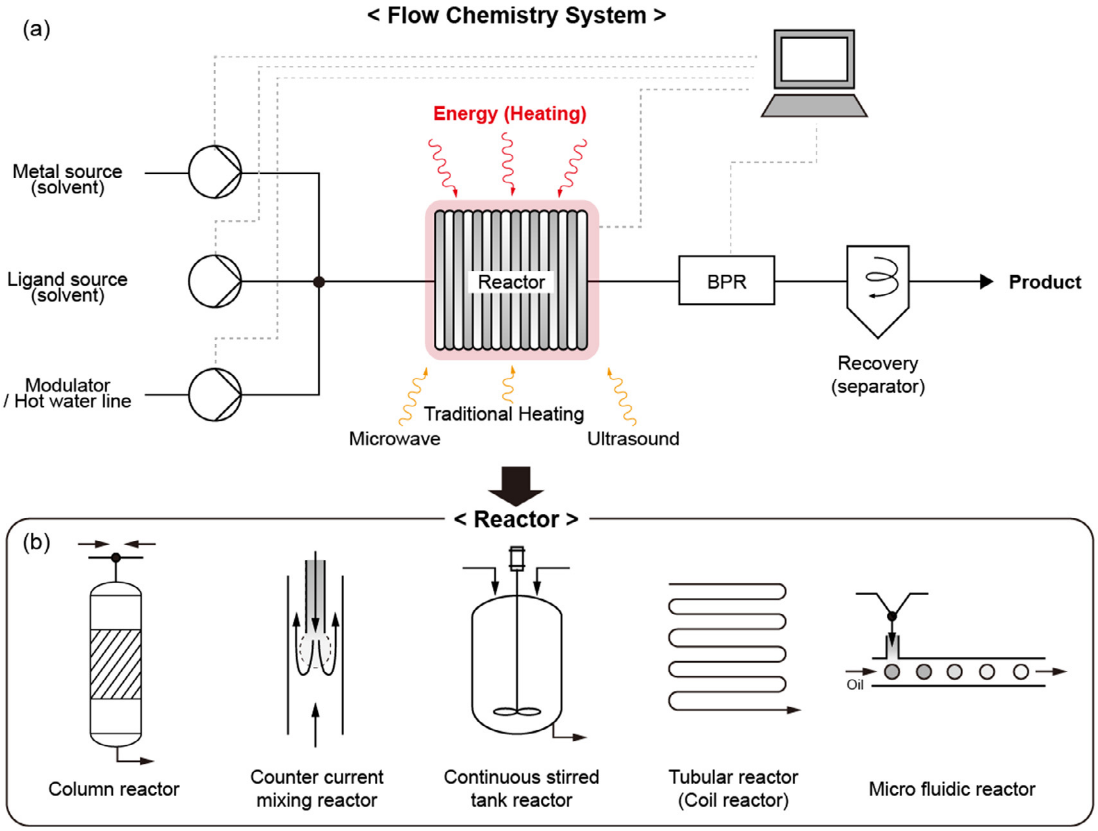

Fig. 8. (a) Schematic illustration of flow chemistry systems. (b) Schematic illustration of reactor for solvent-based continuous process.

- Continuous vacuum systems

Continuous vacuum filtration involves the automated continuous filtration of a uniform amount of sample, unlike batch systems. Continuous vacuum filtration systems are either belt type or rotary drum type, where the same basic principle of filtering a solid using a filter applies to both. For belt-type systems, the sample is placed on a filter cloth that rotates along rollers, causing a cake to form on the belt by an internal vacuum (Fig. 15b). Washing can also be performed while the belt is moving. The cake is separated downward

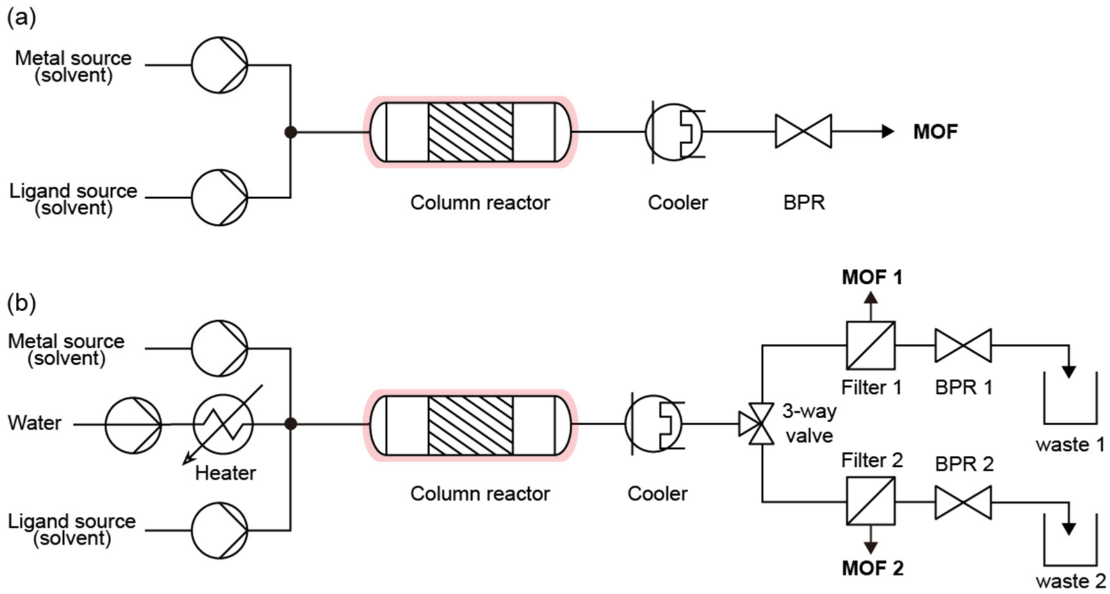

Fig. 9. (a) General flow synthesis system with column reactor (process of [121]) (b) Continuous flow synthesis system with filtration system (process of [122]).

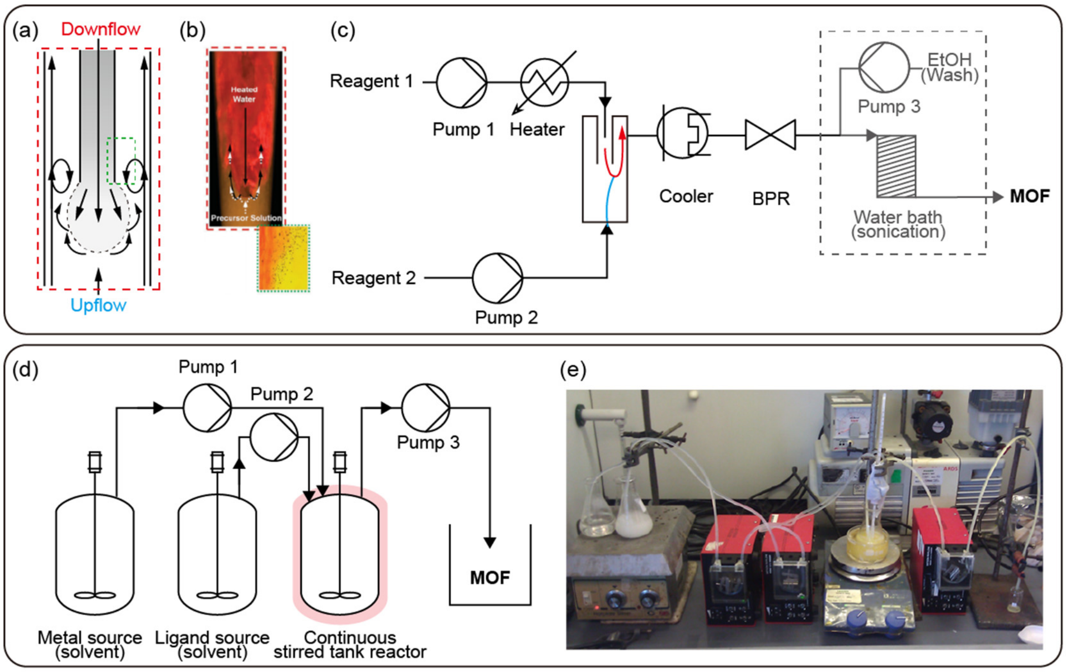

Fig. 10. Counter current mixing reactor (a) Schematic mixing process with a pipe-in-pipe concentric arrangement and (b) heat transfer processes. Reproduced with permission from [123]. Copyright 2012 Royal Society of Chemistry. (c) Flow synthesis system of CCR. **Continuous stirred tank reactor** (d) Flow synthesis system CSTR. (b) Photograph of MOF-5 synthesis system with CSTR. Reproduced with permission from [126]. Copyright 2016 Elsevier.

when the filter passes through the last flat section of the belt, and then the system is reused by washing the filter cloth.

Rotary drum filter systems vacuum the inside of a rotary cylindrical filter to coat a thick solid cake on the outside (Fig. 15c). The equipment is programmed as a continuous system, and when the cake reaches a certain thickness, it is automatically removed from the filter by a blade. In addition, a cleaning solution line allows for simple and cost-effective removal of the reaction solution from the sample attached to the filter. Rotary drum systems have better performances than belt-type systems due to the longer contact time with the washing solvent, but Nutsche filtration is the most effective in terms of vacuum filtration. Although it is difficult to obtain completely dried products using these two methods, they are effective for separating the product from the reaction solvent in a short time and as a continuous process.

3.2.2. Pressure filtration

Pressure filters and press methods are used in a wide range of industrial processes to separate particulate suspensions that exhibit slow settling and poor filtration. The pressure used for filtration

Table 9
Summary of MOF synthesized by column reactor, counter current mixing reactor, and continuous stirred tank reactor.

Reactor type	MOF	Time	Pressure	Reactor size	Temperature (℃)	Solvent	STY (kg m^{-3} day^{-1})	Productivity (g h^{-1})	Yield (%)	Surface area (m^2 g^{-1})	Ref
Column Reactor	HKUST-1	5 min (reaction)	–	1.59 mm ID, 30 cm	60 (60–160)	EtOH/Water	–	2	97	1673	[121]
Column Reactor	MIL-53(Al)	5–6 min (reaction)	230 bar	0.370 in ID, 20.3 mL	250 (200–300)	Water	1,300	–	86	1010	[122]
Column Reactor	HKUST-1	–	75 bar	0.370 in ID, 20.3 mL	300 (200–300)	EtOH	730	–	63	1554	[122]
Counter current mixing reactor	HKUST-1	–	250 bar	–	300 (100–400)	DMF/EtOH/ Water	–	132	–	1950	[123]
Counter current mixing reactor	CPO-27	–	–	–	200	DMF/Water	–	–	–	1030	[123]
Counter current mixing reactor	ZIF-8	1 min (reaction)	240 bar	55 mL	100	Water	3,875	810	–	1800	[124]
Continuous stirred tank reactor	MOF-5	4 h (residence)	atmospheric pressure	Conical flask	100 (reflux)	DMF/DEF	984	4	–	2302	[126]

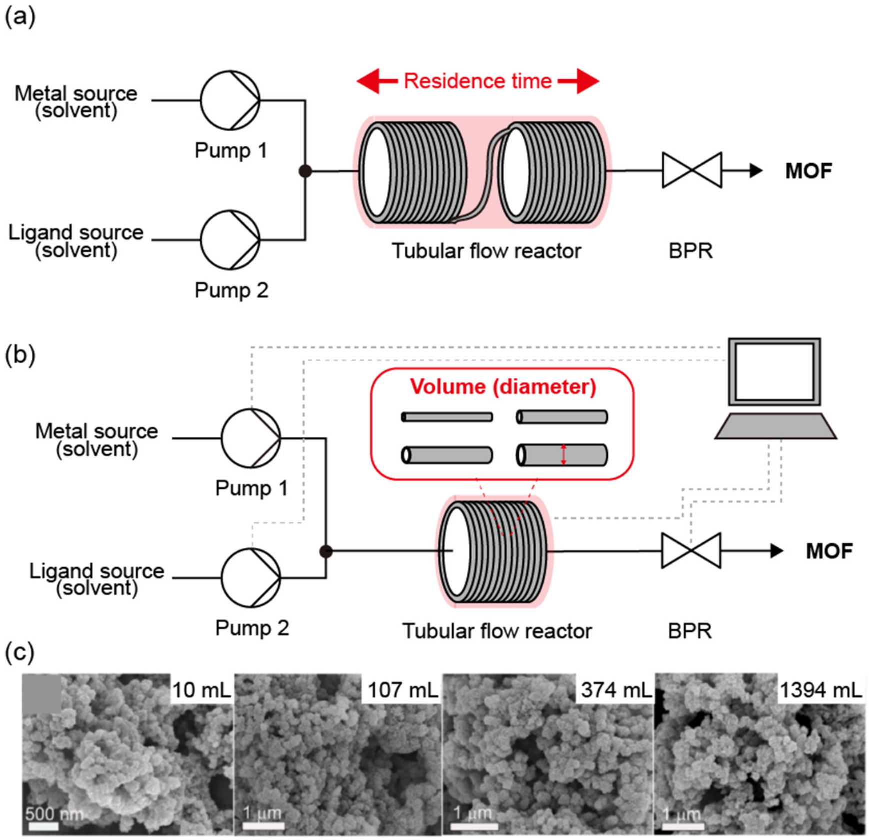

Fig. 11. Tubular flow reactor system by controlling (a) length of tube and (b) diameter of tube. (c) SEM images of Al-Fumarate crystals synthesized by different volume of tubular reactor. Reproduced with permission from [128]. Copyright 2016 John Wiley and Sons.

is usually 0–800 kPa, and a fully automated system can be achieved through cake forming, washing, and dewatering. There are also batch-type filtrations like Nutsche pressure filter systems, but herein we focus on continuous automatic belt press and screw pressure filtration systems.

- Belt press filtration

Belt press filtration is effective for dehydrating flocculated sludge and can be applied to various kinds of materials. As shown in Fig. 16a, the sludge is introduced between two tension filter clothes with rollers outside of each filter. The cloths are continuously pressed between small-diameter rotating rollers. The pressed solid cake is discharged as the cloth moves, and the filtered liquid is separated through the cloth filter. The used filter can be reused after discharging the cake by spray washing. Belt press systems can typically be applied to solids with particle sizes of 1–200 μm and feed concentrations of 0.2–30% w/w. The maximum feed flow rate according to the guidelines is 10–15 m^3 h^{-1} for each meter of the filter width, which is almost the same as loading 850 kg h^{-1} m^{-1} of solid [143]. In addition, belt presses exert a very high force on the solids between the filters, which can produce a solid filter cake even for cases where this would not be possible with other filtration methods. Belt press filtration is highly effective due to the

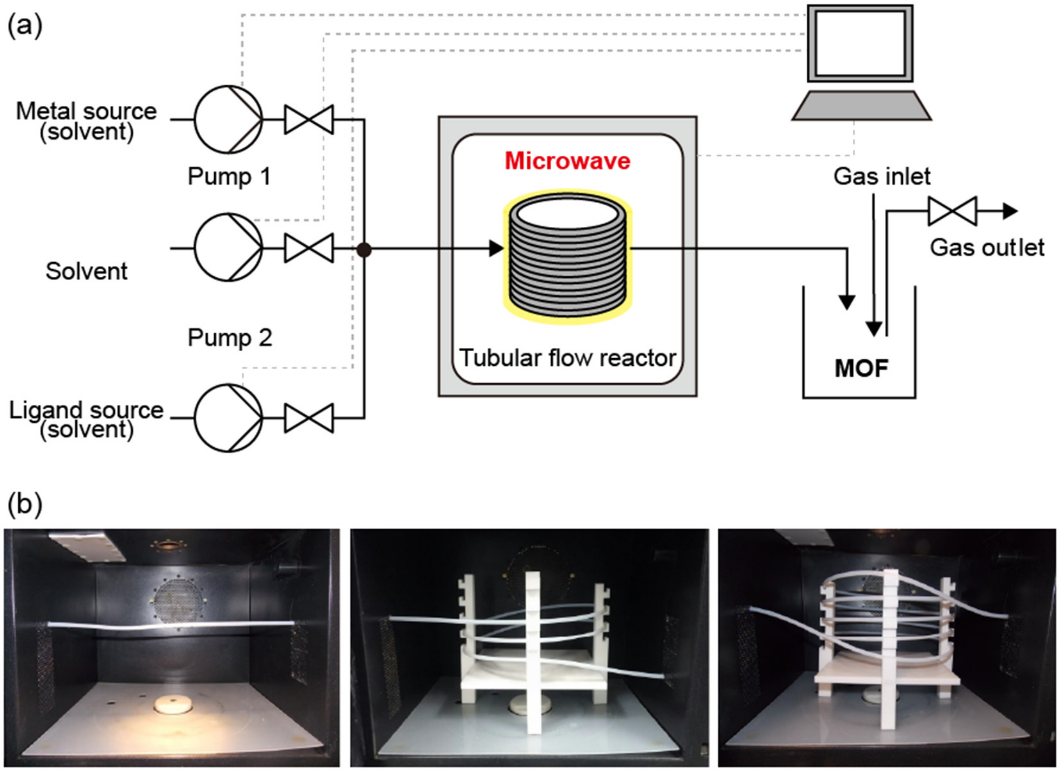

Fig. 12. (a) Tubular flow reactor system reacted by microwave. (b) The 6.2 mL, 29.6 mL, and 53 mL PTFE tubular reactor inside the microwave instrument. Reproduced with permission from [129]. Copyright 2016 John Wiley and Sons.

Table 10
Summary of MOF synthesized by tubular flow reactor.

Energy source	MOF	Residence time (min)	Tube material	Tube size	Temperature (℃)	Solvent	STY (kg m^{-3} day^{-1})	Productivity (g h^{-1})	Yield (%)	Surface area (m^2 g^{-1})	Ref
Heat	HKUST-1 (macroscale)	1.2	PFA	1.0 mm ID/ 20 mL	140	EtOH	4,533	61.2	100	1805	[127]
Heat	HKUST-1 (mesoscale)	10	PFA	1.0 mm ID/ 20 mL	80	EtOH	592	1.48	74	1852	[127]
Heat	UiO66 (mesoscale)	10	PFA	1.0 mm ID/ 20 mL	130	DMF	672	1.68	67	1186	[127]
Heat	NOTT-400 (mesoscale)	115	PFA	1.0 mm ID/ 30 mL	85	DMF/THF/ water	741	2.78	61	1078	[127]
Heat	Al-Fum	1	Stainless-steel	1.0 mm ID/ 10 mL	65	water	81,120	–	–	1070	[128]
Heat	Al-Fum	1.2	Stainless-steel	6.0 mm ID/ 107 mL	65	water	73,009	–	–	1015	[128]
Heat	Al-Fum	0.9	Stainless-steel	4.5 mm ID/ 374 mL	65	water	75,247	–	–	1082	[128]
Heat	Al-Fum	1	Stainless-steel	10.9 mm ID/ 1394mL	65	water	97,159	5,600	–	1054	[128]
Heat	UiO-66	0.44	–	0.8 mm ID	120	DMF	–	–	–	1206	[130]
Heat	ZIF-8	15 s	PFA	1.6 mm/3mL	RT	MeOH/ NH_3	210,000	15,360	54	1770	[131]
Heat	Ce-BDC	30 s	Stainless-steel	0.5 mm ID/1*m*	250	DMF	–	–	–	–	[132]
Microwave	UiO-66	7 (mw: 73 min)	PTFE	4.35 mm ID/ 53 mL	200 W,3bar	DMF	7,204	14.4	94	1052	[129]
Microwave	MIL-53(Al)	4 (mw: 34 min)	PTFE	4.35 mm ID/ 53 mL	200 W, 6 bar	DMF	3,618	7.1	65	1376	[129]
Microwave	HKUST-1	1 (mw: 17 min)	PTFE	4.35 mm ID/ 29.6 mL	360 W,6bar	DMF	64,800	79.4	96	1550	[129]

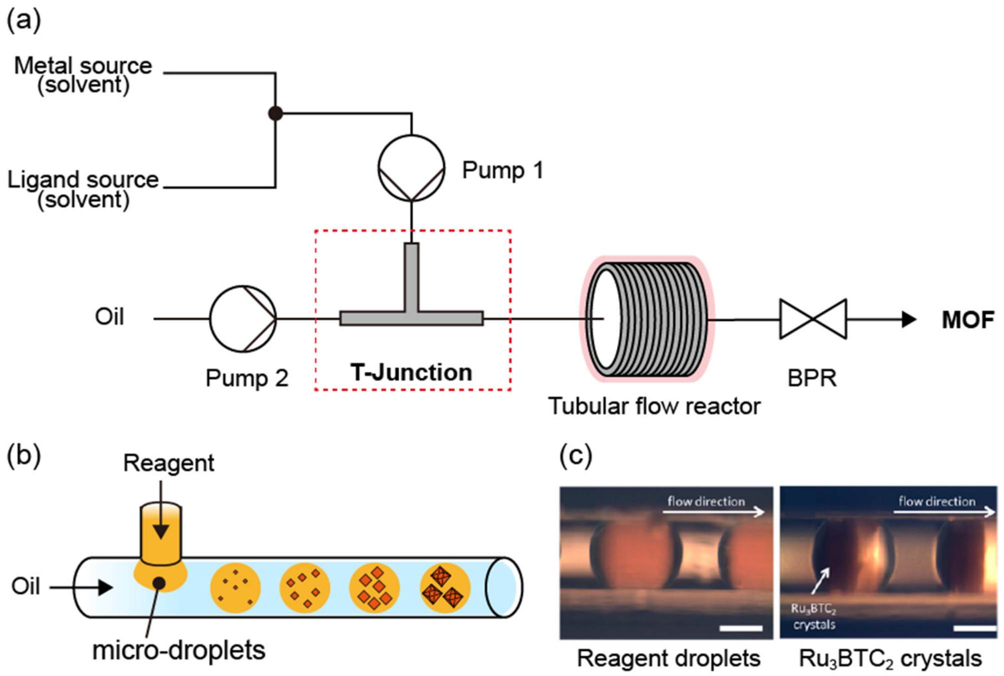

Fig. 13. (a) Schematic representation of micro fluidic reactor system. (b) Schematic illustration of microchemical synthetic process. (c) Optical images of single microdroplets containing (left) precursor solution and (right) segregated Ru_3BTC_2 crystals in the droplet. Adopted with permission from [133]. Copyright 2013 American Chemical Society.

Table 11
Summary of MOF synthesized by microfluidic reactor.

MOF	Residence time (min)	Tube material	Tube size	Temperature (℃)	Solvent	STY (kg m^{-3} day^{-1})	Productivity (g h^{-1})	Yield (%)	Surface area (m^2 g^{-1})	Ref
HKUST-1	12	TFA	0.508 nm ID	90	DMF/EtOH/water	5.8	4.2	68	1911	[133]
MOF-5	3	TFA	0.508 nm ID	120	DMF	–	–	–	3185	[133]
IRMOF-3	3	TFA	0.508 nm ID	120	DMF	–	–	–	2428	[133]
UiO-66	15	TFA	0.508 nm ID	140	DMF/HCl	–	–	–	1059	[133]
Ru_3BTC_2	12	TFA	0.508 nm ID	160	water/EtOH	–	–	–	550	[133]
UiO-66	160	–	2 mm ID/0.5,2,3,4 m	130	DMF	–	–	–	817	[136]
MIL-88B-NH_2	10	Teflon	0.04 in ID	95	DMF/water	–	–	12.4	–	[137]
MIL-88B	4	Teflon	0.04 in ID	95	DMF/water	–	–	1.9	–	[137]
MIL-88B-Br	6	Teflon	0.04 in ID	95	DMF/water	–	–	2.8	–	[137]
UiO-66-NH_2	–	–	–	120	DMF	–	5	–	1700	[134]
ZIF-8	10	PTFE	1.6 mm ID	25–100	Water	–	–	–	1786	[138]

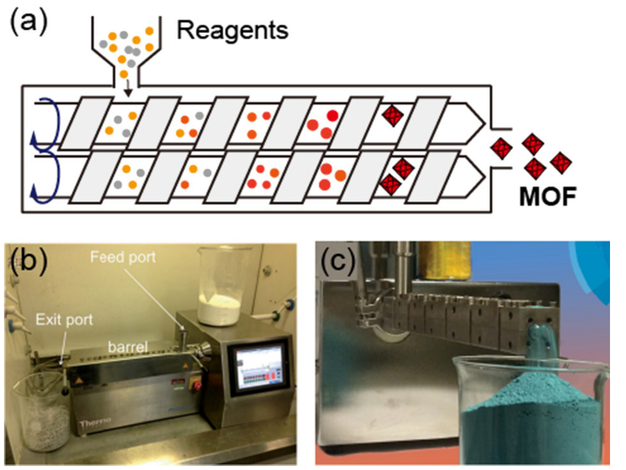

Fig. 14. (a) Schematic illustration of extrusion synthesis with twin screw extruder. (b) Setting of TSE instrument for large-scale MOF synthesis. (c) Synthesis HKUST-1 by TSE. Reproduced with permission from [139]. Copyright 2015 Royal Society of Chemistry.

high throughput and appropriate particle size range for MOFs. However, it requires a long, strong filter cloth that is expensive to replace.

- Screw press dehydration

Screw press filtration, which can be either batch or continuous, is effective for compressing fine suspensions into solid product (Fig. 16b). Typically, the screw filtration system is equipped with a helical screw rotating at 2 rpm inside a cylinder-shaped perforated cage. The slurry introduced into the closed end is moved to the opposite side by the rotating screw. As the volume between the barrels of the screw gradually decreases, pressures up to 40,000 kPa occur. The solid cake is compressed and discharged in the opposite direction, and the separated liquid passes through the porous cage. Screw pressing for continuous filtration is based on a high pressure and can separate 1–200 μm particles in a feed concentration range of 10–80% w/w. There are different sizes and types of equipment depending on the required processes, and the processing capacity depends on the material type and length and diameter of the system. A high-capacity unit with a length of 8 m and diameter of 1 m can handle one ton of solids per hour

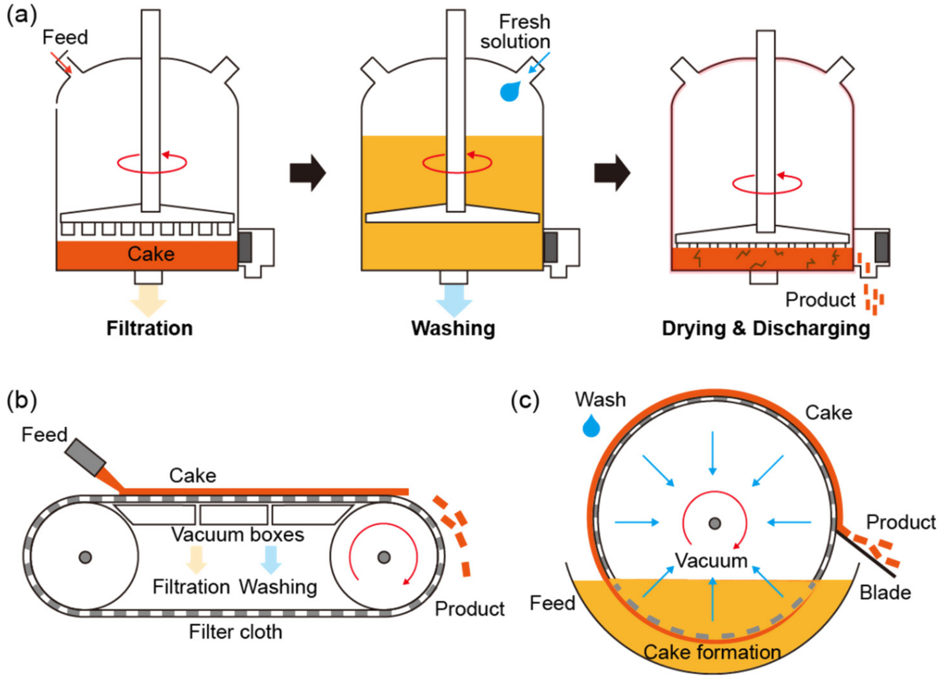

Fig. 15. **Vacuum filtration** Schematic illustration of (a) Nutsche filtration process (b) Belt type vacuum filter system (c) Rotary drum vacuum filter system.

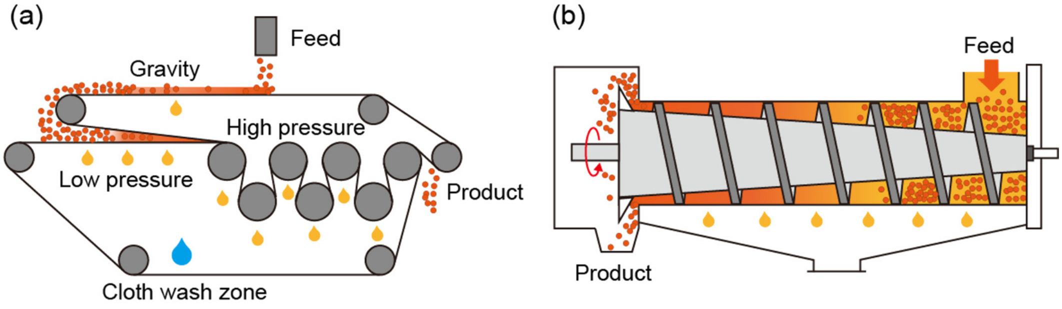

Fig. 16. **Pressure filtration** Schematic illustration of (a) Belt press filtration (b) Screw press dehydrator.

[144]. These systems are already used in industries such as pulp, sewage dehydration, chemicals, pharmaceuticals, etc.

3.2.3. Continuous centrifugation

Besides filtration, centrifugation is another representative method for separating MOF products from reaction solutions in the laboratory. A large-capacity centrifuge operates on the same principle as a lab-scale centrifuge (Fig. 17). There must be a density difference between the solid and liquid to be separated, and the denser solid precipitates on the wall and is separated from the solvent by a centrifugal force. The separation efficiency depends on the type of solvent, amount of solid, rotational speed, and residence time, where increasing the speed and time also increases the efficiency. Whereas filtration requires the hassle of selecting a filter type according to the particle size and concentration and replacing the consumable filter, centrifugation separates various particles more effectively by controlling the operating conditions. Although there are several types of industrial centrifuges, disc stack centrifuges are notable in that they can be operated in both batch mode and continuous mode and can handle large volumes.

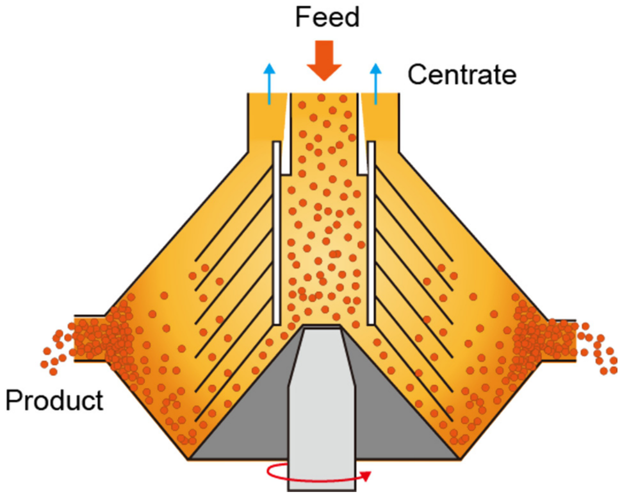

Fig. 17. Schematic illustration of continuous centrifuge.

When solid products build up on the wall, a valve automatically or manually opens to release the product, and the accumulating step repeats. Disc stack centrifuges exert centrifugal forces exceeding 14,000 g and rotational speeds of 3000–10,000 rpm. They are useful for obtaining various sizes of particles from 0.1 to 200 μm, which can be recovered even at low solid concentrations (>25%), making centrifugation an effective way to separate MOFs from solutions.

3.2.4. Ultrasonic separation (megasonic)

Ultrasonic separation is employed to recover substances from suspensions of various components. High-frequency ultrasound is generated by placing a dispersion solution between the transducer (sound source) and reflector (Fig. 18a, b). The ultrasonic standing waves concentrate individual particles at the acoustic pressure nodes or antinodes, and thus the particles migrate closer together and aggregate, even coagulate and coalesce (Fig. 18c). If the MOF is small (nanometers to a few micrometers) or present at a low concentration in solution after the reaction, directly using a conventional filter or centrifuge may be inefficient. Therefore, the processing cost and time can be reduced by performing ultrasonic separation in parallel. Ultrasonic separation can separate solids from dispersions without chemical or physical effects, and in the case of porous structures such as MOFs, activation of the inner pores can be performed simultaneously. In an example of applying ultrasonic separation to MOFs, Al-Fum and MIL-53 were separated in 10 min via 2 MHz sonication in a 1 L chamber (Fig. 18d) [145,146]. Compared with centrifugation, sonication had a 3% lower yield, but the surface areas were improved by 21% and 47% for Al-Fum and MIL-53, respectively.

In addition to solid particles, ultrasonic separation can also be applied to liquids, gases, and biological cells, and thus it is common in the food and bioproduct fields. In particular, the ultrasonic separator used for large-capacity palm oil can process 45 tons h^{-1} due to its high separation rate (Fig. 18e, f) [147]. Combining these technologies with MOF separation and activation is expected to enable high-quality MOF recovery in a cost-effective manner.

3.3. Scalable solvent exchange processes

After recovering the MOF solid from the reaction solution, the final product can be obtained by immediate thermal or vacuum evacuation. However, any solvents, unreacted substances, and counter ions that have not been completely removed from the inner pores will reduce the porous properties such as the surface area. In addition, since MOFs are generally synthesized in solvents with high boiling points, structural collapse and incomplete activation can occur due to high capillary forces and surface tension during evaporation. Solvent exchange to address these issues proceeds in two stages: guest exchange and guest evacuation (Fig. 19). When the MOF is washed with volatile solutions having low boiling points, the washing solvent exchanges with the reaction solvent in the pores. This is a common method for pore activation and has been proven effective in many studies [75,102]. In some cases, an additional chemical treatment is performed to remove specific reactants. Although pore activation processes such as solvent exchange are not essential for MOF production, their use can greatly reduce the total amount of energy input to remove the reaction solvent. Such processes should be performed when counterions that do not evaporate must be removed.

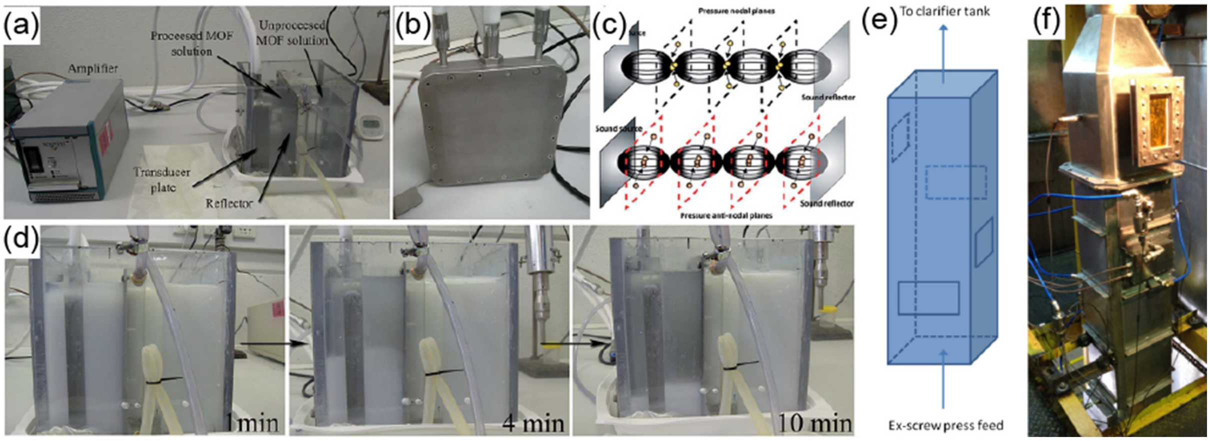

Fig. 18. (a) The ultrasonic reactor set-up with a high frequency system using one 2 MHz plate transducer shown in (b). (c) Schematic representation of the standing wave pattern formed by the superimposition of a reflected sound wave. (d) The megasonic separation and purification process of the Al-MOF by time duration. (e) Schematic representation and (f) digital image of the commercially operating megasonic reactor (45 ton per hour). (a-d) have been reproduced with permission from [145]. Copyright 2016 Royal Society of Chemistry. (e-f) have been reproduced from [147]. Copyright 2015 Springer Nature.

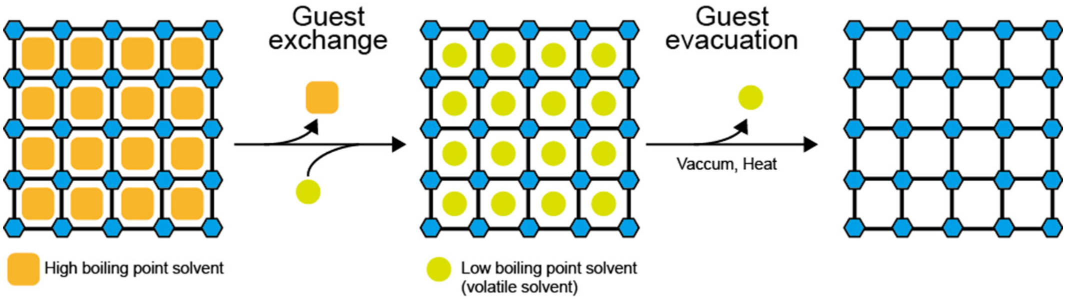

Fig. 19. Schematic illustration of guest exchange and guest evacuation.

3.3.1. Continuous washing system: solvent exchange

A solid–liquid mixer or stirred tank system can be used to exchange solvents in large quantities. Such systems can provide sufficient solvent exchange with full contact between a fresh volatile solvent and solid, but the pure solvents must be replaced with use for efficient washing. Therefore, performing washing and recovery simultaneously on one instrument would save operating costs, time, and factory space. Equipment can be introduced to the recovery part of the system to also carry out washing. In the case of ultrasonic separation, solvent exchange can easily be performed by repeated treatment with a low-boiling-point solvent. In particular, continuous automatic cleaning can be carried out simply by vacuum filtration. Nutsche filtration is the most effective, in which fresh solvent is injected into the filtered batch to perform re-slurry washing with an agitator. The wash cycle lasts long enough for solvent exchange and can be repeated as many times as needed. During washing with rotation, the solid products and solvent are blended homogeneously, allowing for efficient solvent exchange. Additionally, other filtration methods such as belt and rotary systems can be performed for simultaneous recovery and washing when forming a cake by vacuum. Because of the short contact time between the fresh solvent and cake, it is not easy to exchange the solvent in the pores, but the method is appropriate for removing unreacted substances and solvents from the product surface. There are various combinations of residence times and solvent types, which depend on the MOF type and synthetic conditions. To optimize the process, the rates of substitution and surface area enhancement should be determined by nuclear magnetic resonance (NMR) and sorption analysis.

3.3.2. Soxhlet extraction

In the continuous cleaning systems discussed in Sections 3.3.1 and 3.3.2, the washing and recovery processes are cycled, and fresh solvent must be provided for each cleaning step, which increases material costs and causes environmental issues from excess solvent. In contrast, Soxhlet extraction employs a closed batch system consisting of a sample contained in a cup (filter), condenser, distillation flask, and heat source (Fig. 20). As the evaporated solution condenses, the warm solvent drops onto the sample for solvent exchange, and then the solvent is re-evaporated. Therefore, Soxhlet extraction has the significant advantage of reusing a limited amount of solvent through an automatic system. This method has commonly been used for MOF solvent exchange (Mg-MOF-74, Mg-MOF-174, Mg-MOF-184, MIL-100, etc.) [73,76] on the laboratory scale, but it is expected to also be capable of processing a large amount of MOFs with an industrial extractor. Such industrial equipment has capacities from 100 to 1000 L depending on the type and size. However, the process consumes thermal energy to evaporate the solvent and has long residence times of several hours to days. This method is also not suitable for thermolabile frameworks.

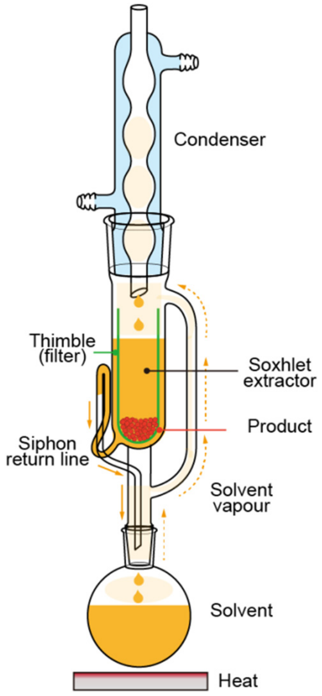

Fig. 20. Schematic illustration of Soxhlet extractor.

3.3.3. Chemical treatment (additives)

Some MOF syntheses involve a chemical treatment for activation along with solvent exchange, mainly to remove excess ligands and modulators as impurities. Seo et al. conducted chemical treatment with NH_4F to remove reaction residues and increase the surface area of MIL-100(Fe) [76], and they confirmed by fourier-transform infrared spectroscopy (FT-IR) analysis that trimesic acid (ligand) was effectively removed. Furthermore, the surface area increased from 1800 to 2000 $m^2\ g^{-1}$ compared with the product subjected to only solvent exchange. In another study, PCN-222 (Fe) and NU-1000 were subjected to chemical treatment with HCl to eliminate benzoic acid as a synthesis modulator [148,149]. HCl removed the benzoic acid bound to the Zr nodes of both Zr-based MOFs and activated their pores effectively. After chemical treatment, PCN-222 had a much higher surface area (2007 to 2229 $m^2\ g^{-1}$) and nitrogen uptake (789 to 1016 $cm^2\ g^{-1}$). Since Zr-based MOFs have outstandingly rigid and stable structures, this strong HCl acidic treatment was possible. Therefore, the stability of the target MOF should be considered when selecting a chemical treatment. Additionally, re-washing is required to remove the chemicals, and thus there is no need for chemical treatment if solvent exchange alone is effective.

3.4. Scalable drying processes

After the wet MOF cake is obtained by the recovery process, a drying process must be performed to ultimately obtain the produced MOF particles in bulk powder form. The following direct and indirect drying methods will be discussed for obtaining this final powder MOF product. With direct drying, the product is heated and dried in direct contact with a hot gas, whereas with indirect drying, there is a wall between the wet product and heating medium, and the product dries by heat transfer from the hot surface. An appropriate method should be chosen depending on the shape, size, and characteristics of the final product. We discuss batch and continuous conveyor dryers, as well as spray drying and freeze-drying for products with a high heat sensitivity.

3.4.1. Dryers

- Batch tray dryer

Batch tray drying is a basic drying method where wet product cakes are placed on pans and trays in heating zone shelves (Fig. 21a). This method is based on heat transfer by the heating medium, which can be considered as a large-capacity oven, as typically used in laboratories. The sample trays are typically metallic for high heat transfer. For heat-sensitive products, a vacuum can be applied for drying at low temperatures. When a vacuum is applied to the drying chamber, steam is removed through an exhaust pipe, passes through a condenser, and is removed. Normally, each tray has a loading depth of 40 mm and can hold 40 kg m^{-2} of wet material [150]. Batch tray dryers are used to treat

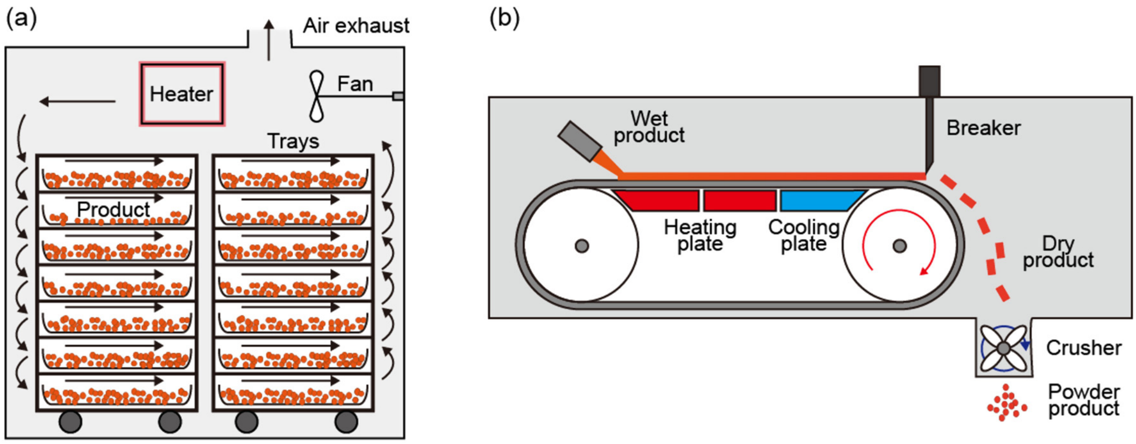

Fig. 21. **Dryers** Schematic illustration of (a) Batch tray dryer (b) Continuous dryer.

various types of samples, such as milk powder, fruit, inorganic materials, ceramics, etc. They have the advantage of easy access due to the simple operation principle and equipment. However, MOFs consisting of nanosized particles exhibit severe agglomeration problems after batch tray drying. There are also significant labor costs for loading and unloading the samples to be dried, and the production efficiency is limited due to the low capacity (20–50 kg h^{-1}) [150].

- Continuous dryers

To effectively dry large capacities of products at once, it is necessary to consider a continuous dryer method. Conveyor dryers operate on the same principle as batch dryers but as continuous systems. The product is continuously transferred to the dryer by a conveyor, and hot air is forced through the bed (Fig. 21b). Vacuum belt conveyor dryers are expected to be more suitable for heat-sensitive products and effective pore activation. The inside of the closed chamber is kept under vacuum, and samples are continuously introduced and dried on the conveyor. In such conveyor systems, the drying yield depends on the size of the equipment and the heating area, but equipment with a water vapor capacity of 210–230 kg h^{-1} can yield up to 500–800 kg h^{-1} of dry powder [151]. The drying rate depends on the condition and type of material, where a continuous conveyor system can process approximately 10–50 kg $m^{-2}h^{-1}$ [152]. To enhance the product drying capacity, stages can be connected to increase the drying rate, retention time, loading amount, as shown in Fig. 21b. In addition, crushing of the agglomerated product after drying can be carried out continuously, which simplifies the process. This type of conveyor system is used for drying chemical products, pharmaceutical products, baking mixes, baby food, etc.

3.4.2. Spray drying

Spray drying is attractive for optimal size control of the MOF powder product with a continuous process. The fluid is sprayed through a nozzle, and the expelled droplets encounter the hot medium immediately (Fig. 22a). Spray drying causes rapid evaporation and maintains the droplets at a low temperature, and thus the product is not affected by heat [150]. In addition, spray drying requires a very short process time compared with other dryers and is mainly used for processing pharmaceuticals, fine chemicals, inorganic chemicals, dairy products, food, and ceramic powders. This type of equipment is not only excellent for drying heat-sensitive samples but also allows for control of the product properties such as particle size, shape, and morphology and can be applied to nanosized particles. In addition, spray drying is also suitable for the mass production of MOF nanopowders because it can be performed continuously in connection with a previous stage, and uniformly sized particles with a high reproducibility can be produced by controlling the spraying conditions. In addition, products can be dried in the form of microcapsules according to the spraying conditions (Fig. 22b). Spray dryers have evaporation capacities from a few kilograms per hour to 50 tons h^{-1} or more [152]. As detailed in a 2006 BASF patent, 12.64 kg of Al-MOF was sprayed and dried using a conical laboratory fluidized-bed dryer, and the surface area of 1333 m^2 h^{-1} of the resulting product was slightly higher than that of the same MOF dried in a convection oven [68]. There are many advantages to spray-drying MOFs, but the high initial installation cost and low thermal efficiency must also be taken into account.

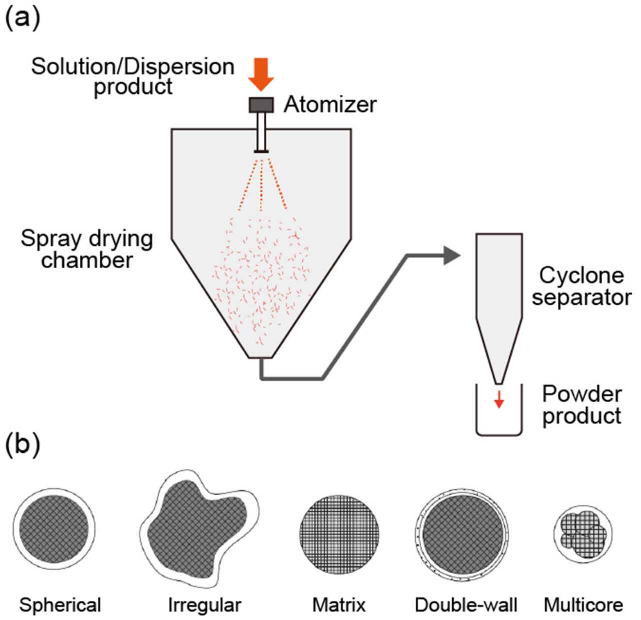

Fig. 22. (a) Schematic illustration of spray dryer. (b) Configuration of the main types of microcapsules. Reproduced with permission from [152]. Copyright 2016 John Wiley and Sons.

3.4.3. Freeze-drying

Freeze-drying, another excellent approach to drying MOFs, involves drying the frozen product in a wet state with water or

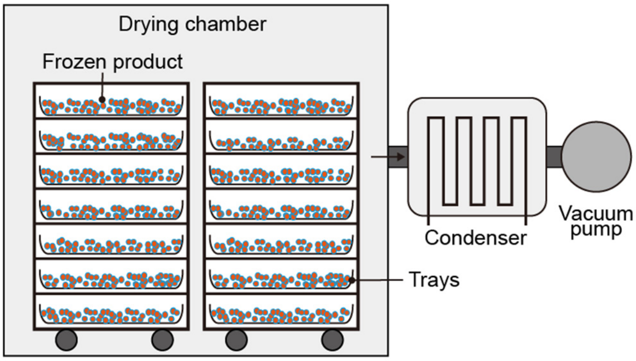

Fig. 23. Schematic illustration of freeze dryer.

other solvents by sublimation in a vacuum chamber (Fig. 23). Since this is not a direct heating method, it is advantageous for heat-sensitive products. Particularly, when drying porous materials such as MOFs, freeze-drying is effective for minimizing structural collapse and obtaining a high surface area. However, due to the long drying times and vacuum process, it is only suitable for the production of expensive, high-quality materials. In particular, the most common freeze-drying system is the tray batch type, which is mainly used for food, but only 2–20 kg can be processed at one time. A multi-batch freeze dryer or tunnel freeze dryer can be used to increase the throughput. Additionally, combining spray- and freeze-drying is excellent for producing uniform products of a certain size continuously. In a previous study on a Cu-MOF composed of tetracarboxylic acid, the surface area was increased by 3 times (1725 m^2 g^{-1}) compared with the vacuum-dried MOF (582 m^2 g^{-1}) [153]. MOFs with stable structures and high surface areas are expected to be produced even on the industrial level by the freeze-drying method.

4. Post-processing of MOFs

It is difficult to directly apply MOFs in powder form to applications on an industrial scale, but they are usually obtained as a powder after synthesis. The use of MOF powders in industrial lines can cause the following problems: i) pressure drop in the pipeline, ii) reduced or blocked flow, iii) abrasion due to powder blowing, and iv) reduced amount of MOF product. These problems can be solved by postprocessing of the MOFs into the form of granules, pellets, tablets, foams, or films. In this section, the criteria, materials, and methods in shaping and dispersion processes are reviewed to make the forms before applying them in the industrial applications.

4.1. Shaping processes

Shaping has been applied to other porous materials such as activated carbon and zeolites, and thus it has a long history of industrial development. In this section of the review, the criteria, binders, and techniques for shaping MOFs are described based on previous studies and summarized in this part.

4.1.1. Criteria for MOF shaping

- Mechanical strength

Applying MOF shaping to industrial lines changes the powder product into a different solid-state form such as pellets or granules. If the product returns to a powder form or to a fragmented solid state, the broken pieces will cause powder or fragment blowing in the line, leading to a pressure drop and fraying. Therefore, for large-scale line processes, a mechanical strength test for MOF shaping must be performed to avoid such issues.

After shaping the MOF, the mechanical strength can be checked by analyzing the Young's modulus or performing an attrition test to ensure that it will maintain its physical and strength properties. Young's modulus indicates the mechanical stiffness of a solid material and is defined by the relationship between stress (force per unit area) and strain (proportional deformation). The value corresponds to the maximum tensile strength before fracture and thus gives a mechanical guideline for process engineers. This value is not related to geometric shapes but instead to the material composition and shaping process conditions.

Attrition tests include both dropping and abrasion analyses. For the dropping test, multiple samples from different batches are dropped from a specific height, and the number of samples that maintain their original shape without breaking into fine particles is counted. Alternatively, a sample is repeatedly dropped from a specific height, and the number of times it can be dropped while maintaining its shape is recorded. For the abrasion test, samples are repeatedly rolled in a rotating container at a specific rotational speed, and the number of samples maintaining their original shape without breaking into fine MOF particles is counted. These methods are suitable for comparing samples measured under the same conditions, but the results cannot be directly compared with reported values measured under different conditions.

- Surface area

When MOF shaping is performed using binders or by applying a high pressure, the binder can sometimes clog the MOF pores, and external mechanical force can collapse the crystalline structure, thus reducing the porosity. Therefore, to determine if the pores are maintained, the total amount of adsorbed nitrogen gas at a low temperature is measured and compared with other references or MOF results. Then, considering the ratio of the binder, it is possible to infer that the porosity is maintained if it is equal to the surface area of the base employed MOF. Additionally, the sizes of the micro- and macro-pores can be compared with those of the MOF when shaping their form.

- Chemical stability

Chemical stability must also be considered to apply MOF shaping for applications. For example, if a shaped MOF is to be used in an application where the performance changes depending on the pH, an acid/base stability test can determine which binders are suitable for obtaining a high stability. This test compares how many fine particles remain relatively with collapsed particles by introducing the shaped MOF to various acid/base solutions. As a result, the binder and shape can be selected to ensure that the cohesion between MOF particles at a particular pH does not collapse the shape or structure.

4.1.2. Binder selection

In most cases, MOFs do not have a cohesive force on their own, and thus they usually cannot be shaped with enough mechanical strength by low-pressure processes. On the other hand, applying a high pressure for shaping readily causes MOFs to lose their inherent crystallinity and porosity. Therefore, the addition of a binder to reduce the required energy and improve the process efficiency is inevitable. According to a literature analysis of previous studies, various binders have been applied depending on the type of MOF and the requirements of the target applications. In this section, organic, inorganic, and composite binder types are discussed in terms of their characteristics, advantages, and disadvantages. Binder-free processes are also examined to highlight their pros

Table 12
Summary of binder selection for shaping processes.

a. Polymer binder

Binder	MOF	Ratio of MOF/Binder	S. A. Before	S. A. After	Process time	Ref
Polyvinyl group	MIL-125-NH$_2$	97%	1259	930	–	[154]
Polyvinyl alcohol (PVA)	UiO-66	22 vol%	710	359	30 min	[155]
Polysiloxane	UiO-66	72.5 vol%	710	418	30 min	[155]
Polyvinyl Butyral (PVB)	SIFSIX-3-Ni	–	360	297	–	[156]
Polyvinyl Butyral (PVB)	SIFSIX-2-Cu-i	–	808	685	–	[156]
Polyvinyl Butyral (PVB)	GeFSIX-2-Cu-i	–	755	659	–	[156]
Polyvinyl Butyral (PVB)	TIFSIX-2-Cu-i	–	740	719	–	[156]
Polyvinyl Butyral (PVB)	Mg-MOF-74	–	915	–	–	[156]
Polyvinyl Butyral (PVB)	HKUST-1	–	–	–	–	[156]
Polyvinylchloride (PVC)	ZIF-8	7.5/15/30 wt%	–	–	–	[157]
Polyvinylformal (PVF)	ZIF-8	7.5/15/30 wt%	–	–	–	[157]
Polyetherimide (PEI)	ZIF-8	7.5/15/30 wt%	–	–	–	[157]
Polystyrene (PS)	ZIF-8	7.5/15/30 wt%	–	–	–	[157]
Cellulose-acetate (CA)	ZIF-8	7.5/15/30 wt%	–	–	–	[157]
Acrylonitrile butadiene styrene (ABS)	MOF-5	1%	–	–	–	[158]
Acrylonitrile butadiene styrene (ABS)	MOF-5	5%	–	–	–	[158]
Acrylonitrile butadiene styrene (ABS)	MOF-5	10%	–	–	–	[158]
Sucrose	UiO-66	90 wt%	1367	674	1 d	[159]
TENAX	(CO)MOF-74	14 wt%	86	55	1 d	[160]
TENAX	(Zn)ZIF-8	8.4 wt%	–	–	1 d	[160]
TENAX	(CO)ZIF-67	9.6 wt%	–	–	1 d	[160]
TENAX	(Zr)UiO-66	8.4 wt%	–	–	1 d	[160]

b. Inorganic binder

Binder	MOF	Ratio of MOF/Binder	S. A. Before	S. A. After	Process time	Ref
Mesoporous Rho Alumina (MRA)	MiL-100(Fe)	95 wt%	2088	1831	12 h	[161]
Mesoporous Rho Alumina (MRA)	MiL-101(Cr)	95 wt%	4066	3685	12 h	[161]
Mesoporous Rho Alumina (MRA)	UiO-66	95 wt%	1050	911	12 h	[161]
Mesoporous Rho Alumina (MRA)	UiO-66-NH$_2$	95 wt%	875	823	12 h	[161]
Bentonite clay	MIL-101(Cr)	60%	202.22	182.84	several days	[162]
Bentonite clay	MIL-101(Cr)	75%	202.22	182.84	several days	[162]
Graphite	UiO-66	99%	1140	885	–	[163]
silica sol	MiL-100(Fe)	90%	1772	1619	12 h	[164]
Silres MSE 100 ($CH_3Si(O)_{1.1}(OCH_3)_{0.8}$)	HKUST-1	88%	–	–	20 min	[165]

c. Binderless (Binder-free)

Binder	MOF	Ratio of MOF/Binder	S. A. Before	S. A. After	Process time	Ref
Binder-free	MOF-5	–	2750	2600 ~ 1200	–	[166]
	CPO-27-Ni	–	1060	1050	30 min	[167]
	CuBTC (Basolite™ C300)	–	–	–	–	[168]
	MIL-53(Al)	–	–	–	–	[168]
	HKUST-1	–	–	–	3 h	[169]
	UiO-66	–	1175	511/417	6–18 h	[155]
	HKUST-1	–	–	–	11 h	[170]
	ZIF-8HT	–	–	1387	1 d	[170]
	ZIF-8LT	–	–	1359	1 d	[171]
	ZIF-8LT-HT	–	–	1423	1 d	[171]
	ZIF-8ER	–	–	1395	1 d	[171]

and cons in comparison. All cases investigated in this review are summarized in Table 12.

- Polymer binders

Shaping using polymer-type binders has been the most widely studied. Specifically, polymer binders with polyvinyl groups such as Polyvinyl group [154–157], polyetherimide (PEI) [157], polystyrene (PS) [157], cellulose-acetate (CA) [157], acrylonitrile butadiene styrene [158], sucrose [159] and TENAX [160] have been combined with MOFs for shaping. Typically, polymer binders are the first choice for MOF shaping because i) they are easy to dissolve in volatile dispersion media, making mixing and drying of the MOF powder relatively simple; ii) they have various chemical bonding groups, and thus the degree of interaction between the chemical functionalities and dangling components of the MOF particles can be controlled; iii) there are many precedents for the use of polymers as binders with other classes of porous materials, such as activated carbon and zeolites, which increases the probability of shaping success; and iv) compared with inorganic binders, organic binders have relatively low weights, and thus the weight of the binder required for shaping is low, which is advantageous in terms of performance per unit weight. On the other hand, there are also disadvantages to the use of polymer binders: i) there is a relatively high possibility of reducing the surface area due to insertion of the polymer binder into the MOF pores; ii) use of an improper polymer can coat the MOF surface and block the pores; and iii) the chemical functionalities of the polymer binder can influence the chemical characteristics of the MOF, which can unexpectedly change or deteriorate the target properties. Therefore, it is important to consider the chemical characteristics and physical behavior of both the polymer binder and MOF in terms of the requirements of the target application.

One notable study used a 4 vol% polyvinyl alcohol (PVA) solution in DI water [155], which was then mixed with UiO-66-COOH (22 vol%). The mixture was freeze-dried for granularization. The

BET (Brunauer–Emmett–Teller) surface area was calculated to be reduced by 58.8% (BET surface area of UiO-66-COOH is 710 and BET surface area of bead is 418 g cm^{-3}), and all of the beads were recovered by the attrition test. The product was passed through a 425-μm sieve to recover fine particles after the shaking and falling tests, which showed that the fine particle content was approximately 1.7% lower than that in the MOF shaped without a binder. Thus, PVA improved the cohesion between MOF crystals, making the product difficult to break.

In another study [156], polyvinyl butyral (PVB) was dispersed in ethanol to 8 wt%, and SIFSIX-3-Ni was mixed to form pellets 1–2 mm in size by extrusion molding. The reduction of the BET surface area after MOF shaping was calculated to be 17.5%. Compared with the proportion of MOF content, this reduction of BET surface area is small.

In [159], a 10 wt% sucrose in H_2O mixture was used as a polymer binder, and a centrifugal granulator (BZL-300, China) was used to shape Zr-MOF powder into pellets with diameters of 0.5–15 mm (Fig. 24a, c). The reduction of the BET surface area between value of the Zr-MOF powder and Zr-MOF powder was calculated to be 50.69% (The BET surface area of Zr-MOF powder is 1367 m^2 g^{-1} and The BET surface area of Zr-MOF pellet is 674 m^2 g^{-1}). Even considering the binder portion, the BET surface area decreased by >10%. However, this amount of binder minimized the surface area reduction while maintaining the robust mechanical strength and shape of the pellets. The fine particle amounts were compared between the Zr-MOF powder and shaped Zr-MOF after attrition tests (Fig. 24b, d). No breakage of the shaped Zr-MOF pellets occurred in the dropping test until 70 drops, and >95% of the fine particles were recovered in the abrasion test.

- Inorganic binders

Alumina and silica are commonly used as inorganic binders. Unlike polymer binders, inorganic binders are not easily deformed even at high temperatures, and they impart a high compressive and abrasion resistance to the shaped product. In addition, they are highly dispersible in hydrophilic media such as water and alcohols in small amounts and can be used to form a rigid, sturdy shape due to OH bonding between the MOF metal and alumina or silica. In this section, we introduce some examples of inorganic materials as shaping binders.

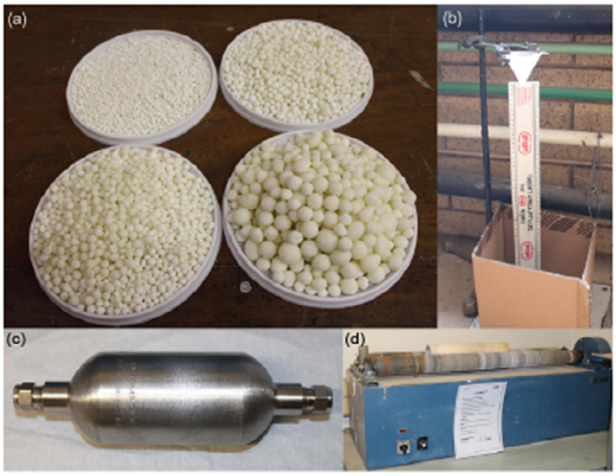

Fig. 24. (a) The pellet with different diameters of Zr-MOF. (b) Set up of drop test for dropping mechanical strength. (c) Cylinder packed with Zr-MOF. (d) Set up of abrasion test for tumbling mechanical strength. Reproduced with permission from [159]. Copyright 2015 Elsevier.

In [161], a mesoporous ρ-alumina (MRA) binder (5–20 wt%), MOF powder (MIL-101, UiO-66), and water as a dispersion medium were mixed using a handmade pan-type granulator. During the mixing process, the requisite amount of water was briefly sprayed onto the granules to achieve the desired particle growth, and then the granules were rolled using a roller machine to enhance the spherical shape. The sample was dried to remove water after shaping. Only 1.0% of the weight-specific surface area was lost by shaping UiO-66(Zr)_NH_2 with 5 wt% MRA binder. In addition, when 5 to 10 wt% binder was added to make MIL-100(Fe) spheres, the crushing strength was improved by >30%. As the amount of MRA increased, the crushing strength also increased since MRA improved the cohesion between MOF particles.

In [162], bentonite clay was used as an inorganic binder to form MIL-101 monoliths. Bentonite clay, water, and MIL-101(Cr) powder were mixed to form a paste, which was extruded into monolith forms using an SSE. The extruded MIL-101 monoliths were dried in a chamber, then fired in a kiln at 150 °C to form sturdy and solid structures. The BET surface areas of the MIL-101 powders were >50% higher than that of their respective monoliths since the latter contained bentonite clay as a binder. The elastic moduli as a measure of mechanical strength for the 60% and 75% (w/w) MIL-101 monoliths upon radical compression were 10.60 and 4.97 N mm^{-2}, respectively. As expected, the monoliths containing more bentonite clay binder had more rigid structures.

Another study produced granules using silica as a binder [164]. The granules were made by simply mixing a 10% silica sol (Sigma Aldrich) solution as a binder with 700 g of MIL-100(Fe) powder using a mixing granulator. The BET surface area after shaping decreased by approximately 10% compared with the MIL-100 powder. As evaluation criteria, the compressive strength was measured using a strength meter, and the average value of 20 units was 2.05 kgf $unit^{-1}$.

- Binder-free shaping

After dispersing the MOF in a medium to form a slurry, the slurry can be shaped by extrusion or pressurization during or after evaporation of the solvent without a binder. This type of shaping process employs only the cohesive force between MOF particles, like rolling snow into a snowball. It is very simple and low-cost, and there are no factors such as polymer using as binder that could block the pore, and thus the porosity can be maintained. However, the cohesive force between the MOF particles must be strong, which limits the MOF types to those such as UiO-66 and HKUST-1. Additionally, only MOFs that can withstand high pressures should be selected. In particular, applying pressure in one direction can collapse the structure of the MOF or cause the loss of porosity or crystallinity.

In [160], MOF-5 pellets were formed with bulk densities between 0.27 and 0.79 g cm^{-3} by pressing. The authors reported that upon shaping MOF-5 pellets by the same method while increasing the material bulk density, the radical crushing strength increased from 0 to 120 N, and the BET surface area decreased from 2750 to 1200 m^2 g^{-1}. The decrease in specific surface area with increased bulk density is linked to the degradation of the intracrystalline porosity of MOF-5 due to amorphization. Nevertheless, the crystallinity of MOF-5 was maintained as determined by powder x-ray diffraction (PXRD) analysis.

One study prepared pellets of CPO-27-Ni without a binder [167] by applying pressures of 0.1 and 1 GPa to the MOF for 30 min. In this case, XRD showed that the crystallinity was maintained for both pressures, and for pelletization at 0.1 GPa, the Langmuir surface area of the product was similar to that of CPO-27-Ni powder. However, when the pellets were made at 1 GPa, no N_2 sorption occurred due to a lack of porosity. Therefore, excessive pressure can decrease or destroy the crystallinity or porosity of MOFs, and thus an appropriate pelletizing pressure should be selected according to the MOF type.

4.1.3. Forming processes

MOF shaping is a necessary process from industrial and application viewpoints. MOFs are highly efficient for gas sorption, gas separation, and catalysis, and many such applications have been studied on the laboratory scale. These reactions require a constant flow rate of gas through a column or reactor. In this case, if the MOF is in powder form, it is likely to be blown, which will cause clogging of the column or reactor and loss of MOF mass. Therefore, the intended application and target flow rate should be considered, and the shaped MOF must have sufficient mechanical strength to withstand the reactor pressure. In addition, the shaped MOF must have enough space to maintain the diffusion effect between particles in order to maximize its effectiveness for the application and maintain a crystallinity and porosity similar to those of the powder form. When using shaped and powder MOFs for an application, if the performance of the two is similar or the same, the shaped MOF has an ideal shape, size, and density.

The type of MOF shaping process largely depends on whether pressure is applied and whether a binder is used. Accordingly, in this section, the shaping processes are divided into the following four categories: i) non-pressurized and binder-free (granulation, monoliths), ii) pressurized and binder-free (pellets, tablets), iii) pressurized with binders (pellets, tablets, monoliths), and iv) non-pressurized with binders (foam, monoliths, granulation). These four types of shaping processes are summarized in Tables 13 and 14. In addition, the properties of the resulting shaped MOFs are discussed in terms of mechanical strength, chemical stability, and bulk density.

- Non-pressurized processes without binders

Shaping MOFs without high pressures or binders is simple and low-cost. In most cases, the MOF is synthesized as a gel instead of a powder, or the powder is converted into a gel. This gel state has a tunable viscosity and adopts the shape of its container. In addition, since this process does not use any binders or high pressures, the micropore structure of the MOF does not collapse.

In one study [171], ZIF-8 was obtained as a powder, and robust monoliths were formed through a sol–gel process. The BET surface area of the monoliths was 1395 m^2 g^{-1}, which is within the ZIF-8 powder surface area range of 1300–1600 m^2 g^{-1}. This evidenced that the ZIF-8 pores were not blocked or collapsed by any factors and that the porosity was maintained. Additionally, mechanical property analysis showed that the monoliths had an elastic modulus and hardness of approximately 4.04 and 0.142 GPa, respectively, which are higher than those of single-crystalline ZIF-8.

Table 13
Summary of shaping processes; (a) non-pressurized processes without binders (granulation, monoliths), (b) pressurized processes without binders (pellets, tablets), (c) pressurized processes with binders.

a. Non-pressurized processes without binders

Process type	MOF	Ratio of MOF/Binder	Forming Pressure	Shape	Ref
High-internal-phase emulsion (HIPE) & freeze drying	HKUST-1	< 3.0 wt%	–	Monolith	[169]
Sol-gel	ZIF-8HT	100 wt%	–	Monolith	[171]
Sol-gel	ZIF-8LT	100 wt%	–	Monolith	[171]
Sol-gel	ZIF-8LT-HT	100 wt%	–	Monolith	[171]
Sol-gel	ZIF-8ER	100 wt%	–	Monolith	[171]
Oil-drop granulation	UiO66	100 wt%	–	Granules (sphere)	[172]
Xero gel	UiO-66	70%	–	Monolith	[172]

b. Pressurized processes with binders

Process type	MOF	Ratio of MOF/Binder	Forming Pressure	shape	Ref
Extrusion-crushing-sieving (ECS)	ZIF-8	–	65 MPa	Pellet	[157]
Pressing	MOF-5	–	–	Pellet	[166]
Mechanical pressure	CPO-27-Ni	–	0.1–1 GPa	Tablet	[167]
Pressing	CuBTC (Basolite™ C300)	–	3.7, 7.4, 29.6, 59.2 kN m-2	Tablet	[168]
Pressing	MIL-53(Al)	–	3.7, 7.4, 29.6, 59.2 kN m-2	Tablet	[168]
Mechanical pressure	SIM-1	–	0.5, 1, 5 kN	Pellet	[173]
Mechanical pressure	HKUST-1	–	0.3, 1, 5 kN	Pellet	[173]
Mechanical pressure	ZIF-8	–	–	Pellet	[173]

c. Pressurized processes with binders

Process type	MOF	Binder	Ratio of MOF/Binder	Forming Pressure	Shape	Ref
Granulation	MiL-100(Fe)	graphite	97 wt%	5000 psi (34 Mpa)	pellet	[161]
Granulation	MiL-101(Cr)	graphite	97 wt%	5000 psi (34 Mpa)	pellet	[161]
Granulation	UiO-66	graphite	97 wt%	5000 psi (34 Mpa)	pellet	[161]
Granulation	UiO66-NH$_2$	graphite	97 wt%	5000 psi (34 Mpa)	pellet	[161]
Compression punching machine	ZIF-8	5 wt% methocel (K15M)	95 wt%	–	pellet	[173]
Single screw extruder	MOF-801	5 wt% PVB	95 wt%	146, 292, 438, 584 Mpa	pellet	[174]
Single screw extruder	MOF-801	5 wt% PVA	95 wt%	146, 292, 438, 584 Mpa	pellet	[174]
Single screw extruder	MOF-801	5 wt% sucrose	95 wt%	146, 292, 438, 584 Mpa	pellet	[174]
Thermally induced phase separation-hot pressing (TIPS-HoP)	NH2-UiO-66	polyethylene (PE)	86 wt%	–	Film	[175]
Thermally induced phase separation-hot pressing (TIPS-HoP)	MIL-100(Cr)	polyethylene (PE)	86 wt%	–	Film	[175]

Table 14
Summary of shaping process; Non-pressurized processes with binders.

d. Non pressurized processes with binders

Process type	MOF	Binder	Ratio of MOF/Binder	Shape	Ref
homemade fan-type granulator	MiL-125-NH$_2$	3 wt% polyvinyl group	97 wt%	Granules	[154]
granulation	UiO-66	Poly(vinyl alcohol) 4 vol%	22 vol%	Granules	[155]
Extrusion	UiO-66	Poly(vinyl alcohol) 4 vol%	22 vol%	Cylindrical garanules	[155]
Freeze granulation	UiO-66-COOH	Polyvinyl alcohole	22 vol%	Bead	[155]
Extrudate	UiO-66-COOH	polysiloxane (silicon resin)-based binder	72.5 vol%	Cylinder	[155]
Extrusion molding	SIFSIX-3-Ni	8 wt% polyvinyl butyral (PVB)	90 wt%	Pellet	[156]
Extrusion molding	SIFSIX-2-Cu-i	8 wt% polyvinyl butyral (PVB)	90.8 wt%	Pellet	[156]
Extrusion molding	GeFSIX-2-Cu-i	8 wt% polyvinyl butyral (PVB)	89.6 wt%	Pellet	[156]
Extrusion molding	TIFSIX-2-Cu-i	8 wt% polyvinyl butyral (PVB)	89.4 wt%	Pellet	[156]
Extrusion molding	HKUST-1	8 wt% polyvinyl butyral (PVB)	90 wt%	Pellet	[156]
Extrusion molding	Mg-MOF-74	8 wt% polyvinyl butyral (PVB)	90 wt%	Pellet	[156]
Extrusion-crushing-sieving(ECS)	ZIF-8	CA (cellulose-acetate)	7.5/15/30 wt%	Pellet	[157]
Extrusion-crushing-sieving(ECS)	ZIF-8	PVC (polyvinylchloride)	7.5/15/30 wt%	Pellet	[157]
Extrusion-crushing-sieving(ECS)	ZIF-8	PVF (polyvinylformal)	7.5/15/30 wt%	Pellet	[157]
Extrusion-crushing-sieving(ECS)	ZIF-8	PEI (polyetherimide)	7.5/15/30 wt%	Pellet	[157]
Extrusion-crushing-sieving(ECS)	ZIF-8	PS (polystyrene)	7.5/15/30 wt%	Pellet	[157]
Extrusion	MOF-5	99% ABS (acrylonitrile butadiene styrene)	1%	Filament	[158]
Extrusion	MOF-5	95% ABS	5%	Filament	[158]
Extrusion	MOF-5	90% ABS	10%	Filament	[158]
Granulation	UiO66	10 wt% sucrose	90 wt%	Pellet	[159]
Casting on pellet	(CO)MOF-74	TENAX (80–100 mesh pellet)	14 wt%	Pellet	[160]
Casting on pellet	(Zn)ZIF-8	TENAX (80–100 mesh pellet)	8.4 wt%	Pellet	[160]
Casting on pellet	(CO)ZIF-67	TENAX (80–100 mesh pellet)	9.6 wt%	Pellet	[160]
Casting on pellet	(Zr)UiO-66	TENAX (80–100 mesh pellet)	8.4 wt%	Pellet	[160]
Hand-made pan-type granulator	MiL-100(Fe)	5 wt% MRA (Mesoporous ρ Alumina)	95 wt%	Sphere	[161]
Hand-made pan-type granulator	MiL-101(Cr)	5 wt% MRA (Mesoporous ρ Alumina)	95 wt%	Sphere	[161]
Hand-made pan-type granulator	UiO-66	5 wt% MRA (Mesoporous ρ Alumina)	95 wt%	Sphere	[161]
Hand-made pan-type granulator	UiO66-NH$_2$	5 wt% MRA (Mesoporous ρ Alumina)	95 wt%	Sphere	[161]
Extrusion	MIL-101(Cr)	40 wt% bentonite clay	60 wt%	Monolith	[162]
Extrusion	MIL-101(Cr)	25 wt% bentonite clay	75 wt%	Monolith	[162]
Rotary press tabletilizer	UiO66	1 wt% graphite	99%	Tablet	[163]
Wet granulation	MiL-125(Fe)	10% silica sol	90 wt%	Granules	[164]
Extrusion	HKUST-1	Silres MSE 100 (CH3Si(O)1.1 (OCH3)0.8	88%	Monolith	[165]
Xero gel	MIL-100(Fe)	resorcinol formaldehyde based Xerogel	57%	Cylindrical monolith	[176]
Xero gel	MIL-100(Fe)	resorcinol formaldehyde based Xerogel	50%	Cylindrical monolith	[176]
Xero gel	MIL-100(Fe)	resorcinol formaldehyde based Xerogel	42%	Cylindrical monolith	[176]
Xero gel	MIL-100(Cr)	resorcinol formaldehyde based Xerogel	57%	Cylindrical monolith	[176]
Xero gel	MIL-100(Cr)	resorcinol formaldehyde based Xerogel	49%	Cylindrical monolith	[176]
Xero gel	MIL-100(Cr)	resorcinol formaldehyde based Xerogel	44%	Cylindrical monolith	[176]
Xero gel	MIL-101(Cr)	resorcinol formaldehyde based Xerogel	65%	Cylindrical monolith	[176]
Xero gel	MIL-101(Cr)	resorcinol formaldehyde based Xerogel	54%	Cylindrical monolith	[176]
Xero gel	MIL-101(Cr)	resorcinol formaldehyde based Xerogel	50%	Cylindrical monolith	[176]
Xero gel	MIL-101(Cr)	resorcinol formaldehyde based Xerogel	33%	Cylindrical monolith	[176]

Thus, ZIF-8 converted into the form of a monolith has sufficient rigidity.

In another study [172], Zr-MOF shaped monoliths were formed by gelation, and spheres were formed by an oil-dropping method. Three parameters are important when making MOF gels: the metal source, reactant concentration, and presence of water. The Zr-based MOF gels were synthesized by controlling these parameters, and the properties of the monoliths and UiO-66 powder were compared. With gelation, the BET surface area increased by 0–300 m^2 g^{-1}, but the micropore volume decreased by 0.1–0.2 cm^3 g^{-1}. The crystal size of the gel-formed UiO-66 was 10–25 nm, and the micropore volume could be considered reasonable compared with that of general nanosized UiO-66.

As illustrated by these two cases, non-pressurized and binder-free processes are highly economical and simple because they can form MOFs immediately without changing their characteristics.

- Pressurized processes without binders

Pressurized binder-free processes can produce pellets, tablets, and films. The MOF powder or metal oxide and organic ligand starting materials are mixed in a dispersion medium or mixed by a solvent-free method. After granulation of the mixture, pellet or tablet shapes are formed by pressurization using an extruder or compression machine. MOFs shaped by these processes have a higher density than those produced by non-pressurized binder-free processes, which results in a high application efficiency per weight. However, too high of a pressure will block the pores or collapse the crystallinity of the MOF.

In [173], several MOF powders were compacted into tablet forms by compression punching, where the speed of the punch was set to 10 mm min^{-1} until the selected pressure was reached. Depending on the type of MOF, punching compression was applied from 0.3 to 5 kN, and the characteristics of each shaped MOF tablet were evaluated. For SIM-1, the BET surface area decreased by as much as 28.3% upon compression into tablets. Applying a pressure of 1 kN to HKUST-1 decreased the BET surface area by approximately 37.59%, whereas applying 5 kN to the same MOF decreased the surface area by 76.12%. Therefore, tablets formed by high pressurization of a MOF powder have a high mechanical strength, but the micropores are easily broken, and thus the porosity of the tablets decreases.

- Pressurized process with binders

Pressurized processes using binders can produce almost any shape such as pellet, monoliths, tablet and so on. The process of forming the shape of the MOF is performed as follows; The MOF powder is dispersed in one medium, and the binder is dispersed in other medium to act as an adhesive; mixing the two results in a composite that can be made into a slurry. The slurry can be extruded into a desired shape, made into a film by hot-pressing, or formed into pellets or tablets under a high pressure. In these processes, the media in which the binder and MOF powder are dissolved must mix well in the slurry, and the amount of added binder must not block the MOF pores.

In [174], pellets were prepared by mixing MOF-801 powder and 5 wt% PVA, PVB, or sucrose as a binder. The powder mixtures were compressed to 146, 292, 438, or 524 MPa for 15 s, 30 s, 2 min, 5 min, 10 min, or 15 min to make 16-mm-diameter pellets. Each pellet maintained its crystallinity, but the BET surface areas decreased by as much as 36.71%. The pellets formed with different binder amounts, compression times, and pressures were mechanically tested by dropping. All the shaped MOF pellets had higher mechanical strengths than the respective MOF powders; especially, 5% PVB acted as a stronger binder than PVA or sucrose. However, the mechanical strength of the pellets did not increase when the molding pressure was higher than 292 MPa.

- Non-pressurized processes with binders

Non-pressurized processes with binders can make shapes such as granules, spherical pellets, foams, and monoliths. These forms are produced by mixing the MOF powder with a binder that acts as a glue without applying a high pressure, which improves the cohesion between MOF particles to achieve a more rigid shape. This is performed by dissolving the MOF powder and binding agent separately in the dispersion medium, using a granulator or spray coater to increase the particle size, and then evaporating the solvent for drying. This process is easy and fast and can be applied to MOFs with weak cohesive forces.

In [157], ZIF-8 and polymer binders such as polyvinylchloride (PVC), polyvinylformal (PVF), PEI, PS, and CA were formed into composite pellets by extrusion. First, the composite of ZIF-8 and binder was prepared by controlling the amount of binder and gradually adding solvent until a thick slurry was obtained. The slurry was extruded into granules and dried overnight. After shaping, the mechanical strength and chemical stability of the ZIF-8 pellets with different solvents and binders, and PVF was found to be the best choice of binder.

In another study [158], a MOF-5 and acrylonitrile–butadienestyrene (ABS) composite was formed by printing with a conventional thermoplastic 3D printer (Fig. 25). The composite was extruded into a filament with the amount of ABS controlled to 0–50%, and it was confirmed by PXRD that the crystallinity of MOF-5 was maintained. After shaping the MOF with the 3D printer, the Young's moduli were determined as 5.2 ± 0.4, 6.5 ± 0.7, 4.05 ± 0.5, and 6.2 ± 0.4 MPa for ABS with 0%, 1%, 5%, and 10% MOF-5, respectively. This demonstrated that the characteristics of the binder were reflected by the shaped MOF and that 3D printing can produce shaped MOFs using ABS as a plasticizer.

4.2. Dispersion processes

To form films or membranes, a solution coating process is typically used, whereby solutions containing well-dispersed reactants are sprayed evenly to coat a substrate or other reactants. In most cases, MOFs are used in conjunction with other materials. In this section, the dispersion agents and methods used to maintain a well-dispersed state of MOFs in solution for the necessary timeframe are described in detail and summarized in Table 15.

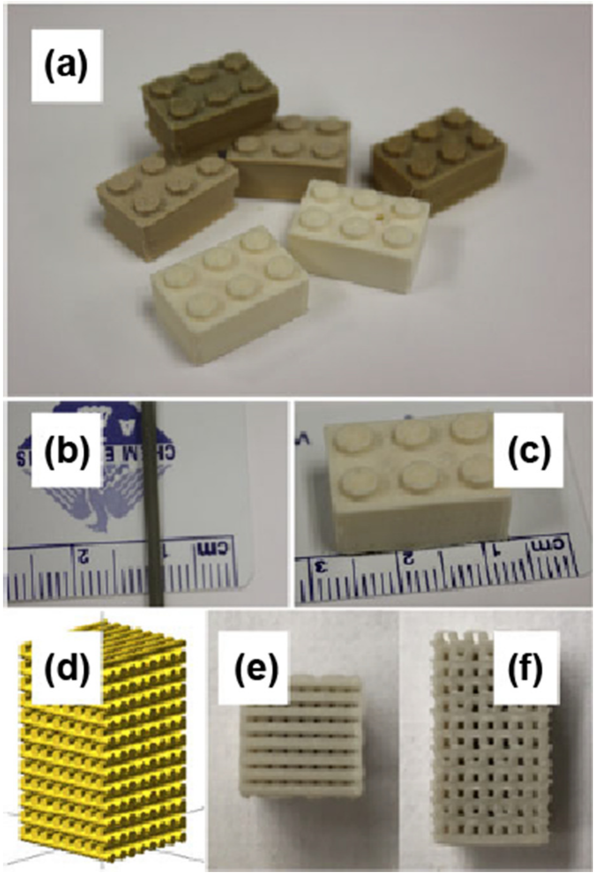

Fig. 25. Image of ABS-MOF-5 filament and 3D printed MOF. (a) 3D printed MOF-5 composites. It contained the MOF with 1 to 10%. (b) Filament formation with cutting and extrusion ABS-MOF-5. (c) Products block with 3D printing. (d) Image rendering for 3D printing, (e) Top view and (f) side view of the product with 3D printed ABS-MOF-5. Reproduced with permission from [158]. Copyright 2015 John Wiley and Sons.

4.2.1. Criteria

- Visualization and Tyndall scattering

The Tyndall effect describes the scattering of light in a colloidal dispersion. This effect is used to determine whether a mixture is a colloid, as no scattering occurs when light passes through a true solution. Light scattering occurs in a colloidal dispersion because visible light is reflected off of particles that are slightly below or near the size of the wavelength of light, such as the scattered particles in a colloid-like substance (e.g., dust in water). Depending on how much light a particular material absorbs, different color light is emitted. Shorter wavelengths of light tend to be scattered more than longer wavelengths. It is easy to judge how well MOF particles are dispersed in a medium by taking photos of various solution conditions or by using laser beams to see how evenly the light is transmitted through the suspension or colloid.

- Dynamic light scattering

Dynamic light scattering (DLS) is used to determine the size distribution of small particles in suspension or polymers in solution. DLS is commonly used to analyze the size of nanoparticles (NPs) such as nanogold, proteins, and colloidal particles. Due to Brownian motion, freely diffusing particles cause rapid fluctuations in scattered laser light, depending on the particle size. The faster the fluctuation rate, the smaller the particle size. DLS measurements are used to measure the particle size of MOFs in solution over time.

Table 15
Summary of dispersion processes.

Dispersion agent	Method	Solvent	MOF	MOF/ dispersion agent Ratio	Dispersion process time	Criteria	Durable time	Ref
4-*tert*-butylcalix[n]arenes	Sonicated	Toluene	UiO-66	0 to 30%	1 h	Tyndall effect/DLS	3 d	[177]
Modified PEG*	Sonication	Water	COF-1	–	–	DLS	2 d	[178]
SR-610	Tip-sonication	–	Cu-BTC	10 wt%	30 min	–	several hours	[179]
SR-339				67 wt%	30 min	–	several hours	[179]
n-dodecyl β-D-maltoside (DDM)	–	50 mM 2-methylimidazole	ZIF-8	–	45–60 min	DLS	–	[180]
Caster Oil **	Oil-in-water	Water	POZIF-8	3%	2 h	Extraction	120 d	[181]
PEGMA***	–	Water	NH$_2$-UiO-66	36.2, 50.2, 62.5, 73.0 wt %	–	DLS	–	[182]
PVDF (7.5 wt% in DMF)	Ultrasonic bath	Acetone	ZiF-67	67%	–	–	–	[183]
PVDF (7.5 wt% in DMF)	Ultrasonic bath	Acetone(MOF)/DMF (PVDF)	MiL-101(Fe)	67%	30 min	–	–	[184]
PVDF (7.5 wt% in DMF)	Ultrasonic bath	Acetone(MOF)/DMF (PVDF)	MiL-101(Cr)	67%	30 min	–	–	[184]
PVDF (7.5 wt% in DMF)	Ultrasonic bath	Acetone(MOF)/DMF (PVDF)	MiL-53(Fe)	67%	30 min	–	–	[184]
PVDF (7.5 wt% in DMF)	Ultrasonic bath	Acetone(MOF)/DMF (PVDF)	UiO-66	67%	30 min	–	–	[184]
PVDF (7.5 wt% in DMF)	Ultrasonic bath	Acetone(MOF)/DMF (PVDF)	UiO66-NH$_2$	67%	30 min	–	–	[184]
PVDF (7.5 wt% in DMF)	Ultrasonic bath	Acetone(MOF)/DMF (PVDF)	HKUST-1	67%	30 min	–	–	[184]
PVDF (7.5 wt% in DMF)	Ultrasonic bath	Acetone(MOF)/DMF (PVDF)	ZiF-8	67%	30 min	–	–	[184]
–	Ultrasonic bath	EtOH	2D [Co(CNS)$_2$(pyz)$_2$]$_n$	–	30 min	Tyndall effect	1 week	[185]
–	Sonication	EtOH	Cd-TP	–	30 min	Tyndall light scattering	–	[186]
–	Sonication	EtOH	Zn-TA	–	30 min	Tyndall light scattering	–	[186]
–	Stirring	MeOH	CCR-3	–	1 h	–	–	[187]
Paraffinic ligand	–	Hexane	MOP	–	–	–	–	[188]
–	2D nano sheet	Water	PCN-134	–	–	Tyndall effect	–	[189]

*Polyethylene-glycol-modified monofunctional curcumin derivatives, **Caster Oil =(industrial grade: density @ 20 °C = 0.951 g/ cm^3, viscosity @ 20 °C = 970–1100 cP, iodine value = 86.3 g iodine/100 g oil), ***Poly(ethylene glycol) methyl ether methacrylate.

4.2.2. Dispersion agents

Many solvents can be used to disperse MOFs, including polar solvents such as water, ethanol, methanol, and acetone, and non-polar solvents such as toluene, benzene, and hexane. To stabilize the dispersion, dispersion agents can be added such as hydrophobically functionalized organic ligand or hydrophobic compounds. However, these additions may reduce the adsorption capacity or catalytic activity.

In [177], calix[n]arenes—well-known macrocycles with intrinsic pores—were added to facilitate the dispersion of UiO-66 in toluene. The calix[n]arene content was adjusted from 0 to 30 wt%, which did not affect the particle size or crystallinity of UiO-66, while the surface area increased from 1245 to 1385 m^2/g. The UiO-66/calix[6]arene suspension in toluene showed the characteristic Tyndall effect with a passing green laser beam (Fig. 26). Zeta potential measurements using DLS indicated an increase in particle dispersity upon the addition of calix[n]arene.

In [178], polyethylene-glycol-modified monofunctional curcumin (PEG-CCM) was used as a dispersion agent with 50 wt% APTES-COF-1 in 1 mL of 1,4-dioxane. The mixture was stirred in a water bath for 20 min. The dispersion was stable in water at room temperature for >2 days.

In [179], a acrylate monomer was added to a Cu-BTC MOF dispersion. Cu-BTC is composed of aromatic ligands bonded to an acrylate monomer such as 2-phenoxyethyl acrylate (Sartomer SR-339). The monomer contained an aromatic group, which increased its affinity toward the MOF and enabled the formation of a stable dispersion without requiring a dispersion agent that might block the surface and pores of the MOF. The 10 wt% Cu-BTC and sartomer mixture was sonicated with a tip-sonic. When comparing the methylene blue (MB) adsorption curve as composition of the MOF, the amount of absorbance of MB reduction and amount of polymer were similar. Therefore, the polymer did not affect the porosity of the MOF.

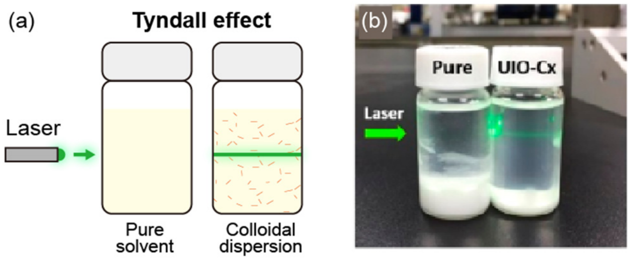

Fig. 26. (a) Schematic illustration of Tyndall effect. (b) Image of Tyndall effect of colloidal suspension. Adapted with permission from [177]. Copyright 2019 American Chemical Society.

4.2.3. Dispersion method

Normally, MOF particles can be kept well-dispersed in a solvent by applying a physical force such as stirring or sonicating, with or without or an added dispersion agent. However, when physical force is applied to the solvent, the cohesion force between the MOF particles increases due to their increased kinetic energy. This effect can cause aggregation among the MOF particles. Therefore, the processing time must be properly considered to prevent aggregation.

In [180], *n*-dodecyl β-D-maltoside (DDM)—a sugar-based surfactant—was used as a dispersant to modify a ZIF-8 colloidal solution. The solution was stirred with an aqueous 2-[4-(2-hydroxyethyl)piperazin-1-yl]ethanesulfonic acid. Glyco-ZIF-8 colloidal suspension was monitored via DLS. The mean particle size of the ZIF-8 and ZIF-8 colloidal suspensions were the same.

5. Upcoming MOFs applications for future commercialization

MOFs and their composites have emerged as suitable materials for numerous applications such as conventional gas storage/separation, energy storage/conversion [190,191] and catalytic application [192,193]. Aside from these current applications in the limelight, we focus on future applications that are not currently well known but have significant potential to serve as new business areas for MOF commercialization. We describe many of the recently designed MOF-based materials for 8 applications; (1) chemical purification, (2) air purification, (3) removal of biological toxicants, (4) antibacterial implementation, (5) ion transport for solid-state electrolyte, (6) electrode material, (7) low-*k* dielectric material, (8) luminescent material. We introduce the required properties of MOFs for the presented applications followed by a couple of selected recent examples. In addition, we tried to emphasize the importance and key point for industrial application of the presented work. Overall, we aim to touch upon many of the new and exciting applications of MOFs and their composites. There are reviews on some of these topics [194], however this manuscript focuses only on the most recent developments from the last few years, as well as describing the directions of academic and industrial attention in the near future.

5.1. Chemical purification

In the past few decades, the increased research interest on development of novel technologies toward separation and purification of vital gases such as N_2/CH_4, N_2/CO_2 and H_2/N_2, etc. as well as light hydrocarbon chemicals like CH_4/CO_2, C_2H_2/C_2H_4, and xylene isomers plays a key attention for various industrial applications. Owing to the similar physicochemical properties including boiling points, freezing points, polarity and molecular shape/sizes, the most significant approaches for separation and purification of those chemical components required high energy consumption and cost-effective conventional distillation techniques, e.g., cryogenic distillation. At these instances, the porous crystalline materials such as MOFs have been placed a crucial role for selective adsorption and separation of those chemical species, and their comprised potential properties overcome the ascribed concerns. Several important review articles covered these topics extensively with numerous examples [195–198]. Herein, we will discuss particularly, very recent advances of application for selective adsorption and separation of important viable chemical species such as N_2/CH_4, C_2H_2/CO_2, and xylene isomer mixtures in industrial applications.

5.1.1. MOFs as adsorbents for chemical separation

The MOF based materials comprising appropriate π-backbonding-donating metal sites could impart π-acidity on adsorbates and thereby improve the selective separation of industrially challenging gaseous mixtures with π-bonding. In this regard, J. R. Long and co-workers prepared vanadium (II) based metal–organic framework (denoted as $V_2Cl_{2.8}$(btdd); H_2btdd = bis(1H-1,2,3-triazolo[4,5-b],[4′,5′-i])dibenzo[1,4]dioxin), which showed selective purification of N_2 over natural gas (CH4) mixture and olefin over paraffin mixture at high temperature. Breakthrough experiments proved that π-backbonding donation of vanadium (II) adsorption sites of the MOF possesses not only selective separation of N_2 gas over CH_4, but also exceptional reversible capacities over several cycles. Interestingly, this material also adsorbs both CO_2 and N_2 from crude natural gas mixture, which is crucial in natural gas purification process. In addition, it achieved great selectivity of ethylene from ethane rich feeds (5: 95 of ethylene/ethane) as well as attained very high capacities at high temperatures (e.g., 80 °C). Finally, the current developed material envisioned the next-generation materials in the field of separation and purification technology [199].

The purification of acetylene (C_2H_2) gas from natural gas such as CO_2, CH_4 is of great interest due to its industrial utility. With this attention, J. Pei and coworkers reported that Hofmann based metal–organic framework (named as Co(pyz)[Ni(CN)$_4$], pyz = pyrazine; ZJU-74) shows selective separation of acetylene over CO_2, C_2H_4 and CH_4 at ambient conditions [200]. Interestingly, the material possesses high C_2H_2 capturing capacity (49 $cm^3\ g^{-1}$ at 0.01 bar and 296 K) and high selectivity over CO_2 (36.5 $cm^3\ g^{-1}$ at 1 bar, 296 K), which is the highest selectivity so far. In addition, this MOF showed better selectivity of 24.2 $cm^3\ g^{-1}$, 1312.9 $cm^3\ g^{-1}$ over C_2H_4 and CH_4 at ambient conditions, respectively. Attributed high concentration of available open metal sites (OMSs) and specific sandwich like binding sites, the MOF shows unusually high of C_2H_2 over natural gas mixtures, which can be usefully used industrial acetylene purification process.

Subsequently, the separation of C_8 aromatic isomers (xylenes isomers) such as p-xylene (PX), o-xylene (OX), and m-xylene (MX) is one of the extraordinary challenging tasks because of their similar physicochemical properties. Recently, Long group reported that two cobalt-based metal–organic frameworks, Co_2(dobdc), (dobdc^{4-} = 2,5-dioxido-1,4-benzenedicarboxylate) and Co_2(m-dobdc) (m-dobdc^{4-} = 4,6-dioxido-1,3-benzenedicarboxylate), exhibited excellent separation of C_8 alkyl aromatics (PX, OX, MX, and ethylbenzene) via multiple adjacent unsaturated Co(II) metal sites [201]. Breakthrough experiment using the MOFs showed that Co_2(dobdc) well separated all four isomers. On the other hand, Co (m-dobc) displayed selectivity towards three isomers since similar binding affinity of m-xylene and ethylbenzene. In addition, the SCXRD (single crystal X-ray diffraction) analysis revealed the facilitated separation of four isomers in both materials is due to extent of interaction with two adjacent Co(II) sites and packing ability of guest isomers in the pores. Therefore, this report paves new platform for developing of novel adsorbent materials in the separation of petrochemical components.

5.1.2. Water purification using MOFs

Among the various natural resources, water is most important essential requirement to run the several activities globally. The rapid growth of economy and industrialization causes water pollution displaying negative impact on environment and human health. Mainly, the water pollution is occurred through various organic and inorganic pollutants (phosphates, pesticides, etc.), toxic heavy metal ions (Pb^{2+}, Cd^{2+}, Hg^{2+}) and anion species (arsenate, chromates, etc.), etc [202]. In this respect, several water treatment technologies have been developed, for example, coagulation, filtration, and chemical precipitation. The ascribed difficulties such as instrument complexity and high system cost lead to encourage the development a new material for adsorptive removal such as clays, zeolites, and porous materials. The high porosity and facile tuning MOF surface property by various methods allows to be used in water purification by adsorptive removal. Due to the low stability of MOFs in water, their application for water purification has been limited. However, several water stable MOFs including MIL-series and UiO-series, water purification using MOFs has been widely studied. The recent review article highlights the history, criteria, and recent advances of MOFs for water purification [203–205].

5.2. Air purification

5.2.1. Necessity of air purification

Rapid economic growth, industrialization, and technological advances have led to the excessive generation of emissions and other waste that severely pollute the air and negatively impact the environment and human health [206,207]. Currently, there is considerable attention on air pollutants such as particulate matter, toxic gases, volatile organic compounds (VOCs), and chemical warfare agents (CWAs) [208]. To maintain the quality of our air, novel materials are required that can purify the air and reestablish a healthy atmosphere. Although several important review articles have highlighted the development of advanced purification filters, in many cases the filters are limited to the removal of only a few major air contaminants [209–213]. In this section, we cover the most severe environmental air pollutants and briefly introduce the pollutants and emphasize their negative impact on the environment and public health. In addition, we discuss the recent advances in the field of MOFs for the removal of these pollutants from air. We have classified the pollutants as follows (Fig. 27): (1) particulate matter, (2) toxic gases, (3) VOCs, and (4) CWAs.

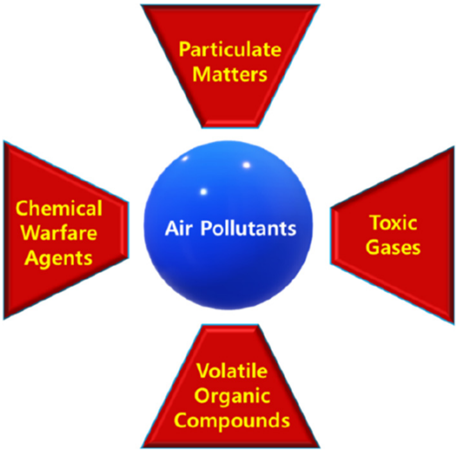

Fig. 27. Classification of air pollutants.

5.2.2. Removal of particulate matter

Particulate matter (PM) pollutants are fine airborne particles with an aerodynamic diameter below 2.5 μM ($PM_{2.5}$) or 10 μM (PM_{10}) [214]. These pollutants are released from various sources such as refineries, power plants, burning coal, agricultural dust, etc. [215]. Owing to the small particle size, particulate matter causes risks to human health by blocking the respiratory tracts and even entering blood vessels, which can lead to severe cardiovascular and respiratory diseases [216,217]. Long-term exposure to $PM_{2.5}$ can increase morbidity and even mortality [218]. Guidelines set by the World Health Organization (WHO) suggest that the concentration limit of $PM_{2.5}$ in the air should not exceed 10 $\mu g\ m^{-3}$. In 2015, air pollutants were responsible for 6.8 million deaths worldwide. Indoor air pollution is accountable for 2.8 million deaths, while environmental pollution severely affects 4.2 million people across the world [219].

Particulate matter has garnered significant attention in recent years owing to its huge effect on public health. Researchers are developing advanced technologies to purify air, including purification filters that can filter out $PM_{2.5}$ and PM_{10} [220,221]. Commercial air purification filters comprising polymers, nanofibers, nanowire-based filters, or porous materials (such as activated carbon) are widely used in the manufacturing industry and highly polluted areas [222,223]. However, these devices have several drawbacks including efficiency and reusability. Therefore, a lot of attention is still focused on the development of new materials for the filtration of $PM_{2.5}$.

In this section, we highlight the design requirements for efficient filters and describe the future challenges for fulfilling current needs, with a focus on recent advances in MOF-derived filters. Air purification filters for particulate matter are divided into two types: (1) air filtration materials for the public, such as commercially available face masks; and (2) air filtration materials at the source of emissions, such as chimneys and automobile exhausts. The main requirements for air purification filters are as follows: high filtration efficiency, good mechanical strength, high thermal stability, low resistance to air flow, relatively low pressure drop, light weight, and long working lifetime. [224]. In addition, air fil-

Table 16
The various MOF derived filters for removal of particulate matters (PMs).

MOF filters	$PM_{2.5}$		PM_{10}		Ref
	Efficiency (%)	Temperature (°C)	Efficiency (%)	Temperature(°C)	
PPC/ZIF-8	91.68 ± 0.57	–	–	–	[229]
Ag-MOFs@CNF@ZIF-8	94.3	–	>95	–	[234]
PAN-ZIF-8	99.97 ($PM_{0.3}$)	–	≥99.99	–	[230]
ZIF-8/rGA	99.3	25	99.6	25	[231]
ZIF-8/rGA	>98.8	200	>99.1	200	[231]
polyimide/ZIF-8	96.6 ± 2.9	300	–	300	[235]
MIL-53(Al)–NH_2@PAN	99.99 ($PM_{0.3}$)	–	–	–	[236]
PLA-ZIF-8 (PZD5)	94.44	–	96.57	–	[237]
ZIF-67@PAN	87.2	–	–	–	[238]
ZIF-8/PAN	88.33 ± 1.52	–	89.67 ± 1.33	–	[233]
CNFs/HKUST-1/stainless steel screen	>95	25	–	25	[239]
H-ZIF-L_PP	92.5 ± 0.8	25	99.5 ± 0.2	25	[240]
UiO-66-NH_2@CNTs/PTFE	99.99 ($PM_{0.3}$)	–	–	–	[241]
ZIF-8@Melamine foam-3rd	99.5 ± 1.7	150	99.3 ± 1.2	150	[232]
ZIF-8@Nonwoven fabric-3rd	99.9 ± 0.2	150–250	99.7 ± 0.1	150–250	[232]
ZIF-8@Glass cloth-3rd	96.8 ± 1.3	200	95.8 ± 1.4	200	[232]
ZIF-8@Metal mesh-3rd	92.1 ± 0.7	300	91.3 ± 0.4	300	[232]
ZIF-8@Plastic mesh-3rd	95.8 ± 1.3	80–100	94.1 ± 1.5%	80–100	[232]

ters for use at the source of emissions should be able to endure harsh conditions such as rapid air flow, high temperatures, and high humidity [225,226].

MOFs are promising materials for air purification filters because of their unique properties such as crystallinity, high thermal stability, large surface area, high porosity, chemical stability, and tunable functionality [227]. In particular, they are widely used as adsorption-based filters because of their high porosity and surface area [228]. However, particulate matter is usually too big to be removed by adsorption in MOF pores. Although the role of MOFs in particulate matter removal applications is not clearly proven, MOF/polymer composite filters offer better recyclability and durability for use in harsh environments.

We examined recent research advances in the field of fibrous and mixed composite MOF membranes for the removal of $PM_{2.5}$ and PM_{10} at ambient and harsh conditions (Table 16). Lin and coworkers developed an MOF-derived membrane by compositing polypropylene/polycarbonate (PPC) and ZIF-8 (Fig. 28) that could filter $PM_{2.5}$ with high efficiency (91.68%) and a low pressure drop (45 Pa) [229]. The filter was prepared using an in-situ growth method by loading ZIF-8 nanocrystals on a fibrous PPC membrane (meltbrown). This simple PCC/ZIF-8 composite showed greater filtration efficiency than the pristine PPC membrane filter, and provides a new application area for MOF composite filter membranes. In addition, the MOF composite membrane was reusable, with excellent water resistance and good long-term stability for the filtration of $PM_{2.5}$.

Wang et al. prepared a multi-level structured membrane by compositing ZIF-8 with polyacrylonitrile (PAN) using a facile electrospinning process (Fig. 29a–c) [230]. The fibrous PAN/ZIF-8 composite membrane demonstrated good moisture wicking ability and particulate matter filtration. The authors proposed that the hydrophilic nature of the PAN fibers and the multiscale surface roughness via ZIF-8 etching was responsible

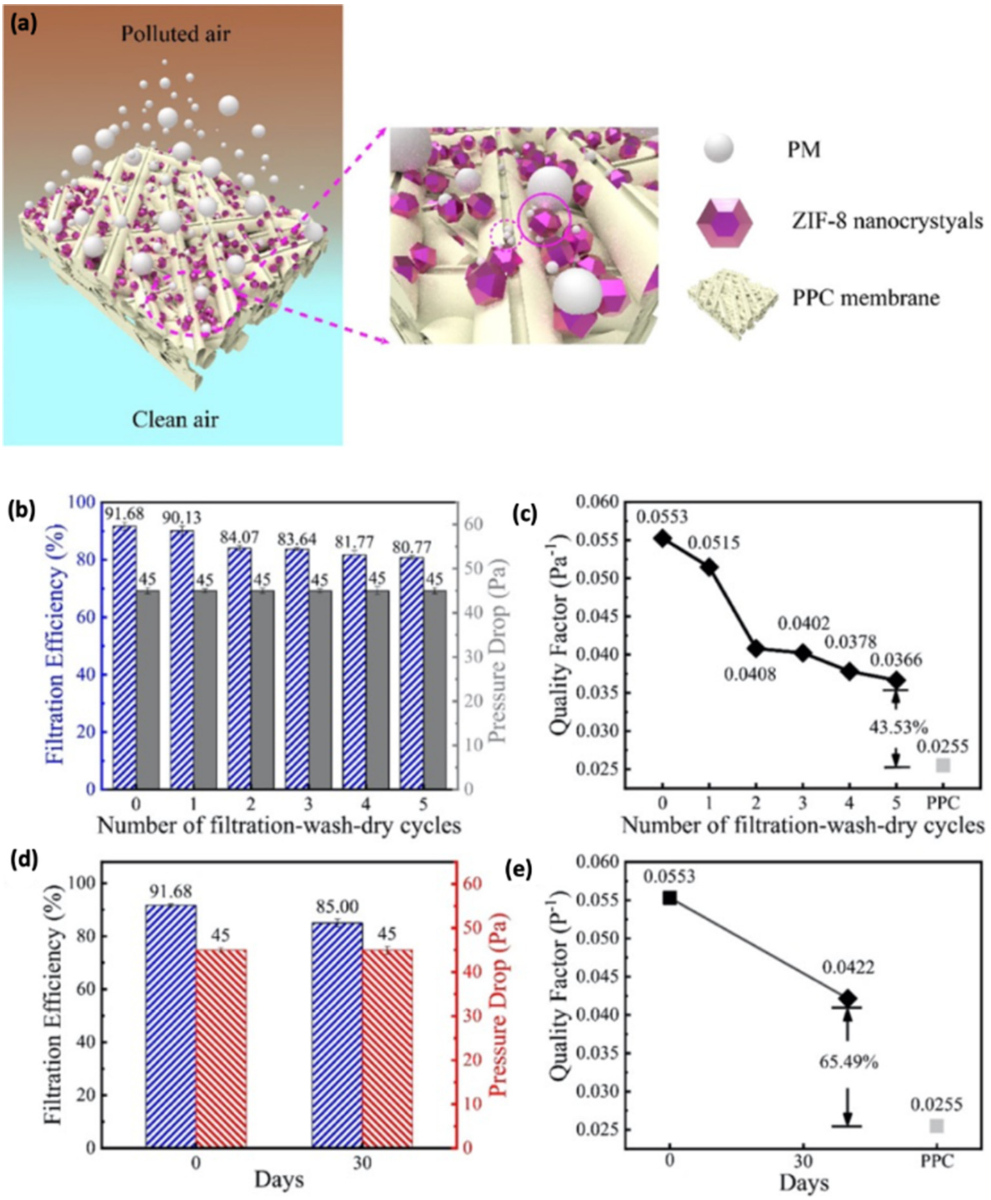

Fig. 28. (a) The proposed filtration mechanism of precursor (ZIF-8) concentration dependent PPC/ZIF8-9 membrane; the filtration efficiency and pressure drop as well as quality factor of the PPC/ZIF8-9 membrane with $PM_{2.5}$ after five consecutive filtration-wash-dry cycles (b-c); the filtration efficiency and pressure drop as well as quality factor of the PPC/ZIF8-9 membrane with $PM_{2.5}$ before and after membrane storage of 30 days (d-e). Adapted with permission from [229]. Copyright 2020 American Chemical Society.

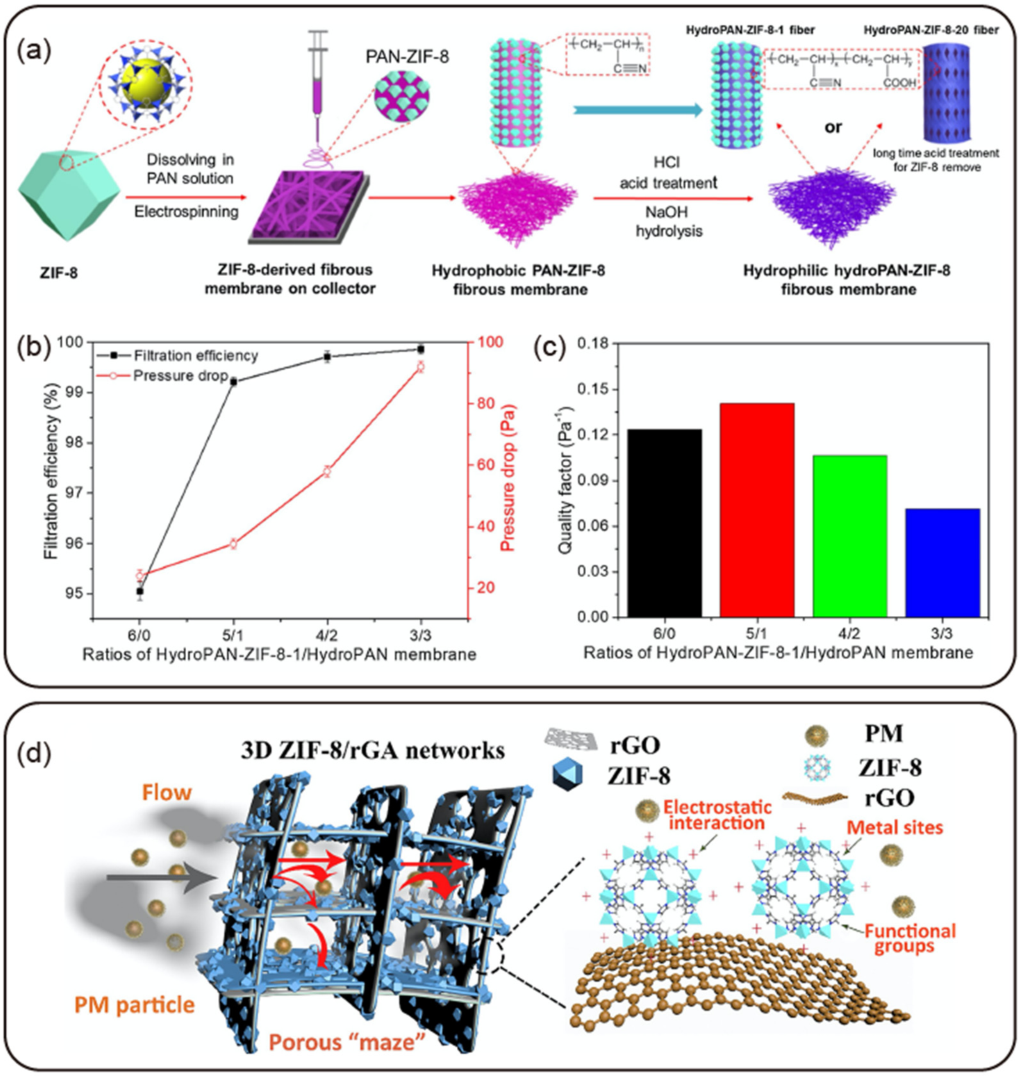

Fig. 29. (a) Schematic illustration of the preparation of hydrophilic hydroPAN-ZIF-8–1 and super-hydrophilic HydroPAN-ZIF-8–20 fibrous membranes; the filtration efficiency, and pressure drop as well as quality factor of one dual-layer HydroPAN-ZIF-8–1/HydroPAN fibrous membrane corresponding to the particle size of 0.3 μm (b-c). Reproduced with permission from [230]. Copyright 2020 Elsevier publisher. (d) The illustration of proposed PM particle capture mechanism of 3D networks of ZIF-8/rGA. Reproduced with permission from [231]. Copyright 2019 Elsevier publisher.

for the dual role of the MOF composite membrane. Moreover, an inner layer of hydrophobic polystyrene fibers acted as an excellent moisture transporter during the moisture wicking process. Notably, the membrane had high removal efficiency (99.97%) for 0.3 μm particles and superb removal efficiency (>99.99%) for larger particles, including harmful ultrafine particles such as COVID-19 for the disease and severe acute respiratory syndrome coronavirus 2. The authors concluded that the proposed approach makes a platform for the development of novel air purification filters.

The development of efficient air filters for $PM_{2.5}$ that can operate under harsh conditions is challenging. In this respect, Mao et al. developed an efficient and thermally stable particulate matter filter with ZIF-8 anchored on reduced graphene aerosol (rGA), denoted as ZIF-8/rGA. The filter exhibited excellent particulate matter removal efficiencies and could remove particulate matter even under harsh conditions [231]. The removal efficiencies under harsh (temperature: 200 °C, air flow rate: 30 L m^{-1}) and ambient conditions were > 98.8% and > 99.3% for $PM_{2.5}$, and > 99.1% and > 99.6% for PM_{10}, respectively. The design was motivated by the properties of the graphene aerogel. The uniform ZIF-8 crystals and 3D porous maze network were key for capturing the particulate matter particles (Fig. 29d).

In 2017, Wang and coworkers synthesized various new ZIF-8 MOF composite filters on a large scale using a roll-to-roll hot pressing method (Fig. 30a–e) [232]. The filters were prepared using various polymer supports, such as melamine foam, metal mesh, glass cloth, plastic mesh, and nonwoven fabric. The prepared composite filters displayed excellent PM removal efficiencies and high robustness at various temperatures (80–300 °C), including under harsh conditions. Furthermore, the filters were found to have excellent performance for particulate matter filtration under purposely designed tests for various fine particulate exhausts, such as baghouse dust collection, pipe filtration, etc. This work not only reports an MOF membrane composite for particulate matter removal under various environments, but also provides a method for the mass production of MOF composite filters for industrial applications.

In 2016, the same research group prepared MOF-based nanofibrous filters by embedding MOF materials on various known polymers (PAN, PS, etc.) using an electrospinning procedure for facile large-scale production (Fig. 30f, g) [233]. In hazy environments,

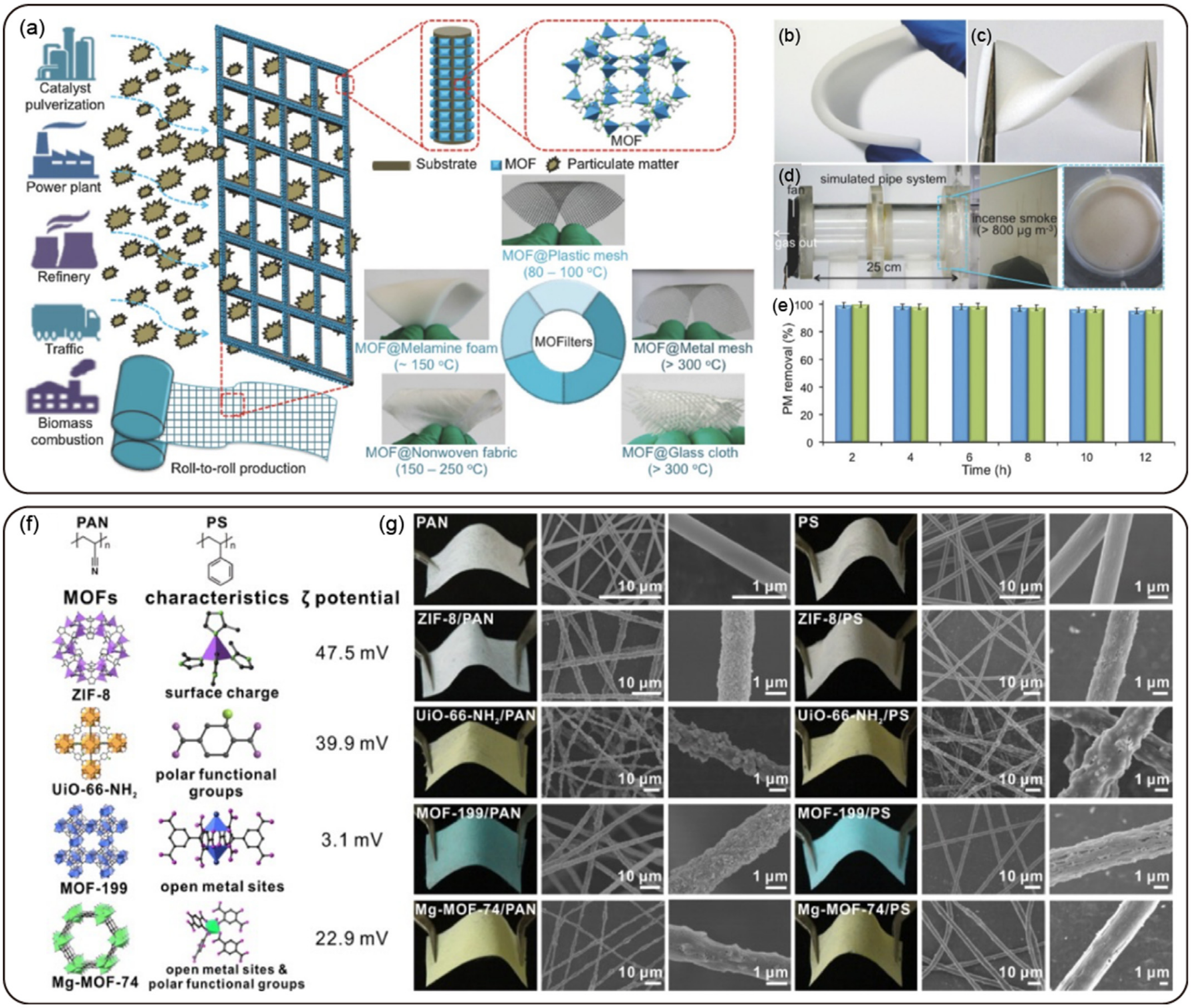

Fig. 30. (a) The schematic illustration of the roll-to-roll production of various MOF filters for PM removal, (b) and (c) are photo images of the bended and twisted ZIF-8@Melamine foam-3rd, respectively, (d) the PM removal test in the presence of simulated pipe conditions where an incense burning was used for generation of smoke, (e) The PM removal efficiency of ZIF-8@Melamine foam-3rd where $PM_{2.5}$ in blue color and PM_{10} in green color. Adapted with permission from [232]. Copyright 2017 John Wiley and Sons. (f) Employed polymers with chemical structures, and corresponding crystal structures, ζ potential of the MOFs. (g) Photo images and SEM pictures of the MOF filters (60 wt% MOF loading) supported on nonwoven fabrics. Reprinted with permission from ref. [233]. Copyright 2016 American Chemical Society.

the ZIF-8/PAN fibrous filter showed better filtration efficiency for $PM_{2.5}$ (88.33%) and PM_{10} (89.67%) than other fibrous filters including Mg-MOF-74/PAN, UiO-66-NH_2/PAN, Al_2O_3/PAN, MOF-199/PAN, and PAN. Zeta potential measurements revealed that electrostatic interactions between the positively charged unsaturated metal ions and highly polar particulate matter were responsible for the extraordinary particulate matter filtration performance of the fibrous filters. This work demonstrates that electrospinning is a suitable method for the large-scale production of various MOF/polymer composite membranes, which show modest–high removal efficiency of particulate matter.

5.2.3. Removal of toxic gases

- Requirements for toxic gas removal

Many anthropogenic activities generate pollutant gases such as sulfur oxides (SO_x, primarily SO_2), hydrogen sulfide (H_2S), nitrogen oxides (NO_x, particularly NO_2), ammonia (NH_3), and carbon monoxide (CO). These toxic gases are a severe environmental and public health issue due to their extensive contamination of the air. Various novel materials have been explored for the sensing, purification, separation, and chemical degradation of these hazardous gases. In this section, we highlight the porous MOFs that have drawn recent attention for the adsorptive removal of toxic gases, and compare them to various commercially available adsorbents (e.g., zeolites, mesoporous materials, and activated carbons) [242,243]. Novel MOF and MOF-based materials are suitable for the adsorptive removal of toxic gases owing to their modular nature, tunable functionality, and large surface area.

The requirements of MOFs for the efficient removal of adsorbates such as toxic gases include: (i) large pores and tunable porosity; (ii) large specific surface area and accessible adsorption sites; (iii) low-cost, durable, and regenerable/recyclable nature; and (iv) stability during adsorption/desorption cycling and/or under dynamic conditions (humidity and temperature).

It is also important for adsorption to occur without interference from atmospheric gases; that is, the MOFs must have high selectivity toward the target gas. In this regard, it is important to consider the adsorption mechanism to develop MOFs that can selectively capture each respective toxic gas. Several methods for endowing selectivity to MOFs have been proposed, including: (1) tuning the pore size to ensure specific adsorbate gases are captured by size discrimination; and (2) incorporating a specific functionality or material for selective interaction with the toxic gas. Specific functionality can be achieved by inserting functional ligands (acidic or basic), open metal centers (coordinatively unsaturated metal sites), metal oxides, or polyoxometalates that provide specific interactions such as acid–base, electrostatic, hydrogen bonding, or π–π complexation/interactions [210,244]. Therefore, the incorporation of organic functional linkers, specific metal coordination, and guests molecules are major considerations for developing materials that can selectively remove toxic gases. With this in mind, we explain in this section some of the various recent advances in MOF-derived materials for the adsorptive removal of toxic gases.

- Removal of sulfur dioxide (SO_2)

SO_2 is a pervasive toxic gas that is released upon the combustion of fossil fuels and other sulfur-containing materials (e.g., sour gas and metal-sulfide ores). In addition, this hazardous gas is widely used in the industrial production of sulfuric acid and as a preservative in the wine industry. When SO_2 reacts with ammonia, it produces $PM_{2.5}$, another major air pollutant, and when it combines with NO_x emissions, it causes photochemical smog and acid rain [245]. Owing to the serious public health and environmental issues associated with SO_2 pollution, there is an urgent need to develop new materials that can selectively and rapidly absorb this toxic gas, thereby maintaining the quality of our air. In this section, we focus on recent progress in the development of MOF-derived adsorbents for the removal of SO_2 from flue gases. For this review, we have classified SO_2 adsorbents into four categories (Table 17): (a) metal–carboxylate MOFs, (b) metal–azolate MOFs, (c) fluorinated MOF-derived materials, and (d) fibrous MOF based thin films.

Seminal work has been carried out on metal–carboxylate MOFs for the removal of SO_2. Schröder and coworkers developed a robust indium-based MOF, denoted as MFM-300(In) (MFM = Manchester Framework Material), which showed a high uptake of SO_2 (8.28 mmol g^{-1} at 298 K and 1 bar) over other gases like CO_2, CH_4, and N_2 [247,250]. Theoretical calculations and breakthrough experiments demonstrated that hydrogen bonding and intermolecular dipole interactions were responsible for its selective adsorption of SO_2. Furthermore, MFM-300(In) showed excellent stability in various environments including dry and humid conditions. MFM-300(In) was compared to another novel MOF, NOTT-202a (NOTT = Nottingham), which showed higher SO_2 uptake (13.6 and 10 mmol g^{-1} at 268 and 298 K, respectively, and 1 bar). Interestingly, the strong interaction between SO_2 and the MOF caused an irreversible structural transformation from NOTT-202a to NOTT-202b, which could be the reason for this high uptake under ambient conditions.

In 2018, an MOF was produced from MFM-600 (comprising UiO-66 SBU; SBU = Secondary Building Unit) by hydrochloride acid treatment, which caused a structural phase transformation and removed the monodentate linkers [249]. The resultant MOF, denoted as MFM-601, had an improved BET surface area and displayed a higher gas adsorption capacity than the original MFM-600. MFM-601 exhibited an SO_2 adsorption uptake of 12.3 mmol g^{-1} at 298 K and 1.0 bar, in preference to CO_2 and N_2. The selectivity toward SO_2 was investigated, and it was revealed that the dipole moment of SO_2 leads to intermolecular interactions with the hydroxyl groups of the Zr_6 nodes, resulting in the stable binding

Table 17
SO_2 adsorptive property of (a) metal-carboxylate MOFs, (b) metal-azolate MOFs, (c) fluorinated MOFs, and (d) fibrous MOF membranes.

MOF compounds	Adsorption Mechanism (SO_2 binding)	SO_2 uptake (mmol g^{-1}) at 298 K	Ref
a. Metal-carboxylate MOFs			
MFM-300 (Al)	H-bonding, dipole interactions	7.1; 8.1 (273 K)	[246]
NOTT-300	H-bonding, dipole interactions	7.1; 8.1 (273 K)	[246]
MFM-300 (In)	H-bonding, dipole interactions	8.28	[247]
MFM-305-CH_3	H-bonding, dipole interactions	6.99	[248]
MFM-305	H-bonding, dipole interactions	5.16	[248]
MFM-600	H-bonding, dipole interactions	5	[249]
MFM-601	H-bonding, dipole interactions	12.3	[249]
NOTT-202a	Host-guest, dipole interactions	13.6	[250]
Ni(TED)(BDC)	Unsaturated metal sites	9.97	[251]
Zn(BDC)(TED)	Unsaturated metal sites	4.41	[251]
MOF-74 (Mg)	Unsaturated metal sites	8.6	[251]
b. Metal-azolate MOFs			
$[Ni_8(OH)_4(H_2O)_2(BDP\_H)_6]$	Polar surfaces, defective crystal sites	2.02	[252]
$[Ni_8(OH)_4(H_2O)_2(BDP\_NH_2)_6]$	Polar surfaces, defective crystal sites	3.35	[252]
$[Ni_8(OH)_4(H_2O)_2(BDP\_OH)_6]$	Polar surfaces, defective crystal sites	2.11	[252]
$K[Ni_8(OH)_3(EtO)_3(BDP\_H)_{5.5}]$	Polar surfaces, defective crystal sites	3.26	[252]
$K[Ni_8(OH)_3(EtO)_3(BDP\_NH_2)_{5.5}]$	Polar surfaces, defective crystal sites	4.38	[252]
$K_3[Ni_8(OH)_3(EtO)(BDP\_O)_5]$	Polar surfaces, defective crystal sites	2.54	[252]
$Ba_{0.5}[Ni_8(OH)_3(EtO)_3(BDP\_H)_{5.5}]$	Polar surfaces, defective crystal sites	4	[252]
$Ba_{0.5}[Ni_8(OH)_3(EtO)_3(BDP\_NH_2)_{5.5}]$	Polar surfaces, defective crystal sites	5.61	[252]
$Ba_{1.5}[Ni_8(OH)_3(EtO)(BDP\_O)_5]$	Polar surfaces, defective crystal sites	3.65	[252]
c. Fluorinated MOFs			
SIFSIX-1-Cu	Dipole, host–guest interactions	11.01	[253]
SIFSIX-2-Cu-i	Dipole, host–guest interactions	6.9	[253]
NbOFFIVE-1-Ni	Host-guest interactions	2.2	[254]
AlFFIVE-1-Ni	Host-guest interactions	2.2	[254]
d. Fibrous MOF membranes (dynamic adsorption of SO_2)			
UiO-66-NH_2/PAN	Electrostatic interactions, un-saturated metal sites	0.019 g/g	[233]
MOF-199/PAN	Electrostatic interactions, un-saturated metal sites	0.014 g/g	[233]
MIL-53(Al)–NH_2/PAN	Electrostatic interactions	0.0028 g/g	[236]

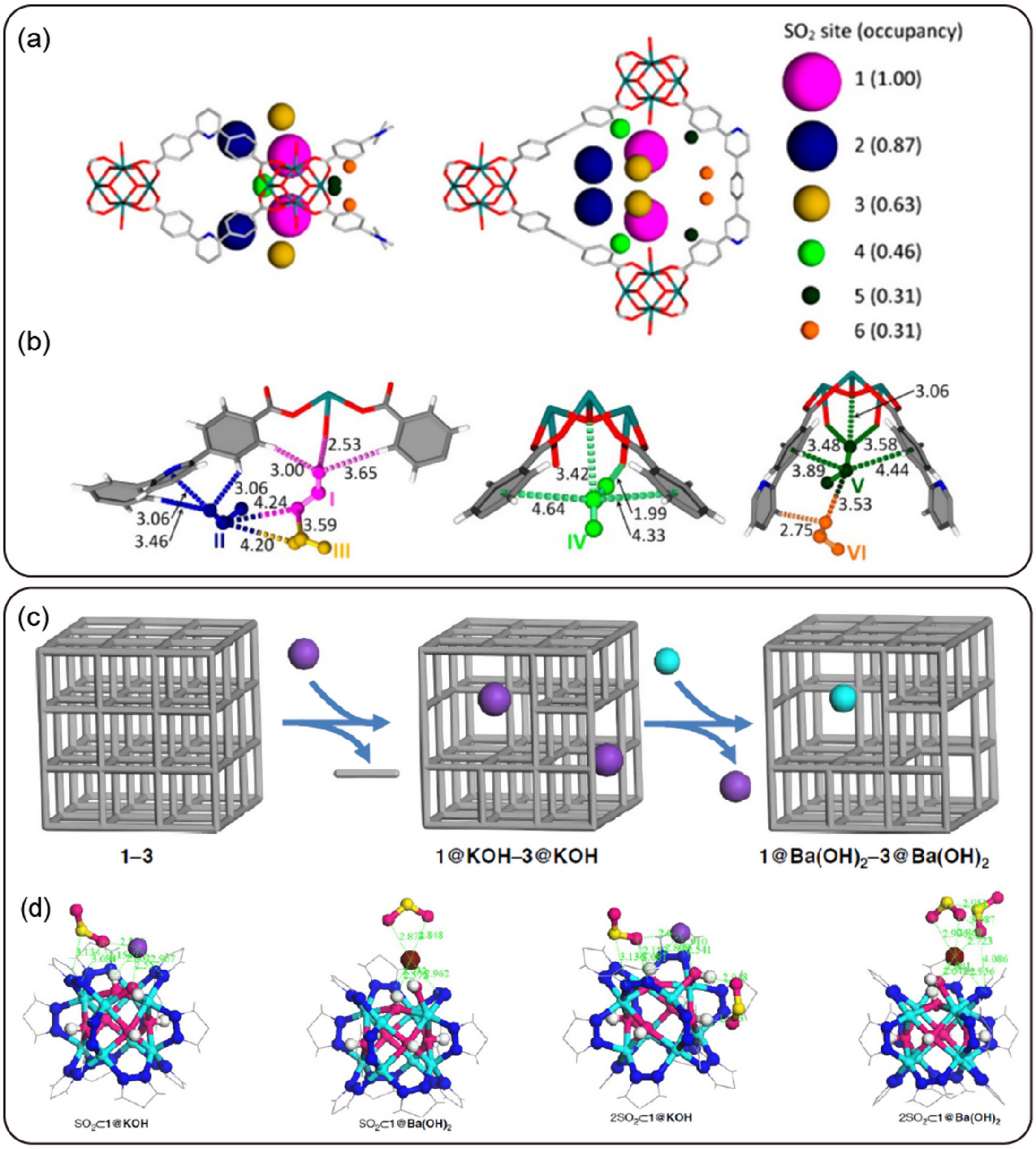

Fig. 31. (a) Site occupancy (illustrated by spheres) of SO_2. (b) Binding sites of SO_2 in MFM-601 as refined by in-situ synchrotron PXRD. Reproduced with permission from [249]. Copyright 2018 American Chemical Society. (c) Schematic illustration of the successive PSMs between potassium (purple) and barium (cyan) from pristine nickel pyrazolate. (d) The DFT structure of sulfur dioxide interaction with crystal defect sites. Reproduced with permission from [252]. Copyright 2017 Springer Nature.

of SO_2 in the MOF pores (Fig. 31a, b). This unprecedented MOF is important due to its high SO_2 selectivity over other gases (CO_2 and N_2), as well as its reversible adsorption properties. Table 17 summarizes these and some further examples of metal–carboxylate MOFs for SO_2 removal.

A few metal–azolate MOFs have also been explored for the adsorptive removal of SO_2. In 2017, a new strategy was reported for the selective capture of SO_2 from flue gas [252]. Extra-framework Ba^{2+} ions were introduced into the defect sites of an Ni-based pyrazolate MOF via an ion-exchange process. Moreover, breakthrough dynamic adsorption experiments and computational studies revealed that the Ba^{2+}-exchanged framework was a key factor in the adsorption of SO_2, as the SO_2 uptake was considerably higher than that of the parent Ni-MOF and K^+-exchanged MOFs (Table 17). This finding allowed the researchers to propose an adsorption mechanism for SO_2 fixation (Fig. 31c, d). The comparatively low reactivity of a barium hydroxide co-crystal toward SO_2 illustrates the importance of having many accessible and disperse adsorptive sites in defect-engineered Ni-MOFs. Hence, this exceptional result provides a new platform for the development of novel metal–azolate MOFs.

Fluorinated MOFs are another class of efficient material for the adsorption of SO_2 from flue gases. Cui et al. designed a series of microporous inorganic moiety (SiF_6^{2-})-based MOFs called "SIFSIX" materials, which exhibited superb capacity and selectivity for SO_2 uptake, even in the presence of other gases such as CO_2 and N_2 [253]. The different structural morphologies of SIFSIX-Cu and SIFSIX-Cu-i ("i" represents an interpenetrated or catenated network) meant that their SO_2 uptake differed, with specific capacities of 11.01 and 6.91 mmol g^{-1} at 298 K and 1 bar, respectively. Interestingly, these MOFs also demonstrated extraordinary SO_2 adsorption capacities at very low SO_2 pressures (1.80 and 2.31 mmol g^{-1} at 0.002 bar, respectively). Breakthrough experiments and density functional theory (DFT) calculations revealed that electrostatic

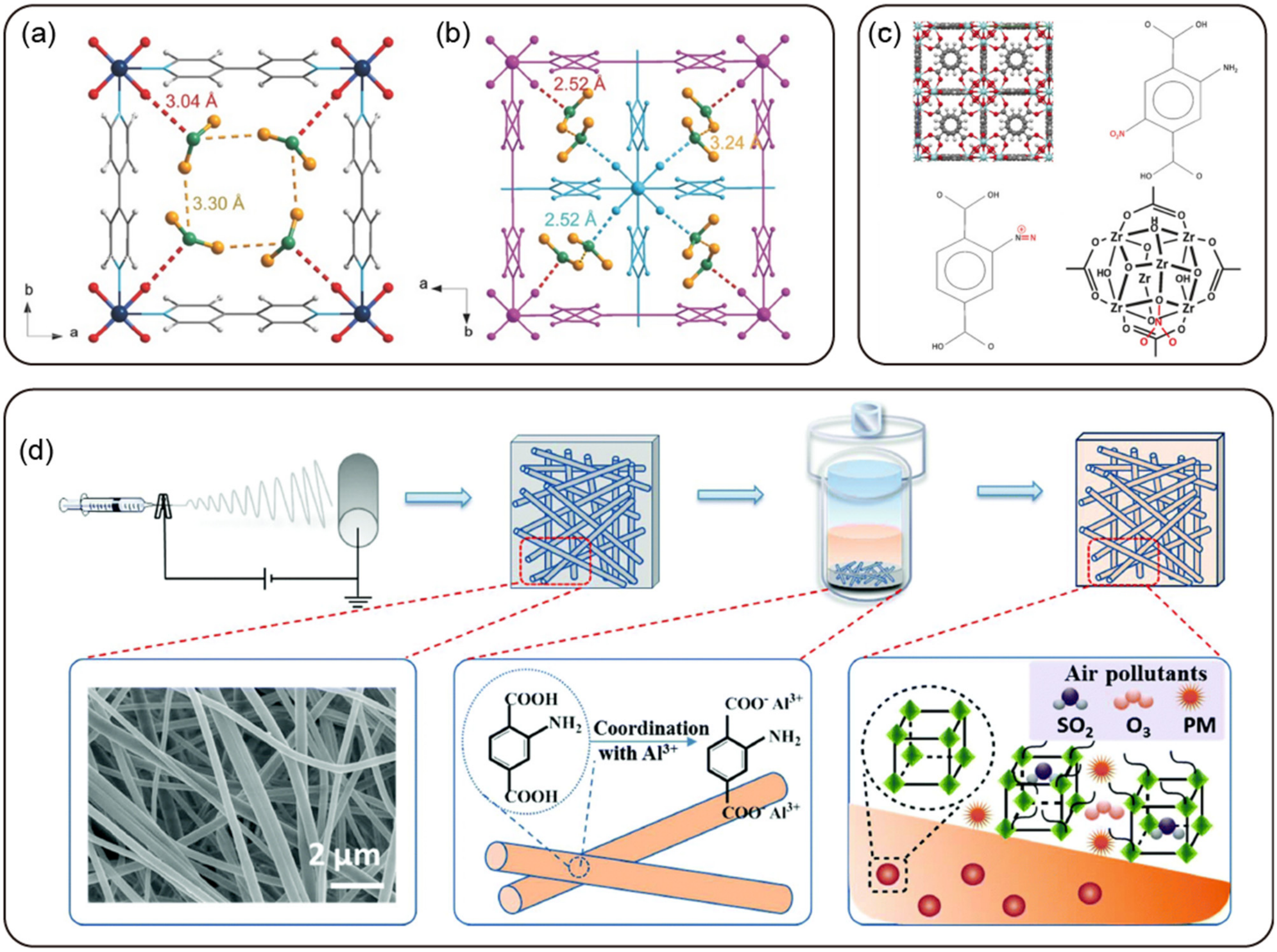

Fig. 32. The crystal structures of SO_2-loaded SIFSIX-1-Cu (a) and SIFSIX-2-Cu-i (b). Adapted with permission from [253]. Copyright 2018 John Wiley and Sons. (c) Crystal structures of UiO-66 analogues with nitration and diazonium ion formation in the benzene ring. Reproduced with permission from [260]. Copyright 2016 John Wiley and Sons. (d) The synthesis protocol and adsorption processes of MOF-based fibrous membranes. Reproduced with permission from [236]. Copyright 2019 Royal Society of Chemistry.

($S^{\delta+}\cdots F^{\delta-}$) and dipole–dipole ($O^{\delta-}\cdots H^{\delta+}$) interactions occurred via a host–guest strategy, while suitable pore sizes enabled guest–guest interactions between the SO_2 molecules that resulted in high SO_2 adsorption capacities under low pressure (Fig. 32a, b). Notably, the SO_2 uptake capacity of SIFSIX-Cu was slightly decreased when the framework was exposed to moisture (1000 ppm), whereas SIFSIX-Cu-i was stable in humid environments—the SO_2 uptake capacity was not significantly affected even at 75% relative humidity (RH).

Very recently, two novel fluorinated MOFs were reported for the adsorptive removal of SO_2 [254]. The isostructural nickel-based pyrazolate MOFs, denoted as KAUST-7 and KAUST-8 (KAUST = King Abdullah University of Science and Technology), were pillared by inorganic moieties [$(NbOF_5)^{2-}$ and $(AlF_5(OH_2))^{2-}$, respectively]. Both frameworks showed similar and considerable SO_2 adsorption uptake of 2.2 mmol g^{-1} for a gaseous mixture of 7% SO_2 and 93% N_2 (ppm). Computational calculations and in-situ SCXRD studies gave insight into the SO_2 adsorption mechanism: the interactions between the sulfur atoms and anionic fluoride pillars and hydrogen bonding interactions between the oxygens of SO_2 and hydrogens of aromatic pyrazines played crucial roles in the high and selective uptake of SO_2. It is expected that these remarkable results and insights may lead to new investigations in the field of fluorinated materials for the removal of SO_2 to control air pollution.

To date, only a few fibrous MOF membranes have been explored for the selective capture of SO_2 under dynamic adsorption conditions. However, the results thus far have been promising. Fibrous MOF membranes or thin films have incredible advantages over solid-state crystalline MOF materials, and can resolve many critical problems such as clogging of pipes and recycling issues. In 2016, Wang and coworkers focused on the fabrication of MOF filters by embedding MOF crystals into polymers through electrospinning [233]. Although there have been several reports on the fabrication of MOF films by electrospinning, systematic investigations are required to give deeper understanding of how to tune the morphology and modify the surface functionality. Analyzing the compatibility of different polymers and MOFs is also important for the development of efficient filters for the capture of SO_2 and particulate matter. The MOF/PAN filters developed by Wang and coworkers [233], denoted as UiO-66-NH_2/PAN and MOF-199/PAN, showed dynamic SO_2 adsorption capacities of 0.019 and 0.014 g g^{-1}, respectively. These filters exhibited very low flow gas resistance and an exceptionally low pressure drop (20 Pa at an air flow rate of 50 mL min^{-1}). In addition, the UiO-66-NH_2/PAN filter showed excellent durability, and could be used several times for the removal of SO_2. Another group reported an electrospun nanofibrous material, MIL-53(Al)–NH_2/PAN (MGP), for the selective removal of SO_2 (Fig. 32d) [236]. Motivated by the previous results, the authors designed a novel fibrous membrane by investigating other amine-functionalized MOF networks. Importantly, the MGP composite membrane had an excellent SO_2 uptake of 0.0028 g g^{-1} under dynamic sorption conditions. When a mixed gas was passed through the MGP filter, its SO_2 concentration dropped from 7000 to 40 ppb. These studies on nanofibrous MOF-based filters have encouraged researchers to investigate their utilization in practical and industrial applications.

- Removal of nitrogen oxides (NO_x)

There are two principal nitrogen oxide (NO_x) gases in the atmosphere: nitric oxide (NO) and nitrogen dioxide (NO_2). These species are toxic and engender high levels of health risk and environmental pollution [255]. They are released from various anthropogenic sources such as vehicle exhausts, combustion power plants, and agricultural dust. In addition, NO_2 is widely used in industry as a nitrating or bleaching agent as well as an inhibitor in polymerization processes [256,257]. Importantly, these components cause photochemical smog and ozone depletion in the troposphere and stratosphere, respectively. In humans, long exposure to NO_x gases can cause severe damage to the respiratory system and skin as well as eye irritation. Therefore, the development of renewed strategies to remove NO_x species is crucial.

In this section, we highlight the recent development of NO_2-capturing materials, as NO_2 is more toxic than NO. Two key issues must be considered for the development of NO_2 adsorbents: (1) although there have been many reported materials for the catalytic conversion of NO_2 to NO, the capture of NO remains an issue; and (2) NO_2 should be easily desorbed from the adsorbent to ensure widescale utility in industrial applications. Several materials (activated carbons, graphite oxides, zeolites, etc.) have been utilized as NO_2 adsorbents, but there are typically critical limitations such as low uptake and/or irreversible NO_2 adsorption. In this regard, MOF-based adsorbents are promising candidates for the selective capture of NO_2 under ambient conditions.

Despite the immediate need to develop novel MOF-derived adsorbents for the capture of NO_2, so far, very few MOF materials have been investigated for this purpose (Table 18). In 2013, Bandosz and coworkers demonstrated the utilization of two Zr-based MOFs (UiO-66 and UiO-67) for NO_2 uptake in dry and humid conditions [258]. Both materials showed similar NO_2 removal properties under dry conditions, but UiO-67 showed higher NO_2 uptake capacity than UiO-66 in humid conditions (2.64 vs. 1.76 mmol g^{-1}). Experimental studies proved that the decreased NO_2 uptake of UiO-66 in humid conditions was due to the structural reactivity of the framework after exposure to humid air, which affected the physisorption of NO_2.

In 2015, a new oxalic acid-incorporated UiO-66 analogue (denoted as UiO-66-ox) was synthesized using a solvent-assisted ligand incorporation (SALI) approach [259]. Experimental analysis demonstrated that UiO-66-ox showed higher NO_2 uptake capacity (8.4 mmol g^{-1}) than UiO-66-vac (vacant sites in UiO-66) and UiO-66 (3.9 and 3.8 mmol g^{-1}, respectively). This increase was identified to be caused by the free carboxylic acids, porosity, and large surface area of UiO-66-ox, as verified by FT-IR and NMR analysis. Furthermore, the NO_2 adsorption properties of NH_2-functionalized UiO-66 have also been investigated [260]. It should be noted that NH_2-functionalized UiO-66 exhibited very low NO generation capability (7 wt%) compared to activated carbon (28 wt%). The MOF also showed very high NO_2 uptake capacities of 20.3 and 31.2 mmol g^{-1} under dry and humid (80% RH) conditions, respectively. The NO_2 adsorption pathways were investigated by NMR, diffuse reflectance infrared fourier transform spectroscopy (DRIFTS) and X-ray photoelectron spectroscopy (XPS) analysis. It was found that the generation of diazonium ions at NH_2 sites, nitration of aromatic linkers, and nitrate formation at bridging oxygens of Zr_6 metal cluster nodes all contributed to NO_2 adsorption (Fig. 32c).

Table 18
List of selective MOF adsorbents for NO_2 uptake at 298 K.

MOF adsorbents	NO_2 uptake (mmol g^{-1})	Ref
UiO-66	1.63 (dry), 0.89 (moist)	[258]
UiO-67	1.76 (dry), 2.64 (moist)	[258]
UiO-66	3.8 (dry)	[259]
UiO-66-vac	3.9 (dry)	[259]
UiO-66-ox	8.4 (dry)	[259]
UiO-66-NH_2	20.3 (dry), 31.2 (moist)	[260]
MFM-300 (Al)	14.1 (dry)	[231]

In 2018, an Al-based MOF, MFM-300(Al), was studied for use as an NO_2 adsorbent [261]. MFM-300(Al) exhibited a high reversible adsorption capacity of NO_2 (14 mmol g^{-1}) under ambient conditions (298 K, 1.0 bar). Moreover, it showed remarkable selectivity for NO_2 in NO_2/CO_2 and NO_2/SO_2 mixed gas conditions. Furthermore, the MOF operates at very low NO_2 concentrations of 5000 ppm and even < 1 ppm NO_2, which implies that there are strong interactions between the MOF and NO_2. Breakthrough experiments via kinetic, dynamic, and static methods revealed that there were five soft supramolecular interactions responsible for this selective adsorption of NO_2. These developments pave the way for novel investigations into superior NO_2 absorption materials.

5.2.4. Removal of volatile organic compounds (VOCs)

VOCs are another class of air pollutant species that can cause severe environmental and public health issues. Emissions from industrial exhausts and household products such as plastics, plywood, and flooring play a key role in the production of most VOCs [262]. The three types of VOC most concerning with regard to air pollution are (1) aromatic hydrocarbons, particularly benzene, toluene, ethylbenzene, and xylenes (BTEX); (2) carbonyl-based compounds such as acetone and formaldehyde; and (3) halogenated compounds including chlorobenzene, dichloromethane, and carbon tetrachloride [263,264]. Adsorption and catalytic conversion approaches are the most common methods for minimizing air pollution from VOCs. Therefore, there is considerable demand for more efficient materials that adopt these approaches. This section focuses on MOF-based adsorbents for VOC capture and removal.

To date, several MOF-derived materials have been developed to capture VOCs from indoor and outdoor air [265,266]. In this review, we will focus on the recent advances in MOF-based adsorbents for the efficient removal of VOCs under ambient conditions, which are summarized in Table 19. For practical applications, moisture-resistive MOFs have a great advantage for the removal of VOCs. Zhao and coworkers reported a hydrophobic MOF denoted as MIL(Cr)-Z1 which showed a high uptake of benzene (7 mmol g^{-1} at 293 K) [267]. In competitive sorption measurements between benzene and water vapor, MIL(Cr)-Z1 showed a higher uptake for benzene than water. The π–π interactions of aromatic linkers with benzene and the relatively large molecular size of benzene with respect to the pores could be responsible for this selective adsorption behavior. Moreover, MIL(Cr)-Z1 gained more attention than the other reported MOF materials (e.g., MIL(Cr)-101) because of its benzene sorption capability at high humidity (60% RH).

Two novel zirconium-based MOFs denoted as BUT-66 and BUT-67 were also employed for VOC adsorption applications [270]. The two hydrophobic MOFs exhibit modest–low benzene adsorption capacities of 3.94 and 6.14 mmol g^{-1} at saturated vapor pressure (10 kPa), temperature (25 °C), respectively. These values are lower than those of other reported materials, such as PAF-1 (20.59 mmol g^{-1}), MIL-101(Cr) (15.84 mmol g^{-1}), and MCM-41

Table 19
Type of VOC and its adsorption capacity on MOFs

MOF adsorbents	Adsorbate	Temperature (K)	Capacity (mmol g^{-1})	Ref
MIL (Cr)-Z1	Benzene	293	~7.0	[267]
UiO-66	Toluene	298	1.8	[268]
UiO-66(NH_2)	Toluene	298	2.7	[268]
MOF-199	Toluene	298	1.7	[268]
ZIF-67	Toluene	298	2.4	[268]
MIL-101(Fe)	Toluene	298	1.1	[268]
MOF-5	Toluene	298	0.3	[268]
MIL-101	Benzene	298	16.3	[269]
MIL-101	Toluene	298	13.6	[269]
MIL-101	Ethyl benzene	298	12	[269]
MIL-101@GO	Benzene	298	20	[269]
MIL-101@GO	Toluene	298	16.6	[269]
MIL-101@GO	Ethyl benzene	298	13.6	[269]
BUT-66	Benzene	298	3.9	[270]
BUT-66	Benzene	298	2.5[a]	[270]
BUT-67	Benzene	298	6.1	[270]
MIL-100(Fe)_A2	Toluene	298	5.6	[271]
MIL-125 NH_2	Benzene	298	4	[272]
MIL-125 NH_2	Toluene	298	3.1	[272]
MIL-125 NH_2	p-xylene	298	2.8	[272]
MIL-125 NH_2	Acetone	298	6.1	[272]
MIL-125 NH_2	2-propanol	298	5.3	[272]
MIL-125 NH_2	Formaldehyde	298	1.3	[272]
CAU-1	Toluene	298	0.07[b]	[273]
HKUST-1**	Toluene	298	1.6	[274]
Foam HK@CMC**	Toluene	298	3.1	[274]
Foam HK@CMC-SA**	Toluene	298	2.1	[274]
Foam HK@CMC-CS**	Toluene	298	2.79	[274]
MIL-101	Acetone [c]	288	16.3	[275]
MIL-101/TC-30	Acetone [c]	288	19.3	[275]
MIL-101/TC-40	Acetone [c]	288	19.5	[275]
MIL-101/TC-50	Acetone [c]	288	13.2	[275]
M-UiO-66(Zr-$N_{3.0}$)	Acetaldehyde	298	9.4	[276]
M-UiO-66(Zr-$N_{3.0}$)	Chlorobenzene	298	4.9	[276]
UiO-66-NH_2	Formaldehyde	298	2.3	[277]
γ-CD-MOF-K	Formaldehyde	293	1.2	[278]
Al-fumarate MOF	Dichloromethane	298	3.4	[279]
MIL-101	Carbon tetrachloride	303	13.3	[280]
MIL-101/GrO-0.25	Carbon tetrachloride	303	15.4	[280]

[a](0.012 kPa, 25C), [b]50% RH, toluene (1 ppm), [c]18.1 kPa, **HKUST-1 was synthesized by using $Cu(OAc)_2$.

(10.49 mmol g^{-1}). Despite the low benzene uptake at saturated pressure and temperature, BUT-66 showed exceptionally high uptake (2.54 mmol g^{-1}) at low concentrations of benzene vapor (0.012 kPa, 25 °C) under humid conditions. X-ray analysis of the crystallographic structure revealed that this high benzene uptake is derived from the small hydrophobic pores in BUT-66 that confine benzene molecules, the mutual response of hydrophilic and hydrophobic sites, and π–π interactions between benzene and the aromatic rings of the framework, which had a T-shaped edge-to-face arrangement (Fig. 33a). Therefore, these water-resistant materials have potential for utilization in practical applications.

For the capture of toluene under atmospheric pressure, six different MOFs (MIL-101(Fe), UiO-66, UiO-66-NH_2, MOF-199, ZIF-67, and MOF-5) were tested and compared [268]. Investigating multiple MOFs may provide insight into the advantages of functional linkers (–NH_2), the role of unsaturated metal sites (MOF-199), and the effects of pore and surface area. Notably, UiO-66-NH_2 (2.7 mmol g^{-1}) and ZIF-67 (2.4 mmol g^{-1}) showed higher toluene uptake under ambient conditions in comparison with UiO-66 (1.8 mmol g^{-1}), MOF-199 (1.7 mmol g^{-1}), MIL-101(Fe) (1.1 mmol g^{-1}), and MOF-5 (0.3 mmol g^{-1}). From a practical point of view, these MOFs are considered moderate adsorbents for the removal of gaseous toluene, as proven by relative humidity studies.

Among the different types of VOCs, carbonyl compounds such as aldehydes and ketones (e.g., formaldehyde, acetaldehyde, and acetone) are a major concern regarding air pollution. Acetone is considered to be a particularly harmful pollutant owing to its high volatility at room temperature. One promising candidate for the removal of acetone vapor is MIL-101 embedded with porous carbon sourced from tobacco stems, denoted as MIL-101/TC [275]. The acetone adsorption was analyzed as a function of the loading of porous carbon. The most promising materials were MIL-101/TC-30 and MIL-101/TC-40 (with 30 and 40 wt% tobacco carbon (TC), respectively), which had acetone adsorption capacities of 19.3 and 19.5 mmol g^{-1}, respectively. These values were improved over that of the pristine MOF, MIL-101 (16.3 mmol g^{-1}). Embedding porous carbon in the MOF network improved the surface dispersive forces and generated more uncoordinated Cr^{3+} metal sites (typically known as defect sites). Owing to these key features, the MOF composite materials displayed better performance toward the adsorption of acetone vapor.

The development of MOF materials comprising green and non-toxic metal nodes is a great challenge for practical adsorbents for the removal of formaldehyde. A novel MOF system comprising a non-toxic metal hydroxide (KOH) and a non-toxic ligand (cyclodextrin, CD) [denoted as CD-MOF-K] prepared by Stoddart's group (Fig. 33b) is a promising candidate [278]. Comparative studies of formaldehyde adsorption by various cyclodextrin based-MOFs revealed that γ-CD-MOF-K has greater formaldehyde uptake than α- and β-CD-MOF-K. Interestingly, γ-CD-MOF-K displayed superb capture speed (15 min) for complete adsorption (0.48 mg m^{-3}) of formaldehyde, whereas the other cyclodextrin based-MOFs took>1 h to reach 50% adsorption. The formaldehyde

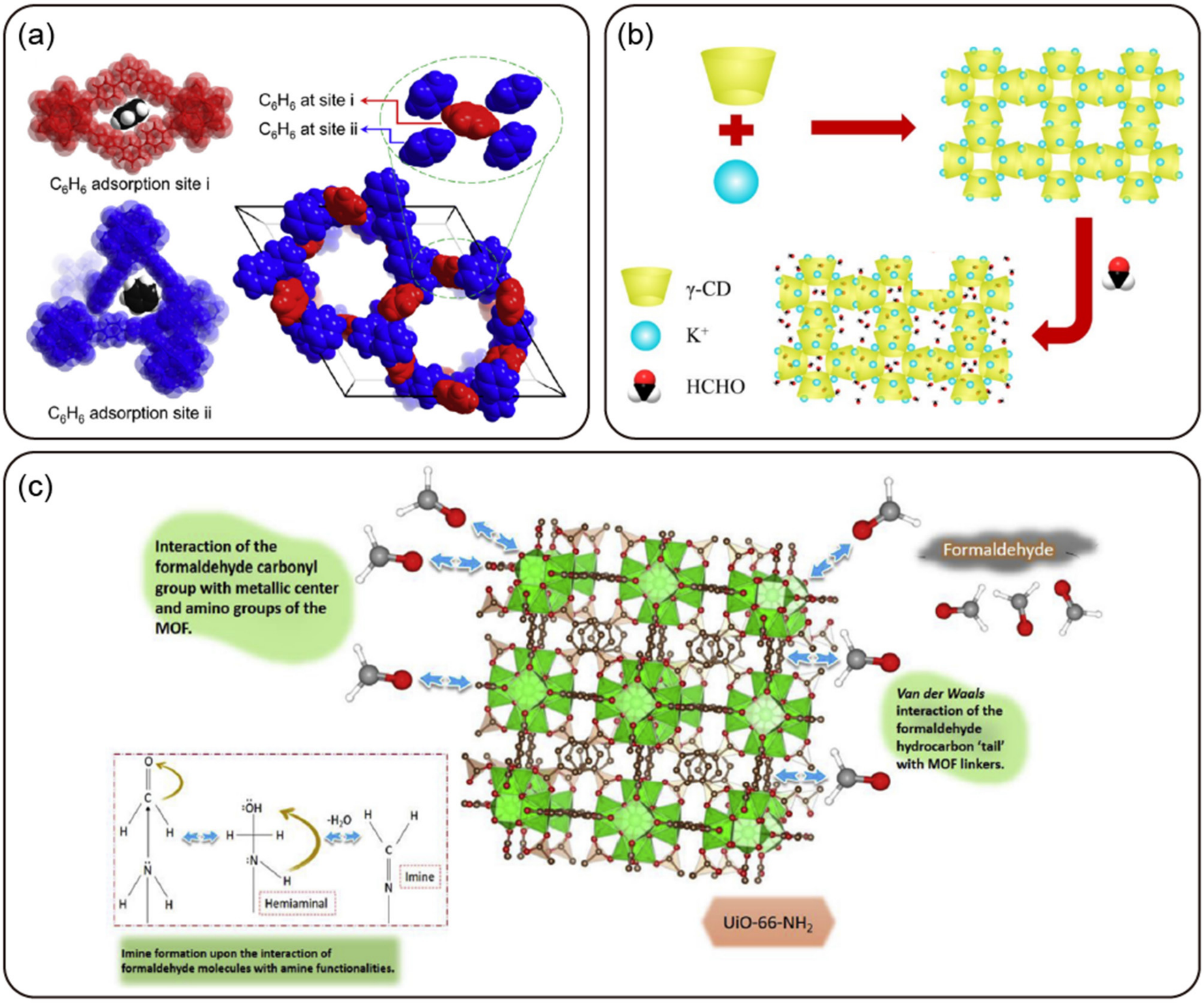

Fig. 33. (a) Benzene adsorption in BUT-66. Reproduced with permission from [270]. Copyright 2018 Elsevier Publisher. (b) HCHO adsorption in γ-CD-MOF. Reproduced with permission from [278]. Copyright 2018 American Chemical Society. (c) The schematic illustration of major interactions between HCHO molecules and UiO-66-NH_2 framework. Reprinted with permission from [277]. Copyright 2019 Elsevier Publisher.

adsorption mechanism involved host–guest interactions derived from multiple hydrogen-bonding interactions between the polar formaldehyde and the hydroxyl groups on the cyclodextrin molecules, which were maximized with γ-CD-MOF-K.

The amine-functionalized UiO-66-NH_2 MOF was employed for formaldehyde sorption applications under ambient conditions [277]. It attained a significantly high breakthrough volume (BTV10) of 137 L g^{-1} at 5 ppm formaldehyde, and showed a significant uptake capacity of 2.3 mmol g^{-1} at 25 ppm formaldehyde and 12% RH. The exceptional behavior of this MOF toward formaldehyde sorption is due to the extraordinary interactions with the NH_2 groups (Fig. 33c), as verified by spectroscopic analysis. Halogenated VOCs such as chlorobenzene, carbon tetrachloride (CCl_4), etc., are similar toxic volatile air pollutants. In a similar fashion, two MOF candidates, MIL-101(Cr) and MIL-101(Cr)/GO (GO = graphene oxide), were prepared to capture CCl_4 from exhausts [280]. As expected, the MIL-101(Cr)/GO composite showed higher CCl_4 uptake (15.4 mmol g^{-1}) than the pristine MIL-101(Cr) (13.3 mmol g^{-1}) at 303 K. It is expected that compositing with graphene oxide has a synergetic effect that increases the CCl_4 adsorption capacity. However, detailed experimental evidence to prove this was not properly presented.

5.2.5. Removal of chemical warfare agents (CWAs)

CWAs or nerve agents are chemically toxic components that have been involved in several global issues and threatened both military personnel and civilians during WWI and WWII. CWAs are categorized as G-type agents [sarin (GB), soman (GD), and tabun (GA)], V-type agents [VX, ethyl({2-[bis(propan-2-yl)amino]ethyl}sulfanyl)(methyl)phosphinate], and vesicants [sulfur mustards, Lewisite, etc.]. Owing to health and safety risks, the usage and production of CWAs is strictly prohibited according to the Chemical Weapons Convention (CWC). Unfortunately, the recent utilization and production of CWAs means that there is an immediate requirement to develop novel technologies that can neutralize or suppress their toxicity under ambient conditions [281]. Owing to the prohibition of using real CWAs for research purposes, alternative chemical compounds named CWA simulants have been produced that display very similar structural features to CWAs but with significantly lower toxicity (Fig. 34a). This has provided enormous relief to researchers, as they can now develop relevant materials to neutralize CWAs using CWA simulants, before the conduction of tests using real CWAs by the appropriate authorities.

For a long time, activated carbon materials played a crucial role for detoxifying/adsorbing CWAs. However, recently, MOFs

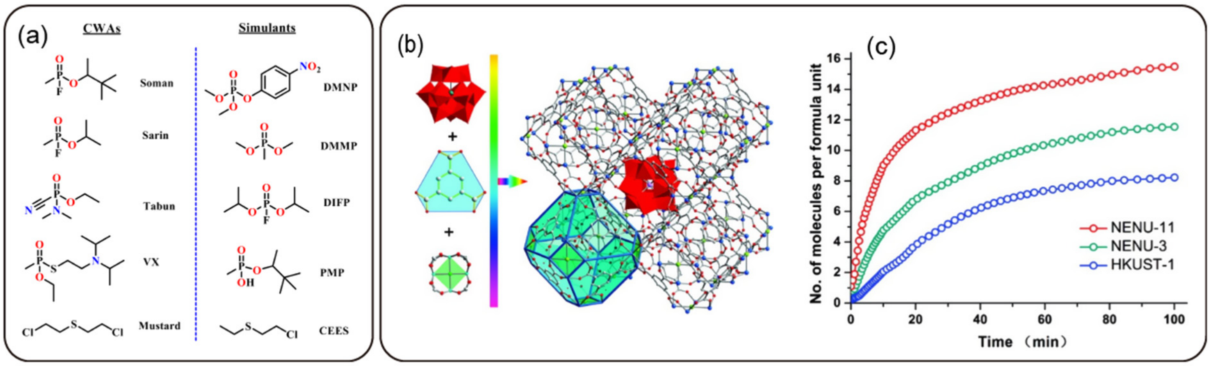

Fig. 34. (a) The examples of real CWAs and less toxic CWA simulants. (b) NENU-11 consisted with Sodalite-type network in which the Keggin polyoxoanions act as noncoordinating guests. (c) Comparison of DMMP uptake with respect to time for NENU-11, NENU-3, and HKUST-1 at 298 K and 1 bar under He flow. Reprinted with permission from [284]. Copyright 2011 American Chemical Society.

emerged as promising candidate for the removal of CWAs. Two major approaches are used for the utilization of MOFs in CWA neutralization: adsorption and detoxification by catalytic processes [282,283]. This section focuses on recent research breakthroughs for the removal of CWAs using adsorbent MOF filters.

Only a few MOF-derived materials have been reported for the adsorption or detoxification of CWAs under ambient conditions. Owing to the long-range order and tailored functional linkers of MOFs, their pores are large enough to confine guest entities. In this regard, Su and coworkers designed a composite with Keggin-type polyoxometalate (POM, $(PW_{12}O_{40})^{3-}$) and a copper-based porous MOF (PMOF) architecture (NENU-11, $H_3[(Cu_4Cl)_3(BTC)_8]_2[(C_4H_{12}N)_6 \cdot PW_{12}O_{40}] \cdot 33H_2O$) [284]. The PMOF/POM composite was used for the efficient removal and decomposition of a CWA sarin simulant, dimethyl methylphosphonate (DMMP), under humid conditions. NENU-11 can adsorb 15.5 DMMP molecules per SBU, which is higher than that of HKUST-1 (8.2 molecules per SBU) and MOF-5 (6 molecules per SBU), as calculated from adsorption uptake experiments. In addition, purposely constructed NENU-3 (POM-incorporated HKUST-1) showed less uptake of DMMP (11.5 molecules per SBU) than NENU-11, which may be due to the different loadings of POM in the MOFs (Fig. 34b, c). The exceptional DMMP adsorption performance of POM-incorporated MOFs can be explained by the hydrogen bonding interactions between the POM and DMMP molecules, and the presence of entatic metal centers in NENU-11. In addition, the Keggin-type POM in NENU-11 MOF was found to acts as an acid catalyst for the hydrolysis of DMMP simulants into methyl alcohol, as evaluated by gas chromatography–mass spectroscopy (GC–MS). Finally, this material was reusable for up to 10 cycles without loss of structural integrity, which will facilitate a new era of POM-incorporated MOF materials for the sorption and decomposition of CWAs in practical applications.

Understanding the reaction mechanisms between CWAs and adsorbents is crucial for the development of superior MOF materials for CWA adsorption. Investigations using in-situ probe experiments are valuable for this purpose. In 2017, four Zr-derived MOFs (UiO-66, UiO-67, MOF-808, and NU-1000) were tested for the adsorptive removal and decomposition of CWA simulants under ambient conditions [285]. The highlight of this work was demonstrating the key aspects of the atomistic reaction mechanisms between MOF adsorbents and CWAs. The authors proposed a mechanism for the adsorption based on in-situ experiments using synchrotron PXRD, EXAFS (Extended X-ray absorption fine structure), and DRIFTS-IR analysis. Although DMMP adsorption occurred in the pores of the selected MOFs, desorption occurred in the UiO-series MOFs owing to collapse of the framework, whereas MOF-808 and NU-1000 survived with small structural changes, as characterized by in-situ PXRD analysis. Le Bail fitting of the PXRD patterns revealed expansion of the unit cell volumes for UiO-66 (1.30%, 60 min), UiO-67 (0.76%, 30 min), MOF-808 (1.33%, 60 min), and NU-1000 (1.17%, 30 min) upon exposure to DMMP for various time intervals (Fig. 35a, b). In addition, in-situ EXAFS revealed that the Zr_6 metal-cluster is a key site for DMMP uptake, which was proven by an increase of disordered Zr–O and Zr–Zr pairs. Moreover, the presence of characteristic peaks corresponding to methyl methylphosphonate (MMP) in the DRIFTS-IR results confirmed that DMMP decomposition occurred. Time-dependent DRIFTS and EXAFS experiments suggested that the decomposition of DMMP gives rise to the formation of covalently bound MMP with Zr_6 cores, with a methanol byproduct (Fig. 35c). It should be noted that the presented MOFs showed good performance for the removal of DMMP from air as well as from various mixed gases, even in humid conditions. Therefore, in-situ probe experiments may provide greater insight for the in-depth understanding of reaction mechanisms for the future development of MOF adsorbents, and emphasize their utilization in air purification applications.

Over the past few years, there has been increased demand for the development of hydrophobic MOFs that can capture nerve agents and CWA simulants. Navarro and coworkers reported the synthesis of a hydrophobic robust MOF, Zn_4O(3,5-dimethyl-4-carboxypyrazolato)$_3$, an isostructure of MOF-5 [286]. The hydrophobic nature of this compound inspired them to investigate its adsorptive removal potential for CWAs under humid conditions. The MOF exhibited remarkable performance for the capture of CWAs, particularly sarin and sulfur-based mustard gas. They used pulsed gas chromatography and zero-coverage gas chromatography to analyze the adsorption behavior, and found that it had a long retention time as well as high heat of adsorption and Henry's constants for DES, a mustard gas simulant, and diisopropylfluorophosphate (DIFP), an analogue of sarin gas, demonstrating the strength of their interaction (Fig. 36a–c). The DES adsorption property of the MOF was compared to that of HKUST-1. Owing to its hydrophobic nature, the prepared MOF showed better DES and DIFP adsorption capacity under humid conditions. This paved the way for the development of hydrophobic materials to capture CWAs for utilization in practical applications.

In 2019, Cho et al. prepared a series of hydrophobic MOF-808 analogues for the adsorption and decomposition of DMMP under dry and humid conditions [287]. The MOFs were synthesized with different charge balancing linkers: formic acid (denoted as MOF-808-F), propionic acid (MOF-808-P), and valeric acid (MOF-808-V). MOF-808-P and MOF-808-V showed identical DMMP uptake

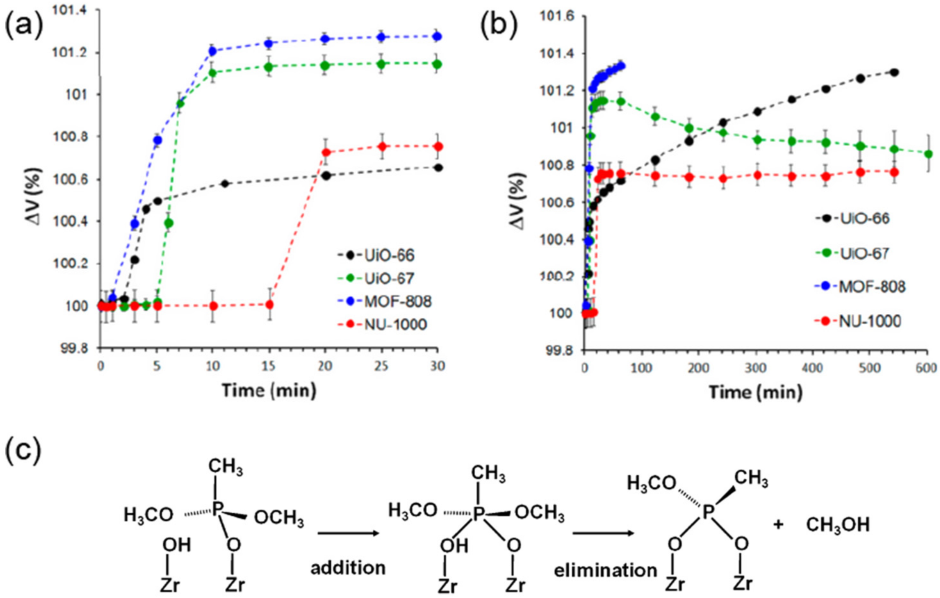

Fig. 35. (a) Evolution of unit cell volumes for UiO-66, UiO-67, MOF-808, and NU-1000 with the dosing of DMMP in first 30 min and (b) the full experiment. (b) Possible mechanism of DMMP decomposition. Reprinted with permission from [285]. Copyright 2017 American Chemical Society.

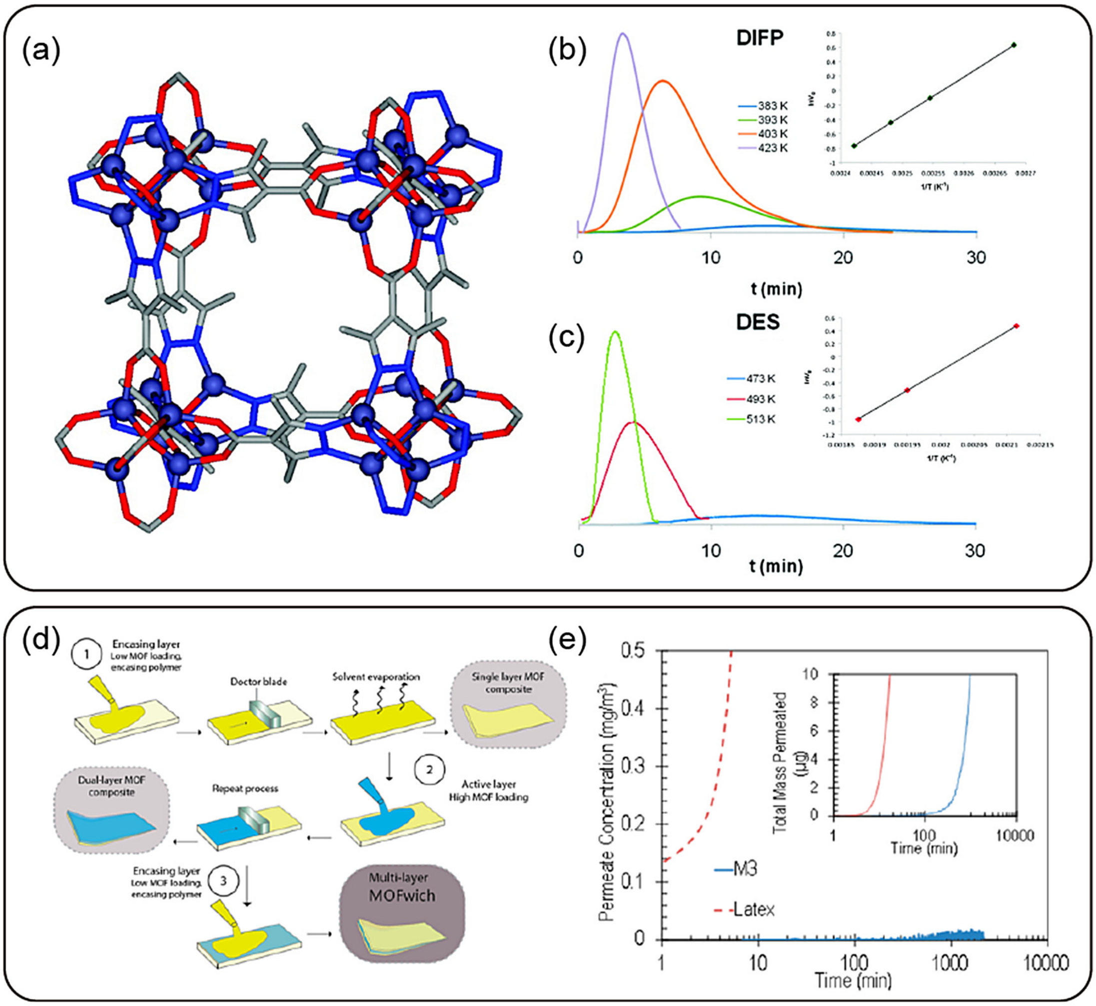

Fig. 36. (a) Crystal structure of $[Zn_4O(3,5\text{-dimethyl-4-carboxypyrazolato})_3]$ MOF. Variable-temperature pulse gas chromatograms for (b) DIFP and (c) DES. Reproduced with permission from [286]. Copyright 2011 American Chemical Society. (d) The synthetic strategy for fabricating the multilayer MOFwich composites. (e) 2-CEES permeation data through M3 and latex. Reprinted with permission from [289]. Copyright 2018 American Chemical Society.

(3.9 and 3.7 mmol g^{-1} under dry and humid conditions, respectively), whereas MOF-808-F showed very low DMMP adsorption capacity (1.4 and 1.3 mmol g^{-1} under dry and humid conditions, respectively). The reason for this difference was related to the concentrations of –OH groups at the defect sites. Time-dependent FT-IR experiments revealed the presence of both DMMP and hydrolyzed DMMP under dynamic adsorption conditions, which proved that the prepared MOFs not only adsorbed but also catalytically decomposed DMMP. Therefore, this series of MOFs has potential for use in practical situations.

Many CWA adsorbents are designed based on the tailoring of functional linkers, reactive defect sites, and atomistic reaction mechanisms. However, the diffusion behavior of CWAs and simulants in porous architectures should also be considered. To date, very few researchers have reported kinetic studies for CWA diffusion in MOF adsorbents. Recently, Sholl and coworkers performed molecular dynamics computer simulations of the diffusion coefficient of sarin and its simulants such as DMMP, diethylchlorophosphonate (DCP), and diisopropyl fluorophosphate (DFP) in four different MOFs (UiO-66, ZIF-8, Cu-BTC, and MIL-47) to better understand the characteristic adsorption properties [288]. The molecular dynamics and dynamically corrected transition state theory (dcTST) simulations revealed that the diffusion is mostly dependent on the sizes of the pore cavities and CWA molecules. The computed results for all MOFs proved that sarin and DMMP possess greater diffusion coefficients than the other simulants (DCP and DFP). Notably, comparing the diffusion times of sarin and simulants in each MOF facilitated the understanding of the adsorption and diffusion properties of MOFs.

MOFs have also been developed for the adsorption of other CWA simulants such as 2-chloroethyl ethyl sulfide (CEES), a mustard gas simulant. Mustard gas played a crucial role in the world wars. A new MOF design strategy based on a sandwich structure (denoted as a "MOFwich"), where high MOF loadings are encased between top and bottom layers of mechanically robust polymers, was recently presented for the development of air purification filters that can remove CEES (Fig. 36d) [289]. The "MOFwich" had high adsorption capacities and an excellent moisture vapor transport rate (MVTR). Considering these advantages, the authors developed two mixed MOF composites (MMCs), SEBS/HKUST-1 and SEBS/UiO-66-NH_2 (named as M3), to test the permeation of CEES and MVTR. The M3 filter showed limited permeation (<0.01 mg m^{-3}) of CEES over 16 h exposure, whereas latex gloves of the same thickness displayed greater permeation (Fig. 36e). M3 did not exhibit breakthrough permeation even when exposed to CEES for>40 h. However, the hydrophilicity of the MOF in M3 meant that its MVTR value (16 g $m^{-2}h^{-1}$) was higher than that of the latex polymer. Therefore, combining the properties of M3 with common polymers such as latex may encourage the development of user-friendly protective barriers against mustard gas-based CWAs.

Later, a new MMC (SIS/HKUST-1) membrane was developed for the adsorptive removal of CEES by incorporating HKUST-1 into layers of polystyrene-*block*-polyisoprene-*block*-polystyrene (SIS) triblock copolymers using a similar method [290]. The researchers investigated the effect of changing the loading of HKUST-1 (10–50 wt%) and the thickness of the film (75–150 μm) on the CEES permeation rate and MVTR. Increasing the MOF loading and thickness reduced the CEES permeation rate and increased the MVTR. Interestingly, the composite also acted as a self-indicator upon exposure to CEES to detect the toxicant. Therefore, this MOF-polymer compositing strategy is expected to support the industrial production of mustard gas protective equipment in the future.

5.3. Removal of biological toxicants

Amongst diverse biological issues, uremic syndrome is a critical disease that severely damages kidney function and causes various uremic toxins to accumulate, ultimately causing death [291,292]. Uremic toxins are human metabolism products, divided into three categories: (1) water soluble (e.g., urea, uric acid, and creatinine), (2) water insoluble (e.g., peptides and leptins), and (3) protein-bound moieties (e.g., *p*-cresyl sulfate, indoxyl sulfate, and hippuric acid). Hemodialysis therapy has been widely used to remove or filter these toxins from human blood. Nevertheless, hemodialysis lacks filtration efficiency and has difficulties removing water insoluble toxins and protein-bound moieties. Therefore, several porous adsorbents such as activated carbons, zeolites, carbon nanotubes, and composite membranes have been investigated for the removal of uremic toxins in artificial kidney applications [293–295]. Crystalline and porous MOFs are expected to play a vital role in addressing the unresolved problems with other porous materials, and provide a competitive alternative for commercially available adsorbents in various applications.

To date, only a limited number of MOF-based bio-toxicant adsorbents have been explored for artificial kidney applications (Table 20). Recently, a new MOF-derived composite membrane (UiO-66-$(COOH)_2$@cotton) was designed for the adsorptive removal of creatinine from an artificial blood solution [300]. A comparative study with various manufactured fabric composites revealed that the prepared MOF composite showed exceptional adsorption capacities both in situ (212.8 mg g^{-1}) and ex situ (192.3 mg g^{-1}) compared to pristine cotton (113.6 mg g^{-1}) (Fig. 37a, b). In addition, the adsorption mechanism was studied, with the results suggesting that weak interactions including hydrogen bonding and dipole–dipole interactions between the active binding sites of the composite and the functional groups (N and O atoms) of creatinine, as well as physical deposition on the composite surface, were the main mechanisms of creatinine removal from artificial blood. The regenerated fabric retained 82% of its initial creatinine removal performance after three cycles. This strategy highlights the opportunities for the development of diverse composite materials for the efficient removal of uremic toxins in artificial kidney applications.

The extended aromatic systems in MOF derivatives are attractive for the removal of protein-bound uremic toxins such as *p*-cresyl sulfate, indoxyl sulfate, and hippuric acid in artificial kidney applications. Very recently, Farha and coworkers investigated the performance of nine Zr_6-based MOFs for the capture of protein-bound uremic toxins to repair chronic kidney disease [301]. Adsorption studies revealed that NU-1000 showed exceptionally

Table 20
Summary of uremic toxin adsorption property of MOFs

MOF adsorbents	Uremic toxins	Adsorption capacity (mg g^{-1})	Temperature (K)	Ref
MIL-100(Fe)	creatinine	190.5	310	[299]
UiO-66-$(COOH)_2$@Cotton	creatinine	212.8	310	[300]
NU-1000	potassium p-cresyl sulfate	440	303	[301]
NU-1000	potassium indoxyl sulfate	254	310	[301]
NU-1000	hippuric acid	199	310	[301]

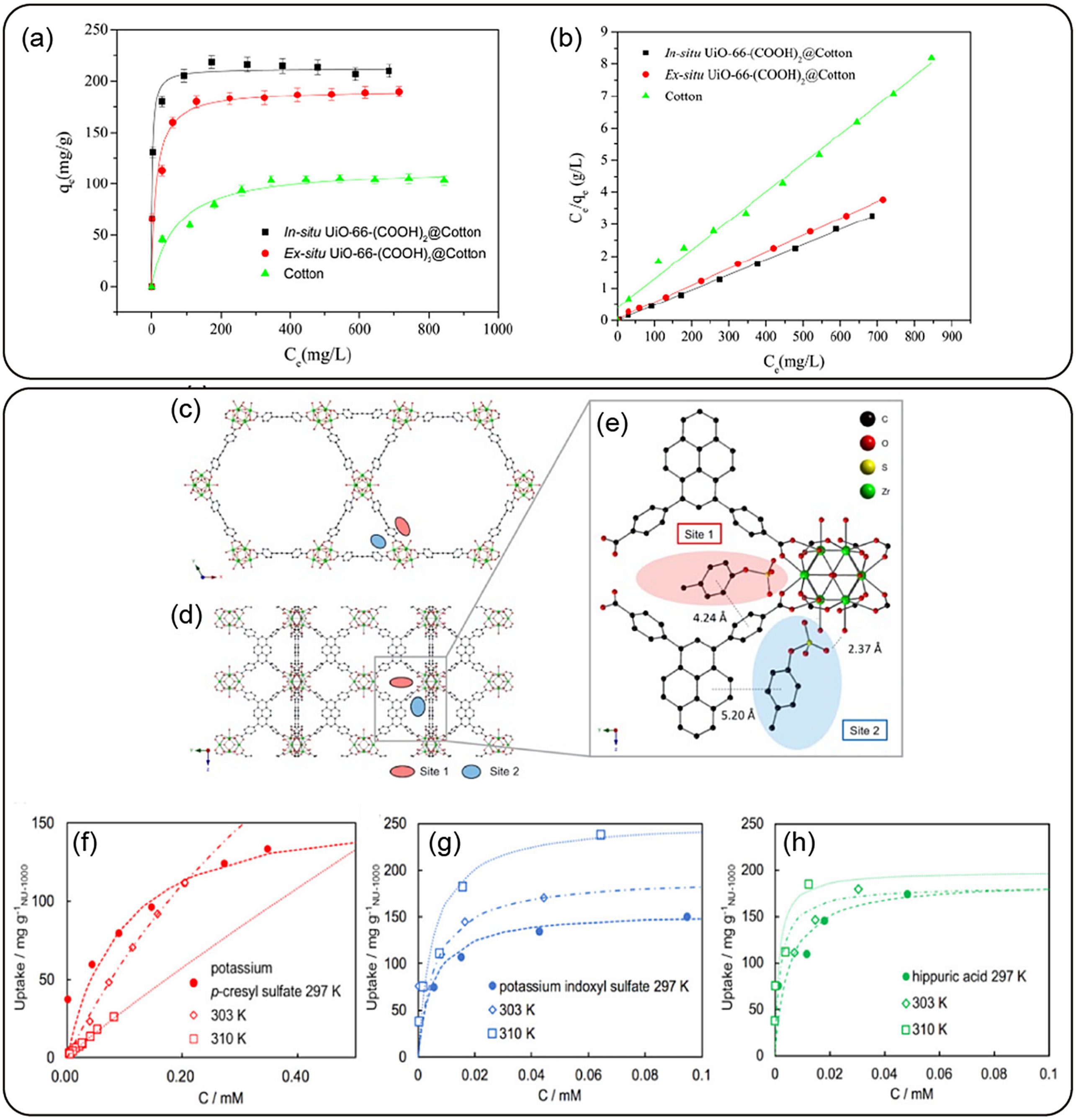

Fig. 37. (a) Isotherm profiles for creatinine adsorption onto native Cotton and *ex-situ* UiO-66-(COOH)$_2$@Cotton composite and *in-situ* UiO-66-(COOH)$_2$@Cotton composite. (b) Linear fitting for isotherm profiles. Reproduced with permission from [300]. Copyright 2008 Elsevier Publisher. (c-d) The crystal structure of NU-1000 and p-cresyl sulfate exposure. (e) Optimized geometry of p-cresyl sulfate-pyrene and Zr$_6$ node domains after p-cresyl sulfate adsorption. Adsorption isotherms of the uremic toxins: (f) potassium p-cresyl sulfate, (g) potassium indoxyl sulfate, and (h) hippuric acid on NU-1000. Reproduced with permission from [301]. Copyright 2019 American Chemical Society.

high uptake of *p*-cresyl sulfate (440 mg g^{-1} at 303 K), indoxyl sulfate (254 mg g^{-1} at 310 K), and hippuric acid (199 mg g^{-1} at 310 K) in comparison to other MOF adsorbents. More excitingly, the *p*-cresyl sulfate crystals that accumulated in the NU-1000 network helped the researchers to develop an understanding of the adsorption mechanism, by utilizing single-crystal structure analysis and DFT calculations (Fig. 37c–h). They found that the extended π-conjugated systems, where hydrophobic sites were sandwiched between pyrene linkers and the hydroxyl groups of Zr$_6$ nodes, were responsible for the high uptake of *p*-cresyl sulfate. These results are promising for the future study of diverse MOF derivatives for the removal of protein-bound uremic toxins in artificial kidney applications.

5.4. Antibacterial implementation of MOF materials

Owing to the wide range of infectious microorganisms, public health remains a significant challenge. Worldwide, bacterial infections threaten the lives of millions of humans [302]. Various antibiotics have been manufactured and are readily available to prevent and treat bacterial infections. However, we are only now beginning to understand the serious drawbacks of antibiotic treatment, including antibiotic resistant superbugs, untargeted site drug release, and several diverse side-effects. Therefore, there is a huge opportunity for the development of effective antimicrobial materials [303].

There have now been three "generations" of antibacterial agents. The first were simple organic compounds (e.g., halides, peroxides, and phenols) or inorganic substances and salts. Following this, metals and metal oxide such as Ag, CuO, CoO, and ZnO were used as antibacterial agents. The third generation are diverse topology materials including colloids and films, which include various "nano" materials [305]. The MOFs covered in this article are comprised in the third generation because of their unique porous nature and structural features. MOFs have emerged as efficient antibacterial agents for various biomedical applications with often exceptional antibacterial behavior [296,297,304]. The fascinating properties of MOFs play a crucial role in their antibacterial effects. Owing to the significant importance of antibacterial material development, researchers have focused on investigating novel strategies for the development MOF-based materials that can fight bacterial infections.

5.4.1. Insight into mechanisms of antibacterial MOFs

Although various chemical combinations and synthetic reaction conditions have engendered a variety of antibacterial MOF compounds, understanding the antibacterial mechanisms of MOFs is sure to facilitate the discovery of better-performing antibacterial agents [298]. Nevertheless, the probable antibacterial mechanism of MOFs is still not clearly understood. One hypothesis is based on the well-studied mechanism of antimicrobial activity in metal/metal oxide NPs [306]. Metal NPs can penetrate the walls and membranes of bacterial cells, thereby damaging the cell membranes. The NPs induce a state of oxidative stress in the bacteria, which plays a crucial role in the destruction of bacteria cells through the generation of reactive oxygen species (ROS), leading to stress-induced cell death (Fig. 38) [303].

It is considered that MOF-anchored NPs provide a similar mechanism of antibacterial activity. Indeed, recent investigations have linked the controlled release of metal ions upon degradation of the MOF to antibacterial efficacy. In addition, it has been found that organic ligands in MOFs exhibit high activity through the controlled release of linkers, which acts synergistically toward antibacterial behavior with the release of metal ions [307]. Noticeably, the large surface area and tunable porosities of MOFs are advantageous for synthesizing NPs of a controlled size, which is challenging in traditional metal NP synthetic procedures [308]. Moreover, the presence of metal ions and structural stability of MOFs influences the antibacterial effect. With this in mind, we highlight in this section the recent breakthroughs in MOF-anchored NPs and MOF-derived materials for practical antibacterial applications. Several important works that present various MOF-based compounds for bactericidal applications are discussed, along with their possible working mechanisms (Table 21).

5.4.2. Antibacterial applications of MOFs

Over the past few decades, protecting materials from bacterial infection has drawn a lot of attention in biomedical research to avoid complications during medical treatment. Recently, researchers have incorporated antibacterial agents into the pores of porous MOFs to bestow them with antibacterial properties. Rifampicin (RFP, antibacterial agent) and 2-nitrobenzaldehyde (*o*-NBA, pH jump reagent) were loaded in the pores of ZIF-8 (RFP&*o*-NBA@ZIF-8) for the effective treatment of in vivo and in vitro bacterial infections as well as wound infection therapy under optimal pH and ultraviolet (UV)-light irradiation [309]. Interestingly, the RFP&*o*-NBA@ZIF-8 material showed high activity against both gram negative (ampicillin-resistant *Escherichia coli, E. coli*) and gram-positive bacteria (methicillin-resistant *Staphylococcus aureus*, MRSA) at optimal conditions, as evaluated by the in vitro studies. Antibacterial activity tests demonstrated that the *E. coli* growth rate decreased with a minimum inhibitory concentration (MIC) of 10 μg mL^{-1} and illumination time of 120 min, whereas the MIC of MRSA was in the range of 65–131 μg mL^{-1}. Furthermore, in vivo studies proved that the MOF material showed high antibacterial efficiency toward bacterial infections upon UV-light (365 nm) irradiation at pH = 8.5. Significantly, this MOF that degrade to generate Zn^{2+} ions upon UV-light exposure, which would induce a local pH change, can be employed for the controlled release of RFP. The idea of combining MOFs with antibacterial agents inspired the development of MOFs with antibacterial activity and wound healing properties. For example, MOFs that

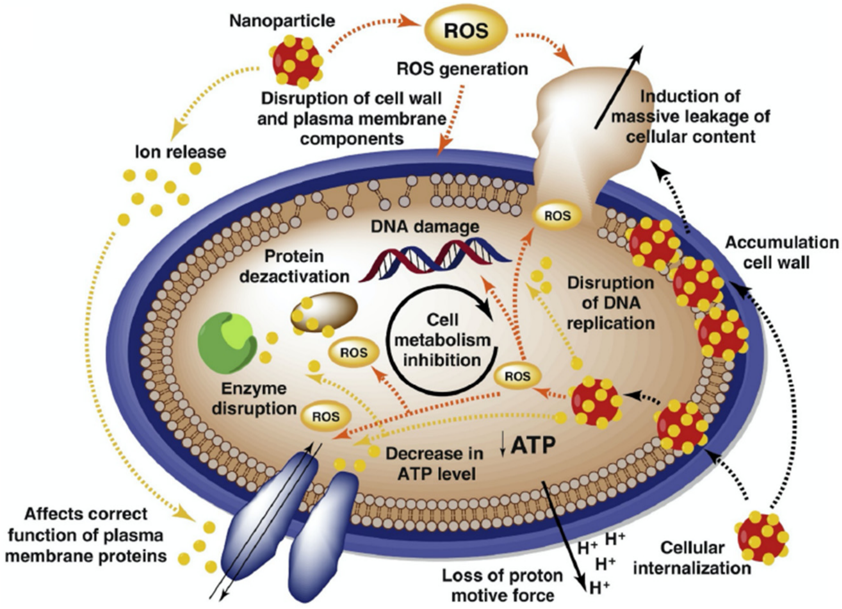

Fig. 38. Antimicrobial mechanisms of nanostructured systems containing metals. Reproduced with permission from [303]. Copyright 2019 Elsevier Publisher.

Table 21
Summary of antibacterial activity of MOFs for specific bacteria

MOF compound	Inhibitors of bacterial activity	Type of bacteria	Antibacterial activity	Ref
RFP&o-NBA@ZIF-8	Zn^{2+} ions and RFP = rifampicin	*E. Coli*	*E. Coli:* MIC = 0–80 μg/mL	[309]
RFP&o-NBA@ZIF-8	Zn^{2+} ions and RFP = rifampicin	MRSA	MRSA: MIC = 65–131 μg/mL	[309]
$Cu_3(NH_2BTC)_2$-cotton	Cu^{2+} ions	*E. coli*	–	[310]
CP/CNF/ZIF-67	Co^{2+} ions	*E. Coli*	*E.* Coli: MIC = 10 μg/mL	[311]
Ag@CD-MOF	Ag NPs	*E. Coli* and *S. aureus*	*E. Coli:* MIC = 16 μg/mL, MBC** = 32 μg/mL	[312]
Ag@CD-MOF	Ag NPs	*E. Coli* and *S. aureus*	*S. aureus:* MIC = 64 μg/mL, MBC = 512 μg/mL	[312]
Ag@Zn-BIF	Ag NPs	*E. Coli* and *S. aureus*	*E. Coli* and *S. aureus:* MIC = 30–50 μg/mL	[313]
$[AgL]_n{\cdot}nH_2O$, L = 4-cyanobenzoate	Ag^+ ions	Oral bacteria*	Oral bacteria: MIC = 21.17 μg/mL for all MOFs	[314]
MOF-5 and ZIF-8	Zn^{2+} ions	Oral bacteria*	Oral bacteria: MIC = 21.17 μg/mL for all MOFs	[314]
Cu_{10}MOF	Cu^{2+} ions	*E. Coli* and *S. aureus*	*E. Coli* and *S. aureus:* MIC = 500 ppm	[315]
HKUST-1/CS	Cu^{2+} ions	*E. Coli* and *S. aureus*	–	[316]

*Streptococcus mutans (UA159), Fusobacterium nucleatum (Fn), Porphyromonas gingivalis (Pg)
** Minimum bactericidal concentration.

degrade to generate Zn^{2+} ions upon UV-light exposure, which would induce a local pH change, can be employed for the controlled release of RFP.

In order to prepare antibacterial surfaces that can prevent bacterial growth, a new cotton/MOF composite material ($Cu_3(NH_2BTC)_2$ MOF-cotton) was developed that exhibited excellent antibacterial activity toward *E. coli* [310]. Substantially, a copper-based MOF was attached on cotton by a post-synthetic modification process, resulting in AM-5-modified MOF (Fig. 39a). The copper delivery performance of the MOF/cotton and AM-5-modified MOF materials were studied, and found to have ~54% and ~90% Cu^{2+} ion (μmol $cm^{-2}h^{-1}$) release in 24 h, respectively (Fig. 39b). Cell viability tests on agar plates showed that the AM-5-modified MOF gave a 4-log (99.99%) reduction in viable cells, whereas the MOF/cotton composite gave a 5-log (99.999%) reduction. Both materials therefore exceeded the industry standard of a 3-log (99.9%) reduction in viable cells. The results demonstrated that the prepared cotton/MOF composite had high performance at limiting bacterial infections under wet and dry conditions and formed an antibacterial surface, which has since encouraged the development of cotton-based wound healing materials.

In the field of antibacterial materials, the design of sustainable and biodegradable materials remains a challenge. The use of biodegradable materials with MOFs may provide a solution to this problem. Qian and coworkers reported a new biodegradable paper-based MOF composite from cellulose paper (CP), cellulose nanofiber (CNF), and Co-based ZIF (ZIF-67) (Fig. 39c) [311]. As compared to Ag^+ ions, the use of less toxic Co^{2+} ions in ZIF-67 enables its use in antibacterial applications. The antibacterial activity of the CP/CNF/ZIF-67 composite toward *E. coli* was tested. Good antibacterial activity was achieved with an antibacterial rate of 80% with an MIC of 10 μg mL^{-1} ZIF-67, suggesting the dependency of antibacterial activity on the loading of ZIF-67 in the composite. Moreover, the cytotoxicity test revealed that ZIF-67 showed exceptional cell via-

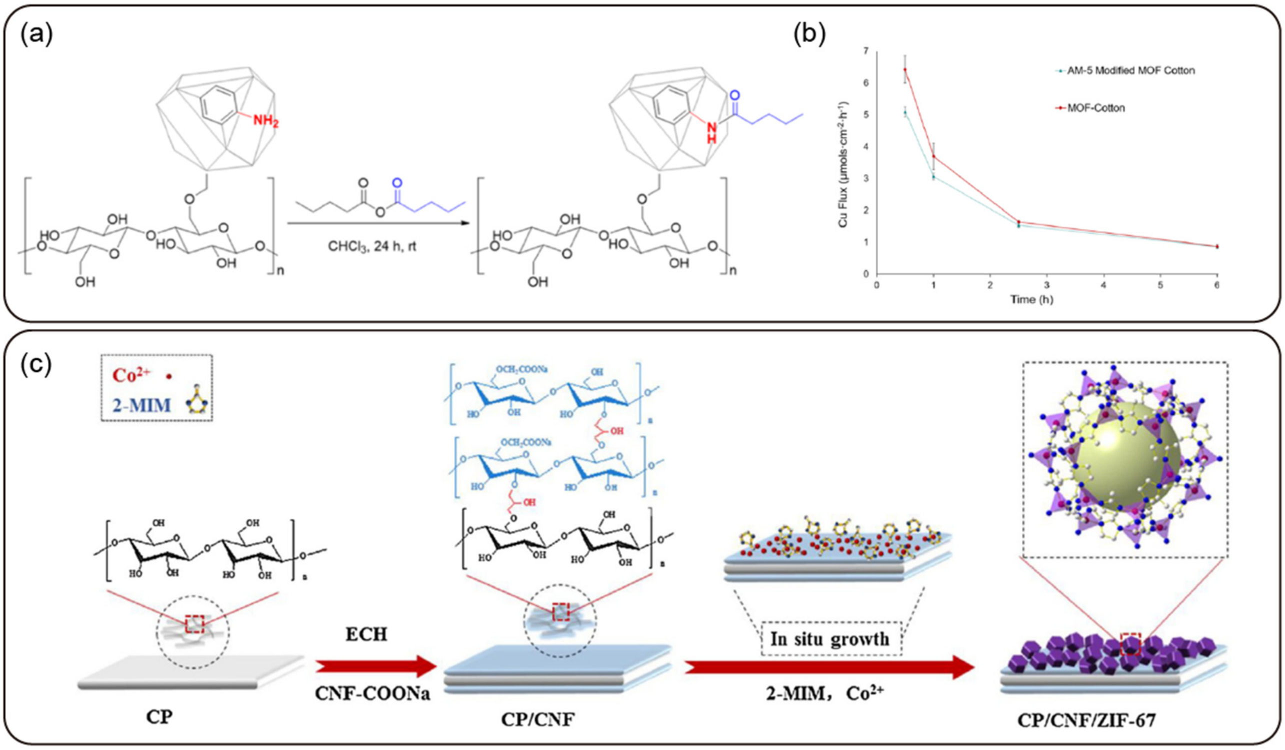

Fig. 39. (a) PSM of the MOF $Cu_3(NH_2BTC)_2$ with valeric anhydride to yield an AM-5-modified MOF. (b) Copper ion-releasing flux data of the MOF – cotton materials soaked in NBM solution for 6 h at 37 °C. Reprinted with permission from [310]. Copyright 2018 American Chemical Society. (c) Schematic representation of the fabrication process of CP/CNF/ZIF-67. Reproduced with permission from [311]. Copyright 2018 Elsevier publisher.

bility of ~94% even at high concentrations of 80 μg mL^{-1} compared to other characteristic MOFs (e.g., ZIF-8), which further confirmed the applicability of the CP/CNF/ZIF-67 composite for antibacterial purposes.

Although MOF-supported Ag-based NPs play a vital role in conventional antibacterial systems, the fabrication of ultrafine NPs using MOF surfaces could be interesting for tuning the antibacterial properties. With this in mind, a biocompatible cyclodextrin-based MOF (CD-MOF) was used as a template for the preparation of ultrafine Ag NPs (Ag@CD-MOF, CL-Ag@CD-MOF, and GS5-CL-Ag@CD-MOF; see Fig. 40a) that inhibited the growth of *E. coli* and *S. aureus* bacteria [312]. The Ag@CD-MOF showed attractive antibacterial efficacy, whereas the other MOF composites showed no further enhancement against bacterial activity. The MICs of the Ag NPs for *E. coli* and *S. aureus* were 16 and 64 μg mL^{-1}, respectively. The thick peptidoglycan layer in *S. aureus* (gram positive bacteria) hindered the penetration of the Ag NPs, which resulted in reduced antibacterial efficacy compared to that for *E. coli*. Interestingly, time-dependent bacteria growth curves revealed that increasing the concentration of Ag NPs was not favorable for improving antibacterial activity (Fig. 40b, c). Finally, a Gly-Arg-Gly-Asp-Ser (GRGDS) peptide-incorporated Ag@CD-MOF exhibited a great response for wound healing therapy, highlighting its importance in drug delivery applications.

Recently, an in situ reduction protocol for synthesizing NPs in Zn-BIF MOF networks was reported for antibacterial applications [313]. The MOF-templated Ag NPs (denoted as Ag@Zn-BIF) showed good antibacterial efficacy toward *E. coli* and *S. aureus*. Live/dead cell culture and plate counting experiments revealed that Ag@Zn-BIF exhibited superior activity against bacterial growth than commercially available Ag NPs. Notably, optical density measurements highlighted that Ag@Zn-BIF performed well with a lower MIC (30–50 μg mL^{-1}) than those of Zn-BIF (500–1000 μg mL^{-1}) and commercial Ag NPs (>300 μg mL^{-1}) (Fig. 41a–e). This result is encouraging for the synthesis of reducing agent-free NPs for enhancing antibacterial activity.

Very recently, a series of MOFs (p-MOF ($[AgL]_n \cdot nH_2O$ (L = 4-cyanobenzoate)), MOF-5, and ZIF-8) were used as antibacterial materials against oral bacteria such as *Streptococcus mutans* (UA159), *Fusobacterium nucleatum* (Fn), and *Porphyromonas gingivalis* (Pg) [314]. In these MOF compounds, the set concentration for Ag^+ and Zn^{2+} metal ions was 21.17 μg mL^{-1}. Among the prepared MOFs, p-MOF showed the best activity against oral bacteria, whereas MOF-5 and ZIF-8 performed moderately. Specifically, solid-phase growth curves demonstrated that the performance of these MOFs and silver nitrate ($AgNO_3$) followed the order p-MOF > $AgNO_3$ > MOF-5 > ZIF-8 (Fig. 41f–h). Hence, the authors suggested that the structural stability and metal ion content of the MOFs was key for better performance in anti-oral bacterial studies. In addition, they explained that the greater the release of specific metal ions from the MOFs, the higher the antibacterial activity.

5.4.3. Future perspectives for the development of antibacterial MOFs

MOFs have been utilized in antibacterial studies for the loading of antibiotics or metal NPs. However, these compounds can encounter difficulties in the controlled release of antibiotic drugs as well as metal NPs. In situations where MOF compounds pose difficulty in the release of NPs, antibacterial agents that utilize MOF compounds in which metal ions and/or organic ligands are synergistically involved in the antibacterial effect are likely to be chosen. In such cases, tailoring of the intrinsic properties of the MOFs and their nanostructures could be beneficial for accomplishing greater antibacterial activity and reducing cytotoxicity. Moreover, the design of MOFs with well-selected metal ions and organic linkers may encourage the synergistic effect between the precursors and improve the antibacterial efficacy.

In the future, it is expected that the development of biodegradable and biocompatible MOFs will be expanded. These types of materials may be most suited to use in biomedical applications such as wound healing bandages, antibacterial surfaces, and biofilms. In addition, the utilization of antibacterial MOFs in food technology and water treatment is still in its infancy. Any related applications should consider the potential toxicity originating from MOF composites. In this regard, future generations of MOF compounds for antibacterial purposes should be developed with biocompatible cations and less toxic ligands.

5.5. Ion transport in MOFs for solid-state electrolyte

5.5.1. Highlights of solid-state electrolytes

The depletion of unrenewable energy resources like coal, oil, and natural gas and increasing human population have impacted the demand for energy in electricity, transportation, industry, and other purposes [317]. In addition, the combustion of fossil fuels releases toxic gases and VOCs into the atmosphere, which has led to a severe global issue with greenhouse gases. Thus, there is an urgent need to develop sustainable and renewable energy sources to solve the present energy and environmental concerns. Fuel cells and batteries/supercapacitors are highly attractive technologies for clean energy production and energy storage applica-

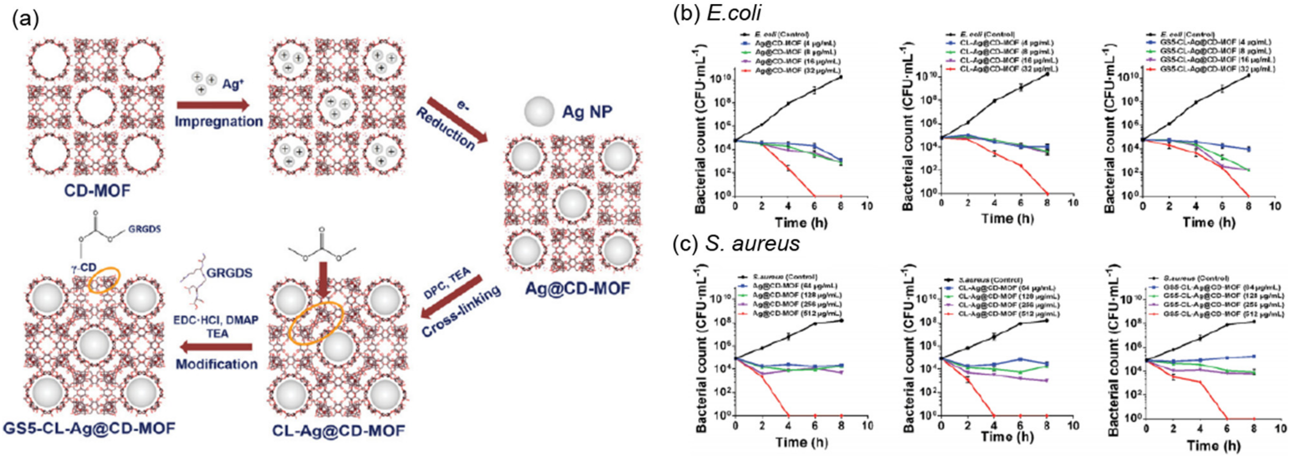

Fig. 40. (a) CD-MOF template guided synthesis of Ag NPs by solution impregnation followed by reduction, cross-linking (CL), and GRGDS surface modification. Bacterial time–kill profiles of (b) *E. coli* and (c) *S. aureus* of Ag@CD-MOF, CL-Ag@CD-MOF, and GS5-CL-Ag@ CD-MOF. Reprinted with permission from [312]. Copyright 2019 John Wiley and Sons.

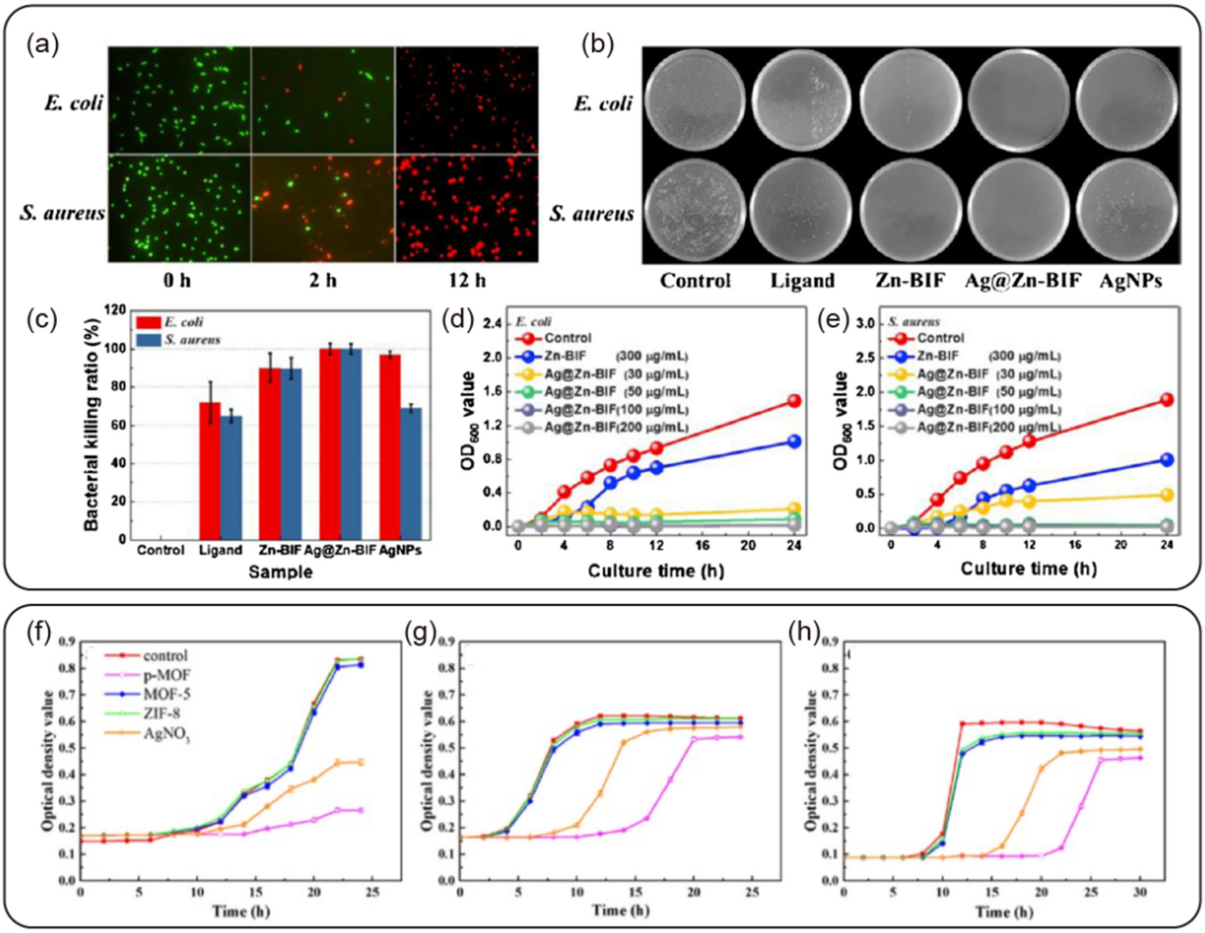

Fig. 41. (a) Fluorescence photographs of *E. coli* and *S. aureus* treated by Ag@Zn-BIF with different time.(b) Photographs and (c) bacterial killing ratio histogram of *E.coli* and *S. aureus* colonies grow on agar plates. Real-time OD_{600} values of the Zn-BIF and Ag@Zn-BIF against (d) *E. coli* and (e) *S. aureus*, respectively. Reproduced with permission from [313]. Copyright 2020 Elsevier publisher. (f) Growth curves of (f) Fn, (g) Pg, and (h) UA159 in different antibacterial materials. Reprinted with permission from [314]. Copyright 2020 American Chemical Society.

tions, respectively [318]. Among the various types of fuel cells, proton-exchange membrane fuel cells (PEMFCs) have emerged as promising candidates for the production of clean and sustainable energy, as they combat the drawbacks of traditional engines, and release only H_2/O_2 as byproducts. The solid electrolyte plays a crucial role in PEMFCs [319,320]. Therefore, there is a strong need to design and develop new solid electrolyte materials that can meet stringent requirements, including: (i) high proton conductivity ($\sigma > 10^{-2}$ S cm^{-1}), (ii) high operation temperature (>100 °C) to avoid electrode poisoning and fuel crossover; (iii) good mechanical strength and processability of solid membrane/electrolyte; (iv) chemical and thermal stability under operating conditions; (v) good compatibility, especially with the electrodes and bipolar plates; (vi) reasonable cost of bulk production; and (vii) porosity tunability or switching by external stimulus.

In comparison with commercially available proton-conducting materials such as Nafion and ceramic oxides, MOFs have intriguing potential for use as solid-state electrolyte materials owing to their modular nature, tunable functionality, and high porosity [321,322]. For fuel cells, two main types of MOF materials have been extensively studied: water-assisted proton-conducting MOFs, and anhydrous proton-conducting MOFs. In water-assisted proton-conducting MOFs, proton transformation relies on guest water molecules, whereas in anhydrous proton-conducting MOFs, proton conduction depends on the existing protons of heterocyclic compounds, organic acids, and inherent water molecules. Therefore, the majority of improvements to proton conductivity involve the introduction of acidic functional groups (e.g., –COOH, $-SO_3H$, and –OH) or guest molecules (e.g., H_2O, imidazole, and triazole) into the MOF network [323,324]. With this in mind, we highlight in this section some of the most recent research into proton-conducting MOFs for fuel cell applications.

The increasing demand on energy storage systems has triggered great importance on electrochemical storage devices such as Li-batteries, redox-flow batteries, and supercapacitors [325,326]. Battery technologies have been widely explored to deliver superior characteristics like high power density, fast charge/discharge rates, and long lifetime [327]. Most conventional batteries including Li-ion batteries (LIBs) utilize a polymer membrane saturated with an organic liquid electrolyte, which can lead to serious safety issues, such as leakage, poor chemical stability, and flammability. In practice, LIBs present several safety concerns; for example, lithium dendrite formation leads to short-circuiting, and leakage of the organic electrolyte can cause explosions [328]. Solid-state electrolytes are therefore promising candidates to replace liquid electrolytes for practical applications. Solid-state electrolytes should meet the following requirements to provide suitable electrochemical performance: (i) high ionic conductivity (on the order of 10^{-3} S cm^{-1}); (ii) reduced electronic conductivity; (iii) single mobile ion species; (iv) high transference number; and (v) good chemical, thermal, and electrochemical stability.

Over the past few decades, inorganic systems composed of ceramics, glasses, or organic polymers have been widely used as solid-state electrolytes [329]. Although inorganic solid-state electrolytes exhibit high ionic conductivity (~10^{-3} S cm^{-1}), they have numerous drawbacks including high interfacial resistance and poor processability. This has inspired research attention toward new classes of solid-state electrolytes. In this regard, MOFs have intriguing properties: tunable MOF networks can provide unique channels for single ion mobility; nano-MOF compounds provide strong electrode–electrolyte interfacial interactions that can to address mobile ion kinetics; and high ionic conductivity functional linkers can be incorporated into MOFs to improve the electrochemical performance. Hence, MOFs go some way toward meeting the requirements for solid-state electrolytes, and are expected to facilitate the development of better performance solid-state batteries in the future [330–333].

In this section, we describe the recent advances in solid-state MOF electrolytes, with a focus on two major applications: (i) proton-conducting MOFs as solid-state electrolytes for fuel cells, and (ii) MOF-derived solid-state electrolytes for batteries.

5.5.2. Proton-conducting MOFs as solid-state electrolytes

There are already several excellent review articles on the applications of proton-conducting MOF materials [323,334]. Herein, we focus on the recent advances in the field of proton-conducting MOF electrolytes that have not been covered in recent reviews (Table 22a).

The tuning and modulation of both ionic conductivity and proton conductivity in crystalline MOF materials is highly attractive for addressing performance and other adverse issues of proton-conducting materials. However, such research investigations are still in their infancy. With this in mind, Yoon and coworkers presented proton conduction switching two microporous MOF compounds, $Mg(HCO_2)_2$, $Co(HCO_2)_2$, that showed a reversible crystal-to-amorphous structural transformation for switching conductivity on/off [335]. Water vapor adsorption and proton conductivity experiments demonstrated that these compounds assumed several different structural states depending on the relative humidity (Fig. 42a, b). Detailed structural analysis proved that there were three phases: (1) an anhydrous phase, (2) a water-adsorbed phase, and (3) a water-coordinated phase. The proton conductivity of the water-coordinated phase was 1.0×10^{-3} S cm^{-1} for $Mg(HCO_2)_2$ and 1.0×10^{-6} S cm^{-1} for $Co(HCO_2)_2$ at 90% RH and 298 K. Interestingly, water-coordinated framework showed the crystalline-to-amorphous transition, upon which the MOFs changed from conductor to insulator, and vice versa. The dynamics of the water-coordinated phase were further analyzed by solid-state ^2H NMR spectroscopy. Although the proton conductivity was moderate, this work presents the first reversible crystal-to-amorphous structure transformation by changing the RH values, which enables proton conductivity switching behavior.

Recently, metal–organic gels (MOGs) have emerged as alternative materials to conventional MOF materials for exceptional proton conducting performance. A recently developed Cr-based MOG (Cr/sBDC-Gel; sBDC = 2-sulfoterephthalic acid) showed higher proton conductivity than MOF pellets comprising a similar functional linker (MIL-101-SO_3H) [336]. The Cr/sBDC-Gel-0.4 M (0.4 M represents concentration of sBDC solution) exhibited a proton conductivity of 7.84×10^{-3} S cm^{-1} at 80 °C and 100% RH, whereas that of the MIL-101-SO_3H pellets was only 8.7×10^{-4} S cm^{-1}. Although the MOG cannot be considered a conventional solid-state material, it is believed that this work can provide a strategy for increasing the conductivity of solid-state materials by incorporating continuous long-range proton transfer channels, such as that of this 3D-percolated MOG network.

Table 22
Conductivity and conduction medium of ion conducting MOFs.

a. Proton conducting MOFs

MOF compound	Pore guest	Proton conductivity	Conditions [Temperature/humidity]	Ref
$Mg(HCO_2)_2$	H_2O	1.0×10^{-3}	25 °C, 90% RH	[335]
$Co(HCO_2)_2$	H_2O	1.0×10^{-6}	25 °C, 90% RH	[335]
Cr/sBDC-Gel-0.4 M	H_3O^+	7.84×10^{-3}	80 °C, 100% RH	[336]
α-PCMOF-21-Br	H_2O	1.69×10^{-3}	85 °C, 95% RH	[337]
α-PCMOF-21-Cl	H_2O	0.95×10^{-3}	85 °C, 95% RH	[337]
UiO-66-NH_2@NFs/Nafion	H_3O^+	0.27	80 °C, 100% RH	[340]
PSM 1	H_2O	1.64×10^{-1}	80 °C, 95% RH	[341]
IM-UiO-66-AS	H_2O	1.54×10^{-1}	80 °C, 98% RH	[342]
(EMI)[N(CN)$_2$]@PCN-777 (f = 62.5%)	EMI-N(CN)$_2$	1.1×10^{-2}	70 °C	[343]
$(NH_4)_3[Zr(H_{2/3}PO_4)_3]$	NH_4^+	1.45×10^{-3}	180 °C	[344]
DNA@ZIF-8–3/25	DNA, H_2O	1.7×10^{-1}	75 °C, 97% RH	[345]
MOF-801@PP-60	H_2O	1.84×10^{-3}	325 K, 98% RH	[346]
SA-EIMS@MIL-101	R-SO_3^-	1.89×10^{-3}	150 °C	[347]
MSA-EIMS@MIL-101	R-SO_3^-	1.02×10^{-4}	150 °C	[347]
PTSA-EIMS@MIL-101	R-SO_3^-	2.78×10^{-4}	150 °C	[347]

b. MOF based SSEs

MOF compound	Pore guest	Ionic conductivity	Transference number	Ref
LCMOF-1 (–COOH)	Li^+	1.06×10^{-3}, 25 °C	0.58	[348]
UiO-66-LiSS	Li^+	6.0×10^{-5}, 25 °C	0.9	[349]
UiO-66-LiSS-EC/PC	Li^+	7.8×10^{-4}, 25 °C	0.88	[349]
NMS/PEO/LiTFSI	Li^+	1.66×10^{-5}, 25 °C	0.378	[350]
MOF-688	Li^+	4.6×10^{-4}, 30 °C	0.87	[338]
PL/UiOLiTFS	Li^+	2.07×10^{-4}, 25 °C	0.84	[333]
WZM SSE	Zn^{2+}	2.1×10^{-4}, 35 °C	0.93	[339]
UIO/IEs	Li^+	1.47×10^{-4}, 30 °C	0.47	[351]
ZIF-8 QSSE	Li^+	1.05×10^{-4}, 25 °C	0.52	[352]
Al-Td-MOF-1	Li^+	5.7×10^{-5}, 25 °C	–	[353]
MIT-20LiBr	Li^+	4.4×10^{-5}, 25 °C	0.66	[354]
MIT-20-Na	Na^+	1.8×10^{-5}, 25 °C	–	[354]
MIT-20-Mg	Mg^{2+}	8.8×10^{-7}, 25 °C	–	[354]

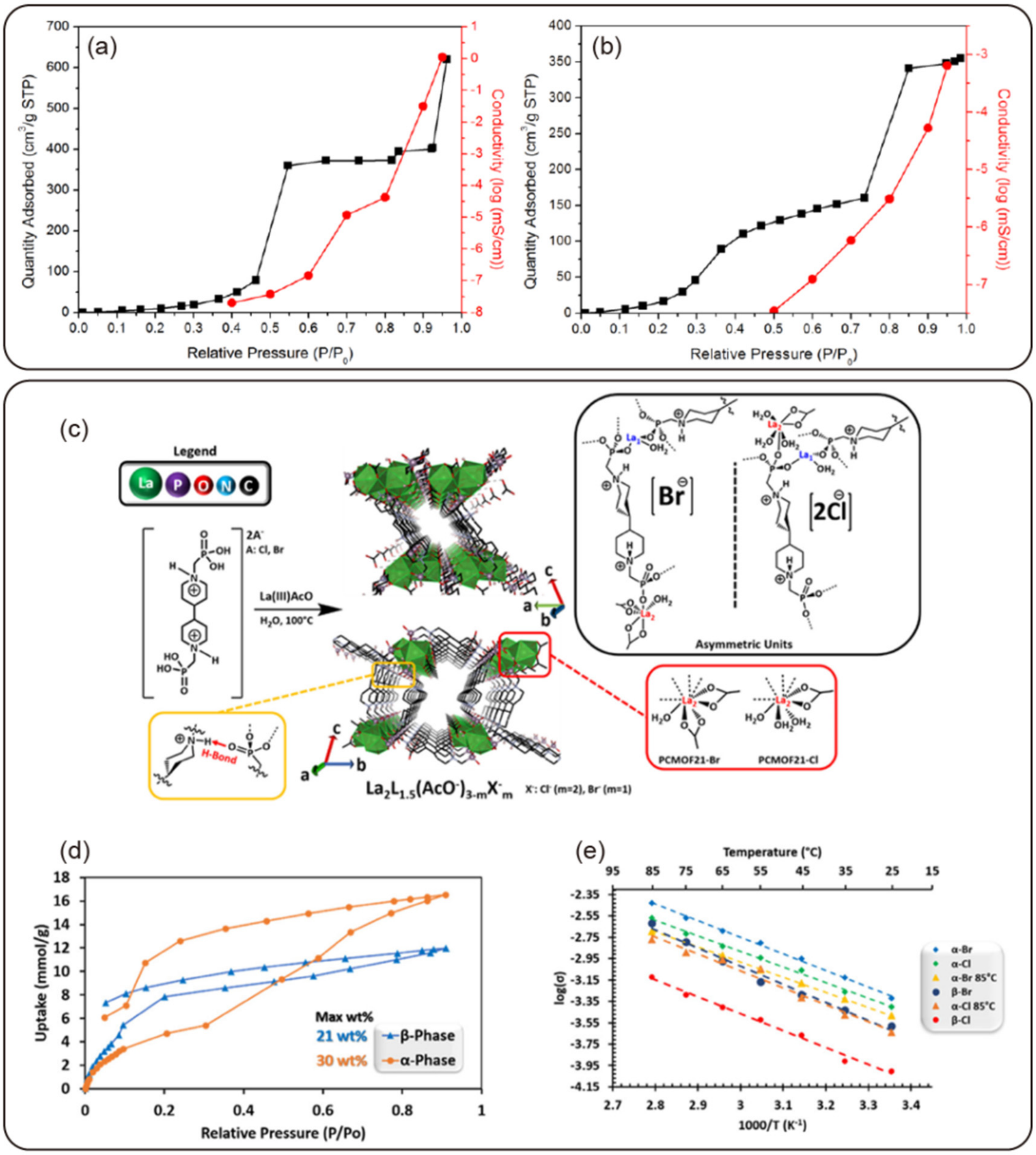

Fig. 42. Water vapor adsorption (black line) and proton conductivity (red line) of (a) $Mg(HCO_2)_2$ and (b) $Co(HCO_2)_2$ at 298 K. Reproduced with permission from [335]. Copyright 2020 Royal Chemical Society. (c) Synthesis scheme and structural schematic representation of α-PCMOF-21 (d) Water adsorption isotherm comparison for phases of PCMOF-21-Cl at 22 °C. (e) Log of conductivity vs inverse temperature comparison of all phases and treatments of α & β-PCMOF-21. Reprinted with permission from [337]. Copyright 2019 American Chemical Society.

Metal–phosphate MOFs have intriguing properties compared to their metal–carboxylate counterparts. The phosphate terminals present proton-donating and proton-accepting functionality, which can be useful for proton conduction at high temperatures or under anhydrous conditions. Levenson et al. prepared four lanthanide phosphonate frameworks with different phases (α or β) and/or different counter anions (Cl^- or Br^-): α-PCMOF-21-Br, α-PCMOF-21-Cl, β-PCMOF-21-Br, and β-PCMOF-21-Cl (Fig. 42c) [337]. The different phases affected the water vapor adsorption property of the materials, which had a significant effect on the proton conductivity (Fig. 42d). In addition, the flexible nature of the α phase allowed an unusual stepped water vapor sorption isotherm with higher water vapor adsorption capacity than that of the β phase, resulting in higher conductivity. Interestingly, the removal of anions from the framework revealed that α-PCMOF-21-Br possessed higher proton conductivity (1.69×10^{-3} S cm^{-1}) than α-PCMOF-21-Cl at 85 °C and 95% RH. It should be noted that the conductivity of most water-assisted proton conducting MOFs decreases rapidly above 80 °C owing to water loss due to evaporation. However, the conductivity of the presented MOFs increased continuously until 85 °C. This was considered to be related to the strong water-binding properties of the phosphate functional groups and the ease of proton donation–acceptance on the phosphate (Fig. 42e). This work has brought insight into opportunities for the development of proton-conducting MOFs that can operate above 100 °C for higher fuel cell performance.

5.5.3. Ion-conducting MOFs for batteries

Overcoming the issue of lithium dendrite formation within solid-state MOF electrolytes is a considerable challenge. Yaghi and coworkers developed a new Li-exchanged Anderson-type polyoxometalate (POM)-based MOF network (MOF-688) [338].

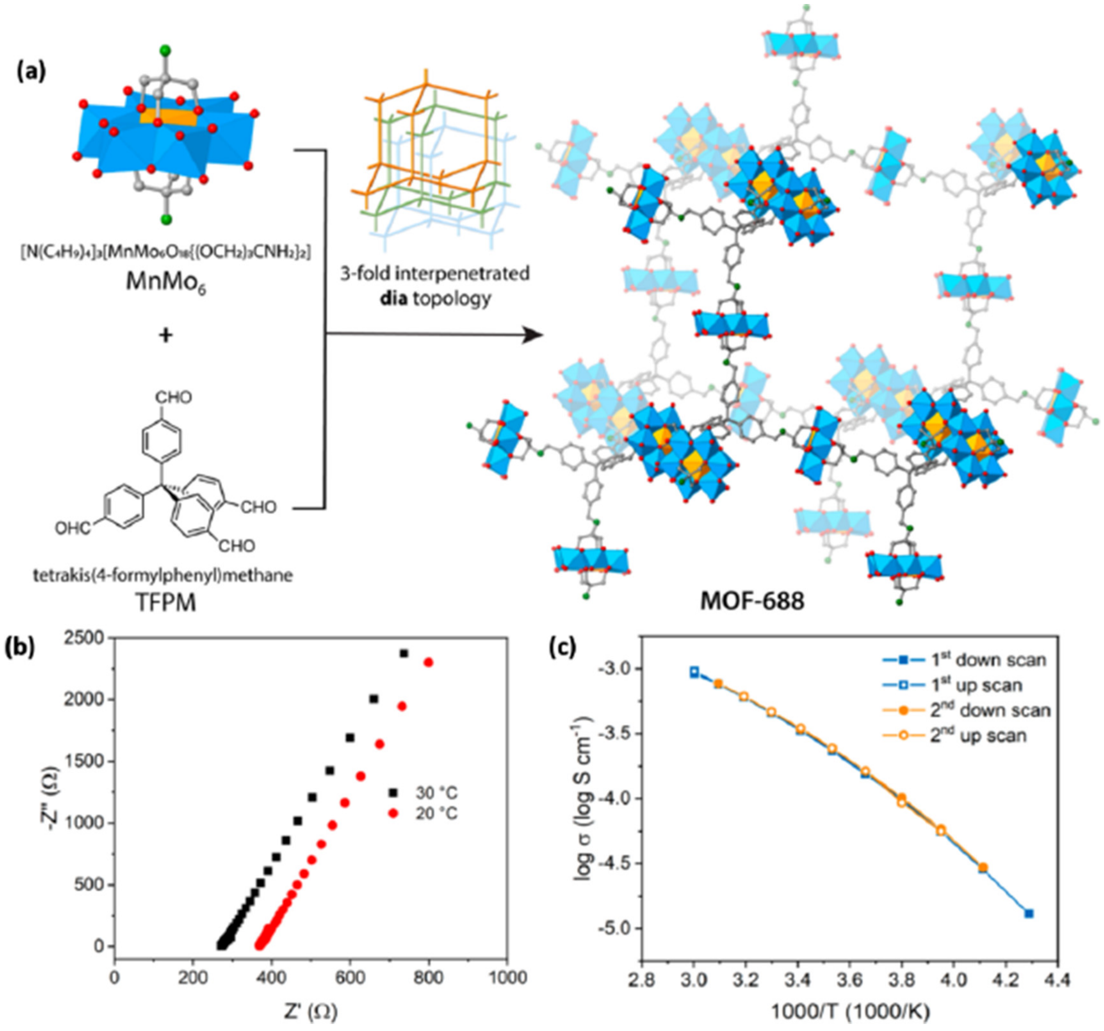

Fig. 43. (a) Synthetic scheme and structural illustration of MOF-688. (b) Nyquist plots of MOF-688 at 20 and 30 °C. (c) Ionic conductivity as a function of temperature from −40 to 60 °C. Reprinted with permission from [338]. Copyright 2019 American Chemical Society.

The prepared MOF had a highly porous structure and exhibited high Li-ion conduction for application as the solid-state electrolyte in LIBs (Fig. 43, Table 22b). MOF-688 attained a high ionic conductivity (3.4×10^{-4} S cm^{-1} at 20 °C) and transference number (t_{Li+} = 0.87), with POM playing a crucial role for efficient Li conduction. Although the exact role of POM is still not clearly understood, this work motivates toward testing in practical solid-state battery applications. Along the same lines, an MOF superionic conductor (PL/UiOLiTFS) was also reported for Li-ion conduction, which possessed high ionic conductivity (2.07×10^{-4} S cm^{-1} at 25 °C) and a large transference number (t_{Li+} = 0.84) [333]. Interestingly, the prepared material worked even at low temperatures (0 °C), which is unusual for conventional Li-ion conducting materials as the liquid tends to freeze. Although the conductivity and transference number were not excellent, the non-freezing behavior presented in this work opens a new avenue for solid-state electrolytes that can allow low-temperature battery operation. Therefore, this development presents a model for future generations of solid-state battery devices.

Owing to the expense and reactivity issues with alkali metal ions, demand for improved transition metal-ion batteries is growing. For the development of such batteries, the fabrication of electrolyte materials for specific metal ions is crucial. Recently, various metals have been investigated for use in transition metal-ion batteries. Zn appears to be a promising candidate owing to its abundancy and stability. Recently, Pan and coworkers prepared post-synthesized MOF-808 (WZM solid-state electrolyte) for the incorporation of Zn^{2+} ions the solid-state electrolyte for practical VS_2/Zn batteries [339]. They inserted single Zn^{2+} ions into the MOF network, which enhanced the ionic conductivity (2.1×10^{-4} S cm^{-1}) and transference number (t_{Zn2+} = 0.93) at 35 °C. Moreover, the electrolyte showed good electrochemical stability, cyclability, and lower self-discharge rates. Although this is a simple demonstration of ion conductivity in MOF materials, the presented work provides an avenue for the development of next-generation transition metal-ion batteries.

5.6. Electrode materials for energy storage applications

In the previous section, we briefly discussed the key role of MOF-based solid-state electrolytes in energy storage and conversion applications. The intriguing properties of MOF-based materials have led to their use as electrode materials (cathode/anode) in electrical energy storage devices such as batteries and supercapacitors with high energy and power densities. In recent years, several excellent review articles have highlighted the MOFs/MOF composites and MOF-derived materials that have been used as electrodes in numerous energy-related applications [355–358]. Therefore, we will focus only on recent research progress of MOFs and their composite electrode materials for two types of energy storage device applications: (i) pristine MOFs/MOF composites as electrodes in LIBs and sodium-ion batteries (SIBs), and (ii) pristine MOFs/MOF composites in supercapacitors.

5.6.1. MOF composites for rechargeable battery electrodes

- Electrodes for Li-ion batteries (LIBs)

LIBs are widely used as energy storage devices in rechargeable batteries. During the charge/discharge process, the intercalation/deintercalation of Li ions from the anode to the cathode through the electrolyte gives rise to the storage/release of electrical energy. Although conventional LIBs have been extensively used in diverse energy-storage fields such as electric vehicles and portable electronics, their energy and power densities are lacking when it comes to large-scale electrical energy storage devices [359,360]. To enhance the electrochemical performance of LIBs for use in large-scale battery systems, the novel design and development of efficient electrode and electrolyte materials is crucial.

Graphite is widely used as an anode material in commercial LIBs, as it offers benefits such as a low working potential, low cost, and comparatively long cycling lifetime [328]. However, there are also several limitations including low theoretical capacity (372 mAh g^{-1}) and inferior Li-ion transportation rate, which make it particularly unsuitable for use in large-scale electrical energy storage devices [361]. The conventional cathode materials for LIBs, such as $LiCoO_2$, $LiFePO_4$, and other inorganic oxides with redox-active sites, also have low capacity values and poor Li-ion transfer performance [362]. Therefore, there are many benefits to developing alternative anode and cathode materials. MOF-based materials are promising candidates as their pores and channels facilitate the increase of Li-ion storage capacity, and their structural stability enhances the reversible Li insertion/desertion rate, thus enabling long-life cyclability. Moreover, MOF-based materials offer tunable functionalities such as redox-active sites, smart topologies, and conductive substrates, which leads to improved performance and Li-ions storage, thus achieving high specific capacities and cyclabilities [363,364]. Herein, we emphasize the recent examples of MOF/MOF composites developed as anode and cathode materials for LIBs.

In 2019, Guo and coworkers reported novel one-dimensional (1D) copper-based MOF nanowires (Cu-CAT NWs) that exhibited good performance as anode materials for LIBs [365]. The unique 1D structural features and bimodal pores led to a high electronic conductivity and large Li ion diffusion coefficients. Interestingly, the specific capacity of the Cu-CAT NW anode was higher than that of a commercial graphite anode material (381 vs. 373 mAh g^{-1}) at a current density of 2 A g^{-1}. Moreover, it retained 81% of its initial capacity after 500 cycles at 0.5 A g^{-1}. Full battery devices constructed with the Cu-CAT NW anode and $LiNi_{0.8}Co_{0.1}Mn_{0.1}O_2$ (NCM811) cathode achieved a high power density of 275 Wh kg^{-1}. Another copper-based MOF ($[Cu_2(BIPA\text{-}TC)(DMA)_2]_n$, denoted as Cu-MOF) showed redox-activity and excellent performance as a LIB anode material [366]. It had a high initial charge capacity of 753.7 mAh g^{-1} at 0.1 A g^{-1} and retained 53% of its initial capacity over 500 cycles. The authors linked the redox-active copper metal ions and unique structural features of Cu-MOF to this superb performance.

A novel rare earth-based MOF, $Tb_2(H_2dobdc)_3(DMF)_4$ (Tb-MOF), also had promising performance as an anode material in LIBs [367]. Its uniform carboxyl oxygens and conjugated aromatic rings acted as Li-ion insertion sites, providing an excellent specific capacity of 627.5 mAh g^{-1} at 0.1 A g^{-1}. The structural stability of Tb-MOF meant that it retained 99.1% of its initial capacity after 300 cycles at 0.8 A g^{-1}.

Although it is possible to achieve a high Li-ion insertion density in an extended π-conjugated aromatic system, the reversible insertion of Li ions from fused aromatic rings is difficult; therefore, it is challenging to develop an efficient strategy for the high and reversible insertion of Li ions in electrode materials. In this respect, Ye and coworkers proposed an electron redistribution strategy into fused C_6 rings, which was induced in Zn-PTCA for boosting the reversible Li-ion insertion performance for LIB electrodes [368]. Owing to electronic structure of Zn-PTCA, the synthesized material achieved a high reversible specific capacity of 700 mAh g^{-1} at a low current density of 0.05 A g^{-1}. In addition, Zn-PTCA retained a high capacity of 323 mAh g^{-1} at 1.0 A g^{-1} over 1100 cycles. This work presents the importance of facile and reversible Li ions insertion for the electrode materials in LIBs.

Despite the various advantages of MOFs, pristine MOFs have poor conductivity and low rate capacity, which limits their widespread application. These drawbacks have inspired the development of MOF-based composite materials to improve the conductivity while meeting the required theoretical capacities. Wang and coworkers prepared a new MOF-based composite material with CuS, CuS/Cu-BTC, which was found to be an efficient anode material for LIBs [369]. The optimized CuS(70 wt%)@Cu-BTC composite material demonstrated high conductivity and electrochemical performance with an initial discharge capacity of 1184 mAh g^{-1} at 0.1 A g^{-1}. Interestingly, the structural features and synergistic effect between the CuS nanocomposite and Cu-BTC MOF actually caused the discharge capacity to improve over 200 cycles to 1609 mAh g^{-1} at 0.1 A g^{-1}.

In addition, an Al-MOF/graphene composite (AMG) was prepared by a simple thermal treatment with vitamin C on the graphene oxide and Al-MOF composite material (Fig. 44a) [370]. The resulting AMG composite was used as an anode material in LIBs and showed a significantly higher discharge capacity than pristine Al-MOF (400 vs. 60 mAh g^{-1}) at 0.1 A g^{-1}. The authors suggested that structural disordering during the charge/discharge process opened more channels within the MOF, which improved the Li-ion diffusion and storage capacity. This work presents the first example of an MOF-based material (AMG) displaying increased trend in capacity below current densities of 1 A g^{-1} as 484 and 284 mAh g^{-1} at 0.5, 0.8 A g^{-1}, respectively, after 1000 cycles.

MOFs have also been employed as cathode materials for LIBs. In fact, there has been considerable research focus on the development of MOF-based cathode materials in recent years. Inspired by the inorganic salt $LiCoO_2$, two ternary Li-Co–MOF composites were synthesized and employed as cathodes in LIBs [371]. The two Li-Co–MOF composite materials (SNNU-73 and SNNU-76) were examined by SCXRD and XPS, and found to have different chemical and structural features; SNNU-73 comprised a helical chain structure with equal sharing of Li/Co sites, whereas SNNU-76 possessed a cage-type structure with a difference in the Li/Co occupied sites. Electrochemical measurements revealed that SNNU-73 had a higher discharge capacity than SNNU-76 (155.6 vs. 87.9 mAh g^{-1}) at 0.05 A g^{-1}. However, owing to the stability of its cage-based structure, SNNU-76 showed high cycling stability than SNNU-73.

A novel two-dimensional (2D) copper–benzoquinoid MOF (Cu-THQ) was also prepared for the cathode material of LIBs, which showed excellent electrochemical performance [372]. Electrochemical studies revealed that Cu-THQ had a high reversible specific capacity of 387 mAh g^{-1} at a current density of 0.05 A g^{-1}, a high power density of 775 Wh kg^{-1}, and efficient cycling stability, with 85% retained capacity (340 mAh g^{-1}) after 100 cycles. The exceptional performance of Cu-THQ was ascribed to the redox activity of both the copper metal ions and organic linkers. The in-depth mechanism was extensively studied by various spectroscopic experiments such as hXAS (hard X-ray absorption spectroscopy), sXAS (soft X-ray absorption spectroscopy), and FT-IR, as well as by EPR (electron paramagnetic resonance), and DFT calculations (Fig. 44b, c).

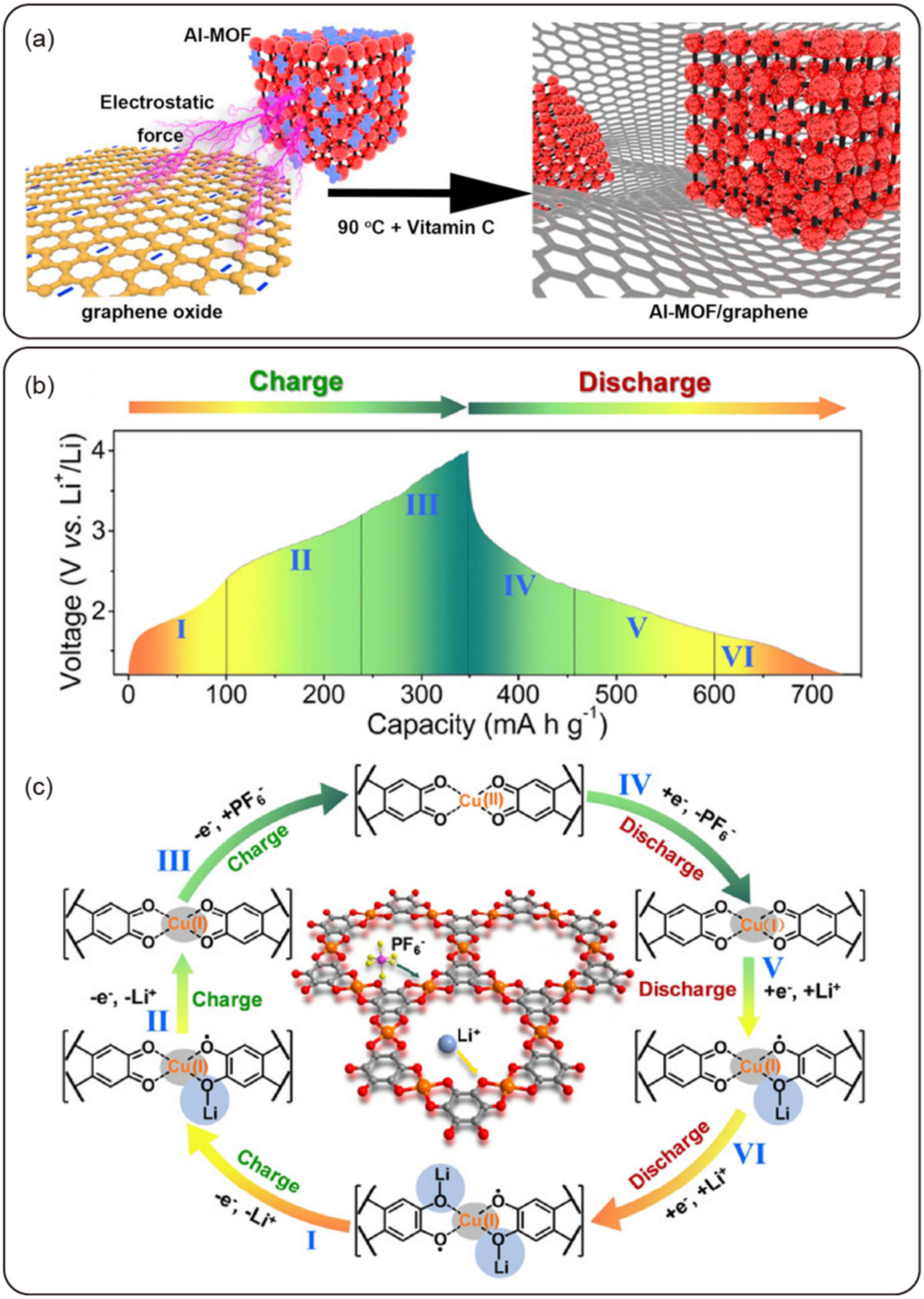

Fig. 44. (a) Preparation process of Al-MOF/graphene composite. Reproduced with permission from [370]. Copyright 2019 Elsevier Publisher. (b) Galvanostatic charge/discharge curves of 2D Cu-THQ MOF electrode at 50 mA g^{-1}. (b) The evolution of electronic states of the repeating coordination unit of 2D Cu-THQ MOF during the charge/discharge process. Reproduced with permission from [372]. Copyright 2020 John Wiley and Sons.

- Electrodes for sodium-ion batteries (SIBs)

SIBs are another class of rechargeable battery with significant importance in energy-storage devices. Sodium resources are abundant and low cost, making the development of SIBs that can compete with LIBs attractive. However, because the ionic radius and atomic mass of Na ions are larger than those of Li ions, there are several challenges for SIB development including poor diffusion kinetics, low rate capacity performance, and lower cycling stability [373]. In addition, although several transition metal oxides, sulfides, and organic salts have been used as electrodes for SIBs, they are often soluble in organic electrolytes and reduce the cycling stability, leading to efforts to develop alternative electrode materials [374]. In the last few years, MOF compounds have been developed to overcome these issues and are promising electrode candidates for practical SIB applications [375–377]. Here, we describe a few examples of MOFs used as electrode materials for SIBs.

Xu and coworkers reported two Co and Cd-based hybrid MOF composites, denoted as Co(L)/RGO and Cd(L)/RGO, for use as anode materials in SIBs [378]. Successive electrochemical studies revealed that the two MOF composites displayed exceptional capacity performance, while Co(L)/RGO achieved a higher discharge capacity than Cd(L)/RGO (646.9 vs. 163.7 mAh g^{-1}) at a current density of 1 A g^{-1}. In addition, both MOF composites possessed greater electrochemical efficiency than the pristine Co (L) and Cd(L) MOFs. Furthermore, Co(L)/RGO and Cd(L)/RGO exhibited good reversibility (coulombic efficiency of 98%) and long-life cyclability; their respective discharge capacities were 206 and 166 mAh g^{-1} at 0.5 A g^{-1} over 330 cycles.

In 2018, a new Co-based MOF a using long linear ligand (4,4′-biphenyldicarboxylic acid, denoted as bpdc) was prepared for the anode of SIBs [379]. The as-synthesized Co-bpdc MOF possessed a high specific capacity of 269 mAh g^{-1} at 20 mA g^{-1}. Moreover, electrochemical experiments revealed that the MOF had 100% columbic efficiency and retained 79% of its initial capacity (209 mAh g^{-1} at 0.1 A g^{-1}) after 1000 cycles. The authors demonstrated that the MOF compound had low solubility in the electrolyte, and its stable layered structure and relatively greater unit cell volume facilitated the insertion/desertion of Na ions. This led to its exceptional performance in SIBs.

In many cases, redox-active metal cations and organic linkers are key for developing promising electrode materials for SIBs. With this in mind, a Cu-based MOF (Cu-TCNQ) was developed for the cathode material of SIBs [380]. This MOF possessed a high discharge capacity (255 mAh g^{-1}) and even reached a high power density (>900 Wh kg^{-1}) due to the synergistic effect of the redox-active copper metal ions ($Cu^{II} \rightarrow Cu^{I}$) and two TCNQ linkers for electron transfer. In addition, Cu-TCNQ showed excellent reversibility, with a discharge capacity of 214 mAh g^{-1} over 50 cycles, and attained capacity retention of 89% after 200 cycles at 0.05 A g^{-1}. Although there are not many examples of MOF-based SIB electrodes, the presented examples demonstrate the possibility of the application. Therefore, further effort should be devoted to developing these materials for practical applications.

5.6.2. Electrodes for supercapacitors

Supercapacitors are another class of energy-storage device. They are more efficient than conventional rechargeable batteries owing to their high power densities, faster charge/discharge rates, and long cycle lives. Supercapacitors are mainly divided into two categories based on the energy-storage mechanism: (1) electrochemical double-layer capacitors (EDLCs), and (2) pseudocapacitors. In electrochemical double-layer capacitors, electrical energy is stored on the internal "surface" of the electrode through electrostatic interactions, whereas pseudocapacitors utilize fast and reversible redox reactions on the electrode surface [381]. Among the essential working components of supercapacitors, the electrode material has attracted significant attention because of its potential to enhance the supercapacitor performance. Therefore, there is a strong focus on the design and development of efficient electrode materials that meet key requirements such as high specific surface area, high conductivity, thermal stability, facile processability, corrosion resistance, and low cost. In this respect, MOFs have emerged as promising electrode materials for use in energy-storage supercapacitor applications owing to their characteristic properties. Several important review articles have already discussed MOF-derived electrodes for supercapacitors [355,382,383]. Therefore, we will focus this section on recent examples of pristine MOFs and their composites that could pave the way for the development of next-generation electrodes for practical supercapacitor applications.

Recently, Feng and coworkers reported the excellent pseudocapacitive behavior of two 2D-conductive HAB-MOFs, Ni-HAB and Cu-HAB (HAB = hexaaminobenzene), as electrode materials [384]. The prepared MOFs achieved superb gravimetric capacitances of 420 and 215 F g^{-1}, respectively. Interestingly, the Ni-HAB MOF possessed a high volumetric capacity of 760 F cm^{-3} and areal capacitance of 20 F cm^{-2}, which are higher than the recently reported values for various porous carbon electrode materials. Furthermore, the Ni-HAB MOF-based electrode displayed excellent chemical stability, with a retention capacity of 90% over 12,000 cycles at a current density of 10 A g^{-1}. Another Ni-based MOF, $Ni_3(HITP)_2$, was also employed as am electrode material in a symmetrically structured supercapacitor [385]. The MOF was fabricated by a electrophoretic deposition process and enabled the supercapacitor to reach a high areal capacitance of 15.69 mF cm^{-2} over a potential window of 0–1.0 V. Interestingly, the authors reported superb electrochemical cyclability with this MOF electrode, with a retained capacitance of 84% over 100,000 cycles. This is one of the best reported values thus far among MOF-based supercapacitor electrode materials.

Although pristine MOF-based electrodes have shown exceptional electrochemical performance in supercapacitors, composited MOFs can offer improved conductivity and electrochemical performance in comparison to their pristine counterparts. Furthermore, compositing can enhance the flexibility of the device for utilization in practical applications such as wearable electronic devices. With this in mind, two MOF composites with conductive Ni-based nanolayers grown on cellulose nanofibers (denoted as CNF@Ni-HITP and CNF@Ni-HHTP) were prepared for supercapacitor electrode applications [386]. Analysis of their electrochemical properties revealed that the asymmetric electrodes achieved a gravimetric capacitance of 125 F g^{-1} for CNF@Ni-HITP and 75 F g^{-1} for CNF@Ni-HHTP at current densities of 0.33 and 0.2 A g^{-1}, respectively. In addition, the flexibility, mechanical strength, and high conductivity of the CNF@Ni-HITP composite material meant it showed a high gravimetric capacitance of 141.5 F g^{-1} at 0.075 A g^{-1} and exceptional volumetric capacitance of up to 2800 mF cm^{-3} in a symmetrical supercapacitor device.

A similar composite of conducting polymer/MOF (PANI/ZnO@ZIF-8-CC; PANI = polyaniline) was synthesized using a "root–etch–wrap" method [387]. This unique composite material showed superb performance as an electrode in symmetric supercapacitors. The flexible MOF composite achieved an ultrahigh areal capacity of 4839 mF cm^{-2} at a current density of 5 mA cm^{-2}. Further electrochemical studies of symmetric supercapacitors revealed energy densities as high as 0.137–0.089 mWh cm^{-3} at power densities of 1.421–23.629 W cm^{-3}. Moreover, the composite demonstrated outstanding cyclability with 87% retained capacitance over 10,000 cycles. The authors demonstrated that this exceptional performance was attributed to the inevitable interactions between the ZnO and ZIF-8 substrate, abundant space of hollow core–shell structure (ZnO/ZIF-8-CC) and the synergistic effect between the ZnO/ZIF-8 and PANI conductive polymer.

5.7. Low-k dielectric MOF materials

5.7.1. Requirements for low-k dielectric MOF materials

The development of integrated circuit devices with high speeds and decreased size for microelectronic applications has attracted considerable research interest [388]. According to Moore's law, the number of transistors on integrated circuits has doubled every two years, which is promising for the development of microelectronic devices [389]. However, increasing the speed of integrated circuits while reducing the size engenders several practical issues, including resistive–capacitive (RC) delay, power dissipation, and crosstalk noise. Two major actions have been proposed to overcome these issues. (1) The low resistivity Cu can be used to replaced Al components. (2) The SiO_2 components (dielectric constant $k \approx 3.9$–4.5 depending on the deposition and processing protocol) can be replaced with low-k interlayer dielectric (ILD) materials. According to the International Technology Roadmap for Semiconductors, materials with low k values of 2.1–2.5 should be used in future electric devices [390].

Widespread research has been conducted for the development of interlayer dielectrics (ILDs) to meet the required low k values. Air or vacuum ($k = 1$), aerogels, xerogels ($k < 2$), and various porous materials have emerged as low-k ILD materials. However, the ILDs should meet the following requirements for improving the performance of electronic devices: (a) low dielectric constant, (b) electric insulation, (c) high thermal stability (>400 °C), (d) good mechanical strength, (e) good adhesive properties, and (f) ease of large-scale processability with low cost.

Recently, MOFs have been employed to develop low-k ILD materials for microelectronic device applications [391,392]. The uniform pore structure, low dielectric constant, and suitable thermal and mechanical stabilities of MOFs mean that they already meet many of the requirements for ILD materials. Although the development of MOF-based ILDs is still at the early stages, seminal work has done over the last decade. In 2010, first the dielectric constants of various MOFs were estimated using the simple Clausius–Mossotti approach [393]. Following this, the first experimental dielectric constant measurements were conducted on solution-deposited ZIF-8 films. The k value of 2.33 was already very close to the target value for future electric devices [394]. Owing to the success of these initial works, several MOFs have since been extensively studied to combat the abovementioned ILD concerns. Several excellent review articles have already highlighted the potential challenges and device integration properties of MOFs for practical microelectronic applications [391,392,395]. Therefore, in this section, we discuss recent advances in the field of MOF-based low-k dielectric materials for microelectronic devices.

5.7.2. Low-k MOF materials for microelectronic devices

In recent years, a series of fluorinated MOFs have been developed with the aim of reducing the dielectric constant k. Omary and coworkers reported several low-k materials, including fluorous MOFs ($Ag_2[Ag_4Tz_6]$ and [Cu(FBTB)(DMF)], denoted as FMOF-1 and FMOF-3, respectively) and fluorous nonporous coordination polymers ($[Ag_2(FBTB)]$, denoted as FN-PCP-1), that exhibited remarkable superhydrophilicity and high thermal stability [396]. Dielectric measurements of these materials in pellet form (pressed at 0.5 kbar) revealed low k values under ambient conditions of 2.00 (1), 2.44(3), and 2.57(3) for FMOF-1, FMOF-3, and FN-PCP-1, respectively. Interestingly, FMOF-1 showed an exceptional ultra-low k value of 1.63(1) when the pellet was pressed at 0.7 kbar (Fig. 45a). In addition, comparative studies between the fluorous MOFs and their non-fluorous analogues revealed the high efficacy of their dielectric properties as low-k materials. The authors suggested that the unusual hydrophobicity was due to the presence of $-CF_3$ groups on the ligand. The achievement of materials with ultralow k values provides a platform for the development of superior microelectronic devices.

The development of gap-filling low-k dielectrics with appropriate MOF integration strategies are highly attractive for on-chip interconnects. With this in mind, novel dielectric ZIF films were prepared by chemical vapor deposition (CVD) [ZIF-8-CVD and ZIF-67-CVD], which exhibited suitable gap-filling performance in fork–fork capacitors with low-k dielectrics (Fig. 45b, c) [397] . Metal–insulator–metal (MIM) measurements revealed low k values of 2.23 ± 0.11 and 2.39 ± 0.18 for ZIF-8 and ZIF-67 at 100 kHz, respectively. Moreover, these low k values were insensitive to heating up to 150 °C, proving the thermal stability of these dielectric films. In addition, the authors reported that the ZIF-67-CVD film had high mechanical stability with a greater Young's modulus than that of the ZIF-8-CBD film (3.79 ± 1.83 vs. 3.44 ± 1.42 GPa). In gap-filling tests, the ZIF-67-CVD film attained an effective low k value of 2.71 (Fig. 45b, c). These results are encouraging for future integration

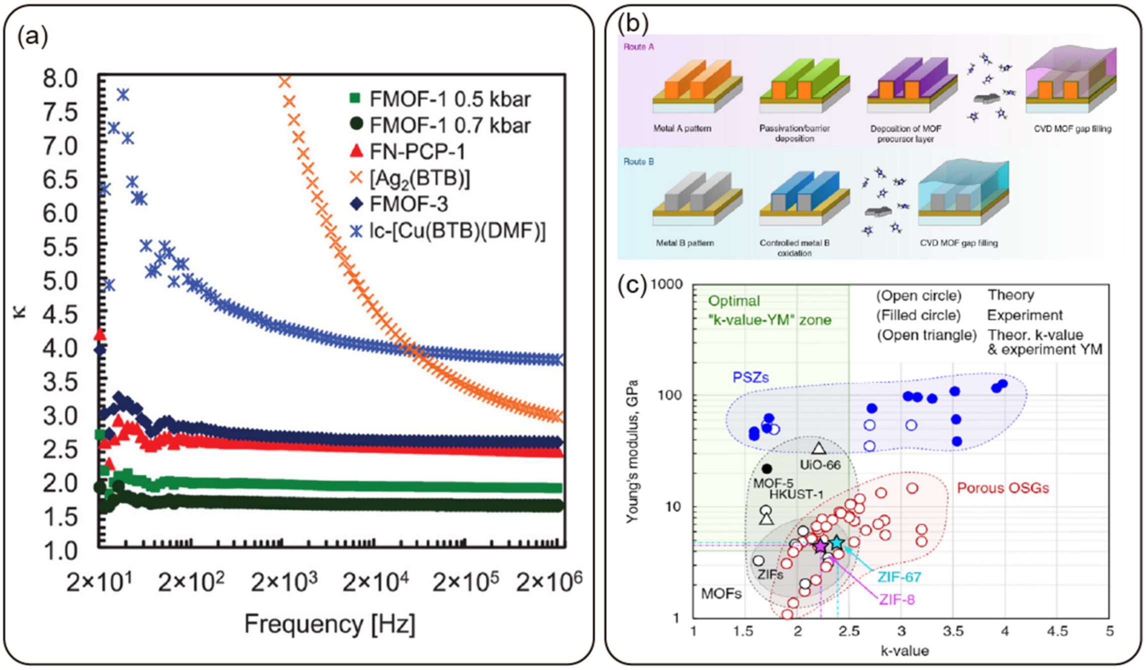

Fig. 45. (a) Variation of κ as a function of frequency at 2 V for FMOF-1, FN-PCP-1, $Ag_2(BTB)$, FMOF-3, and lc-[Cu(BTB)(DMF)]. Reproduced with permission from [396]. Copyright 2019 John Wiley and Sons. (b) Two proposed routes for the integration of ultra-low-k MOF dielectrics in on-chip interconnects via the MOF-CVD process. (c) Positioning of MOFs on the Young's modulus/k-value map in comparison with other classes of advanced low-k dielectrics. Reproduced with permission from [397]. Copyright 2019 Springer Nature.

protocols with considerable optimizations to achieve the better low-*k* gap-filling performance.

Xu et al. prepared a novel MOF, $[NH_2(CH_3)_2]_2\cdot[Zn_3(bpdc)_4]\cdot 3DMF)$ which showed two-step dielectric relaxation upon heating from 30 to 135 °C that was attributed to polarization of the surface-absorbed water molecules and guest DMF molecules, reaching a *k* value of 174.4 at 10^3 Hz, while further heating caused a loss of the dielectric peaks [398]. In contrast, the guest-free framework exhibited an ultralow *k* value of 1.80 at 100 kHz, with constant dielectric properties over wide temperature range (40–130 °C). These results demonstrate the effect of small counter ions on the *k* value, and how removing the guest molecules from the porous material can reduce *k* to ultralow values. Very recently, Zhou et al. prepared a HMS@ZIF-8/6FPBO (HMS@ZIF-8 = hollow silica@ZIF-8, 6FPBO = fluorinated polybenzoxazole) composite film via an in-situ polymerization and coating method, which showed a low *k* value of 2.12 at 1 kHz [399]. MIM studies revealed that dielectric constant was unaltered over a wide temperature range (from room temperature to 200 °C). The lower *k* value of the composite material compared to the fluorinated polybenzoxazole (6FPBO) matrix (*k* = 2.12 vs. 2.67) was related to the empty space (nanopores) in the ZIF-8 and HMS framework. In addition, the composite film possessed high thermal stability up to 480 °C and a tensile strength of 2.11 GPa with 6 wt% of HMS@ZIF-8/6FPBO, which is useful for practical applications in electric devices. The dielectric constants of recent dielectric MOFs and their composites are summarized in Table 23.

Table 23
Property summary of MOFs as a dielectric material.

MOF compound	k value	Frequency (kHz)	Ref
HMS@ZIF-8	2.12	1	[399]
FMOF-1	1.63(1)	2.0×10^3	[396]
FMOF-3	2.44(3)	2.0×10^3	[396]
FN-PCP-1	2.57(3)	2.0×10^3	[396]
lc-[Cu(BTB) (DMF)]	2.94(8)	2.0×10^3	[396]
$[Ag_2(BTB)]$	3.79(1)	2.0×10^3	[396]
$[NH_2(CH_3)_2]_2[Zn_3(bpdc)_4]$.3DMF	1.8	100	[398]
MOF-CVD ZIF-8	2.23 ± 0.11	100	[397]
MOF-CVD ZIF-67 film	2.39 ± 0.18	100	[397]
$[Co(amtd)_2]_n$	2.43	1.0×10^3	[400]
$[Mn(amtd)_2]_n$	2.57	1.0×10^3	[400]
Epoxy/ZIF-8 nanocomposite	3.2	100	[401]

5.8. Applications of luminescent MOF (LMOF) materials

5.8.1. Importance of LMOFs

Luminescence is one of the unique properties of MOFs that provides many opportunities for practical applications. The photochemical properties of luminescent MOFs (LMOFs) can be modulated by inserting metal nodes, functional ligands, and guest molecules in the pores of the MOF, which allows diverse modularity of the material. The exceptional behavior of LMOFs, including high quantum yield and long lifetime, have motivated researchers to investigate their use in a wide variety of industrial applications [402,403]. In this section, we will cover some recent examples of

Table 24
Type of analyte, detection limit and recyclability of MOF-based sensor materials.

MOF compounds	Sensing targets	LOD	Number of recycles	Ref
a. Metal ion sensors				
NH_2-MIL-125(Ti)	Pb^{2+}	0.70×10^{-2} nM	5	[405]
$[Cd(Hcip)(bpea)_{0.5}(H_2O)]_n$ (Cd-CP)	Fe^{3+}	3.24 μM	5	[406]
$[Cd(Hcip)(bpea)_{0.5}(H_2O)]_n$ (Cd-CP)	Al^{3+}	1.31 μM	5	[406]
$[Cd(Hcip)(bpea)_{0.5}(H_2O)]_n$ (Cd-CP)	Cr^{3+}	1.84 μM	5	[406]
MOF NU-902	Cd^{2+}	0.3 ppb	–	[407]
MOF NU-902 PVC membrane	Cd^{2+}	–	–	[407]
CAU-10-V-H	Pd^{2+}	110 nM	5	[408]
MIL-53(Al)–NH2-MPA	Fe^{3+}	0.36 μM	–	[416]
$[[Zn(4,4'\text{-AP})(5\text{-AIA})].(DMF)0.5]_n$	Hg^{2+}	0.01 nM	–	[409]
b. Anion sensors				
TMU-41	$Cr_2O_7^{2-}$	0.02 μM	4	[410]
TMU-41	CrO_4^{2-}	0.03 μM	4	[410]
TMU-41	MnO_4^-	0.03 μM	4	[410]
$Tb(Hmcd)(H_2O)(DMF)_2]_n$	$Cr_2O_7^{2-}$	1.32 μM	3	[411]
$Tb(Hmcd)(H_2O)(DMF)_2]_n$	CrO_4^{2-}	0.13 μM	3	[411]
$Eu(Hmcd)(H_2O)(DMF)_2]_n$	$Cr_2O_7^{2-}$	0.38 μM	3	[411]
$Eu(Hmcd)(H_2O)(DMF)_2]_n$	CrO_4^{2-}	0.02 μM	3	[411]
$(H_2bpp)\cdot[(UO_2)_2(nip)_3]\cdot H_2O$	MnO_4^-	1.79 μM	5	[417]
NU-1000-BzTz	CN^-	1.08 μM	–	[418]
$[[Cu^I_2(ttpa)_2][Cu^{II}(bptc)]. 3H_2O. DMF]_n$	$Cr_2O_7^{2-}$	0.058 μM	5	[419]
$[[Cu^I_2(ttpa)_2][Cu^{II}(bptc)]. 3H_2O. DMF]_n$	CrO_4^{2-}	0.07 μM	5	[419]
Cd-MOF	$S_2O_8^{2-}$	–	–	[412]
$[Eu_2L_3(DMF)]\cdot 2$ DMF	PO_4^{3-}	6.62 μM	–	[420]
c. Sensors for explosive compounds				
AuNCs/ZIF-8	TNT	5 nM	–	[413]
$[Tb(TCBA)(H_2O)_2]_2\cdot DMF$	TNP	1.64 ppb	5	[414]
UIO-66-Py	TNP	0.45 μM	–	[421]
Eu-MOF	TNP	0.03 mM	–	[422]
Eu-MOF	NB	0.04 mM	–	[422]
Eu-MOF	PNT	0.09 mM	–	[422]
Eu-MOF	PNP	0.08 mM	–	[422]
HNU-34	TNP	36.15 nM	5	[415]
HNU-34	2,4 DNP	42.55 nM	5	[415]
HNU-34	2,6 DNP	29.45 nM	5	[415]
TMU-18	TNP	10 μM	3	[423]
EuL	TNP	0.1 μM	5	[424]
TbL	TNP	5 μM	5	[424]

the exploitation LMOFs in sensing, explosive detection, and light-emitting diode (LED) applications.

5.8.2. Sensor applications

The luminescence of MOFs can be easily tuned by inserting guest molecules into the pores of the MOF. This can be readily adopted for sensing applications: when guest molecules are introduced into empty pores or exchanged with the present guest molecules in the pores, the fluorescence of the LMOF will change. Therefore, the LMOFs are good candidates for sensing various analytes including metal ions, anions, and organic molecules. Furthermore, the large surface area and uniform pore size of MOFs imparts high sensitivity and selectivity in sensing applications [404]. Among various potential analytes, in this section, we will cover the use of LMOFs for sensing metal ions, anions, and explosives (Table 24).

- Metal-ion sensing

High concentrations of toxic Pb^{2+} ions in aqueous systems are a risk to human health. There is therefore an urgent need to develop a suitable sensor to identify high Pb concentrations. Recently, NH_2-MIL-125(Ti) was employed as a sensing probe for the detection of Pb^{2+} ions in real water samples [405]. Among various metal ions, the developed sensor showed high selectivity toward Pb^{2+} and detected concentrations as low as 7.7 pM, which is one of the lowest detection limits ever reported. Notably, the fluorescence quenching upon addition of Pb^{2+} ions was attributed to ligand-to-cluster charge transfer of $-NH_2$ functional groups in the MOF with Pb^{2+} ions, as analyzed by FT-IR, XPS, and UPS (ultraviolet photoelectron spectroscopy). Furthermore, the NH_2-MIL-125(Ti) colloid particles dispersed well in water and were easily processible. Stamping the MOF solution onto a surface using a rubber stamp allowed the MOF to be transferred to the surface, which facilitated the preparation of paper-based Pb^{2+} sensors. The paper sensor was suitable for reversible Pb^{2+} sensing, which provides opportunities for information encryption and decryption applications (Fig. 46). However, the authors observed that the Pb^{2+} ion selectivity decreased in real water samples due to interference from other inorganic salt ions (Na, K, Ca, etc.) and organic molecules present in the water.

Other pollutant metal ions such as Al^{3+}, Cr^{3+}, and Fe^{3+} also cause public health and environmental issues. Thus, research has been conducted into the development of selective and sensitive sensor probes for their detection. A Cd-based coordination polymer ($[Cd(Hcip)(bpea)_{0.5}\cdot(H_2O)]_n$, denoted as Cd-CP) was prepared recently for sensing these metal cations [406]. The researchers analyzed the fluorescence signals at various metal ion concentrations, and found that the Cd-CP MOF shows detections limits of 1.31, 1.84, and 3.24 μM for Al^{3+}, Cr^{3+}, and Fe^{3+}, respectively. Interestingly, Al^{3+} and Cr^{3+} enhanced the luminescence of the Cd-CP sensor probe ("turn-on" effect), whereas Fe^{3+} quenched the luminescence ("turn-off" effect). Competitive experiments revealed that addition of Al^{3+} to Fe^{3+}@Cd-CP suspension showed a enhanced luminescence to greater degree rather than addition of Cr^{3+}. Cd-CP-coated test papers enabled the visual detection of metal ions under UV light. These results pave the way for practical biological and environmental applications of MOF sensors.

Among various toxic metal ions, Cd^{2+} plays a significant role in the contamination of water sources. Hibbard *et al.* adopted a water stable zirconium–porphyrin MOF (NU-902) for the detection of Cd^{2+} in drinking water, and found that it shows exceptional chemosensing efficiency [407]. For practical convenience, the authors developed a PVC-based membrane by immobilizing the NU-902 MOF powder on a PVC support. Interestingly, the NU-902 sensor could detect very low concentrations of Cd^{2+} ions (0.3 ppb), which is far below acceptable concentrations according to EPA (environmental protection agency) and WHO (world health organization) guidelines. Therefore, this sensor has practical importance for the detection of Cd^{2+} in drinking water.

The increasing use of Pd in industry and pharmaceutical applications causes severe health risks. A new aluminum-based MOF (denoted as CAU-10-V-H, where CAU stands for Christian-Albrecht University) was prepared for the detection of Pd^{2+} ions in aqueous media [408]. The sensor probe had a low limit of detection (LOD) of 110 nM Pd^{2+} ion concentrations with excellent selectivity in the presence of the other competitive metal ions. In addition, the researchers investigated the quenching mechanism and revealed that interactions between Pd^{2+} and the vinyl functional groups in the MOF formed a Pd(II)–alkene complex that quenched the fluorescence of the MOF.

Mercury ions can cause fatal poisoning. For their detection, Mandal's group developed a new Zn-based MOF, $[Zn(4,4'\text{-AP})(5\text{-AIA})]\cdot(DMF)_{0.5}$, that shows selective and sensitive detection of Hg^{2+} in aqueous media [409]. The authors reported that the MOF could detect picomolar concentrations of Hg^{2+} ions, with a LOD of 9.9×10^{-12} M. This is one of the lowest values ever reported. In addition, it had a high binding constant of $1.01 \times 10^9\ M^{-1}\ s^{-1}$. Moreover, the probe showed exceptional sensing ability in four different natural water sources, including seawater, tap water, river water, and drinking water.

- Anion sensing

Various anions such as chromates, manganates, and arsenates are extremely toxic toward living organisms. Therefore, the development of novel materials that can detect them with low LOD is required. Morsali and coworkers reported a luminescent Zn-MOF

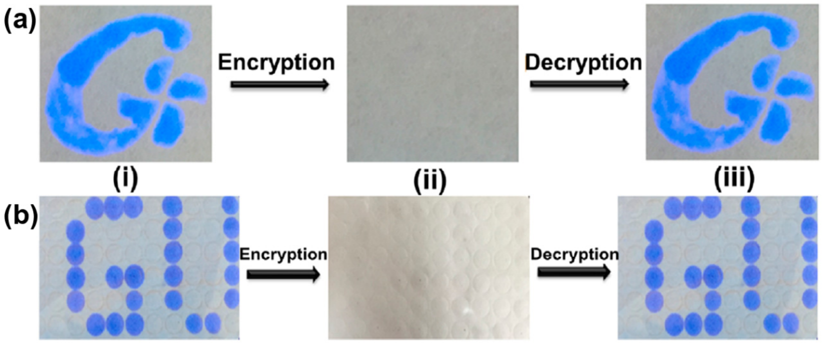

Fig. 46. Encryption using (a) a rubber stamp and (b) an ink pen and subsequent decryption of (i) pure NH_2-MIL-125(Ti), (ii) with Pb^{2+} addition, and (iii) after EDTA addition, as observed in the UV – vis region (260–360 nm). Reprinted with permission from [405]. Copyright 2020 American Chemical Society.

(denoted as TMU-41) that could detect various toxic anions including MnO_4^- and $Cr_2O_7^{2-}/CrO_4^{2-}$ in aqueous media [410]. Fluorescence studies revealed that the probe could efficiently detect MnO_4^-, $Cr_2O_7^{2-}$, and CrO_4^{2-} with concentrations of 0.03, 0.02, and 0.03 μM, respectively. In real water samples, the fluorescence probe successfully detected these anions and exhibited excellent water stability and recyclability.

Two lanthanide MOFs (Tb(Hmcd)(H_2O)($DMF)_2]_n$ and [Eu(Hmcd) (H_2O)($DMF)_2]_n$) were also prepared for the highly sensitive and selective detection of $Cr_2O_7^{2-}$ and CrO_4^{2-} [411]. The Tb- and Eu-based probes detected $Cr_2O_7^{2-}$ with LODs of 1.32 × 10^{-6} and 1.34 × 10^{-5} M, respectively, and CrO_4^{2-} with LODs of 3.88 × 10^{-5} and 2.37 × 10^{-4} M, respectively. Although the site at which fluorescence quenching occurred was not clearly analyzed, it was hypothesized that the fluorescent property of lanthanide may play a crucial role in the highly sensitive detection of these chromates.

Although several electrochemical methods have been developed for the detection of $S_2O_8^{2-}$, the luminescence sensing of $S_2O_8^{2-}$ has not been extensively studied. Recently, Zhao and coworkers reported a viologen-based Cd-MOF that exhibited excellent $S_2O_8^{2-}$ detection by enhancement of luminescence [412]. Interestingly, the MOF showed a very fast response of only 2 min. Spectroscopic analysis proved that the nitrate (NO_3^-) anions in the pores of the Cd-MOF were responsible for the selective detection of $S_2O_8^{2-}$ in aqueous media.

- Explosive sensing

The development of simple, sensitive, and efficient sensors for the analysis of toxic explosives is urgently needed to overcome the associated environmental and human health issues. In this regard, Zhao and coworkers reported an MOF composite material (AuNCs/ZIF-8) that exhibited selective detection of 2,4,6-trinitrotoluene (TNT) over other nitroaromatic explosives [413]. Time-dependent quenching studies revealed the sensor probe reached equilibration within 2 min. Moreover, concentration-dependent signal analysis demonstrated that the MOF sensor had a detection limit of 5 nM for TNT (Fig. 47). It should be noted that the quenching efficiency of the sensor for TNT, among other nitroaromatic explosives, followed the order of the electron-withdrawing ability of the analytes: TNT > 2,4,6-trinitrophenol (TNP) > 2,4-dinitrotoluene (2,4-DNT) > 4-nitrophenol (4-NP) > 1,3,5-trinitro-1,3,5-triazinane (RDX).

A lanthanide-based MOF ([Tb(TCBA)($H_2O)_2]_2$·DMF) was employed for the selective sensing of TNP, a simulant of TNT [414]. The luminescent probe exhibited excellent sensing ability, with an extremely low detection limit of 1.64 ppb. The strong quenching efficiency of the probe toward TNP was attributed to dipole–dipole interactions and π–π stacking between TNP and the π-conjugated MOF ligand. These results highlight the importance of ligand selection for aromatic explosive detection. A novel fluorescent MOF (HNU-34, HNU = Hainan University) was also prepared for the detection of various aromatic nitrophenol explosives [415]. The HNU-34 probe showed high efficiency and selectivity for the detection of nitrophenol derivatives. Sensing studies revealed that the quenching effect was higher for 2,6-DNP (2,6-dinitrophenol) than for TNP, with evaluated LODs of 29.45 and 36.15 nM, respectively. The authors proposed that the photoinduced electron transfer mechanism influenced the quenching effect of dinitro and trinitro phenols.

5.8.3. Light-emitting diodes (LEDs)

The exceptional photoluminescence behavior of LMOFs has been widely exploited in LED applications. Indeed, the photoluminescence can occur from diverse energy or charge transfer mechanisms ensuing from the structure–property relationships of MOFs [425]. Therefore, there is a key focus on effective strategies such as metal–ligand combinations and immobilizing luminescent guest molecules and multifunctional moieties into the MOF network to enhance and tune the luminescence properties. In this section, we highlight the recent developments in LMOFs for utilization in LED applications (Table 25).

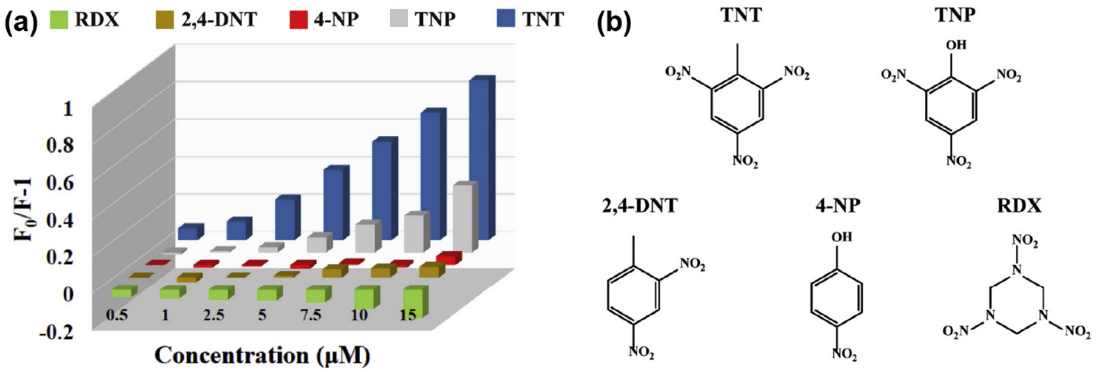

Fig. 47. Selectivity of the fluorescent sensor with AuNCs/ZIF-8. (a) Fluorescence quenching efficiency towards different concentrations of explosives. (b) Structure of the studied nitro explosives. Reproduced with permission from [413]. Copyright 2020 Elsevier Publisher.

Table 25
Emission and quantum yield of light emitting MOFs.

MOF compound	Emission wavelength (nm)	Quantum yield (%)	Emission lifetime	CIE color coordinates	Ref
LMOF-305	550	88.2	3.98 ns	–	[426]
CdTe-CP1	412, 563	18	11 ns	(0.33, 0.32)	[427]
FSDCd	585	–	218 ps	–	[429]
$TCPP_y$@UiO-66-($(NH_2)_{0.62}(diOH)_{0.3}$ (y = 0.098)	645	–	13.6 ns	(0.30, 0.30)	[430]
R6G@ZIF-8^2	553	63.1	–	–	[428]
DBNT@UiO-66	~ 538	22.7	–	–	[428]
CDs/Zr-MOF	450, 550	37	7 ns	(0.31, 0.34)	[431]

The development of rare-earth-free yellow phosphors has enormous advantages for white LED applications. In this context, Li's group prepared lanthanide-free MOFs for yellow LEDs [426]. To achieve yellow light emission, a highly conjugated organic ligand was prepared and reacted with Zn ions for MOF synthesis, resulting in the formation of an LMOF denoted as LMOF-305. Although LMOF-305 originated from the reported LMOF-231, improved photoluminescence quantum yield was obtained owing to the inclusion of the fluorinated ligand (H_4tcbpe-F) into the MOF network. Through spectroscopic measurements and DFT calculations, the authors predicted the structure of the organic ligand before the synthesis of LMOF-305 for yellow light emission. The LED performance test revealed that LMOF-305 emitted yellow light at 550 nm with 88.2% quantum yield. The luminescence lifetime was 3.98 ns with 450 nm excitation. It should be noted that the high quantum yield of was attributed to the 20% increase in blue light absorption owing to the inclusion of guest linker in LMOF-305.

The incorporation of light-emitting NPs into the pores of an MOF network has also been used for the preparation of a white LEDs. Light-emitting CdTe quantum dots were prepared and immobilized in/on a Cd-based MOF network, CP1 [427]. Photoluminescence measurements showed that the CdTe quantum dot-functionalized CP1 (CdTe-CP1) showed two emission peaks at 412 and 563 nm with 330 nm excitation (Fig. 48a, b), which clearly indicates the white-light emission with CIE index (CIE = Commission international ed'Eclairage) of (0.33, 0.32). The intense white-light emission of CdTe-CP1 was attributed to charge-transfer phenomenon, as confirmed by quantum yield calculations and lifetime decay studies.

Fluorescent dye-doped MOFs have attracted great attention for white LED (WLED) applications. Li's group reported two novel dye-encapsulated MOF composites prepared by the in-situ incorporation of yellow phosphor dyes, rhodamine 6G (R6G), and 4,9-dibromonaphtho[2,3-c][1,2,5]thiadiazole (DBNT), into ZIF-8 and UiO-66 MOFs [428]. These LMOFs exhibited white-light emission upon excitation by blue light (Fig. 48c). To combat luminescence interference of the nanocomposites from the surface of the R6G guest molecules, R6G@ZIF-8 was covered with an additional shell of ZIF-8 (denoted as R6G@ZIF-8^2). Under blue light excitation at 450 nm, R6G@ZIF-8^2 emitted a bright yellow light and possessed a high internal quantum yield of 63.1%. However, the DBNT@UiO-66 nanocomposite exhibited white light emission with a poor quantum yield of 22.7% under similar excitation wavelengths. The coated R6G@ZIF-8^2 composite therefore has practical use in white-LED applications for commercial blue light bulbs (450 nm) (Fig. 48d).

Similarly, Maity et al. developed three MOF composites with encapsulated fluorescein dye (FSD): $[Co_2(FSD)_2(H_2O)_4]\cdot H_2O\cdot MeOH$, $[Mn_2(FSD)_2(H_2O)_4]\cdot H_2O\cdot MeOH$, and $[Cd_2(FSD)_2(H_2O)_3(MeOH)]\cdot 2(H_2O)$, denoted as FSDCo, FSDMn, and FSDCd, respectively [429]. The prepared MOF composites showed multi-color light emissions under unpolarized and polarized light. Under unpolarized light, FSDCo and FSDMn exhibited a shiny green color, while FSDCd possessed a dark brownish color. Upon irradiation with polarized light, FSDCo and FSDMn showed multi-colors of green, blue, and brown, while FSDCd strictly emitted green and brown colors. The exhibition of multi-colors was attributed to the low optical bandgaps of 1.8 and 1.83 eV for FSDCo and FSDMn, respectively, while FSDCd had a notably higher optical bandgap of 2.11 eV. In addition, the researchers investigated the light-emitting properties by confocal microscopy, and found that FSDCd responded with rare tricolor (blue, green, and red) light emissions, whereas FSDCo and FSDMn exhibited dual color emissions (blue and green) under various laser

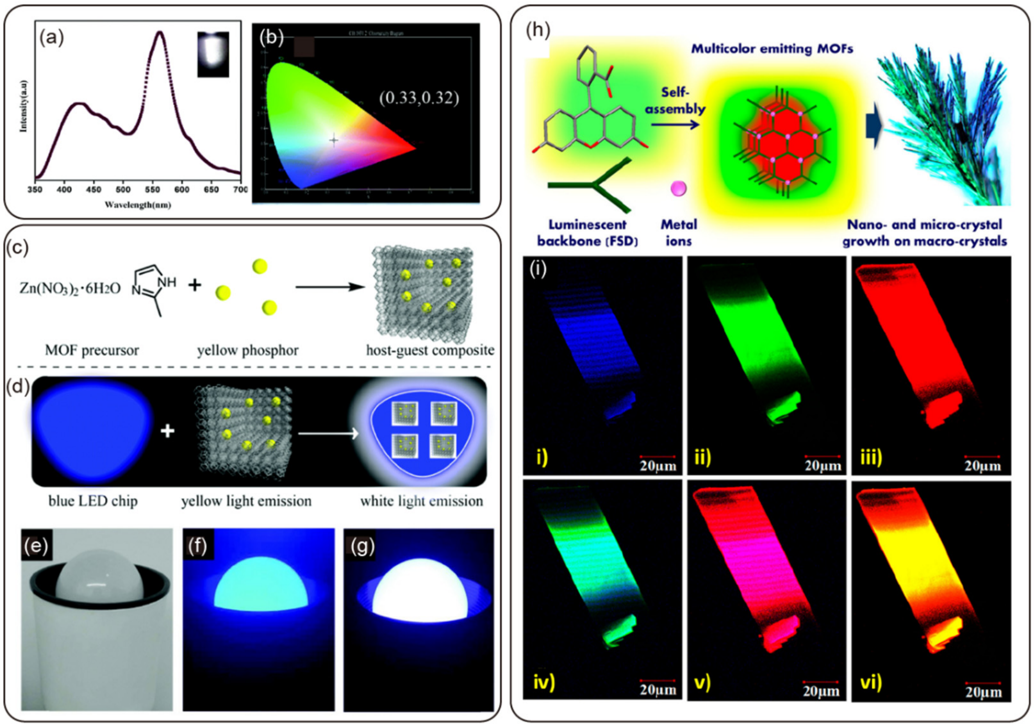

Fig. 48. (a) Photoluminescence spectrum of CdTe@CP1 at excitation wavelength of 330 nm and (inset) the photograph of white light emission after illumination. (b) CIE index diagram. Reproduced with permission from [427]. Copyright 2020 Royal Chemical Society. (c) Scheme for synthesis of MOF and yellow phosphor based host–guest composites. (d) The generation of white light from a blue light source and a blue-excitable yellow phosphor. (e) Photographs of blue light LED lamp (450 nm) is turned (e)off and (f) on; and the (g) LED lamp coated with R6G@ZIF-8^2 when turned on. Reproduced with permission from [428]. Copyright 2019 Royal Chemical Society. (h) Illustration of self-assembly of luminescent dye fluorescein and metal ions into functional MOFs. (i) Confocal microscopic images and merged images of the single crystals of FSDCd at different excitation wavelengths. Reprinted with permission from [429]. Copyright 2019 American Chemical Society.

excitation wavelengths (Fig. 48h, i). Interestingly, the authors reported pleochroism and reversible piezochromism in the dye-encapsulated MOFs, which was previously unprecedented for MOF-based LED chromophores.

6. Conclusions and outlook

During the last a couple of decades, most of the research effort has been devoted to the development of new MOFs and the demonstration of unique properties such as gas sorption/separation, catalysis, transport, and light-emitting, for practical applications. Based on the fundamental research, interest in MOFs has moved beyond purely academic to engineering processes and new applications, which open new opportunities in various industries. It is a good time to review the latest advances in MOF researches for the developments in engineering processes and future applications. In this review, we surveyed the criteria for commercial use, the engineering process for mass production and post-process, and future application areas of the MOFs along with representative examples of recent studies. In particular, principle requirements, including stability, producibility, regulation, and production cost of the MOFs are reviewed. Engineering processes for the mass production of MOFs are reviewed in processes of synthesis, product recovery, solvent exchange, and drying. Each process are separately discussed as the manufacturing process can be composed depends on the on-site situation and demands. We also explored the post-processing of MOFs, including shaping and dispersion processes, making MOFs used in large-scale applications.

We then turn to the recent developments in upcoming applications of MOFs. We describe their use as adsorbent materials for air purification devices, with a particular focus on removal of particulate matter, toxic gases, volatile organic compounds, and chemical warfare agents. Following this, we discuss their use as adsorbents for the removal of biological toxicants. Several porous adsorbents have been investigated for the removal of uremic toxins in artificial kidney applications, yet crystalline and porous MOFs are expected to play a vital role in addressing the unresolved problems with other porous materials for this application. The porous structure of MOFs has led to their use as efficient antibacterial agents for various biomedical applications, with often exceptional antibacterial behavior. We discuss the different methods of imparting antibacterial functionality to MOFs, as well as the mechanisms by which their antibacterial activity occurs. Several important works that present various MOF-based compounds for bactericidal applications are discussed, along with their possible working mechanisms. Another key research area for MOFs is their use in solid-state electrolytes in energy storage and conversion applications, as well as electrode materials for energy storage applications. We cover some of the most recent research into proton- and ion-conducting MOFs for fuel cell and battery solid-state electrolyte applications. Following this, we describe the developments in MOF-based materials for anode and cathode materials in rechargeable batteries (Li- and Na-ion batteries) and supercapacitors. Recently, MOFs have been employed to develop interlayer dielectric materials with low dielectric constants (k) for microelectronic device applications. Low-k dielectric materials are necessary to overcome issues with the miniaturization of integrated circuits with higher speeds. We describe many of the recently designed MOF-based materials with ultralow k values, which provide a platform for the development of superior microelectronic devices. Finally, we describe the luminescent behavior of MOFs and utilization of luminescent MOFs for sensing and light-emitting diode applications. The luminescence of MOFs can be easily tuned by inserting guest molecules into the pores of the MOF, which can be readily adopted for sensing applications and has been widely exploited in LED applications.

With remarkable industrial interest, commercialization and industrialization of MOFs are emerging in various areas. Although many challenges and opportunities are still remaining, the manufacturing process would eventually be developed, and low-cost production can be achieved by economies of scale. The commercialization of MOFs would also be arisen in upcoming applications that are not currently well known in MOF field. We believe that the MOFs should be commercialized in the new area with relatively small quantity during the development of their processes engineering to the larger scale and lower production cost. Therefore, more efforts from academia, and various startup and global companies should be devoted to develop the production and engineering process, and game-changing applications of MOFs that can create added value for a better future.

Declaration of Competing Interest

The authors declare that they have no known competing financial interests or personal relationships that could have appeared to influence the work reported in this paper.

Acknowledgements

This work was supported by the Basic Science Research Program (NRF-2019R1A2C4069764, NRF-2019H1D3A1A01102895 and NRF-2020R1A4A3079200) funded by the Korea Government (MSIT) through the National Research Foundation of Korea (NRF).

References

[1] X. Li, S. Zheng, L. Jin, Y. Li, P. Geng, H. Xue, H. Pang, Q. Xu, Metal-Organic Framework-Derived Carbons for Battery Applications, Adv. Energy Mater. 8 (23) (2018) 1800716.

[2] A.G. Márquez, T. Hidalgo, H. Lana, D. Cunha, M.J. Blanco-Prieto, C. Álvarez-Lorenzo, C. Boissière, C. Sánchez, C. Serre, P. Horcajada, Biocompatible polymer–metal–organic framework composite patches for cutaneous administration of cosmetic molecules, J. Mater. Chem. B 4 (43) (2016) 7031–7040, https://doi.org/10.1039/c6tb01652a.

[3] H. Li, L. Li, R.-B. Lin, W. Zhou, Z. Zhang, S. Xiang, B. Chen, Porous metal-organic frameworks for gas storage and separation: Status and challenges, EnergyChem 1 (1) (2019) 100006, https://doi.org/10.1016/j.enchem.2019.100006.

[4] X. Li, X. Yang, H. Xue, H. Pang, Q. Xu, Metal–organic frameworks as a platform for clean energy applications, EnergyChem 2 (2) (2020) 100027, https://doi.org/10.1016/j.enchem.2020.100027.

[5] S. Zheng, Q. Li, H. Xue, H. Pang, Q. Xu, A highly alkaline-stable metal oxide@metal–organic framework composite for high-performance electrochemical energy storage, Natl. Sci. Rev. 7 (2020) 305–314, https://doi.org/10.1093/nsr/nwz137.

[6] M. Du, Q. Li, Y. Zhao, C.-S. Liu, H. Pang, A review of electrochemical energy storage behaviors based on pristine metal–organic frameworks and their composites, Coord. Chem. Rev. 416 (2020) 213341, https://doi.org/10.1016/j.ccr.2020.213341.

[7] X. Li, J. Wei, Q. Li, S. Zheng, Y. Xu, P. Du, C. Chen, J. Zhao, H. Xue, Q. Xu, H. Pang, Nitrogen-Doped Cobalt Oxide Nanostructures Derived from Cobalt-Alanine Complexes for High-Performance Oxygen Evolution Reactions, Adv. Funct. Mater. 28 (23) (2018) 1800886, https://doi.org/10.1002/adfm.v28.2310.1002/adfm.201800886.

[8] Z. Liang, R. Zhao, T. Qiu, R. Zou, Q. Xu, Metal-organic framework-derived materials for electrochemical energy applications, EnergyChem 1 (1) (2019) 100001, https://doi.org/10.1016/j.enchem.2019.100001.

[9] S. Yuan, L. Feng, K. Wang, J. Pang, M. Bosch, C. Lollar, Y. Sun, J. Qin, X. Yang, P. Zhang, Q.i. Wang, L. Zou, Y. Zhang, L. Zhang, Y.u. Fang, J. Li, H.-C. Zhou, Stable Metal-Organic Frameworks: Design, Synthesis, and Applications, Adv. Mater. 30 (37) (2018) 1704303, https://doi.org/10.1002/adma.201704303.

[10] Q.i. Wang, D. Astruc, State of the Art and Prospects in Metal–Organic Framework (MOF)-Based and MOF-Derived Nanocatalysis, Chem. Rev. 120 (2) (2020) 1438–1511, https://doi.org/10.1021/acs.chemrev.9b00223.

[11] N. Stock, S. Biswas, Synthesis of Metal-Organic Frameworks (MOFs): Routes to Various MOF Topologies, Morphologies, and Composites, Chem. Rev. 112 (2) (2012) 933–969, https://doi.org/10.1021/cr200304e.

[12] U. Ryu, H.S. Lee, K.S. Park, K.M. Choi, The rules and roles of metal–organic framework in combination with molecular dyes, Polyhedron 154 (2018) 275–294, https://doi.org/10.1016/j.poly.2018.07.043.

[13] S.K. Bhardwaj, N. Bhardwaj, R. Kaur, J. Mehta, A.L. Sharma, K.-H. Kim, A. Deep, An overview of different strategies to introduce conductivity in metal–

organic frameworks and miscellaneous applications thereof, J. Mater. Chem. A 6 (31) (2018) 14992–15009, https://doi.org/10.1039/c8ta04220a.

[14] C. Chen, Q. Jiang, H. Xu, Z. Lin, Highly Efficient Synthesis of a Moisture-Stable Nitrogen-Abundant Metal–Organic Framework (MOF) for Large-Scale CO_2 Capture, Ind. Eng. Chem. Res. 58 (4) (2019) 1773–1777.

[15] C. Wang, X. Liu, N. Keser Demir, J.P. Chen, K. Li, Applications of water stable metal–organic frameworks, Chem. Soc. Rev. 45 (18) (2016) 5107–5134.

[16] D. Song, J. Bae, H. Ji, M.-B. Kim, Y.-S. Bae, K.S. Park, D. Moon, N.C. Jeong, Coordinative Reduction of Metal Nodes Enhances the Hydrolytic Stability of a Paddlewheel Metal–Organic Framework, J. Am. Chem. Soc. 141 (19) (2019) 7853–7864.

[17] L. Liang, C. Liu, F. Jiang, Q. Chen, L. Zhang, H. Xue, H.-L. Jiang, J. Qian, D. Yuan, M. Hong, Carbon dioxide capture and conversion by an acid-base resistant metal-organic framework, Nat. Commun. 8 (1) (2017), https://doi.org/10.1038/s41467-017-01166-3.

[18] X.u. Chen, Y. Peng, X. Han, Y. Liu, X. Lin, Y. Cui, Sixteen isostructural phosphonate metal-organic frameworks with controlled Lewis acidity and chemical stability for asymmetric catalysis, Nat. Commun. 8 (1) (2017), https://doi.org/10.1038/s41467-017-02335-0.

[19] M. Schubert, U. Mueller, M. Hesse, U. Diehlmann; BASF SE, Process for preparing porous metal-organic framework materials, US Patent US8115024B2, 2007 Feb 5.

[20] J. Burckhart, S. Marx, L. Arnold, C. Hofmann, U. Müller; BASF SE, Ultrafast high space-time-yield synthesis of metal-organic frameworks, US Patent US20180333696A1, 2016 Nov 23.

[21] M. R. Martinez, M. R. Hill, M. Batten, K. S. Lim, A. Polyzost, T. R. Barton, T. D. Hadley, A. A. Monch; Commonwealth Scientific and Industrial Research Organization, Production of metal-organic frameworks, US Patent US 9630163B2, 2015 May 27.

[22] U.-H. LEE, J.-S. Chang, Y. K. Hwang, Y. -K. Seo, C. Serre, P. H. Cortes, H. Chevreau, F. Ragon, T. Devic; Korea Research Institute of Chemical Technology, Method for preparing porous organic-inorganic hybrid materials, US Patent US 9175025B2, 2012 Jun 1.

[23] H. Li, M. Eddaoudi, M. O'Keeffe, O.M. Yaghi, Design and synthesis of an exceptionally stable and highly porous metal-organic framework, Nature 402 (6759) (1999) 276–279.

[24] O.K. Farha, I. Eryazici, N.C. Jeong, B.G. Hauser, C.E. Wilmer, A.A. Sarjeant, R.Q. Snurr, S.T. Nguyen, A.Ö. Yazaydın, J.T. Hupp, Metal–Organic Framework Materials with Ultrahigh Surface Areas: Is the Sky the Limit?, J. Am. Chem. Soc. 134 (36) (2012) 15016–15021.

[25] J. Yang, A. Grzech, F.M. Mulder, T.J. Dingemans, Methyl modified MOF-5: a water stable hydrogen storage material, Chem. Commun. 47 (18) (2011) 5244, https://doi.org/10.1039/c1cc11054c.

[26] G. Mouchaham, S. Wang, C. Serre, The Stability of Metal-Organic Frameworks, in: G. Mouchaham, S. Wang, C. Serre (Eds.), Metal-Organic Frameworks: Applications in Separations and Catalysis, Wiley-VCH Verlag GmbH & Co, Germany, KGaA, Weinheim, 2018, pp. 1–28.

[27] J.J. Low, A.I. Benin, P. Jakubczak, J.F. Abrahamian, S.A. Faheem, R.R. Willis, Virtual High Throughput Screening Confirmed Experimentally: Porous Coordination Polymer Hydration, J. Am. Chem. Soc. 131 (43) (2009) 15834–15842.

[28] P.Z. Moghadam, A. Li, S.B. Wiggin, A. Tao, A.G.P. Maloney, P.A. Wood, S.C. Ward, D. Fairen-Jimenez, Development of a Cambridge Structural Database Subset: A Collection of Metal–Organic Frameworks for Past, Present, and Future, Chem. Mater. 29 (7) (2017) 2618–2625.

[29] C. Férey, C. Mellot-Draznieks, C. Serre, F. Millange, J. Dutour, S. Surblé, I. Margiolaki, Chemistry: A chromium terephthalate-based solid with unusually large pore volumes and surface area, Science. 309 (2005) 2040–2042, https://doi.org/10.1126/science.1116275.

[30] M.A. Simon, E. Anggraeni, F.E. Soetaredjo, S.P. Santoso, W. Irawaty, T.C. Thanh, S.B. Hartono, M. Yuliana, S. Ismadji, Hydrothermal Synthesize of HF-Free MIL-100(Fe) for Isoniazid-Drug Delivery, Sci. Rep. 9 (1) (2019), https://doi.org/10.1038/s41598-019-53436-3.

[31] C.-G. Lin, W. Zhou, X.-T. Xiong, W. Xuan, P.J. Kitson, D.-L. Long, W. Chen, Y.-F. Song, L. Cronin, Digital Control of Multistep Hydrothermal Synthesis by Using 3D Printed Reactionware for the Synthesis of Metal–Organic Frameworks, Angew. Chem. Int. Ed. 57 (51) (2018) 16716–16720.

[32] N. Trukhan, U. Müller; BASF SE, Process for preparing porous metal-organic framework composed of zinc methylimidazolate, EU Patent EP2729452B1,2012 Jul 03.

[33] Commission regulation(EU) 2018/1513 of 10 October 2018 amending Annex XVII to regulation (EC) NO 1907/2006 of the European Parliament and of the Council concerning the Registration, Evaluation, Authorisation and Restriction of Chemicals (REACH) as a regards certain substances classified as carcinogenic, mutagenic or toxic for reproduction (CMR) category 1A or 1B.

[34] P.W. Dunne, E. Lester, R.I. Walton, Towards scalable and controlled synthesis of metal–organic framework materials using continuous flow reactors, React. Chem. Eng. 1 (4) (2016) 352–360.

[35] M. Rubio-Martinez, C. Avci-Camur, A.W. Thornton, I. Imaz, D. Maspoch, M.R. Hill, New synthetic routes towards MOF production at scale, Chem. Soc. Rev. 46 (11) (2017) 3453–3480.

[36] P.A. Julien, C. Mottillo, T. Friščić, Metal–organic frameworks meet scalable and sustainable synthesis, Green Chem. 19 (12) (2017) 2729–2747.

[37] J. Ren, X. Dyosiba, N.M. Musyoka, H.W. Langmi, M. Mathe, S. Liao, Review on the current practices and efforts towards pilot-scale production of metal-organic frameworks (MOFs), Coord. Chem. Rev. 352 (2017) 187–219.

[38] T. Johnson, M.M. Łozińska, A.F. Orsi, P.A. Wright, S. Hindocha, S. Poulston, Improvements to the production of ZIF-94; a case study in MOF scale-up, Green Chem. 21 (20) (2019) 5665–5670.

[39] B. Yilmaz, N. Trukhan, U. Müller, Industrial Outlook on Zeolites and Metal Organic Frameworks, Chinese J. Catal. 33 (1) (2012) 3–10.

[40] D. DeSantis, J.A. Mason, B.D. James, C. Houchins, J.R. Long, M. Veenstra, Techno-economic Analysis of Metal–Organic Frameworks for Hydrogen and Natural Gas Storage, Energ. Fuels 31 (2) (2017) 2024–2032.

[41] D.J. Tranchemontagne, J.R. Hunt, O.M. Yaghi, Room temperature synthesis of metal-organic frameworks: MOF-5, MOF-74, MOF-177, MOF-199, and IRMOF-0, Tetrahedron 64 (36) (2008) 8553–8557.

[42] S. Cadot, L. Veyre, D. Luneau, D. Farrusseng, E. Alessandra Quadrelli, A water-based and high space-time yield synthetic route to MOF Ni_2(dhtp) and its linker 2,5-dihydroxyterephthalic acid, J. Mater. Chem. A. 2 (2014) 17757–17763, https://doi.org/10.1039/c4tă6d.

[43] J.E. Bachman, M.T. Kapelewski, D.A. Reed, M.I. Gonzalez, J.R. Long, M_2(*m* -dobdc) (M = Mn, Fe, Co, Ni) Metal–Organic Frameworks as Highly Selective, High-Capacity Adsorbents for Olefin/Paraffin Separations, J. Am. Chem. Soc. 139 (43) (2017) 15363–15370.

[44] S. Kim, Y. Lee, S. Hong, M. Jang, W. Ahn, Pilot-scale synthesis of a zirconium-benzenedicarboxylate UiO-66 for CO_2 adsorption and catalysis, Catal. Today 245 (1) (2015) 54–60.

[45] A. Pichon, A. Lazuen-Garay, S.L. James, Solvent-free synthesis of a microporous metal–organic framework, CrystEngComm 8 (3) (2006) 211, https://doi.org/10.1039/b513750k.

[46] P. Zhang, S. Dai, Mechanochemical synthesis of porous organic materials, J. Mater. Chem. A 5 (31) (2017) 16118–16127.

[47] E. Troschke, S. Grätz, T. Lübken, L. Borchardt, Mechanochemical Friedel-Crafts Alkylation-A Sustainable Pathway Towards Porous Organic Polymers, Angew. Chem. Int. Ed. 56 (24) (2017) 6859–6863.

[48] K. Preet, G. Gupta, M. Kotal, S.K. Kansal, D.B. Salunke, H.K. Sharma, S. Chandra Sahoo, P. Van Der Voort, S. Roy, Mechanochemical Synthesis of a New Triptycene-Based Imine-Linked Covalent Organic Polymer for Degradation of Organic Dye, Cryst. Growth Des. 19 (5) (2019) 2525–2530.

[49] D. Lv, Y. Chen, Y. Li, R. Shi, H. Wu, X. Sun, J. Xiao, H. Xi, Q. Xia, Z. Li, Efficient Mechanochemical Synthesis of MOF-5 for Linear Alkanes Adsorption, J. Chem. Eng. Data 62 (7) (2017) 2030–2036.

[50] Z. Akimbekov, A.D. Katsenis, G.P. Nagabhushana, G. Ayoub, M. Arhangelskis, A.J. Morris, T. Friščić, A. Navrotsky, Experimental and Theoretical Evaluation of the Stability of True MOF Polymorphs Explains Their Mechanochemical Interconversions, J. Am. Chem. Soc. 139 (23) (2017) 7952–7957.

[51] A.K. Chaudhari, J.-C. Tan, Mechanochromic MOF nanoplates: spatial molecular isolation of light-emitting guests in a sodalite framework structure, Nanoscale 10 (8) (2018) 3953–3960.

[52] M. Samal, J. Panda, B.P. Biswal, R. Sahu, Kitchen grinder: a tool for the synthesis of metal–organic frameworks towards size selective dye adsorption, CrystEngComm 20 (18) (2018) 2486–2490.

[53] J. Spekreijse, L. Öhrström, J.P.M. Sanders, J.H. Bitter, E.L. Scott, Mechanochemical Immobilisation of Metathesis Catalysts in a Metal-Organic Framework, Chem. Eur. J. 22 (43) (2016) 15437–15443.

[54] MOF Technologiestm, https://www.moftechnologies.com/, 2020 (accessed June 12, 2020).

[55] N.L. Rosi, J. Eckert, M. Eddaoudi, D.T. Vodak, J. Kim, M. O'Keeffe, O.M. Yaghi, Hydrogen Storage in Microporous Metal-Organic Frameworks, Science 300 (2003) 1127–1129, https://doi.org/10.1126/science.1083440.

[56] Y. Li, R.T. Yang, Hydrogen Storage in Metal−Organic Frameworks by Bridged Hydrogen Spillover, J. Am. Chem. Soc. 128 (25) (2006) 8136–8137.

[57] J.L.C. Rowsell, A.R. Millward, K.S. Park, O.M. Yaghi, Hydrogen Sorption in Functionalized Metal−Organic Frameworks, J. Am. Chem. Soc. 126 (18) (2004) 5666–5667.

[58] D.J. Tranchemontagne, K.S. Park, H. Furukawa, J. Eckert, C.B. Knobler, O.M. Yaghi, Hydrogen Storage in New Metal–Organic Frameworks, J. Phys. Chem. C 116 (24) (2012) 13143–13151.

[59] J. Goldsmith, A.G. Wong-Foy, M.J. Cafarella, D.J. Siegel, Theoretical Limits of Hydrogen Storage in Metal–Organic Frameworks: Opportunities and Trade-Offs, Chem. Mater. 25 (16) (2013) 3373–3382.

[60] X. Zhang, R.-B. Lin, J. Wang, B. Wang, B. Liang, T. Yildirim, J. Zhang, W. Zhou, B. Chen, Optimization of the Pore Structures of MOFs for Record High Hydrogen Volumetric Working Capacity, Adv. Mater. 32 (17) (2020) 1907995, https://doi.org/10.1002/adma.v32.1710.1002/adma.201907995.

[61] BASF to showcase metal organic frameworks (MOFs) for energy storage at NGV Americas Conference. https://www.basf.com/us/en/media/news-releases/2013/11/p-13-452.html (accessed August 03, 2020).

[62] Versum Materials and NuMat Technologies to Commercialize Next-Generation Adsorbent Technology for Delivery of Dopant Gases. https://www.businesswire.com/news/home/20170731005340/en/Versum-Materials-NuMat-Technologies-Commercialize-Next-Generation-Adsorbent (accessed August 03, 2020).

[63] J. Huo, M. Brightwell, S. El Hankari, A. Garai, D. Bradshaw, A versatile, industrially relevant, aqueous room temperature synthesis of HKUST-1 with high space-time yield, J. Mater. Chem. A 1 (48) (2013) 15220, https://doi.org/10.1039/c3ta14409g.

[64] N.A.H.M. Nordin, A.F. Ismail, A. Mustafa, P.S. Goh, D. Rana, T. Matsuura, Aqueous room temperature synthesis of zeolitic imidazole framework 8 (ZIF-8) with various concentrations of triethylamine, RSC Adv. 4 (63) (2014) 33292–33300.

[65] M. Sánchez-Sánchez, N. Getachew, K. Díaz, M. Díaz-García, Y. Chebude, I. Díaz, Synthesis of metal–organic frameworks in water at room temperature: salts as linker sources, Green Chem. 17 (3) (2015) 1500–1509.

[66] Y. Yue, Z.-A. Qiao, P.F. Fulvio, A.J. Binder, C. Tian, J. Chen, K.M. Nelson, X. Zhu, S. Dai, Template-Free Synthesis of Hierarchical Porous Metal–Organic Frameworks, J. Am. Chem. Soc. 135 (26) (2013) 9572–9575.

[67] M. Díaz-García, Á. Mayoral, I. Díaz, M. Sánchez-Sánchez, Nanoscaled M-MOF-74 Materials Prepared at Room Temperature, Cryst. Growth Des. 14 (5) (2014) 2479–2487.

[68] E. Leung, U. Müller, N. Trukhan, H. Mattenheimer, G. Cox, S. Blei; BASF SE, Process for preparing porous metal-organic frameworks based on aluminum fumarate, US Patent US20120082864A1, 2012 Apr 5.

[69] T. He, X. Xu, B. Ni, H. Wang, Y. Long, W. Hu, X. Wang, Fast and scalable synthesis of uniform zirconium-, hafnium-based metal–organic framework nanocrystals, Nanoscale 9 (48) (2017) 19209–19215.

[70] S. Yuan, J.-S. Qin, C.T. Lollar, H.-C. Zhou, Stable Metal–Organic Frameworks with Group 4 Metals: Current Status and Trends, ACS Cent. Sci. 4 (4) (2018) 440–450.

[71] H. Motegi, K. Yano, N. Setoyama, Y. Matsuoka, T. Ohmura, A. Usuki, A facile synthesis of UiO-66 systems and their hydrothermal stability, J. Porous Mater. 24 (5) (2017) 1327–1333.

[72] M. Gaab, N. Trukhan, S. Maurer, R. Gummaraju, U. Müller, The progression of Al-based metal-organic frameworks – From academic research to industrial production and applications, Micropor. Mesopor. Mater. 157 (2012) 131–136.

[73] H. Oh, S. Maurer, R. Balderas-Xicohtencatl, L. Arnold, O.V. Magdysyuk, G. Schütz, U. Müller, M. Hirscher, Efficient synthesis for large-scale production and characterization for hydrogen storage of ligand exchanged MOF-74/174/184-M (M = Mg^{2+}, Ni^{2+}), Int. J. Hydrog. Energy 42 (2017) 1027–1035, https://doi.org/10.1016/j.ijhydene.2016.08.153.

[74] D. Lenzen, P. Bendix, H. Reinsch, D. Fröhlich, H. Kummer, M. Möllers, P.P.C. Hügenell, R. Gläser, S. Henninger, N. Stock, Scalable Green Synthesis and Full-Scale Test of the Metal-Organic Framework CAU-10-H for Use in Adsorption-Driven Chillers, Adv. Mater. 30 (6) (2018) 1705869, https://doi.org/10.1002/adma.201705869.

[75] T. Zhao, F. Jeremias, I. Boldog, B. Nguyen, S.K. Henninger, C. Janiak, High-yield, fluoride-free and large-scale synthesis of MIL-101(Cr), Dalton Trans. 44 (38) (2015) 16791–16801.

[76] Y.-K. Seo, J.W. Yoon, J.S. Lee, U.-H. Lee, Y.K. Hwang, C.-H. Jun, P. Horcajada, C. Serre, J.-S. Chang, Large scale fluorine-free synthesis of hierarchically porous iron(III) trimesate MIL-100(Fe) with a zeolite MTN topology, Micropor. Mesopor. Mater. 157 (2012) 137–145.

[77] Q. Min Wang, D. Shen, M. Bülow, M. Ling Lau, S. Deng, F.R. Fitch, N.O. Lemcoff, J. Semanscin, Metallo-organic molecular sieve for gas separation and purification, Micropor. Mesopor. Mater. 55 (2) (2002) 217–230.

[78] Y.K. Hwang, J. Chang, Y. Seo, D.W. Hwang; Korea Research Institute of Chemical Technology, Porous organic-inorganic hybrid materials with crystallinity and method for preparing thereof, US Patent US008252950B2, 2012 Aug 28.

[79] J. Hafizovic, U. Olsbye, K.P. Lillerud, S. Jacobsen, N. Nathalie; Universiteteti Oslo, Metal organic framework compounds, US Patent US20120115961A1, 2012. May 10.

[80] N.A. Khan, S.H. Jhung, Synthesis of metal-organic frameworks (MOFs) with microwave or ultrasound: Rapid reaction, phase-selectivity, and size reduction, Coord. Chem. Rev. 285 (2015) 11–23.

[81] J. Klinowski, F.A. Almeida Paz, P. Silva, J. Rocha, Microwave-Assisted Synthesis of Metal–Organic Frameworks, Dalton Trans. 40 (2) (2011) 321–330.

[82] C.O. Kappe, A. Stadler, D. Dallinger, Microwaves in Organic and Medicinal Chemistry, 1st ed., Wiley-VCH Verlag GmbH & Co. KGaA, Weinheim, 2005.

[83] P. Priecel, J.A. Lopez-Sanchez, Advantages and Limitations of Microwave Reactors: From Chemical Synthesis to the Catalytic Valorization of Biobased Chemicals, ACS Sustain. Chem. Eng. 7 (1) (2019) 3–21.

[84] M. Taddei, P.V. Dau, S.M. Cohen, M. Ranocchiari, J.A. van Bokhoven, F. Costantino, S. Sabatini, R. Vivani, Efficient microwave assisted synthesis of metal–organic framework UiO-66: optimization and scale up, Dalton Trans. 44 (31) (2015) 14019–14026.

[85] N.E. Tari, A. Tadjarodi, J. Tamnanloo, S. Fatemi, Facile and fast, one pot microwave synthesis of metal organic framework copper terephthalate and study CO_2 and CH_4 adsorption on it, J. Porous Mater. 22 (5) (2015) 1161–1169.

[86] G. Blanita, G. Borodi, M.D. Lazar, A.-R. Biris, L. Barbu-Tudoran, I. Coldea, D. Lupu, Microwave assisted non-solvothermal synthesis of metal–organic frameworks, RSC Adv. 6 (31) (2016) 25967–25974.

[87] E. Haque, N. Khan, J. Park, S.H. Jhung, Synthesis of a Metal-Organic Framework Material, Iron Terephthalate, by Ultrasound, Microwave, and Conventional Electric Heating: A Kinetic Study, Chem. Eur. J. 16 (3) (2010) 1046–1052.

[88] S.H. Jhung, J.-H. Lee, J.W. Yoon, C. Serre, G. Férey, J.-S. Chang, Microwave Synthesis of Chromium Terephthalate MIL-101 and Its Benzene Sorption Ability, Adv. Mater. 19 (1) (2007) 121–124.

[89] E. Haque, N.A. Khan, C.M. Kim, S.H. Jhung, Syntheses of Metal–Organic Frameworks and Aluminophosphates under Microwave Heating: Quantitative Analysis of Accelerations, Cryst. Growth Des. 11 (10) (2011) 4413–4421.

[90] T. Chalati, P. Horcajada, R. Gref, P. Couvreur, C. Serre, Optimisation of the synthesis of MOF nanoparticles made of flexible porous iron fumarate MIL-88A, J. Mater. Chem. 21 (7) (2011) 2220–2227.

[91] J.-S. Choi, W.-J. Son, J. Kim, W.-S. Ahn, Metal–organic framework MOF-5 prepared by microwave heating: Factors to be considered, Micropor. Mesopor. Mater. 116 (1–3) (2008) 727–731.

[92] G. Blăniţă, O. Ardelean, D. Lupu, G. Borodi, M. Miheţ, M. Coroş, M. Vlassa, I. Mişan, I. Coldea, G. Popeneciu, Microwave assisted synthesis of MOF-5 at atmospheric pressure, Rev. Roum. Chim. 56 (2011) 583–588.

[93] Z. Ni, R.I. Masel, Rapid Production of Metal−Organic Frameworks via Microwave-Assisted Solvothermal Synthesis, J. Am. Chem. Soc. 128 (38) (2006) 12394–12395.

[94] X. Wu, Z. Bao, B. Yuan, J. Wang, Y. Sun, H. Luo, S. Deng, Microwave synthesis and characterization of MOF-74 (M=Ni, Mg) for gas separation, Micropor. Mesopor. Mater. 180 (2013) 114–122.

[95] Y. Liu, J. Hu, Y. Li, Y.T. Shang, J.Q. Wang, Y. Zhang, Z.L. Wang, Microwave assisted synthesis of metal-organic framework MIL-101 nanocrystals as sorbent and pseudostationary phase in capillary electrophoresis for the separation of anthraquinones in environmental water samples, Electrophoresis. 38 (2017) 2521–2529, https://doi.org/10.1002/elps.201700116.

[96] H. Xu, B.W. Zeiger, K.S. Suslick, Sonochemical synthesis of nanomaterials, Chem. Soc. Rev. 42 (7) (2013) 2555–2567.

[97] H.-Y. Cho, J. Kim, S.-N. Kim, W.-S. Ahn, High yield 1-L scale synthesis of ZIF-8 via a sonochemical route, Micropor. Mesopor. Mater. 169 (2013) 180–184.

[98] J. Gordon, H. Kazemian, S. Rohani, Rapid and efficient crystallization of MIL-53(Fe) by ultrasound and microwave irradiation, Micropor. Mesopor. Mater. 162 (2012) 36–43.

[99] A.A. Tehrani, V. Safarifard, A. Morsali, G. Bruno, H.A. Rudbari, Ultrasound-assisted synthesis of metal–organic framework nanorods of Zn-HKUST-1 and their templating effects for facile fabrication of zinc oxide nanorods via solid-state transformation, Inorg. Chem. Commun. 59 (2015) 41–45.

[100] M.Y. Masoomi, A. Morsali, P.C. Junk, Ultrasound assisted synthesis of a Zn(ii) metal-organic framework with nano-plate morphology using non-linear dicarboxylate and linear N-donor ligands, RSC Adv. 4 (2014) 47894–47898, https://doi.org/10.1039/c4ra09186h.

[101] E. Haque, S.H. Jhung, Synthesis of isostructural metal–organic frameworks, CPO-27s, with ultrasound, microwave, and conventional heating: Effect of synthesis methods and metal ions, Chem. Eng. J. 173 (3) (2011) 866–872.

[102] U. Müller, M. Schubert, F. Teich, H. Puetter, K. Schierle-Arndt, J. Pastré, Metal–organic frameworks—prospective industrial applications, J. Mater. Chem. 16 (7) (2006) 626–636.

[103] N. Campagnol, T.R.C. Van Assche, M. Li, L. Stappers, M. Dincă, J.F.M. Denayer, K. Binnemans, D.E. De Vos, J. Fransaer, On the electrochemical deposition of metal–organic frameworks, J. Mater. Chem. A 4 (10) (2016) 3914–3925.

[104] N. Campagnol, T. Van Assche, T. Boudewijns, J. Denayer, K. Binnemans, D. De Vos, J. Fransaer, High pressure, high temperature electrochemical synthesis of metal–organic frameworks: films of MIL-100 (Fe) and HKUST-1 in different morphologies, J. Mater. Chem. A 1 (19) (2013) 5827, https://doi.org/10.1039/c3ta10419b.

[105] K.-Y. Cheng, J.-C. Wang, C.-Y. Lin, W.-R. Lin, Y.-A. Chen, F.-J. Tsai, Y.-C. Chuang, G.-Y. Lin, C.-W. Ni, Y.-T. Zeng, M.-L. Ho, Electrochemical synthesis, characterization of Ir–Zn containing coordination polymer, and application in oxygen and glucose sensing, Dalton Trans. 43 (17) (2014) 6536, https://doi.org/10.1039/c3dt53504e.

[106] M. Li, M. Dincă, Reductive Electrosynthesis of Crystalline Metal–Organic Frameworks, J. Am. Chem. Soc. 133 (33) (2011) 12926–12929.

[107] A. Martinez Joaristi, J. Juan-Alcañiz, P. Serra-Crespo, F. Kapteijn, J. Gascon, Electrochemical Synthesis of Some Archetypical Zn^{2+} , Cu^{2+} , and Al^{3+} Metal Organic Frameworks, Cryst. Growth Des. 12 (7) (2012) 3489–3498.

[108] W.-J. Li, J. Lü, S.-Y. Gao, Q.-H. Li, R. Cao, Electrochemical preparation of metal–organic framework films for fast detection of nitro explosives, J. Mater. Chem. A 2 (45) (2014) 19473–19478.

[109] S.D. Worrall, H. Mann, A. Rogers, M.A. Bissett, M.P. Attfield, R.A.W. Dryfe, Electrochemical deposition of zeolitic imidazolate framework electrode coatings for supercapacitor electrodes, Electrochim. Acta 197 (2016) 228–240.

[110] M. Li, M. Dincă, On the Mechanism of MOF-5 Formation under Cathodic Bias, Chem. Mater. 27 (9) (2015) 3203–3206.

[111] M. Dinca, M. Li; Massachusetts Institute of Technology, Methods for electrochemically induced cathodic deposition of crystalline metal-organic frameworks, US Patent US008764887B2, 2014. Jul 1.

[112] M. Klimakow, P. Klobes, A.F. Thu̕nemann, K. Rademann, F. Emmerling, Mechanochemical Synthesis of Metal−Organic Frameworks: A Fast and Facile Approach toward Quantitative Yields and High Specific Surface Areas, Chem. Mater. 22 (18) (2010) 5216–5221.

[113] T. Friščić, D. Reid, I. Halasz, R. Stein, R. Dinnebier, M. Duer, Ion- and Liquid-Assisted Grinding: Improved Mechanochemical Synthesis of Metal-Organic Frameworks Reveals Salt Inclusion and Anion Templating, Angew. Chem. Int. Ed. 49 (4) (2010) 712–715.

[114] G. Zhan, H.C. Zeng, Alternative synthetic approaches for metal–organic frameworks: transformation from solid matters, Chem. Commun. 53 (1) (2017) 72–81.

[115] G. Ayoub, B. Karadeniz, A.J. Howarth, O.K. Farha, I. Đilović, L.S. Germann, R.E. Dinnebier, K. Užarević, T. Friščić, Rational Synthesis of Mixed-Metal Microporous Metal–Organic Frameworks with Controlled Composition Using Mechanochemistry, Chem. Mater. 31 (15) (2019) 5494–5501.

[116] C.V. Kumar, A. Pattammattel, Inorganic analogues of graphene: synthesis, characterization, and applications, in: C.V. Kumar, A. Pattammattel (Eds.), Introduction to Graphene, Amsterdam, Elsevier, 2017, pp. 75–101.

[117] A. Lazuen-Garay, A. Pichon, S.L. James, Solvent-free synthesis of a microporous metal–organic framework, CrystEngComm 8 (3) (2006) 211–214, https://doi.org/10.1039/b513750k.

[118] R. Zhang, C.A. Tao, R. Chen, L. Wu, X. Zou, J. Wang, 2018. Ultrafast synthesis of Ni-MOF in one minute by ball milling, Nanomaterials. 8, 1067. https://doi.org/10.3390/NANO8121067.

[119] K. Užarević, T.C. Wang, S.-Y. Moon, A.M. Fidelli, J.T. Hupp, O.K. Farha, T. Friščić, Mechanochemical and solvent-free assembly of zirconium-based metal–organic frameworks, Chem. Commun. 52 (10) (2016) 2133–2136.

[120] R.M. Myers, D.E. Fitzpatrick, R.M. Turner, S.V. Ley, Flow Chemistry Meets Advanced Functional Materials, Chem. Eur. J. 20 (39) (2014) 12348–12366.

[121] K.-J. Kim, Y.J. Li, P.B. Kreider, C.-H. Chang, N. Wannenmacher, P.K. Thallapally, H.-G. Ahn, High-rate synthesis of Cu–BTC metal–organic frameworks, Chem. Commun. 49 (98) (2013) 11518, https://doi.org/10.1039/c3cc46049e.

[122] P.A. Bayliss, I.A. Ibarra, E. Pérez, S. Yang, C.C. Tang, M. Poliakoff, M. Schröder, Synthesis of metal–organic frameworks by continuous flow, Green Chem. 16 (8) (2014) 3796–3802.

[123] M. Gimeno-Fabra, A.S. Munn, L.A. Stevens, T.C. Drage, D.M. Grant, R.J. Kashtiban, J. Sloan, E. Lester, R.I. Walton, Instant MOFs: continuous synthesis of metal–organic frameworks by rapid solvent mixing, Chem. Commun. 48 (86) (2012) 10642, https://doi.org/10.1039/c2cc34493a.

[124] A.S. Munn, P.W. Dunne, S.V.Y. Tang, E.H. Lester, Large-scale continuous hydrothermal production and activation of ZIF-8, Chem. Commun. 51 (64) (2015) 12811–12814.

[125] C.J. Tighe, R.I. Gruar, C.Y. Ma, T. Mahmud, X.Z. Wang, J.A. Darr, Investigation of counter-current mixing in a continuous hydrothermal flow reactor, J. Supercrit. Fluids 62 (2012) 165–172.

[126] C. McKinstry, R.J. Cathcart, E.J. Cussen, A.J. Fletcher, S.V. Patwardhan, J. Sefcik, Scalable continuous solvothermal synthesis of metal organic framework (MOF-5) crystals, Chem. Eng. J. 285 (2016) 718–725.

[127] M. Rubio-Martinez, M.P. Batten, A. Polyzos, K.-C. Carey, J.I. Mardel, K.-S. Lim, M.R. Hill, Versatile, High Quality and Scalable Continuous Flow Production of Metal-Organic Frameworks, Sci. Rep. 4 (1) (2015), https://doi.org/10.1038/srep05443.

[128] M. Rubio-Martinez, T.D. Hadley, M.P. Batten, K. Constanti-Carey, T. Barton, D. Marley, A. Mönch, K.-S. Lim, M.R. Hill, Scalability of Continuous Flow Production of Metal-Organic Frameworks, ChemSusChem 9 (9) (2016) 938–941.

[129] M. Taddei, D.A. Steitz, J.A. van Bokhoven, M. Ranocchiari, Continuous-Flow Microwave Synthesis of Metal-Organic Frameworks: A Highly Efficient Method for Large-Scale Production, Chem. Eur. J. 22 (10) (2016) 3245–3249.

[130] S. Tai, W. Zhang, J. Zhang, G. Luo, Y.u. Jia, M. Deng, Y. Ling, Facile preparation of UiO-66 nanoparticles with tunable sizes in a continuous flow microreactor and its application in drug delivery, Micropor. Mesopor. Mater. 220 (2016) 148–154.

[131] A. Polyzoidis, T. Altenburg, M. Schwarzer, S. Loebbecke, S. Kaskel, Continuous microreactor synthesis of ZIF-8 with high space–time-yield and tunable particle size, Chem. Eng. J. 283 (2016) 971–977.

[132] L. D'Arras, C. Sassoye, L. Rozes, C. Sanchez, J. Marrot, S. Marre, C. Aymonier, Fast and continuous processing of a new sub-micronic lanthanide-based metal–organic framework, New J. Chem. 38 (4) (2014) 1477–1483.

[133] M. Faustini, J. Kim, G.-Y. Jeong, J.Y. Kim, H.R. Moon, W.-S. Ahn, D.-P. Kim, Microfluidic Approach toward Continuous and Ultrafast Synthesis of Metal–Organic Framework Crystals and Hetero Structures in Confined Microdroplets, J. Am. Chem. Soc. 135 (39) (2013) 14619–14626.

[134] S.R. Jambovane, S.K. Nune, R.T. Kelly, B.P. McGrail, Z. Wang, M.I. Nandasiri, S. Katipamula, C. Trader, H.T. Schaef, Continuous, One-pot Synthesis and Post-Synthetic Modification of NanoMOFs Using Droplet Nanoreactors, Sci Rep 6 (1) (2016), https://doi.org/10.1038/srep36657.

[135] R. Ameloot, F. Vermoortele, W. Vanhove, M.B.J. Roeffaers, B.F. Sels, D.E. De Vos, Interfacial synthesis of hollow metal–organic framework capsules demonstrating selective permeability, Nature Chem 3 (5) (2011) 382–387.

[136] Y. Wang, L. Li, P. Dai, L. Yan, L. Cao, X. Gu, X. Zhao, Missing-node directed synthesis of hierarchical pores on a zirconium metal–organic framework with tunable porosity and enhanced surface acidity via a microdroplet flow reaction, J. Mater. Chem. A 5 (42) (2017) 22372–22379.

[137] L. Paseta, B. Seoane, D. Julve, V. Sebastián, C. Téllez, J. Coronas, Accelerating the Controlled Synthesis of Metal–Organic Frameworks by a Microfluidic Approach: A Nanoliter Continuous Reactor, ACS Appl. Mater. Interfaces 5 (19) (2013) 9405–9410.

[138] O. Kolmykov, J.-M. Commenge, H. Alem, E. Girot, K. Mozet, G. Medjahdi, R. Schneider, Microfluidic reactors for the size-controlled synthesis of ZIF-8 crystals in aqueous phase, Mater. Des. 122 (2017) 31–41.

[139] D. Crawford, J. Casaban, R. Haydon, N. Giri, T. McNally, S.L. James, Synthesis by extrusion: continuous, large-scale preparation of MOFs using little or no solvent, Chem. Sci. 6 (3) (2015) 1645–1649.

[140] S. Lloyd James, A. Lazuen-Garay, A. Pichon; The Queen's University of Belfast, Use of grinding in chemical synthesis, US Patent US008466285B2, 2013 Jun 18.

[141] S. James, T. Mcnally, R. Haydon; The Queen's University of Belfast, Process for the preparation of a metal-organic compound, US Patant US20160176070A1 2016 Jun 23.

[142] Bachiller Barcelona, Agitated Nutsche Filter Dryer for solid-liquid separation. https://bachiller.com/en/nutsche-filter-dryer/#stock, 2020 (accessed June 11, 2020).

[143] S. Tarleton, R. Wakeman, Particle Separations by Filtration and Sedimentation, in: H.G. Merkus, G.M.H. Meesters (Eds.), Production, Handling and Characterization of Particulate Materials, in, Springer, Switzerland, 2016, pp. 327–387.

[144] E.S. Tarleton, R.J. Wakeman, in: Solid/liquid separation equipment, Elsevier, Amsterdam, 2007, pp. 1–77.

[145] M. Rubio-Martinez, T. Leong, P. Juliano, T.D. Hadley, M.P. Batten, A. Polyzos, K.-S. Lim, M.R. Hill, Scalable simultaneous activation and separation of metal–organic frameworks, RSC Adv. 6 (7) (2016) 5523–5527.

[146] M.R. MARTINEZ, P. Juliano, T. LEONG, M.R. Hill, K.S. Lim; Commonwealth Scientific and Industrial Research Or ganisation, Separation of metal-organic frameworks, US Patent US20190092794A1, 2019 Mar 28.

[147] T. Leong, K. Knoerzer, F.J. Trujillo, L. Johansson, R. Manasseh, G.V. Barbosa-Cánovas, P. Juliano, Megasonic Separation of Food Droplets and Particles: Design Considerations, Food. Eng. Rev. 7 (3) (2015) 298–320.

[148] D. Feng, Z.-Y. Gu, J.-R. Li, H.-L. Jiang, Z. Wei, H.-C. Zhou, Zirconium-Metalloporphyrin PCN-222: Mesoporous Metal-Organic Frameworks with Ultrahigh Stability as Biomimetic Catalysts, Angew. Chem. Int. Ed. 51 (41) (2012) 10307–10310.

[149] J.E. Mondloch, W. Bury, D. Fairen-Jimenez, S. Kwon, E.J. DeMarco, M.H. Weston, A.A. Sarjeant, S.T. Nguyen, P.C. Stair, R.Q. Snurr, O.K. Farha, J.T. Hupp, Vapor-Phase Metalation by Atomic Layer Deposition in a Metal–Organic Framework, J. Am. Chem. Soc. 135 (28) (2013) 10294–10297.

[150] A.S. Mujumdar (Ed.), Handbook of Industrial Drying, third ed., CRC Press, Cleveland, 2006.

[151] Haichang Machinery, HCDF-VACUUM BELT CONTINUOUS DRYER FOR POWDER - Industrial Drying Equipment Manufacturer. http://www.mach-hc.com/Vacuum-Belt-Continuous-Dryer-For-Powder, 2020 (accessed June 11, 2020).

[152] İ. Dinçer, C. Zamfirescu, Drying Phenomena, John Wiley & Sons Ltd, Chichester, 2015.

[153] L. Ma, A. Jin, Z. Xie, W. Lin, Freeze drying significantly increases permanent porosity and hydrogen uptake in 4,4-connected metal-organic frameworks, Angew. Chem. Int. Ed. 48 (2009) 9905–9908, https://doi.org/10.1002/anie.200904983.

[154] M.J. Regufe, J. Tamajon, A.M. Ribeiro, A. Ferreira, U.-H. Lee, Y.K. Hwang, J.-S. Chang, C. Serre, J.M. Loureiro, A.E. Rodrigues, Syngas Purification by Porous Amino-Functionalized Titanium Terephthalate MIL-125, Energy Fuels 29 (7) (2015) 4654–4664.

[155] Y. Khabzina, J. Dhainaut, M. Ahlhelm, H.-J. Richter, H. Reinsch, N. Stock, D. Farrusseng, Synthesis and Shaping Scale-up Study of Functionalized UiO-66 MOF for Ammonia Air Purification Filters, Ind. Eng. Chem. Res. 57 (24) (2018) 8200–8208.

[156] J. Zheng, X. Cui, Q. Yang, Q. Ren, Y. Yang, H. Xing, Shaping of ultrahigh-loading MOF pellet with a strongly anti-tearing binder for gas separation and storage, Chem. Eng. J. 354 (2018) 1075–1082.

[157] J. Cousin-Saint-Remi, A.-L. Finoulst, C. Jabbour, G.V. Baron, J.F.M. Denayer, Selection of binder recipes for the formulation of MOFs into resistant pellets for molecular separations by fixed-bed adsorption, Micropor. Mesopor. Mater. 304 (2020) 109322, https://doi.org/10.1016/j.micromeso.2019.02.009.

[158] M.C. Kreider, M. Sefa, J.A. Fedchak, J. Scherschligt, M. Bible, B. Natarajan, N.N. Klimov, A.E. Miller, Z. Ahmed, M.R. Hartings, Toward 3D printed hydrogen storage materials made with ABS-MOF composites, Polym. Adv. Technol. 29 (2) (2018) 867–873.

[159] J. Ren, N.M. Musyoka, H.W. Langmi, A. Swartbooi, B.C. North, M. Mathe, A more efficient way to shape metal-organic framework (MOF) powder materials for hydrogen storage applications, Int. J. Hydrog. Energy 40 (13) (2015) 4617–4622.

[160] I. Luz, L. Toy, F. Rabie, M. Lail, M. Soukri, Synthesis of Soluble Metal Organic Framework Composites for Mixed Matrix Membranes, ACS Appl. Mater. Interfaces 11 (17) (2019) 15638–15645.

[161] A.H. Valekar, K.-H. Cho, U.-H. Lee, J.S. Lee, J.W. Yoon, Y.K. Hwang, S.G. Lee, S.J. Cho, J.-S. Chang, Shaping of porous metal–organic framework granules using mesoporous ρ-alumina as a binder, RSC Adv. 7 (88) (2017) 55767–55777.

[162] W.Y. Hong, S.P. Perera, A.D. Burrows, Manufacturing of metal-organic framework monoliths and their application in CO$_2$ adsorption, Micropor. Mesopor. Mater. 214 (2015) 149–155, https://doi.org/10.1016/j.micromeso.2015.05.014.

[163] M.A. Moreira, J.C. Santos, A.F.P. Ferreira, J.M. Loureiro, F. Ragon, P. Horcajada, K.-E. Shim, Y.-K. Hwang, U.-H. Lee, J.-S. Chang, C. Serre, A.E. Rodrigues, Reverse Shape Selectivity in the Liquid-Phase Adsorption of Xylene Isomers in Zirconium Terephthalate MOF UiO-66, Langmuir 28 (13) (2012) 5715–5723.

[164] P.-J. Kim, Y.-W. You, H. Park, J.-S. Chang, Y.-S. Bae, C.-H. Lee, J.-K. Suh, Separation of SF$_6$ from SF$_6$/N$_2$ mixture using metal–organic framework MIL-100(Fe) granule, Chem. Eng. J. 262 (2015) 683–690.

[165] P. Küsgens, A. Zgaverdea, H.-G. Fritz, S. Siegle, S. Kaskel, Metal-Organic Frameworks in Monolithic Structures, J. Am. Ceram. Soc. 93 (2010) 2476–2479. https://doi.org/10.1111/j.1551-2916.2010.03824.x.

[166] J.J. Purewal, D. Liu, J. Yang, A. Sudik, D.J. Siegel, S. Maurer, U. Müller, Increased volumetric hydrogen uptake of MOF-5 by powder densification, Int. J. Hydrog. Energy 37 (3) (2012) 2723–2727.

[167] M. Tagliabue, C. Rizzo, R. Millini, P.D.C. Dietzel, R. Blom, S. Zanardi, Methane storage on CPO-27-Ni pellets, J. Porous Mater. 18 (3) (2011) 289–296.

[168] I. Majchrzak-Kucęba, A. Ściubidło, Shaping metal–organic framework (MOF) powder materials for CO_2 capture applications—a thermogravimetric study, J. Therm. Anal. Calorim. 138 (6) (2019) 4139–4144.
[169] B. Zhang, J. Zhang, C. Liu, L.i. Peng, X. Sang, B. Han, X. Ma, T. Luo, X. Tan, G. Yang, High-internal-phase emulsions stabilized by metal-organic frameworks and derivation of ultralight metal-organic aerogels, Sci. Rep. 6 (1) (2016), https://doi.org/10.1038/srep21401.
[170] S. Wei, Y. Liu, J. Zheng, S. Huang, G. Chen, F. Zhu, J. Zheng, J. Xu, G. Ouyang, Boosting loading capacities of shapeable metal–organic framework coatings by closing the interparticle spaces of stacked nanocrystals, Chem. Commun. 55 (50) (2019) 7223–7226.
[171] T. Tian, J. Velazquez-Garcia, T.D. Bennett, D. Fairen-Jimenez, Mechanically and chemically robust ZIF-8 monoliths with high volumetric adsorption capacity, J. Mater. Chem. A 3 (6) (2015) 2999–3005.
[172] B. Bueken, N. Van Velthoven, T. Willhammar, T. Stassin, I. Stassen, D.A. Keen, G.V. Baron, J.F.M. Denayer, R. Ameloot, S. Bals, D. De Vos, T.D. Bennett, Gel-based morphological design of zirconium metal–organic frameworks, Chem. Sci. 8 (5) (2017) 3939–3948.
[173] D. Bazer-Bachi, L. Assié, V. Lecocq, B. Harbuzaru, V. Falk, Towards industrial use of metal-organic framework: Impact of shaping on the MOF properties, Powder Technol. 255 (2014) 52–59.
[174] M. Taddei, M.J. McPherson, A. Gougsa, J. Lam, J. Sewell, E. Andreoli, An Optimised Compaction Process for Zr-Fumarate (MOF-801), Inorganics 7 (2019) 110. https://doi.org/10.3390/inorganics7090110.
[175] H. Wang, S. Zhao, Y.i. Liu, R. Yao, X. Wang, Y. Cao, D. Ma, M. Zou, A. Cao, X. Feng, B.o. Wang, Membrane adsorbers with ultrahigh metal-organic framework loading for high flux separations, Nat. Commun. 10 (1) (2019), https://doi.org/10.1038/s41467-019-12114-8.
[176] M. Wickenheisser, A. Herbst, R. Tannert, B. Milow, C. Janiak, Hierarchical MOF-xerogel monolith composites from embedding MIL-100(Fe,Cr) and MIL-101(Cr) in resorcinol-formaldehyde xerogels for water adsorption applications, Micropor. Mesopor. Mater. 215 (2015) 143–153.
[177] U. Jeong, N.A. Dogan, M. Garai, T.S. Nguyen, J.F. Stoddart, C.T. Yavuz, Inversion of Dispersion: Colloidal Stability of Calixarene-Modified Metal–Organic Framework Nanoparticles in Nonpolar Media, J. Am. Chem. Soc. 141 (31) (2019) 12182–12186.
[178] G. Zhang, X. Li, Q. Liao, Y. Liu, K. Xi, W. Huang, X. Jia, Water-dispersible PEG-curcumin/amine-functionalized covalent organic framework nanocomposites as smart carriers for in vivo drug delivery, Nat. Commun. 9 (1) (2018), https://doi.org/10.1038/s41467-018-04910-5.
[179] O. Halevi, J.M.R. Tan, P.S. Lee, S. Magdassi, Hydrolytically Stable MOF in 3D-Printed Structures, Adv. Sustain. Syst. 2 (2) (2018) 1700150, https://doi.org/10.1002/adsu.v2.210.1002/adsu.201700150.
[180] R.E. Giménez, E. Piccinini, O. Azzaroni, M. Rafti, Lectin-Recognizable MOF Glyconanoparticles: Supramolecular Glycosylation of ZIF-8 Nanocrystals by Sugar-Based Surfactants, ACS Omega 4 (1) (2019) 842–848.
[181] A. Sardari, A.A. Sabbagh Alvani, S.R. Ghaffarian, Preparation of castor oil-based fatliquoring agent via a Pickering emulsion method for use in leather coating, J. Coat. Technol. Res. 16 (6) (2019) 1765–1772.
[182] K. Xie, Q. Fu, Y. He, J. Kim, S.J. Goh, E. Nam, G.G. Qiao, P.A. Webley, Synthesis of well dispersed polymer grafted metal–organic framework nanoparticles, Chem. Commun. 51 (85) (2015) 15566–15569.
[183] A. Figuerola, D.A.V. Medina, A.J. Santos-Neto, C.P. Cabello, V. Cerdà, G.T. Palomino, F. Maya, Metal–organic framework mixed-matrix coatings on 3D printed devices, Appl. Mater. Today 16 (2019) 21–27.
[184] M.S. Denny Jr., S.M. Cohen, In Situ Modification of Metal-Organic Frameworks in Mixed-Matrix Membranes, Angew. Chem. Int. Ed. 54 (31) (2015) 9029–9032.
[185] Y.-H. Luo, C. Chen, C. He, Y.-Y. Zhu, D.-L. Hong, X.-T. He, P.-J. An, H.-S. Wu, B.-W. Sun, Single-Layered Two-Dimensional Metal–Organic Framework Nanosheets as an in Situ Visual Test Paper for Solvents, ACS Appl. Mater. Interfaces 10 (34) (2018) 28860–28867.
[186] A. Mukhopadhyay, V.K. Maka, G. Savitha, J.N. Moorthy, Photochromic 2D Metal-Organic Framework Nanosheets (MONs): Design, Synthesis, and Functional MON-Ormosil Composite, Chem 4 (5) (2018) 1059–1079.
[187] Y. Zhang, Y.u. Xiong, J. Ge, R. Lin, C. Chen, Q. Peng, D. Wang, Y. Li, Porous organic cage stabilised palladium nanoparticles: efficient heterogeneous catalysts for carbonylation reaction of aryl halides, Chem. Commun. 54 (22) (2018) 2796–2799.
[188] K. Omoto, N. Hosono, M. Gochomori, S. Kitagawa, Paraffinic metal–organic polyhedrons: solution-processable porous modules exhibiting three-dimensional molecular order, Chem. Commun. 54 (53) (2018) 7290–7293.
[189] Y. Wang, L. Feng, J. Pang, J. Li , N. Huang, G. S. Day, L. Cheng, H. F. Drake, Y. Wang, C. Lollar, J. Qin, Z. Gu, T. Lu, S. Yuanand H. C. Zhou, Photosensitizer-Anchored 2D MOF Nanosheets as Highly Stable and Accessible Catalysts toward Artemisinin Production, Adv. Sci. 6 (2019) 1802059. https://doi.org/10.1002/advs.201802059.
[190] R.B. Getman, Y.-S. Bae, C.E. Wilmer, R.Q. Snurr, Review and Analysis of Molecular Simulations of Methane, Hydrogen, and Acetylene Storage in Metal–Organic Frameworks, Chem. Rev. 112 (2) (2012) 703–723.
[191] L.J. Murray, M. Dincă, J.R. Long, Hydrogen storage in metal–organic frameworks, Chem. Soc. Rev. 38 (5) (2009) 1294, https://doi.org/10.1039/b802256a.
[192] M. Yoon, R. Srirambalaji, K. Kim, Homochiral Metal–Organic Frameworks for Asymmetric Heterogeneous Catalysis, Chem. Rev. 112 (2) (2012) 1196–1231.
[193] W.-G. Cui, G.-Y. Zhang, T.-L. Hu, X.-H. Bu, Metal-organic framework-based heterogeneous catalysts for the conversion of C1 chemistry: CO, CO_2 and CH_4, Coord. Chem. Rev. 387 (2019) 79–120.
[194] P. Silva, S.M.F. Vilela, J.P.C. Tomé, F.A. Almeida Paz, Multifunctional metal–organic frameworks: from academia to industrial applications, Chem. Soc. Rev. 44 (19) (2015) 6774–6803.
[195] Y. Yang, P. Bai, X. Guo, Separation of Xylene Isomers: A Review of Recent Advances in Materials, Ind. Eng. Chem. Res. 56 (50) (2017) 14725–14753.
[196] W.-G. Cui, T.-L. Hu, X.-H. Bu, Metal–Organic Framework Materials for the Separation and Purification of Light Hydrocarbons, Adv. Mater. 32 (3) (2020) 1806445, https://doi.org/10.1002/adma.v32.310.1002/adma.201806445.
[197] Q. Qian, P.A. Asinger, M.J. Lee, G. Han, K. Mizrahi Rodriguez, S. Lin, F.M. Benedetti, A.X. Wu, W.S. Chi, Z.P. Smith, MOF-Based Membranes for Gas Separations, Chem. Rev. (2020). in press. https://doi.org/10.1021/acs.chemrev.0c00119.
[198] R.-B. Lin, S. Xiang, W. Zhou, B. Chen, Microporous Metal-Organic Framework Materials for Gas Separation, Chem 6 (2) (2020) 337–363.
[199] D.E. Jaramillo, D.A. Reed, H.Z.H. Jiang, J. Oktawiec, M.W. Mara, A.C. Forse, D.J. Lussier, R.A. Murphy, M. Cunningham, V. Colombo, D.K. Shuh, J.A. Reimer, J.R. Long, Selective nitrogen adsorption via backbonding in a metal–organic framework with exposed vanadium sites, Nat. Mater. 19 (5) (2020) 517–521.
[200] J. Pei, K. Shao, J.-X. Wang, H.-M. Wen, Y.u. Yang, Y. Cui, R. Krishna, B. Li, G. Qian, A Chemically Stable Hofmann-Type Metal–Organic Framework with Sandwich-Like Binding Sites for Benchmark Acetylene Capture, Adv. Mater. 32 (24) (2020) 1908275, https://doi.org/10.1002/adma.v32.2410.1002/adma.201908275.
[201] M.I. Gonzalez, M.T. Kapelewski, E.D. Bloch, P.J. Milner, D.A. Reed, M.R. Hudson, J.A. Mason, G. Barin, C.M. Brown, J.R. Long, Separation of Xylene Isomers through Multiple Metal Site Interactions in Metal–Organic Frameworks, J. Am. Chem. Soc. 140 (9) (2018) 3412–3422.
[202] S. Kim, J. Lee, Y. Son, M. Yoon, Study of the Dye Adsorption Kinetics of Metal–Organic Frameworks in Aqueous Media, Bull. Kor. Chem. Soc. 41 (8) (2020) 843, https://doi.org/10.1002/bkcs.12076.
[203] B.-M. Jun, Y.A.J. Al-Hamadani, A. Son, C.M. Park, M. Jang, A.m. Jang, N.C. Kim, Y. Yoon, Applications of metal-organic framework based membranes in water purification: A review, Sep. Purif. Technol. 247 (2020) 116947, https://doi.org/10.1016/j.seppur.2020.116947.
[204] S. Rojas, P. Horcajada, Metal–Organic Frameworks for the Removal of Emerging Organic Contaminants in Water, Chem. Rev. (2020). in press. https://doi.org/10.1021/acs.chemrev.9b00797.
[205] J. Li, H. Wang, X. Yuan, J. Zhang, J.W. Chew, Metal-organic framework membranes for wastewater treatment and water regeneration, Coord. Chem. Rev. 404 (2020) 213116, https://doi.org/10.1016/j.ccr.2019.213116.
[206] U. Pöschl, Atmospheric Aerosols: Composition, Transformation, Climate and Health Effects, Angew. Chem. Int. Ed. 44 (46) (2005) 7520–7540.
[207] G. Soreanu, M. Dixon, A. Darlington, Botanical biofiltration of indoor gaseous pollutants – A mini-review, Chem. Eng. J. 229 (2013) 585–594.
[208] M. Kampa, E. Castanas, Human health effects of air pollution, Environ. Pollut. 151 (2) (2008) 362–367.
[209] X. Li, L.i. Zhang, Z. Yang, P. Wang, Y. Yan, J. Ran, Adsorption materials for volatile organic compounds (VOCs) and the key factors for VOCs adsorption process: A review, Sep. Purif. Technol. 235 (2020) 116213, https://doi.org/10.1016/j.seppur.2019.116213.
[210] E. Barea, C. Montoro, J.A.R. Navarro, Toxic gas removal – metal–organic frameworks for the capture and degradation of toxic gases and vapours, Chem. Soc. Rev. 43 (16) (2014) 5419–5430.
[211] A.J. Rieth, A.M. Wright, M. Dincă, Kinetic stability of metal–organic frameworks for corrosive and coordinating gas capture, Nat. Rev. Mater. 4 (11) (2019) 708–725.
[212] P. Kumar, K.-H. Kim, E.E. Kwon, J.E. Szulejko, Metal–organic frameworks for the control and management of air quality: advances and future direction, J. Mater. Chem. A 4 (2) (2016) 345–361.
[213] N.S. Bobbitt, M.L. Mendonca, A.J. Howarth, T. Islamoglu, J.T. Hupp, O.K. Farha, R.Q. Snurr, Metal–organic frameworks for the removal of toxic industrial chemicals and chemical warfare agents, Chem. Soc. Rev. 46 (11) (2017) 3357–3385.
[214] J. Gao, A. Woodward, S. Vardoulakis, S. Kovats, P. Wilkinson, L. Li, L. Xu, J. Li, J. Yang, J. Li, L. Cao, X. Liu, H. Wu, Q. Liu, Haze, public health and mitigation measures in China: A review of the current evidence for further policy response, Sci. Total Environ. 578 (2017) 148–157.
[215] A.M. Fiore, V. Naik, D.V. Spracklen, A. Steiner, N. Unger, M. Prather, D. Bergmann, P.J. Cameron-Smith, I. Cionni, W.J. Collins, S. Dalsøren, V. Eyring, G. A. Folberth, P. Ginoux, L.W. Horowitz, B. Josse, J.-F. Lamarque, I.A. MacKenzie, T. Nagashima, F.M. O'Connor, M. Righi, S.T. Rumbold, D.T. Shindell, R.B. Skeie, K. Sudo, S. Szopa, T. Takemura, G. Zeng, Global air quality and climate, Chem. Soc. Rev. 41 (19) (2012) 6663, https://doi.org/10.1039/c2cs35095e.
[216] B.A. Maher, I.A.M. Ahmed, V. Karloukovski, D.A. MacLaren, P.G. Foulds, D. Allsop, D.M.A. Mann, R. Torres-Jardón, L. Calderon-Garciduenas, Magnetite pollution nanoparticles in the human brain, Proc Natl Acad Sci USA 113 (39) (2016) 10797–10801.
[217] J. Lelieveld, J.S. Evans, M. Fnais, D. Giannadaki, A. Pozzer, The contribution of outdoor air pollution sources to premature mortality on a global scale, Nature 525 (7569) (2015) 367–371.
[218] Y. Hwang, J. An, K. Lee, Characterization of a High $PM_{2.5}$ Exposure Group in Seoul Using the Korea Simulation Exposure Model for $PM_{2.5}$ (KoSEM-PM) Based on Time–Activity Patterns and Microenvironmental Measurements,

Int. J. Environ. Res. Public Health. 15 (2018) 2808. https://doi.org/10.3390/ijerph15122808.

[219] W.-J. Guan, X.-Y. Zheng, K.F. Chung, N.-S. Zhong, Impact of air pollution on the burden of chronic respiratory diseases in China: time for urgent action, Lancet 388 (10054) (2016) 1939–1951.

[220] J.-R. Li, J. Sculley, H.-C. Zhou, Metal–Organic Frameworks for Separations, Chem. Rev. 112 (2) (2012) 869–932.

[221] J. Yao, H. Wang, Zeolitic imidazolate framework composite membranes and thin films: synthesis and applications, Chem. Soc. Rev. 43 (13) (2014) 4470–4493.

[222] B. Khalid, X. Bai, H. Wei, Y.a. Huang, H. Wu, Y.i. Cui, Direct Blow-Spinning of Nanofibers on a Window Screen for Highly Efficient PM$_{2.5}$ Removal, Nano Lett. 17 (2) (2017) 1140–1148.

[223] C. Liu, P.-C. Hsu, H.-W. Lee, M. Ye, G. Zheng, N. Liu, W. Li, Y.i. Cui, Transparent air filter for high-efficiency PM$_{2.5}$ capture, Nat. Commun. 6 (1) (2015), https://doi.org/10.1038/ncomms7205.

[224] R. Zhang, C. Liu, P.-C. Hsu, C. Zhang, N. Liu, J. Zhang, H.R. Lee, Y. Lu, Y. Qiu, S. Chu, Y.i. Cui, Nanofiber Air Filters with High-Temperature Stability for Efficient PM $_{2}$.5 Removal from the Pollution Sources, Nano Lett. 16 (6) (2016) 3642–3649.

[225] K. Zhao, J. Huang, J. Mao, Z. Bao, Z. Chen, Y. Lai, Charged graphene aerogel filter enabled superior particulate matter removal efficiency in harsh environment, Chem. Eng. J. 395 (2020) 125086, https://doi.org/10.1016/j.cej.2020.125086.

[226] X. Zhao, Y. Li, T. Hua, P. Jiang, X. Yin, J. Yu, B. Ding, Low-Resistance Dual-Purpose Air Filter Releasing Negative Ions and Effectively Capturing PM$_{2.5}$, ACS Appl. Mater. Interfaces 9 (13) (2017) 12054–12063.

[227] H. Furukawa, K.E. Cordova, M. O'Keeffe, O.M. Yaghi, The Chemistry and Applications of Metal-Organic Frameworks, Science 341 (6149) (2013), 1230444-1230444.

[228] G. Férey, C. Serre, T. Devic, G. Maurin, H. Jobic, P.L. Llewellyn, G. De Weireld, A. Vimont, M. Daturi, J.-S. Chang, Why hybrid porous solids capture greenhouse gases?, Chem. Soc. Rev. 40 (2) (2011) 550–562.

[229] T.-T. Li, X. Cen, H.-T. Ren, L. Wu, H.-K. Peng, W. Wang, B.o. Gao, C.-W. Lou, J.-H. Lin, Zeolitic Imidazolate Framework-8/Polypropylene–Polycarbonate Barklike Meltblown Fibrous Membranes by a Facile in Situ Growth Method for Efficient PM $_{2}$.5 Capture, ACS Appl. Mater. Interfaces 12 (7) (2020) 8730–8739.

[230] Z. Wang, Y. Zhang, X.Y.D. Ma, J. Ang, Z. Zeng, B.F. Ng, M.P. Wan, S.-C. Wong, X. Lu, Polymer/MOF-derived multilayer fibrous membranes for moisture-wicking and efficient capturing both fine and ultrafine airborne particles, Sep. Purif. Technol. 235 (2020) 116183, https://doi.org/10.1016/j.seppur.2019.116183.

[231] J. Mao, Y. Tang, Y. Wang, J. Huang, X. Dong, Z. Chen, Y. Lai, Particulate Matter Capturing via Naturally Dried ZIF-8/Graphene Aerogels under Harsh Conditions, iScience 16 (2019) 133–144.

[232] Y. Chen, S. Zhang, S. Cao, S. Li, F. Chen, S. Yuan, C. Xu, J. Zhou, X. Feng, X. Ma, B. o. Wang, Roll-to-Roll Production of Metal-Organic Framework Coatings for Particulate Matter Removal, Adv. Mater. 29 (15) (2017) 1606221, https://doi.org/10.1002/adma.201606221.

[233] Y. Zhang, S. Yuan, X. Feng, H. Li, J. Zhou, B.o. Wang, Preparation of Nanofibrous Metal–Organic Framework Filters for Efficient Air Pollution Control, J. Am. Chem. Soc. 138 (18) (2016) 5785–5788.

[234] S. Ma, M. Zhang, J. Nie, J. Tan, B. Yang, S. Song, Design of double-component metal–organic framework air filters with PM$_{2.5}$ capture, gas adsorption and antibacterial capacities, Carbohydr. Res. 203 (2019) 415–422.

[235] Z. Hao, J. Wu, C. Wang, J. Liu, Electrospun Polyimide/Metal-Organic Framework Nanofibrous Membrane with Superior Thermal Stability for Efficient PM $_{2}$.5 Capture, ACS Appl. Mater. Interfaces 11 (12) (2019) 11904–11909.

[236] X. Wang, W. Xu, J. Gu, X. Yan, Y.i. Chen, M. Guo, G. Zhou, S. Tong, M. Ge, Y. Liu, C. Chen, MOF-based fibrous membranes adsorb PM efficiently and capture toxic gases selectively, Nanoscale 11 (38) (2019) 17782–17790.

[237] X. Dai, X.u. Li, X. Wang, Morphology controlled porous poly(lactic acid)/zeolitic imidazolate framework-8 fibrous membranes with superior PM$_{2.5}$ capture capacity, Chem. Eng. J. 338 (2018) 82–91.

[238] Y.e. Bian, R. Wang, S. Wang, C. Yao, W. Ren, C. Chen, L.i. Zhang, Metal–organic framework-based nanofiber filters for effective indoor air quality control, J. Mater. Chem. A 6 (32) (2018) 15807–15814.

[239] X. Zhao, L. Chen, Y.i. Guo, X.u. Ma, Z. Li, W. Ying, X. Peng, Porous cellulose nanofiber stringed HKUST-1 polyhedron membrane for air purification, Appl. Mater. Today 14 (2019) 96–101.

[240] W.-T. Koo, J.-S. Jang, S. Qiao, W. Hwang, G. Jha, R.M. Penner, I.-D. Kim, Hierarchical Metal–Organic Framework-Assembled Membrane Filter for Efficient Removal of Particulate Matter, ACS Appl. Mater. Interfaces 10 (23) (2018) 19957–19963.

[241] S. Feng, X. Li, S. Zhao, Y. Hu, Z. Zhong, W. Xing, H. Wang, Multifunctional metal organic framework and carbon nanotube-modified filter for combined ultrafine dust capture and SO$_2$ dynamic adsorption, Environ. Sci.: Nano 5 (12) (2018) 3023–3031.

[242] J.B. DeCoste, G.W. Peterson, Metal–Organic Frameworks for Air Purification of Toxic Chemicals, Chem. Rev. 114 (11) (2014) 5695–5727.

[243] A.U. Czaja, N. Trukhan, U. Müller, Industrial applications of metal–organic frameworks, Chem. Soc. Rev. 38 (5) (2009) 1284, https://doi.org/10.1039/b804680h.

[244] N.A. Khan, Z. Hasan, S.H. Jhung, Adsorptive removal of hazardous materials using metal-organic frameworks (MOFs): A review, J. Hazard. Mater. 244-245 (2013) 444–456.

[245] I. Ahmed, S.H. Jhung, Adsorptive desulfurization and denitrogenation using metal-organic frameworks, J. Hazard. Mater. 301 (2016) 259–276.

[246] S. Yang, J. Sun, A.J. Ramirez-Cuesta, S.K. Callear, W.I.F. David, D.P. Anderson, R. Newby, A.J. Blake, J.E. Parker, C.C. Tang, M. Schröder, Selectivity and direct visualization of carbon dioxide and sulfur dioxide in a decorated porous host, Nat. Chem. 4 (11) (2012) 887–894.

[247] M. Savage, Y. Cheng, T.L. Easun, J.E. Eyley, S.P. Argent, M.R. Warren, W. Lewis, C. Murray, C.C. Tang, M.D. Frogley, G. Cinque, J. Sun, S. Rudić, R.T. Murden, M.J. Benham, A.N. Fitch, A.J. Blake, A.J. Ramirez-Cuesta, S. Yang, M. Schröder, Selective Adsorption of Sulfur Dioxide in a Robust Metal-Organic Framework Material, Adv. Mater. 28 (39) (2016) 8705–8711.

[248] L. Li, I. da Silva, D.I. Kolokolov, X. Han, J. Li, G. Smith, Y. Cheng, L.L. Daemen, C. G. Morris, H.G.W. Godfrey, N.M. Jacques, X. Zhang, P. Manuel, M.D. Frogley, C. A. Murray, A.J. Ramirez-Cuesta, G. Cinque, C.C. Tang, A.G. Stepanov, S. Yang, M. Schroder, Post-synthetic modulation of the charge distribution in a metal–organic framework for optimal binding of carbon dioxide and sulfur dioxide, Chem. Sci. 10 (5) (2019) 1472–1482.

[249] J.H. Carter, X. Han, F.Y. Moreau, I. da Silva, A. Nevin, H.G.W. Godfrey, C.C. Tang, S. Yang, M. Schröder, Exceptional Adsorption and Binding of Sulfur Dioxide in a Robust Zirconium-Based Metal–Organic Framework, J. Am. Chem. Soc. 140 (46) (2018) 15564–15567.

[250] S. Yang, L. Liu, J. Sun, K.M. Thomas, A.J. Davies, M.W. George, A.J. Blake, A.H. Hill, A.N. Fitch, C.C. Tang, M. Schröder, Irreversible Network Transformation in a Dynamic Porous Host Catalyzed by Sulfur Dioxide, J. Am. Chem. Soc. 135 (13) (2013) 4954–4957.

[251] K. Tan, P. Canepa, Q. Gong, J. Liu, D.H. Johnson, A. Dyevoich, P.K. Thallapally, T. Thonhauser, J. Li, Y.J. Chabal, Mechanism of Preferential Adsorption of SO$_2$ into Two Microporous Paddle Wheel Frameworks M(bdc)(ted)$_{0.5}$, Chem. Mater. 25 (23) (2013) 4653–4662.

[252] L.M. Rodríguez-Albelo, E. López-Maya, S. Hamad, A.R. Ruiz-Salvador, S. Calero, J.A.R. Navarro, Selective sulfur dioxide adsorption on crystal defect sites on an isoreticular metal organic framework series, Nat. Commun. 8 (1) (2017), https://doi.org/10.1038/ncomms14457.

[253] X. Cui, Q. Yang, L. Yang, R. Krishna, Z. Zhang, Z. Bao, H. Wu, Q. Ren, W. Zhou, B. Chen, H. Xing, Ultrahigh and Selective SO$_2$ Uptake in Inorganic Anion-Pillared Hybrid Porous Materials, Adv. Mater. 29 (28) (2017) 1606929, https://doi.org/10.1002/adma.v29.2810.1002/adma.201606929.

[254] M.R. Tchalala, P.M. Bhatt, K.N. Chappanda, S.R. Tavares, K. Adil, Y. Belmabkhout, A. Shkurenko, A. Cadiau, N. Heymans, G. De Weireld, G. Maurin, K.N. Salama, M. Eddaoudi, Fluorinated MOF platform for selective removal and sensing of SO$_2$ from flue gas and air, Nat. Commun. 10 (1) (2019), https://doi.org/10.1038/s41467-019-09157-2.

[255] M. Almaraz, E. Bai, C. Wang, J. Trousdell, S. Conley, I. Faloona, B.Z. Houlton, Agriculture is a major source of NO$_x$ pollution in California, Sci. Adv. 4 (1) (2018) eaao3477, https://doi.org/10.1126/sciadv.aao3477.

[256] R.K. Srivastava, W. Neuffer, D. Grano, S. Khan, J.E. Staudt, W. Jozewicz, Controlling NO$_x$ emission from industrial sources, Environ. Prog. 24 (2) (2005) 181–197.

[257] M.S. Kharasch W Nldenberg Elwqod V Jensen Pal L E Fischer, D.L. Mayfield, INHIBITION OF POLYMERIZATION Laboratory and Plant Control of Popcorn Polymer Growth, 2020. https://pubs.acs.org/sharingguidelines (accessed June 13, 2020).

[258] A.M. Ebrahim, B. Levasseur, T.J. Bandosz, Interactions of NO$_2$ with Zr-Based MOF: Effects of the Size of Organic Linkers on NO$_2$ Adsorption at Ambient Conditions, Langmuir 29 (1) (2013) 168–174.

[259] J.B. DeCoste, T.J. Demasky, M.J. Katz, O.K. Farha, J.T. Hupp, A UiO-66 analogue with uncoordinated carboxylic acids for the broad-spectrum removal of toxic chemicals, New J. Chem. 39 (4) (2015) 2396–2399.

[260] G.W. Peterson, J.J. Mahle, J.B. DeCoste, W.O. Gordon, J.A. Rossin, Extraordinary NO$_2$ Removal by the Metal-Organic Framework UiO-66-NH$_2$, Angew. Chem. Int. Ed. 55 (21) (2016) 6235–6238.

[261] X. Han, H.G.W. Godfrey, L. Briggs, A.J. Davies, Y. Cheng, L.L. Daemen, A.M. Sheveleva, F. Tuna, E.J.L. McInnes, J. Sun, C. Drathen, M.W. George, A.J. Ramirez-Cuesta, K.M. Thomas, S. Yang, M. Schröder, Reversible adsorption of nitrogen dioxide within a robust porous metal–organic framework, Nat. Mater. 17 (8) (2018) 691–696.

[262] H.-l. Wang, S.-a. Jing, S.-o. Lou, Q.-y. H., L. Li, S.-k. Tao, C. Huang, L.-p. Qiao, C.-h. Chen, Volatile organic compounds (VOCs) source profiles of on-road vehicle emissions in China, Sci. Total Environ. 607-608 (2017) 253–261.

[263] B. Huang, C. Lei, C. Wei, G. Zeng, Chlorinated volatile organic compounds (Cl-VOCs) in environment — sources, potential human health impacts, and current remediation technologies, Environ. Int. 71 (2014) 118–138.

[264] M.A. Bari, W.B. Kindzierski, Ambient volatile organic compounds (VOCs) in Calgary, Alberta: Sources and screening health risk assessment, Sci. Total Environ. 631-632 (2018) 627–640.

[265] K. Vellingiri, P. Kumar, K.-H. Kim, Coordination polymers: Challenges and future scenarios for capture and degradation of volatile organic compounds, Nano Res. 9 (11) (2016) 3181–3208.

[266] P. Falcaro, R. Ricco, C.M. Doherty, K. Liang, A.J. Hill, M.J. Styles, MOF positioning technology and device fabrication, Chem. Soc. Rev. 43 (16) (2014) 5513–5560.

[267] M. Zhu, P. Hu, Z. Tong, Z. Zhao, Z. Zhao, Enhanced hydrophobic MIL(Cr) metal-organic framework with high capacity and selectivity for benzene VOCs capture from high humid air, Chem. Eng. J. 313 (2017) 1122–1131.

[268] K. Vellingiri, P. Kumar, A. Deep, K.-H. Kim, Metal-organic frameworks for the adsorption of gaseous toluene under ambient temperature and pressure, Chemical Engineering Journal 307 (2017) 1116–1126.

[269] X. Sun, D. Lv, Y. Chen, Y. Wu, Q. Wu, Q. Xia, Z. Li, Enhanced Adsorption Performance of Aromatics on a Novel Chromium-Based MIL-101@Graphite Oxide Composite, Energy Fuels 31 (12) (2017) 13985–13990.

[270] L.-H. Xie, X.-M. Liu, T. He, J.-R. Li, Metal-Organic Frameworks for the Capture of Trace Aromatic Volatile Organic Compounds, Chem 4 (8) (2018) 1911–1927.

[271] C. Duan, Y.i. Yu, P. Yang, X. Zhang, F. Li, L. Li, H. Xi, Engineering New Defects in MIL-100(Fe) via a Mixed-Ligand Approach To Effect Enhanced Volatile Organic Compound Adsorption Capacity, Ind. Eng. Chem. Res. 59 (2) (2020) 774–782.

[272] B. Kim, Y.-R. Lee, H.-Y. Kim, W.-S. Ahn, Adsorption of volatile organic compounds over MIL-125-NH_2, Polyhedron 154 (2018) 343–349.

[273] X. Zheng, S. Liu, S. Rehman, Z. Li, P. Zhang, Highly improved adsorption performance of metal-organic frameworks CAU-1 for trace toluene in humid air via sequential internal and external surface modification, Chem. Eng. J. 389 (2020) 123424, https://doi.org/10.1016/j.cej.2019.123424.

[274] X. Cui, X. Sun, L. Liu, Q. Huang, H. Yang, C. Chen, S. Nie, Z. Zhao, Z. Zhao, In-situ fabrication of cellulose foam HKUST-1 and surface modification with polysaccharides for enhanced selective adsorption of toluene and acidic dipeptides, Chem. Eng. J. 369 (2019) 898–907.

[275] D. Li, L. Li, R. Chen, C. Wang, H. Li, H. Li, A MIL-101 Composite Doped with Porous Carbon from Tobacco Stem for Enhanced Acetone Uptake at Normal Temperature, Ind. Eng. Chem. Res. 57 (18) (2018) 6226–6235.

[276] P. Hu, X. Liang, M. Yaseen, X. Sun, Z. Tong, Z. Zhao, Z. Zhao, Preparation of highly-hydrophobic novel N-coordinated UiO-66(Zr) with dopamine via fast mechano-chemical method for (CHO-/Cl-)-VOCs competitive adsorption in humid environment, Chem. Eng. J. 332 (2018) 608–618.

[277] K. Vikrant, M. Cho, A. Khan, K.-H. Kim, W.-S. Ahn, E.E. Kwon, Adsorption properties of advanced functional materials against gaseous formaldehyde, Environ. Res. 178 (2019) 108672, https://doi.org/10.1016/j.envres.2019.108672.

[278] L.u. Wang, X.-Y. Liang, Z.-Y. Chang, L.-S. Ding, S. Zhang, B.-J. Li, Effective Formaldehyde Capture by Green Cyclodextrin-Based Metal–Organic Framework, ACS Appl. Mater. Interfaces 10 (1) (2018) 42–46.

[279] L. Zhou, X. Zhang, Y. Chen, Facile synthesis of Al-fumarate metal–organic framework nano-flakes and their highly selective adsorption of volatile organic compounds, Mater. Let. 197 (2017) 224–227.

[280] Y. Zheng, F. Chu, B. Zhang, J. Yan, Y. Chen, Ultrahigh adsorption capacities of carbon tetrachloride on MIL-101 and MIL-101/graphene oxide composites, Micropor. Mesopor. Mater. 263 (2018) 71–76.

[281] B. Picard, I. Chataigner, J. Maddaluno, J. Legros, Introduction to chemical warfare agents, relevant simulants and modern neutralisation methods, Org. Biomol. Chem. 17 (27) (2019) 6528–6537.

[282] Y. Liu, A.J. Howarth, N.A. Vermeulen, S.-Y. Moon, J.T. Hupp, O.K. Farha, Catalytic degradation of chemical warfare agents and their simulants by metal-organic frameworks, Coord. Chem. Rev. 346 (2017) 101–111.

[283] T. Islamoglu, Z. Chen, M.C. Wasson, C.T. Buru, K.O. Kirlikovali, U. Afrin, M.R. Mian, O.K. Farha, Metal-Organic Frameworks against Toxic Chemicals, Chem. Rev. 120 (2020), https://doi.org/10.1021/acs.chemrev.9b00828.

[284] F.-J. Ma, S.-X. Liu, C.-Y. Sun, D.-D. Liang, G.-J. Ren, F. Wei, Y.-G. Chen, Z.-M. Su, A Sodalite-Type Porous Metal–Organic Framework with Polyoxometalate Templates: Adsorption and Decomposition of Dimethyl Methylphosphonate, J. Am. Chem. Soc. 133 (12) (2011) 4178–4181.

[285] A.M. Plonka, Q.i. Wang, W.O. Gordon, A. Balboa, D. Troya, W. Guo, C.H. Sharp, S.D. Senanayake, J.R. Morris, C.L. Hill, A.I. Frenkel, In Situ Probes of Capture and Decomposition of Chemical Warfare Agent Simulants by Zr-Based Metal Organic Frameworks, J. Am. Chem. Soc. 139 (2) (2017) 599–602.

[286] C. Montoro, Fátima Linares, E. Quartapelle Procopio, I. Senkovska, S. Kaskel, S. Galli, N. Masciocchi, E. Barea, J.A.R. Navarro, Capture of Nerve Agents and Mustard Gas Analogues by Hydrophobic Robust MOF-5 Type Metal–Organic Frameworks, J. Am. Chem. Soc. 133 (31) (2011) 11888–11891.

[287] K.H. Cho, S.K. Chitale, S.-J. Kim, G.-Y. Cha, D.-Y. Hong, S.G. Ryu, J.-S. Chang, Y.K. Hwang, Adsorptive removal of nerve-agent simulant with zirconium-based metal-organic frameworks modified by hydrophobic monocarboxylic acids, Micropor. Mesopor. Mater. 285 (2019) 61–69.

[288] M. Agrawal, S.E. Boulfelfel, D.F. Sava Gallis, J.A. Greathouse, D.S. Sholl, Determining Diffusion Coefficients of Chemical Warfare Agents in Metal–Organic Frameworks, J. Phys. Chem. Lett. 10 (24) (2019) 7823–7830.

[289] G.W. Peterson, A.X. Lu, M.G. Hall, M.A. Browe, T. Tovar, T.H. Epps III, MOFwich: Sandwiched Metal–Organic Framework-Containing Mixed Matrix Composites for Chemical Warfare Agent Removal, ACS Appl. Mater. Interfaces 10 (8) (2018) 6820–6824.

[290] G.W. Peterson, M.A. Browe, E.M. Durke, T.H. Epps III, Flexible SIS/HKUST-1 Mixed Matrix Composites as Protective Barriers against Chemical Warfare Agent Simulants, ACS Appl. Mater. Interfaces 10 (49) (2018) 43080–43087.

[291] R. Vanholder, R. De Smet, G. Glorieux, A. Argilés, U. Baurmeister, P. Brunet, W. Clark, G. Cohen, P.P. De Deyn, R. Deppisch, B. Descamps-Latscha, T. Henle, A. Jörres, H.D. Lemke, Z.A. Massy, J. Passlick-Deetjen, M. Rodriguez, B. Stegmayr, P. Stenvinkel, C. Tetta, C. Wanner, W. Zidek, Review on uremic toxins: Classification, concentration, and interindividual variability, Kidney Int. 63 (5) (2003) 1934–1943.

[292] R.J. Glassock, C. Winearls, The Global Burden of Chronic Kidney Disease: How Valid Are the Estimates?, Nephron Clin. Pract. 110 (1) (2008) c39–c47.

[293] C. Ye, Q. Gong, F. Lu, J. Liang, Adsorption of uraemic toxins on carbon nanotubes, Sep. Purif. Technol. 58 (1) (2007) 2–6.

[294] D. Bergé-Lefranc, O. Schäf, R. Denoyel, J.-L. Bergé-Lefranc, R. Guieu, P. Brunet, V. Hornebecq, The extraction of creatinine from a physiological medium by a microporous solid and its quantification by diffuse reflectance UV spectroscopy, Micropor. Mesopor. Mater. 129 (1–2) (2010) 144–148.

[295] H.-A. Tsai, M.-J. Syu, Synthesis and characterization of creatinine imprinted poly(4-vinylpyridine-co-divinylbenzene) as a specific recognition receptor, Anal. Chim. Acta 539 (1–2) (2005) 107–116.

[296] R.C. Huxford, J. Della Rocca, W. Lin, Metal–organic frameworks as potential drug carriers, Curr. Opin. Chem. Biol. 14 (2) (2010) 262–268.

[297] K.L. Taylor, A. Jin, W. Lin, Surfactant-Assisted Synthesis of Nanoscale Gadolinium Metal-Organic Frameworks for Potential Multimodal Imaging, Angew. Chem. Int. Ed. 47 (40) (2008) 7722–7725.

[298] R.K. Alavijeh, S. Beheshti, K. Akhbari, A. Morsali, Investigation of reasons for metal–organic framework's antibacterial activities, Polyhedron 156 (2018) 257–278.

[299] C.-X. Yang, C. Liu, Y.-M. Cao, X.-P. Yan, Metal–organic framework MIL-100(Fe) for artificial kidney application, RSC Adv. 4 (77) (2014) 40824–40827.

[300] R.M. Abdelhameed, M. Rehan, H.E. Emam, Figuration of Zr-based MOF@cotton fabric composite for potential kidney application, Carbohydr. Polym. 195 (2018) 460–467.

[301] S. Kato, K.-i. Otake, H. Chem, I. Akpinar, C.T. Buru, T. Islamoglu, R.Q. Snurr, O.K. Farha, Zirconium-Based Metal–Organic Frameworks for the Removal of Protein-Bound Uremic Toxin from Human Serum Albumin, J. Am. Chem. Soc. 141 (6) (2019) 2568–2576, https://doi.org/10.1021/jacs.8b12525.

[302] T. Ding, X.-Y. Liao, Q.L. Dong, X.-T. Xuan, S Chen -G., X.-Q. Ye, D.-H. Liu, Predictive modeling of microbial single cells: A review, Crit. Rev. Food. Sci. Untr. 58 (5) (2018) 711–725.

[303] G. Wyszogrodzka, B. Marszałek, B. Gil, P. Dorożyński, Metal-organic frameworks: mechanisms of antibacterial action and potential applications, Drug Discov. Today 21 (6) (2016) 1009–1018.

[304] P. Li, J. Li, X. Feng, J. Li, Y. Hao, J. Zhang, H. Wang, A. Yin, J. Zhou, X. Ma, B.o. Wang, Metal-organic frameworks with photocatalytic bactericidal activity for integrated air cleaning, Nat. Commun. 10 (1) (2019), https://doi.org/10.1038/s41467-019-10218-9.

[305] M. Shen, F. Forghani, X. Kong, D. Liu, X. Ye, S. Chen, T. Ding, Antibacterial applications of metal–organic frameworks and their composites, Compr. Rev. Food Sci. Food Saf. 19 (4) (2020) 1397–1419.

[306] Y.N. Slavin, J. Asnis, U.O. Häfeli, H. Bach, Metal nanoparticles: understanding the mechanisms behind antibacterial activity, J. Nanobiotechnol. 15 (1) (2017), https://doi.org/10.1186/s12951-017-0308-z.

[307] X. Lu, J. Ye, D. Zhang, R. Xie, R.F. Bogale, Y. Sun, L. Zhao, Q.i. Zhao, G. Ning, Silver carboxylate metal–organic frameworks with highly antibacterial activity and biocompatibility, J. Inorg. Biochem. 138 (2014) 114–121.

[308] M.Y. Masoomi, A. Morsali, Morphological study and potential applications of nano metal–organic coordination polymers, RSC Adv. 3 (42) (2013) 19191, https://doi.org/10.1039/c3ra43346c.

[309] Z. Song, Y. Wu, Q.i. Cao, H. Wang, X. Wang, H. Han, pH-Responsive, Light-Triggered on-Demand Antibiotic Release from Functional Metal-Organic Framework for Bacterial Infection Combination Therapy, Adv. Funct. Mater. 28 (23) (2018) 1800011, https://doi.org/10.1002/adfm.v28.2310.1002/adfm.201800011.

[310] H.N. Rubin, B.H. Neufeld, M.M. Reynolds, Surface-Anchored Metal–Organic Framework–Cotton Material for Tunable Antibacterial Copper Delivery, ACS Appl. Mater. Interfaces 10 (17) (2018) 15189–15199.

[311] L. Qian, D. Lei, X. Duan, S. Zhang, W. Song, C. Hou, R. Tang, Design and preparation of metal-organic framework papers with enhanced mechanical properties and good antibacterial capacity, Carbohydr. Polym. 192 (2018) 44–51.

[312] S. Shakya, Y. He, X. Ren, T. Guo, A. Maharjan, T. Luo, T. Wang, R. Dhakhwa, B. Regmi, H. Li, R. Gref, J. Zhang, Ultrafine Silver Nanoparticles Embedded in Cyclodextrin Metal-Organic Frameworks with GRGDS Functionalization to Promote Antibacterial and Wound Healing Application, Small 15 (27) (2019) 1901065, https://doi.org/10.1002/smll.v15.2710.1002/smll.201901065.

[313] Y.e. Qi, J. Ye, S. Ren, J. Lv, S. Zhang, Y. Che, G. Ning, In-situ synthesis of metal nanoparticles@metal–organic frameworks: Highly effective catalytic performance and synergistic antimicrobial activity, J. Hazard. Mater. 387 (2020) 121687, https://doi.org/10.1016/j.jhazmat.2019.121687.

[314] P. Cao, X. Wu, W. Zhang, L. Zhao, W. Sun, Z. Tang, Killing Oral Bacteria Using Metal–Organic Frameworks, Ind. Eng. Chem. Res. 59 (4) (2020) 1559–1567.

[315] D. Han, Y. Han, J. Li, X. Liu, K.W.K. Yeung, Y. Zheng, Z. Cui, X. Yang, Y. Liang, Z. Li, S. Zhu, X. Yuan, X. Feng, C. Yang, S. Wu, Enhanced photocatalytic activity and photothermal effects of cu-doped metal-organic frameworks for rapid treatment of bacteria-infected wounds, Appl. Catal. B Environ. 261 (2020) 118248, https://doi.org/10.1016/j.apcatb.2019.118248.

[316] X. Ren, C. Yang, L. Zhang, S. Li, S. Shi, R. Wang, X.u. Zhang, T. Yue, J. Sun, J. Wang, Copper metal–organic frameworks loaded on chitosan film for the efficient inhibition of bacteria and local infection therapy, Nanoscale 11 (24) (2019) 11830–11838.

[317] J. Goldemberg, Ethanol for a Sustainable Energy Future, Science 315 (5813) (2007) 808–810.

[318] D. Larcher, J.-M. Tarascon, Towards greener and more sustainable batteries for electrical energy storage, Nat. Chem. 7 (1) (2015) 19–29.

[319] S.J. Peighambardoust, S. Rowshanzamir, M. Amjadi, Review of the proton exchange membranes for fuel cell applications, Int. J. Hydrog. Energy 35 (17) (2010) 9349–9384.

[320] Y. Ye, L. Gong, S. Xiang, Z. Zhang, B. Chen, Metal–Organic Frameworks as a Versatile Platform for Proton Conductors, Adv. Mater. 32 (21) (2020) 1907090, https://doi.org/10.1002/adma.v32.2110.1002/adma.201907090.

[321] M. Yoon, K. Suh, S. Natarajan, K. Kim, Proton Conduction in Metal-Organic Frameworks and Related Modularly Built Porous Solids, Angew. Chem. Int. Ed. 52 (10) (2013) 2688–2700.

[322] G.K.H. Shimizu, J.M. Taylor, S. Kim, Proton Conduction with Metal-Organic Frameworks, Science 341 (6144) (2013) 354–355.

[323] D.-W. Lim, M. Sadakiyo, H. Kitagawa, Proton transfer in hydrogen-bonded degenerate systems of water and ammonia in metal–organic frameworks, Chem. Sci. 10 (1) (2019) 16–33.

[324] S. Chand, S.M. Elahi, A. Pal, M.C. Das, Metal-Organic Frameworks and Other Crystalline Materials for Ultrahigh Superprotonic Conductivities of 10^{-2} S cm^{-1} or Higher, Chem. Eur. J. 25 (2019) 6259–6269, https://doi.org/10.1002/chem.201806126.

[325] P.G. Bruce, S.A. Freunberger, L.J. Hardwick, J.-M. Tarascon, Li–O$_2$ and Li–S batteries with high energy storage, Nat. Mater. 11 (1) (2012) 19–29.

[326] Z. Yang, J. Zhang, M.C.W. Kintner-Meyer, X. Lu, D. Choi, J.P. Lemmon, J. Liu, Electrochemical Energy Storage for Green Grid, Chem. Rev. 111 (5) (2011) 3577–3613.

[327] P.W. Jaschin, Y. Gao, Y. Li, S.-H. Bo, A materials perspective on magnesium-ion-based solid-state electrolytes, J. Mater. Chem. A 8 (6) (2020) 2875–2897.

[328] X.-B. Cheng, R. Zhang, C.-Z. Zhao, Q. Zhang, Toward Safe Lithium Metal Anode in Rechargeable Batteries: A Review, Chem. Rev. 117 (15) (2017) 10403–10473.

[329] J.C. Bachman, S. Muy, A. Grimaud, H.-H. Chang, N. Pour, S.F. Lux, O. Paschos, F. Maglia, S. Lupart, P. Lamp, L. Giordano, Y. Shao-Horn, Inorganic Solid-State Electrolytes for Lithium Batteries: Mechanisms and Properties Governing Ion Conduction, Chem. Rev. 116 (1) (2016) 140–162.

[330] L.i. Shen, H.B. Wu, F. Liu, J.L. Brosmer, G. Shen, X. Wang, J.I. Zink, Q. Xiao, M. Cai, G.e. Wang, Y. Lu, B. Dunn, Creating Lithium-Ion Electrolytes with Biomimetic Ionic Channels in Metal-Organic Frameworks, Adv. Mater. 30 (23) (2018) 1707476, https://doi.org/10.1002/adma.v30.2310.1002/adma.201707476.

[331] C. Yuan, J. Li, P. Han, Y. Lai, Z. Zhang, J. Liu, Enhanced electrochemical performance of poly(ethylene oxide) based composite polymer electrolyte by incorporation of nano-sized metal-organic framework, J. Power Sources 240 (2013) 653–658.

[332] H.B. Wu, X.W.(. Lou, Metal-organic frameworks and their derived materials for electrochemical energy storage and conversion: Promises and challenges, Sci. Adv. 3 (12) (2017) eaap9252, https://doi.org/10.1126/sciadv.aap9252.

[333] F. Zhu, H. Bao, X. Wu, Y. Tao, C. Qin, Z. Su, Z. Kang, High-Performance Metal–Organic Framework-Based Single Ion Conducting Solid-State Electrolytes for Low-Temperature Lithium Metal Batteries, ACS Appl. Mater. Interfaces 11 (46) (2019) 43206–43213.

[334] X.-X. Xie, Y.-C. Yang, B.-H. Dou, Z.-F. Li, G. Li, Proton conductive carboxylate-based metal–organic frameworks, Coord. Chem. Rev. 403 (2020) 213100, https://doi.org/10.1016/j.ccr.2019.213100.

[335] Y. Song, A.E. Khudozhitkov, J. Lee, H. Kang, D.I. Kolokolov, A.G. Stepanov, M. Yoon, Transformation of a proton insulator to a conductor via reversible amorphous to crystalline structure transformation of MOFs, Chem. Commun. 56 (32) (2020) 4468–4471.

[336] M. Qiu, H. Wu, L.i. Cao, B. Shi, X. He, H. Geng, X. Mao, P. Yang, Z. Jiang, Metal–Organic Nanogel with Sulfonated Three-Dimensional Continuous Channels as a Proton Conductor, ACS Appl. Mater. Interfaces 12 (17) (2020) 19788–19796.

[337] D.A. Levenson, J. Zhang, P.M.J. Szell, D.L. Bryce, B.S. Gelfand, R.P.S. Huynh, N.D. Fylstra, G.K.H. Shimizu, Effects of Secondary Anions on Proton Conduction in a Flexible Cationic Phosphonate Metal–Organic Framework, Chem. Mater. 32 (2) (2020) 679–687.

[338] W. Xu, X. Pei, C.S. Diercks, H. Lyu, Z. Ji, O.M. Yaghi, A Metal–Organic Framework of Organic Vertices and Polyoxometalate Linkers as a Solid-State Electrolyte, J. Am. Chem. Soc. 141 (44) (2019) 17522–17526.

[339] Z. Wang, J. Hu, L. Han, Z. Wang, H. Wang, Q. Zhao, J. Liu, F. Pan, A MOF-based single-ion Zn^{2+} solid electrolyte leading to dendrite-free rechargeable Zn batteries, Nano Energy 56 (2019) 92–99.

[340] L. Wang, N. Deng, Y. Liang, J. Ju, B. Cheng, W. Kang, Metal-organic framework anchored sulfonated poly(ether sulfone) nanofibers as highly conductive channels for hybrid proton exchange membranes, J. Power Sources 450 (2020) 227592, https://doi.org/10.1016/j.jpowsour.2019.227592.

[341] S. Mukhopadhyay, J. Debgupta, C. Singh, R. Sarkar, O. Basu, S.K. Das, Designing UiO-66-Based Superprotonic Conductor with the Highest Metal–Organic Framework Based Proton Conductivity, ACS Appl. Mater. Interfaces 11 (14) (2019) 13423–13432.

[342] X.-M. Li, J. Liu, C. Zhao, J.-L. Zhou, L. Zhao, S.-L. Li, Y.-Q. Lan, Strategic hierarchical improvement of superprotonic conductivity in a stable metal–organic framework system, J. Mater. Chem. A 7 (43) (2019) 25165–25171.

[343] Y. Yoshida, K. Fujie, D.-W. Lim, R. Ikeda, H. Kitagawa, Superionic Conduction over a Wide Temperature Range in a Metal–Organic Framework Impregnated with Ionic Liquids, Angew. Chem. Int. Ed. 58 (32) (2019) 10909–10913.

[344] D. Gui, X. Dai, Z. Tao, T. Zheng, X. Wang, M.A. Silver, J. Shu, L. Chen, Y. Wang, T. Zhang, J. Xie, L. Zou, Y. Xia, J. Zhang, J. Zhang, L. Zhao, J. Diwu, R. Zhou, Z. Chai, S. Wang, Unique Proton Transportation Pathway in a Robust Inorganic Coordination Polymer Leading to Intrinsically High and Sustainable Anhydrous Proton Conductivity, J. Am. Chem. Soc. 140 (19) (2018) 6146–6155.

[345] Y.i. Guo, Z. Jiang, W. Ying, L. Chen, Y. Liu, X. Wang, Z.-J. Jiang, B. Chen, X. Peng, A DNA-Threaded ZIF-8 Membrane with High Proton Conductivity and Low Methanol Permeability, Adv. Mater. 30 (2) (2018) 1705155, https://doi.org/10.1002/adma.v30.210.1002/adma.201705155.

[346] J. Zhang, H.J. Bai, Q. Ren, H. Bin Luo, X.M. Ren, Z.F. Tian, S. Lu, Extra Water- and Acid-Stable MOF-801 with High Proton Conductivity and Its Composite Membrane for Proton-Exchange Membrane, ACS Appl, Mater. Interfaces. 10 (2018) 28656–28663, https://doi.org/10.1021/acsami.8b09070.

[347] H. Chen, S.-Y. Han, R.-H. Liu, T.-F. Chen, K.-L. Bi, J.-B. Liang, Y.-H. Deng, C.-Q. Wan, High conductive, long-term durable, anhydrous proton conductive solid-state electrolyte based on a metal-organic framework impregnated with binary ionic liquids: Synthesis, characteristic and effect of anion, J. Power Sources 376 (2018) 168–176.

[348] Q.i. Zhang, D. Li, J. Wang, S. Guo, W. Zhang, D. Chen, Q.i. Li, X. Rui, L. Gan, S. Huang, Multiscale optimization of Li-ion diffusion in solid lithium metal batteries via ion conductive metal–organic frameworks, Nanoscale 12 (13) (2020) 6976–6982.

[349] H. Yang, B. Liu, J. Bright, S. Kasani, J. Yang, X. Zhang, N. Wu, A Single-Ion Conducting UiO-66 Metal–Organic Framework Electrolyte for All-Solid-State Lithium Batteries, ACS Appl. Energy Mater. 3 (4) (2020) 4007–4013.

[350] Q. Han, S. Wang, Z. Jiang, X. Hu, H. Wang, Composite Polymer Electrolyte Incorporating Metal–Organic Framework Nanosheets with Improved Electrochemical Stability for All-Solid-State Li Metal Batteries, ACS Appl. Mater. Interfaces 12 (18) (2020) 20514–20521.

[351] Z. Zhang, Y. Huang, H. Gao, J. Hang, C. Li, P. Liu, MOF-derived ionic conductor enhancing polymer electrolytes with superior electrochemical performances for all solid lithium metal batteries, J. Membr. Sci. 598 (2020) 117800, https://doi.org/10.1016/j.memsci.2019.117800.

[352] C. Sun, J.-H. Zhang, X.-F. Yuan, J.-N. Duan, S.-W. Deng, J.-M. Fan, J.-K. Chang, M.-S. Zheng, Q.-F. Dong, ZIF-8-Based Quasi-Solid-State Electrolyte for Lithium Batteries, ACS Appl. Mater. Interfaces 11 (50) (2019) 46671–46677.

[353] S. Fischer, J. Roeser, T.C. Lin, R.H. DeBlock, J. Lau, B.S. Dunn, F. Hoffmann, M. Fröba, A. Thomas, S.H. Tolbert, A Metal–Organic Framework with Tetrahedral Aluminate Sites as a Single-Ion Li$^+$ Solid Electrolyte, Angew. Chem. Int. Ed. 57 (51) (2018) 16683–16687.

[354] S.S. Park, Y. Tulchinsky, M. Dincă, Single-Ion Li$^+$, Na$^+$, and Mg^{2+} Solid Electrolytes Supported by a Mesoporous Anionic Cu–Azolate Metal–Organic Framework, J. Am. Chem. Soc. 139 (38) (2017) 13260–13263.

[355] Z. Liang, C. Qu, W. Guo, R. Zou, Q. Xu, Pristine Metal-Organic Frameworks and their Composites for Energy Storage and Conversion, Adv. Mater. 30 (37) (2018) 1702891, https://doi.org/10.1002/adma.v30.3710.1002/adma.201702891.

[356] H. Wang, Q.-L. Zhu, R. Zou, Q. Xu, Metal-Organic Frameworks for Energy Applications, Chem 2 (1) (2017) 52–80.

[357] V. Shrivastav, S. Sundriyal, P. Goel, H. Kaur, S.K. Tuteja, K. Vikrant, K.-H. Kim, U.K. Tiwari, A. Deep, Metal-organic frameworks (MOFs) and their composites as electrodes for lithium battery applications: Novel means for alternative energy storage, Coord. Chem. Rev. 393 (2019) 48–78.

[358] L. Kong, M. Zhong, W. Shuang, Y. Xu, X.-H. Bu, Electrochemically active sites inside crystalline porous materials for energy storage and conversion, Chem. Soc. Rev. 49 (8) (2020) 2378–2407.

[359] V. Etacheri, R. Marom, R. Elazari, G. Salitra, D. Aurbach, Challenges in the development of advanced Li-ion batteries: a review, Energy Environ. Sci. 4 (9) (2011) 3243, https://doi.org/10.1039/c1ee01598b.

[360] J.-M. Tarascon, M. Armand, Issues and challenges facing rechargeable lithium batteries, Nature 414 (6861) (2001) 359–367.

[361] L. Ji, Z. Lin, M. Alcoutlabi, X. Zhang, Recent developments in nanostructured anode materials for rechargeable lithium-ion batteries, Energy Environ. Sci. 4 (8) (2011) 2682, https://doi.org/10.1039/c0ee00699h.

[362] R. Zhao, Z. Liang, R. Zou, Q. Xu, Metal-Organic Frameworks for Batteries, Joule 2 (11) (2018) 2235–2259.

[363] J. Zhou, B.o. Wang, Emerging crystalline porous materials as a multifunctional platform for electrochemical energy storage, Chem. Soc. Rev. 46 (22) (2017) 6927–6945.

[364] W. Xia, A. Mahmood, R. Zou, Q. Xu, Metal–organic frameworks and their derived nanostructures for electrochemical energy storage and conversion, Energy Environ. Sci. 8 (7) (2015) 1837–1866.

[365] L. Guo, J. Sun, W. Zhang, L. Hou, L. Liang, Y. Liu, C. Yuan, Bottom-Up Fabrication of 1D Cu-based Conductive Metal–Organic Framework Nanowires as a High-Rate Anode towards Efficient Lithium Storage, ChemSusChem 12 (22) (2019) 5051–5058.

[366] Y. Luo, M. Wu, B. Pang, J. Ge, R. Li, P. Zhang, M. Zhou, L. Han, S. Okada, Metal-organic Framework of [Cu$_2$(BIPA-TC)(DMA)$_2$]n: A Promising Anode Material for Lithium-Ion Battery, ChemistrySelect 5 (14) (2020) 4160–4164.

[367] S.-B. Xia, F.-S. Li, X. Shen, X. Li, F.-X. Cheng, C.-K. Sun, H. Guo, J.-J. Liu, A lanthanide-based coordination polymer as lithium ion battery anode with high cyclic stability, Mater. Let. 238 (2019) 171–174.

[368] Z. Ye, Y. Liu, C. Fang, W. Chen, M. Ou, L. Li, X. Lin, Z. Rao, Y. Liao, R. Zhao, W. Chen, Y. Huang, Coordination induced electron redistribution to achieve

highly reversible Li-ion insertion chemistry in metal–organic frameworks, Chem. Commun. 56 (47) (2020) 6424–6427.

[369] P. Wang, M. Shen, H.u. Zhou, C. Meng, A. Yuan, MOF-Derived CuS@Cu-BTC Composites as High-Performance Anodes for Lithium-Ion Batteries, Small 15 (47) (2019) 1903522, https://doi.org/10.1002/smll.v15.4710.1002/smll.201903522.

[370] C. Gao, P. Wang, Z. Wang, S.K. Kær, Y. Zhang, Y. Yue, The disordering-enhanced performances of the Al-MOF/graphene composite anodes for lithium ion batteries, Nano Energy 65 (2019) 104032, https://doi.org/10.1016/j.nanoen.2019.104032.

[371] Z.-Q. Du, Y.-P. Li, X.-X. Wang, J. Wang, Q.-G. Zhai, Enhanced electrochemical performance of Li–Co-BTC ternary metal–organic frameworks as cathode materials for lithium-ion batteries, Dalton Trans. 48 (6) (2019) 2013–2018.

[372] Q. Jiang, P. Xiong, J. Liu, Z. Xie, Q. Wang, X.-Q. Yang, E. Hu, Y.u. Cao, J. Sun, Y. Xu, L. Chen, A Redox-Active 2D Metal–Organic Framework for Efficient Lithium Storage with Extraordinary High Capacity, Angew. Chem. Int. Ed. 59 (13) (2020) 5273–5277, https://doi.org/https://doi.org/10.1002/anie.201914395.

[373] K.T. Lee, T.N. Ramesh, F. Nan, G. Botton, L.F. Nazar, Topochemical Synthesis of Sodium Metal Phosphate Olivines for Sodium-Ion Batteries, Chem. Mater. 23 (16) (2011) 3593–3600.

[374] Y. Zhang, J. Wang, S.N. Riduan, Strategies toward improving the performance of organic electrodes in rechargeable lithium (sodium) batteries, J. Mater. Chem. A 4 (39) (2016) 14902–14914.

[375] J. Park, M. Lee, D. Feng, Z. Huang, A.C. Hinckley, A. Yakovenko, X. Zou, Y.i. Cui, Z. Bao, Stabilization of Hexaaminobenzene in a 2D Conductive Metal–Organic Framework for High Power Sodium Storage, J. Am. Chem. Soc. 140 (32) (2018) 10315–10323.

[376] Y. Huang, C. Fang, R. Zeng, Y. Liu, W. Zhang, Y. Wang, Q. Liu, Y. Huang, In Situ-Formed Hierarchical Metal-Organic Flexible Cathode for High-Energy Sodium-Ion Batteries, ChemSusChem 10 (23) (2017) 4704–4708.

[377] L. Kong, J. Zhu, W. Shuang, X.-H. Bu, Nitrogen-Doped Wrinkled Carbon Foils Derived from MOF Nanosheets for Superior Sodium Storage, Adv. Energy Mater. 8 (25) (2018) 1801515, https://doi.org/10.1002/aenm.v8.2510.1002/aenm.201801515.

[378] C. Dong, L. Xu, Cobalt- and Cadmium-Based Metal–Organic Frameworks as High-Performance Anodes for Sodium Ion Batteries and Lithium Ion Batteries, ACS Appl. Mater. Interfaces 9 (8) (2017) 7160–7168.

[379] Y. Zhang, S. Yang, X. Chang, H. Guo, Y. Li, M. Wang, W. Li, L. Jiao, Y. Wang, MOF based on a longer linear ligand: electrochemical performance, reaction kinetics, and use as a novel anode material for sodium-ion batteries, Chem. Commun. 54 (83) (2018) 11793–11796.

[380] C. Fang, Y. Huang, L. Yuan, Y. Liu, W. Chen, Y. Huang, K. Chen, J. Han, Q. Liu, Y. Huang, A Metal-Organic Compound as Cathode Material with Superhigh Capacity Achieved by Reversible Cationic and Anionic Redox Chemistry for High-Energy Sodium-Ion Batteries, Angew. Chem. Int. Ed. 56 (24) (2017) 6793–6797, https://doi.org/https://doi.org/10.1002/anie.201701213.

[381] Y. Shao, M.F. El-Kady, J. Sun, Y. Li, Q. Zhang, M. Zhu, H. Wang, B. Dunn, R.B. Kaner, Design and Mechanisms of Asymmetric Supercapacitors, Chem. Rev. 118 (18) (2018) 9233–9280.

[382] L.u. Wang, Y. Han, X. Feng, J. Zhou, P. Qi, B.o. Wang, Metal–organic frameworks for energy storage: Batteries and supercapacitors, Coord. Chem. Rev. 307 (2016) 361–381.

[383] G. Xu, P. Nie, H. Dou, B. Ding, L. Li, X. Zhang, Exploring metal organic frameworks for energy storage in batteries and supercapacitors, Mater. Today 20 (4) (2017) 191–209.

[384] D. Feng, T. Lei, M.R. Lukatskaya, J. Park, Z. Huang, M. Lee, L. Shaw, S. Chen, A.A. Yakovenko, A. Kulkarni, J. Xiao, K. Fredrickson, J.B. Tok, X. Zou, Y.i. Cui, Z. Bao, Robust and conductive two-dimensional metal−organic frameworks with exceptionally high volumetric and areal capacitance, Nat. Energy 3 (1) (2018) 30–36.

[385] D.K. Nguyen, I.M. Schepisi, F.Z. Amir, Extraordinary cycling stability of Ni$_3$(HITP)$_2$ supercapacitors fabricated by electrophoretic deposition: Cycling at 100,000 cycles, Chem. Eng. J. 378 (2019) 122150, https://doi.org/10.1016/j.cej.2019.122150.

[386] S. Zhou, X. Kong, B. Zheng, F. Huo, M. Strømme, C. Xu, Cellulose Nanofiber @ Conductive Metal–Organic Frameworks for High-Performance Flexible Supercapacitors, ACS Nano 13 (8) (2019) 9578–9586.

[387] X.-M. Cao, Z.-B. Han, Hollow core–shell ZnO@ZIF-8 on carbon cloth for flexible supercapacitors with ultrahigh areal capacitance, Chem. Commun. 55 (12) (2019) 1746–1749.

[388] W. Volksen, R.D. Miller, G. Dubois, Low Dielectric Constant Materials, Chem. Rev. 110 (1) (2010) 56–110.

[389] S.E. Thompson, S. Parthasarathy, Moore's law: the future of Si microelectronics, Mater. Today 9 (6) (2006) 20–25.

[390] P. Gargini, The International Technology Roadmap for Semiconductors (ITRS): "Past, present and future", IEEE (2002) 3–5, https://doi.org/10.1109/gaas.2000.906261.

[391] M. Usman, K.-L. Lu, Metal–organic frameworks: The future of low-κ materials e333-e333 NPG Asia Mater. 8 (12) (2016).

[392] S. Mendiratta, M. Usman, K.-L. Lu, Expanding the dimensions of metal–organic framework research towards dielectrics, Coord. Chem. Rev. 360 (2018) 77–91.

[393] K. Zagorodniy, G. Seifert, H. Hermann, Metal-organic frameworks as promising candidates for future ultralow-k dielectrics, Appl. Phys. Lett. 97 (25) (2010) 251905, https://doi.org/10.1063/1.3529461.

[394] S. Eslava, L. Zhang, S. Esconjauregui, J. Yang, K. Vanstreels, M.R. Baklanov, E. Saiz, Metal-Organic Framework ZIF-8 Films As Low-κ Dielectrics in Microelectronics, Chem. Mater. 25 (1) (2013) 27–33.

[395] M. Usman, S. Mendiratta, K.-L. Lu, Metal-Organic Frameworks: New Interlayer Dielectric Materials, ChemElectroChem 2 (6) (2015) 786–788.

[396] S. Galli, A. Cimino, J.F. Ivy, C. Giacobbe, R.K. Arvapally, R. Vismara, S. Checchia, M.A. Rawshdeh, C.T. Cardenas, W.K. Yaseen, A. Maspero, M.A. Omary, Fluorous, Metal-Organic Frameworks and Nonporous Coordination Polymers as Low-κ Dielectrics, Adv. Funct. Mater. 29 (2019) 1904707, https://doi.org/10.1002/adfm.201904707.

[397] M. Krishtab, I. Stassen, Y. Stassin, A.J. Cruz, O.O. Okudur, S. Armini, C. Wilson, S. De Gendt, R. Ameloot, Vapor-deposited zeolitic imidazolate frameworks as gap-filling ultra-low-k dielectrics, Nat. Commun. 10 (1) (2019), https://doi.org/10.1038/s41467-019-11703-x.

[398] W. Xu, S.S. Yu, H. Zhang, H.B. Duan, A three-dimensional metal–organic framework for a guest-free ultra-low dielectric material, RSC Adv. 9 (28) (2019) 16183–16186.

[399] X. Zhou, X. Liu, Z. Cui, J. Gu, S. Lin, Q. Zhuang, Design and development of HMS@ZIF-8/fluorinated polybenzoxazole composite films with excellent low- k performance, mechanical properties and thermal stability, J. Mater. Chem. C 8 (22) (2020) 7476–7484.

[400] Y.-C. Kao, S. Mendiratta, M. Usman, Y.-S. Wen, C.-M. Wang, L. Zhao, M.-K. Wu, K.-L. Lu, Exceptional Low Dielectric Behavior of Chemically Robust, Guest-Free Co- and Mn-Based Coordination Polymers, ChemElectroChem 6 (3) (2019) 623–626.

[401] C. Liu, M. Mullins, S. Hawkins, M. Kotaki, H.-J. Sue, Epoxy Nanocomposites Containing Zeolitic Imidazolate Framework-8, ACS Appl. Mater. Interfaces 10 (1) (2018) 1250–1257.

[402] K. Leong, O.K. Farha, M. Allendorf, R.P. Van Duyne, J.T. Hupp, Metal–Organic Framework Materials as Chemical Sensors, Chem. Rev. 112 (2) (2012) 1105–1125.

[403] W.P. Lustig, S. Mukherjee, N.D. Rudd, A.V. Desai, J. Li, S.K. Ghosh, Metal–organic frameworks: functional luminescent and photonic materials for sensing applications, Chem. Soc. Rev. 46 (11) (2017) 3242–3285.

[404] T. Rasheed, F. Nabeel, Luminescent metal-organic frameworks as potential sensory materials for various environmental toxic agents, Coord. Chem. Rev. 401 (2019) 213065, https://doi.org/10.1016/j.ccr.2019.213065.

[405] S. Venkateswarlu, A.S. Reddy, A. Panda, D. Sarkar, Y. Son, M. Yoon, Reversible Fluorescence Switching of Metal–Organic Framework Nanoparticles for Use as Security Ink and Detection of Pb^{2+} Ions in Aqueous Media, ACS Appl. Nano Mater. 3 (4) (2020) 3684–3692.

[406] Y. Yu, Y. Wang, H. Yan, J. Lu, H. Liu, Y. Li, S. Wang, D. Li, J. Dou, L. Yang, Z. Zhou, Multiresponsive Luminescent Sensitivities of a 3D Cd-CP with Visual Turn-on and Ratiometric Sensing toward Al^{3+} and Cr^{3+} as Well as Turn-off Sensing toward Fe^{3+}, Inorg. Chem. 59 (6) (2020) 3828–3837.

[407] H.A.J. Hibbard, M.J. Burnley, H.N. Rubin, J.A. Miera, M.M. Reynolds, Porphyrin-based metal-organic framework and polyvinylchloride composites for fluorescence sensing of divalent cadmium ions in water, Inorg. Chem. Commun. 115 (2020) 107861, https://doi.org/10.1016/j.inoche.2020.107861.

[408] S. Nandi, H. Reinsch, S. Biswas, A vinyl functionalized mixed linker CAU-10 metal-organic framework acting as a fluorescent sensor for the selective detection of H$_2$S and palladium(II), Micropor. Mesopor. Mater. 293 (2020) 109790, https://doi.org/10.1016/j.micromeso.2019.109790.

[409] A. Pankajakshan, D. Kuznetsov, S. Mandal, Ultrasensitive Detection of Hg(II) Ions in Aqueous Medium Using Zinc-Based Metal–Organic Framework, Inorg. Chem. 58 (2) (2019) 1377–1381.

[410] N. Abdollahi, A. Morsali, Highly sensitive fluorescent metal-organic framework as a selective sensor of MnVII and CrVI anions (MnO$_4^-$/Cr$_2$O$_7^{2-}$/CrO$_4^{2-}$) in aqueous solutions, Anal. Chim. Acta 1064 (2019) 119–125.

[411] X. Li, J. Tang, H. Liu, K. Gao, X. Meng, J. Wu, H. Hou, A Highly Sensitive and Recyclable Ln-MOF Luminescent Sensor for the Efficient Detection of Fe^{3+} and Cr^{VI} Anions, Chem. Asian J. 14 (20) (2019) 3721–3727.

[412] J. Zhao, X. Qu, J. Wang, B. Yan, Photophysical Tuning of Viologen-Based Metal–Organic Framework Hybrids via Anion Exchange and Chemical Sensing on Persulfate (S$_2$O$_8^{2-}$), Ind. Eng. Chem. Res. 58 (40) (2019) 18533–18539.

[413] Y. Zhao, M. Pan, F. Liu, Y. Liu, P. Dong, J. Feng, T. Shi, X. Liu, Highly selective and sensitive detection of trinitrotoluene by framework-enhanced fluorescence of gold nanoclusters, Anal. Chim. Acta 1106 (2020) 133–138.

[414] W. Xu, H. Chen, Z. Xia, C. Ren, J. Han, W. Sun, Q. Wei, G. Xie, S. Chen, A Robust Tb^{III} -MOF for Ultrasensitive Detection of Trinitrophenol: Matched Channel Dimensions and Strong Host–Guest Interactions, Inorg. Chem. 58 (12) (2019) 8198–8207.

[415] X. Zhang, G. Ren, M. Li, W. Yang, Q. Pan, Selective Detection of Aromatic Nitrophenols by a Metal–Organic Framework-Based Fluorescent Sensor, Crystal Growth & Design 19 (11) (2019) 6308–6314.

[416] C. Li, L. Zhu, W. Yang, X. He, H. Zhao, W. Tang, T. Yue, Z. Li, Post-functionalized Al-based metal-organic frameworks for fluorescent detection of total iron in food matrix, J. Food Compos. Anal. 86 (2020) 103352, https://doi.org/10.1016/j.jfca.2019.103352.

[417] L. Wang, B. Tu, W. Xu, Y. Fu, Y. Zheng, Uranyl Organic Framework as a Highly Selective and Sensitive Turn-on and Turn-off Luminescent Sensor for Dual Functional Detection Arginine and MnO^{4-}, Inorg. Chem. 59 (7) (2020) 5004–5017.

[418] L. Luconi, G. Mercuri, T. Islamoglu, A. Fermi, G. Bergamini, G. Giambastiani, A. Rossin, Benzothiazolium-functionalized NU-1000: a versatile material for

carbon dioxide adsorption and cyanide luminescence sensing, J. Mater. Chem. C 8 (22) (2020) 7492–7500.

[419] L.-L. Qian, Z.-X. Wang, J.-G. Ding, H.-X. Tian, K. Li, B.-L. Li, H.-Y. Li, A 2D copper (I) metal-organic framework: Synthesis, structure and luminescence sensing for cupric, ferric, chromate and TNP, Dyes Pigm. 175 (2020) 108159, https://doi.org/10.1016/j.dyepig.2019.108159.

[420] P.C. Rao, S. Mandal, Europium-Based Metal–Organic Framework as a Dual Luminescence Sensor for the Selective Detection of the Phosphate Anion and Fe^{3+} Ion in Aqueous Media, Inorg. Chem. 57 (19) (2018) 11855–11858.

[421] Y. Tang, H. Wu, J. Chen, J. Jia, J. Yu, Wei Xu, Y. Fu, Q. He, H. Cao, J. Cheng, A highly fluorescent metal organic framework probe for 2,4,6-trinitrophenol detection via post-synthetic modification of UIO-66-NH_2, Dyes Pigm. 167 (2019) 10–15.

[422] X.-J. Zhang, F.-Z. Su, D.-M. Chen, Y. Peng, W.-Y. Guo, C.-S. Liu, M. Du, A water-stable Eu^{III} -based MOF as a dual-emission luminescent sensor for discriminative detection of nitroaromatic pollutants, Dalton Trans. 48 (5) (2019) 1843–1849.

[423] M. Sharafizadeh, J. Mokhtari, H. Saeidian, Z. Mirjafary, Urea metal-organic frameworks as a highly selective fluorescent sensor for the explosive nitroaromatics and carbonyl compounds, J. Porous Mater. 27 (2) (2020) 603–609.

[424] W. Liu, X. Huang, C. Chen, C. Xu, J. Ma, L. Yang, W. Wang, W. Dou, W. Liu, Function-Oriented: The Construction of Lanthanide MOF Luminescent Sensors Containing Dual-Function Urea Hydrogen-Bond Sites for Efficient Detection of Picric Acid, Chem. Eur. J. 25 (4) (2019) 1090–1097.

[425] H. Kaur, S. Sundriyal, V. Pachauri, S. Ingebrandt, K.-H. Kim, A.L. Sharma, A. Deep, Luminescent metal-organic frameworks and their composites: Potential future materials for organic light emitting displays, Coord. Chem. Rev. 401 (2019) 213077, https://doi.org/10.1016/j.ccr.2019.213077.

[426] W.P. Lustig, Z. Shen, S.J. Teat, N. Javed, E. Velasco, D.M. O'Carroll, J. Li, Rational design of a high-efficiency, multivariate metal–organic framework phosphor for white LED bulbs, Chem. Sci. 11 (7) (2020) 1814–1824.

[427] T. Mondal, D. Haldar, A. Ghosh, U.K. Ghorai, S.K. Saha, A MOF functionalized with CdTe quantum dots as an efficient white light emitting phosphor material for applications in displays, New J. Chem. 44 (1) (2020) 55–63.

[428] X.-Y. Liu, Y. Li, C.-K. Tsung, J. Li, Encapsulation of yellow phosphors into nanocrystalline metal–organic frameworks for blue-excitable white light emission, Chem. Commun. 55 (72) (2019) 10669–10672.

[429] K. Maity, D. Mukherjee, M. Sen, K. Biradha, Fluorescent Dye-Based Metal–Organic Framework Piezochromic and Multicolor-Emitting Two-Dimensional Materials for Light-Emitting Devices, ACS Appl. Nano Mater. 2 (3) (2019) 1614–1620.

[430] Q. Wang, Q. Liu, X.-M. Du, B. Zhao, Y. Li, W.-J. Ruan, A white-light-emitting single MOF sensor-based array for berberine homologue discrimination, J. Mater. Chem. C 8 (4) (2020) 1433–1439.

[431] A. Wang, Y.-L. Hou, F. Kang, F. Lyu, Y. Xiong, W.-C. Chen, C.-S. Lee, Z. Xu, A.L. Rogach, J. Lu, Y.Y. Li, Rare earth-free composites of carbon dots/metal–organic frameworks as white light emitting phosphors, J. Mater. Chem. C 7 (8) (2019) 2207–2211.